Approximate Methods for the Real-Time Evolution of Quantum Systems and Fields

Autor: Fermín Nuevo España

Tésis realizada bajo la tultela de:
D. Antonio González-Arroyo [b]
[b] Catedrático de la UAM e investigador del Instituto de Física Teórica UAM/CSIC

Lugar de realización: Departamento de Física Teórica.
Facultad de Ciencias. UAM.

September 10, 2012

Contents

1 Introduction and Overview

1.1 Motivations

The time evolution of quantum systems is relevant for many areas of Modern Physics. In QM (Quantum Mechanics) the evolution is governed by the Schroedinger equation. This is a linear partial differential equation that evolves the wave function and that depends on the considered Hamiltonian (which can depend on time or not) [1]. An exact analytical solution is only available for a few cases that are well documented in the literature [1][2]. In the remaining cases it is necessary to make some approximations or use computational methods.
The application of computational techniques allow us to solve numerically the Schroedinger equation for a few degrees of freedom. These techniques involve the use of numerical methods in order to implement computer programs to perform the corresponding computational simulations. The programs can be implemented in any of the programming languages available, as for example FORTRAN or C.
About the numerical methods, there are several ways to numerically solve differential equations, as for example the successive approximations or finite differences method [3][4]. Usually one uses this last method to discretize the Schroedinger equation and solve it with the required accuracy. To discretize the derivatives that appear in differential equations one can choose several methods with different accuracy, as the Euler method with symmetrized derivatives or the Runge-Kutta method. One can see a good report about the implementation of these and many other numerical techniques in [5].

However, when the number of degrees of freedom grows, the aforementioned techniques to solve the quantum evolution become very difficult to perform. This is what happens in QFT (Quantum Field Theory), where an infinite number of degrees of freedom is involved. The analytical study of the evolution of quantum fields and their expectation values can be seen in many text-books as [6][7]. This study includes perturbative techniques that lead to a diagrammatic representation of the expectation values (Feynman diagrams) and allow us to perform analytical calculations to a concrete order in the expansion parameter (which can be, for example, the coupling constant or the inverse of the number of field components). Nevertheless, in many modern problems one studies non-perturbative effects in the evolution of quantum

fields, so that one has to employ numerical computational methods.
About the numerical treatment of fields, an entire area of Physics has been developed for this purpose: the Lattice Field Theory [8][9]. Here the space-time is discretized and one works in a lattice of finite size. The fields are defined at lattice sites and the expectation values can be obtained from stochastic simulation techniques. Later the continuum physics is recovered taking the lattice spacing to zero together with the corresponding renormalization of the parameters. These techniques can be applied to different kinds of fields, as for example to gauge fields (Lattice Gauge Theory [10]), where the lattice sites are connected by links (gauge fields) and where the Wilson action [11] is usually used.

Many authors invested considerable effort to develop approximate methods that allow suitable calculations in QFT through computational methods.
When computing expectation values of operators in the vacuum or in the equilibrium state, one can use the path-integral approach. By a Wick-rotation the complex quantum weight of each trajectory is transformed into a positive-definite probability weight and one can compute the (Wick-rotated) Green functions of the theory. This allows the use of efficient standard importance sampling techniques, such as the Metropolis algorithm or other Monte Carlo techniques [12]. The same applies when studying Quantum Field Theory at equilibrium. However, even in this situation, there are important exceptions in which the weights are not positive definite and the standard Monte Carlo methods fail. This is often referred as *the sign problem*. The physicists have had to deal with this problem in different areas and have searched to avoid it, as for example in quantum mechanical system with large number of strongly-interacting fermions [13] or in field theories to simulate lattice QCD at finite baryon density [14]. However, it is generally accepted that, despite the efforts, no fully satisfactory solution has been found. This is particularly unwelcome, since full-proof predictions in certain areas of Physics, which are of great relevance and timeliness, are lacking.

When studying the quantum evolution away from equilibrium or from a initial state which is not an eigenstate of the Hamiltonian the situation is even more severe. The abundance of experimental data from relativistic heavy-ion collision experiments, as well as applications in astrophysics and cosmology requires a quantitative understanding of *far from equilibrium* quantum field theory. In this context, path integral methods for time-dependent expecta-

tion values follow from the Schwinger-Keldysh formalism [15][16]. This allows systematic perturbative calculations. However, non-perturbative phenomena are often crucial and we lack an efficient numerical computational method to deal with this situation (for a review see Ref. [17]).
A review about heavy-ion collision can be found in [18][19].

One of the areas that requires the calculation of non-linear quantum evolution, and that actually triggered our interest in the problem, is Cosmology. Quantum fluctuations play a role at different instances in the early Universe. One such case is at the inflationary era, by generating the density fluctuations which act as sources for the anisotropies of the cosmic background radiation and the formation of structures. Many authors argued that the fluctuations develop from quantum to classical, and can be treated as classical at late times [20]-[26]. Another interesting epoch which depends crucially on the understanding of the quantum evolution of a quantum field theory, is that of preheating and reheating after inflation [27]-[29]. Properties of the present Universe, such as baryon number density, gravitational waves or magnetic field remnants, might depend upon this dynamics. Obtaining reliable estimates demand an appropriate treatment of the quantum field theory evolution from an initial state after inflation to the fully thermalized reheated Universe. To estimate these effects, several authors [30]-[41] have employed (besides other methods) the so-called classical approximation (for a somewhat different context see also Refs. [42][43]). To make these statements more precise, we are now going to describe the particular case of a concrete Hybrid Inflation model, which served as basis and motivation of our research. Later, we will use this model to illustrate and explain the mentioned classical approximation.

1.1.1 Illustrative model: Hybrid Inflation

We perform here a brief description of a Hybrid Inflation model as an example where the classical approximation (besides other methods) has been applied, following ref. [33]. In this concrete model, inflation ends at electroweak energy scale driven by the coupling of the inflaton to the ordinary Higgs boson. These last stages are accompanied by the evolution of the system to the standard symmetry breaking vacuum. At this scale one can ignore the rate of expansion and consider the fields in Minkowski space.
The hybrid inflation model used is a simple generalization of the symmetry

breaking sector on the standard model. We will consider the Higgs field, Φ, and a scalar field called Inflaton, χ. The inflaton will couple with the Higgs, with a coupling constant g. To simplify the dynamics analysis we will ignore the Gauge fields and we will consider only one Higgs component (ϕ). The fundamental conclusions will be not affected by this simplification [33].
The inflaton will be, as usual, a homogeneous and isotropic field, i.e., $\chi = \chi(t)$. The coupling of the inflaton with the Higgs will give an effective mass square dependent on time for the latter. The evolution can make this parameter negative recovering the stage of symmetry breaking for the Higgs.

Hybrid inflation potential

For our model, the coupled field potential is:

$$V(\phi,\chi) = \frac{\lambda}{4}\left(\phi^2 - v^2\right)^2 + \frac{g^2}{2}\phi^2\chi^2 + \frac{1}{2}\mu^2\chi^2 \tag{1}$$

where we have real fields with one component. Here $v = 246$ Gev is the Higgs field expectation value in true vacuum and μ is the inflaton mass in the false vacuum. If we expand the square and group the terms that multiply ϕ^2 we get

$$V(\phi,\chi) = \frac{1}{2}\left(g^2\chi^2 - \lambda v^2\right)\phi^2 + \frac{1}{2}\mu\chi^2 + \frac{\lambda}{4}\phi^4 + \frac{\lambda}{4}v^4 \tag{2}$$

Since we have considered the inflaton an isotropic and homogeneous field, $\chi = \chi(t)$, the effective Higgs mass square has a time dependence due to the coupling. But the inflaton field evolves from very high values at the beginning of the inflationary period to practically zero after a Slow-Roll period [44]. This means that the effective Higgs mass square changes from a positive value to a negative one as the system evolves. The point when the value is zero is called *bifurcation point* $\chi \equiv \chi_c = m/g$, con $m^2 = \lambda v^2$. Thus, we can write the effective Higgs mass square in this manner:

$$m_\phi^2(t) = m^2\left(\frac{\chi^2(t)}{\chi_c^2} - 1\right) \tag{3}$$

When the system evolves beyond the bifurcation point and $m_\phi^2(t)$ becomes negative there appear tachyonic modes that grow quickly under a process of tachyonic preheating [32].

Fourier expansion of the field

Consider the effective action for the Higgs field ($\phi(\mathbf{x},t)$):

$$S=\int d^3\mathbf{x}dt\,\frac{1}{2}\left[(\dot{\phi})^2-(\nabla\phi)^2-m_\phi^2(t)\phi^2-\frac{\lambda}{2}\phi^4\right] \tag{4}$$

that corresponds to the Hamiltonian:

$$H=\int d^3\mathbf{x}\frac{1}{2}\left[\pi^2+(\nabla\phi)^2+m_\phi^2(t)\phi^2+\frac{\lambda}{2}\phi^4\right] \tag{5}$$

with the conjugate momentum of the field expressed as $\pi=\frac{\partial\mathcal{L}}{\partial\dot{\phi}}=\dot{\phi}$. If we expand the Higgs field on Fourier terms

$$\phi(\mathbf{k},t)=\int\frac{d^3\mathbf{x}}{(2\pi)^{3/2}}\phi(\mathbf{x},t)\,\exp(-i\mathbf{x}\cdot\mathbf{k}) \tag{6}$$

and rewrite the Hamiltonian in the space of momenta, using the expansion above, we obtain:

$$H=\int d^3\mathbf{k}\frac{1}{2}\Big[|\pi(\mathbf{k},t)|^2+(k^2+m_\phi^2(t))|\phi(\mathbf{k},t)|^2+$$
$$+\frac{\lambda}{2(2\pi)^3}\phi(\mathbf{k},t)\int d^3\mathbf{k}'\int d^3\mathbf{k}''\;\phi(\mathbf{k}',t)\phi(\mathbf{k}'',t)\phi(-\mathbf{k}-\mathbf{k}'-\mathbf{k}'',t)\Big] \tag{7}$$

Evolution after inflation

The goal is to study the evolution of the afore-mentioned system from the end of inflation till the reheating of the universe. The first few stages of this process involve fast changes denoted as preheating period, in which symmetry breaking takes place.

In the inflationary paradigm, an usual assumption is that the perturbations were initially in a particular state: the Bunch-Davies vacuum [45]. Given that the effective mass of the Higgs boson is positive and very large during inflation, it is customary to assume that its quantum state is well approximated by a narrow gaussian state.

The quantum evolution of the previous quantum field theory system from this initial state towards symmetry breaking is a very complicated issue. Several authors have employed different approximations to describe this process. Here we will focus mostly in the approach given in Ref. [33].

Gaussian approximation

During the very early stages of preheating one can argue that it is a good approximation to neglect the self-interaction of the Higgs boson. This is called the *gaussian approximation*, and amounts to setting $\lambda = 0$. This is due to the smallness of the quartic term relative to the quadratic one. Besides the value of the coupling itself, the Higgs field is small due to the narrowness of its wave function.
This gaussian approximation allow us to obtain the exact quantum evolution. The corresponding Hamiltonian is given by

$$H = \int d^3\mathbf{k}\frac{1}{2}\left[|\pi(\mathbf{k},t)|^2 + (k^2 + m_\phi^2(t))|\phi(\mathbf{k},t)|^2\right] \tag{8}$$

As we have taken $\phi(\mathbf{x},t)$ real, then $\phi(-\mathbf{k},t) = \phi^*(\mathbf{k},t)$. So the modes $\mathbf{k}$ and $-\mathbf{k}$ are not independent. Therefore each pair $(\mathbf{k},-\mathbf{k})$ is associated with two real degrees of freedom, $Re[\phi(\mathbf{k},t)]$ and $Im[\phi(\mathbf{k},t)]$. From (8), all these degrees of freedom correspond with a set of decoupled harmonic oscillators. In this case the frequency of each oscillator is time dependent. The decoupling of the modes means that to study this quantum system with ∞ degrees of freedom, reduces to doing it for each dof separately.
For this reason we can take a generic quantum field operator $\phi(t) \equiv Re[\phi(\mathbf{k},t)]$ or $\phi(t) \equiv Im[\phi(\mathbf{k},t)]$, for a particular mode, and we have a quantum mechanical system with one degree of freedom. Therefore, in this case, the potential can be expressed as:

$$V(\phi) = \frac{1}{2}(k^2 + m_\phi^2(t))\phi^2 \equiv \frac{1}{2}w^2(t)\phi^2 \tag{9}$$

The gaussian evolution of the modes is very different depending on the value of its momentum k. For a time t beyond the bifurcation point $m_\phi^2(t)$ is negative and the modes with $k^2 < |m_\phi^2(t)|$ are tachyonic. These modes will grow very fast, while higher momenta will remain small. As the tachyonic modes grow, the validity of the approximation which neglects self-coupling ceases to be correct, and the gaussian approximation breaks down. Fortunately, the authors of Ref. [33] argue that the big modes can be treated as classical fields. This is the basis of the so-called *classical approximation*.

Classical approximation with modified initial conditions

As explained before, at later times for which the non-linear behavior cannot be neglected, the tachyonic modes become classical. This is true because, in

our system, the gaussian evolution of tachyonic modes leads to a squeezed state with high occupation numbers. But there remains an infinite number of modes that maintain a quantum behavior. Although small, these infinite modes lead to divergences even in the initial state, which has to be treated through renormalization. However, several authors solve the problem with modified initial conditions [33][46].
The particular proposal of Ref. [33] is to study the classical evolution of the system setting all non-tachyonic modes initially to zero. The starting time for this classical evolution is given by a time later than the bifurcation point at which several modes are argued to behave classically while still small enough to justify the gaussian approximation. This defines a possible window of starting times for the classical evolution equations. The insensitivity of the results to the particular value taken in this window is used to justify the robustness of the approach. The initial conditions for the tachyonic modes are determined by the wave function obtained for them from the gaussian evolution.

1.1.2 Review of the classical approximation

With the framework of inflationary universe, several authors have established the classical behavior of the involved quantum systems at late times. This result has been obtained for different models more or less simple.
In [20] the authors discuss the theory of the upside-down harmonic oscillator with a quadratic potential function which changes from stable to unstable as a function of time, and show that the system can be described at late times by a classical probability distribution. Then they construct a similar model for the scalar field to illustrate the behavior in the inflationary universe, and verify that it can also be described at late times by a classical probability distribution. In [47] one can see a classical study of the onset of inflation for more general initial conditions of the scalar field configuration, with a non-vanishing spatial average of the field. A complete review about classical an quantum cosmological perturbations can be seen in [21], where the classical behavior of perturbations at late times is established. In [22][23][25] the authors also study the quantum-to-classical transition of perturbations in the early Universe, and show the squeezed state as classicality condition. This especial state and the perturbation decoherence justify the classical behavior observed today. The same is studied in [24] for non-vacuum initial states. They use (besides others) the Wigner function formalism, and argue that

the non-positivity of this function does not affect the transition to a semiclassical behavior because in a squeezed state the Wigner function becomes concentrated near a classical trajectory in phase space.
As mentioned, another important epoch is that of preheating and reheating after inflation [30]-[41], whose study requires to give an initial condition and calculate the corresponding non-lineal evolution in QFT. The first results in a numerical study of the semiclassical decay of the Inflaton for a real scalar field with $\lambda\phi^4$ potential can be found in [30], and for the case of two fields (Hybrid Inflation) in [31]. Special attention deserves Ref. [33], where the authors focus on a hybrid inflation stage and give a general framework to solve the gaussian ($\lambda = 0$) evolution equations for time-dependent potentials (also they present the solution for a linear dependence). Thus, the correlation functions for the gaussian evolution of the fields can be written as a function of initial equal time functions. Also the classical approximation is applied to study primordial magnetic fields from preheating in [40][41].

On the other hand, in [42] the non-equilibrium time evolution of quantum scalar fields in the O(N) model for 1+1 dimensions is studied using other approximations (2PI-1/N to NLO quantum and classical) and comparing it with the classical approximation. Both evolutions match with a good accuracy at not too late times for moderate values of N and for sufficiently high initial occupation numbers. After, as one hopes, both evolutions differ for sufficiently late times, since quantum and classical thermal equilibrium are distinct. In [43]) one can see a description of classical fields approximation at high temperature, focusing in a scalar field theory in 2+1 dimensions.

1.2 Objectives of this thesis

One of our main goals, that inspired this work, is to determine the validity of the classical approximation. We aim at estimaty the size of the errors induced by it, and to check the classicality conditions given by several authors. Also we want to propose some dimensionless control parameters involving the Hamiltonian parameters and the initial conditions, in order to test the accuracy of the classical approximation when one changes these control parameters. Moreover, in the same hybrid inflation context, we want to check if indeed there is a window of connection times in which the subsequent classical evolution is the same, because this would be an indication of classicality.

We have also analyzed other frequently used approximate methods to perform the non-lineal evolution. We want to test their validity and compare them with the classical approximation.

Moreover we aimed at obtaining some new ways to go beyond the classical approximation, by incorporating quantum corrections to the results. These alternative approaches might give us extra classicality conditions.

To analyze the validity of each method, we consider simple quantum systems with very few degrees of freedom whose quantum evolution can be obtained by numerical integration of the Schroedinger equation. The initial conditions and the type of Hamiltonians considered are inspired by the field theoretical and cosmological applications. Thus, we focus upon quartic interactions and gaussian initial conditions.

We restricted ourselves to the usual methods used in QFT, which can be implemented to calculate numerically the evolution of systems with many degrees of freedom. The alternative methods that we will propose must follow the same philosophy. In the following we give a brief description of the methods that we will check and their features, including the additional methods that we will present.

Brief description of the methods

It is convenient to show a brief description of the methods that we will check and their features, which will be analyzed and tested along this work, including the alternative methods that we will propose:

Classical Approximation
In the classical approximation, one takes initially a distribution function in the phase space obtained from the quantum state of the system. Then one performs the classical evolution of this function (Liouville).
To implement this evolution numerically, one has to generate an initial sample of points in the phase space according with the mentioned distribution, and evolve each trajectory with the classical equations of motion. The expectation values are calculated as statistical averages over the evolved sample.
We should emphasize that this is not an ordinary classical evolution, because

in this case the position and momentum are random variables whose initial values are given by the initial distribution. Thus, each classical trajectory has a deterministic evolution, but coming from initial random values. In short, we have a classical evolution of a quantum initial state.

2PI Approximations
Another very interesting technique is the two-particle irreducible effective action supplemented with a certain truncation of the number of diagrams involved (2PI method) [48]-[50]. This truncation can be based on the loop expansion or on the 1/N expansion [51]. The latter behaves in a more stable fashion. We remark that the traditional Hartree method can be considered a particular case of the 2PI method [52]-[54]. In any case the method is limited to the determination of the quantum evolution of certain observables, such as the 2-point correlation function of the system (see Ref. [17] for a more complete list of early references on the subject).
A similar method can be also applied in the classical case, and it is noted as 2PI Classical method.
We use the 2PI approximation on systems of QM and compare the results with other approximations and with the exact quantum evolution. From this approximation we also extract a new method that we denote as *Hybrid Method* and that is mentioned in the following paragraph.

Alternative Hybrid Method
Usually, the perturbative expansion and the associated description with Feynman diagrams is performed for time independent Hamiltonians [6]. In [55] the *in-in* or *CPT* formalism [15][16] is reviewed and extended by the author, showing a complicated diagrammatic formalism to calculate equal-time correlation functions and writing the corresponding Feynman rules for time dependent Hamiltonians. These results have been used by other authors (as for instance in [56][57]).
We use the diagrammatic formalism shown in [55] as the basis for a new description in which we use two propagators that appear in the quantum and classical perturbative expansion. This leads to a Feynman rules so that the classical diagrams are a subset of the quantum ones.
Thus, if we rewrite the diagrams involved in the 2PI approximation with our two propagators, the diagrams of the 2PI Classical evolution are a subset of the diagrams of the 2PI Quantum evolution. Of course, the diagrams of the 2PI Classical evolution are also a subset of all classical ones in-

volved in the classical approximation. Therefore, if we calculate any expectation value A with the three mentioned approximations, then the quantity $A_{Hybrid} \equiv A_{2PI-Q} - A_{2PI-Cl} + A_{Cl}$ contains all classical diagrams and the additional purely quantum diagrams coming from the 2PI quantum approximation. So, one hopes that A_{Hybrid} is more accurate. This method is noted as Hybrid Method.

Complex Langevin Method
Another technique which has been recently applied in the context of Quantum Field Theory is the complex Langevin method [58]-[61]. This is based on complexifying the fields and studying the dynamics of the field trajectories induced by a Langevin equation in an additional Langevin-time variable with a purely imaginary drift term. Instabilities are often found in the numerical integration of this equation, although authors have given several recipes to avoid them. It is easy to see that this is a feature of the complex evolution in the discretized new variable and in the absence of random noise. Both the problem and the possible cures have been documented in the literature of the subject. One can employ more refined discretizations or use a much smaller Langevin step [61], but this pays an obvious price in computational cost. A way out proposed in Ref. [62] is to use an adaptive stepsize. Another possibility is a modification of the noise [63].
With this technique, good results have been reported in certain cases, as in [63] [64], but these same authors encounter some problems mentioned in the literature: the occurrence of instabilities and the wrong convergence. Thus, we thought it was very interesting to apply the method to our examples and analyze the results.

New nQC Method
In parallel to the usual methods explained before to do quantum evolution in real time, we present an additional new method to quantify and incorporate quantum effects based upon the *Wigner function* [65]. This is a pseudo-distribution function, whose expectation values give us the matrix elements of Weyl-ordered products of operators in the quantum state of the system. The function is real, but not positive definite (see Ref. [66] for an account of all its properties). The Wigner function satisfies an evolution equation [67] in time, which determines the time-dependence of all these expectation values. One of the advantages of this method, is that it is particularly simple to see what is the meaning of the classical evolution and what is the nature of

quantum corrections. This will be explained in chapter 2. This observation is not novel, and has led different researchers in different fields to focus on the Wigner function and its evolution equation when attempting to describe quantum evolution [68]-[72]. One example, is in Nuclear Physics where several authors [73][74] have developed methodologies which are very similar in spirit to our goal. So, an evolution with signed points was proposed in [69]. Another example is the use of the quantum tomographic approach presented in [75], that involve a positive definite function built from the Wigner function and noted as tomogram. Unfortunately, the detailed techniques seem hard to extend to a large number of degrees and thus to quantum field theory, because these methods need to perform a histogram (to obtain the shape of the Wigner function from the corresponding sample-points) and then only are feasible in QM.

We propose a method involving also the evolution of signed samples in order to emulate the evolution of the Wigner function with a Langevin equation, but that is feasible in QFT. In our particular proposal we have dedicated some time to study the way in which the numerical effort involved scales with the number of degrees of freedom. A power-like growth is acceptable even if it involves an enormous computational effort. Experience teaches us that the development of computer technology and algorithms will diminish the load in due time. An exponential growth is a killer. Our results presented in this thesis are promising and seem to allow the computation of quantum corrections in typical situations relevant for cosmological applications.

Firstly, we will apply this method to quantum-mechanical systems in which we have the advantage of knowing the exact quantum result. So we can test the method, evaluate the errors and compare with other methods. After we will show how to extend the method to QFT, and we will display several results that prove their usefulness. If the number of sample-points remains constant, the computational cost scales proportionally to the number of degrees of freedom N. Moreover, we verified that the statistical errors do not grow too when N is increasing and they remain in a low percentage. So the method is promising, although it presents a limited validity time that can be fixed in each system by controlling certain parameters that will explain in a later chapter.

Of course, the field theoretical case demands a much higher computational cost than the quantum mechanical case, in addition with the necessity of dealing with issues as renormalization.

1.3 Summary

We present a brief description of contents included in this thesis:

- **Chapter 1:** We present the motivations for this work centered around problems in Cosmology. In particular, we give an overview about a concrete model of Hybrid Inflation, and the approximations used to address its evolution. An important ingredient being the *classical approximation* which is described next. This case serves to pose the questions and define the main goals of this thesis.

- **Chapter 2:** We show a review about the evolution of physical systems in quantum mechanics (QM) and classical mechanics (CM). We define the Wigner function and write their classical and quantum evolution equations. We particularize to polynomial Hamiltonians motivated by the hybrid inflationary model. In this context, we particularly study the gaussian states and give a definition of squeezed state. Finally we discuss the comparison between the quantum and classical evolution, define some useful dimensionless control parameters, and study the ultraquantum case.

- **Chapter 3:** Here we perform a particular quantum and classical perturbative expansion to order λ^2 for one degree of freedom. We focus in a time-dependent quartic Hamiltonian. This expansion use the same propagators for the quantum and classical case. We analyze the diagrams for different expectation values, obtaining that the classical diagrams are a subset of quantum ones.

- **Chapter 4:** Extending the results of the previous chapter, we present a general quantum and classical perturbative expansion. We expose Feynman rules that are valid for any time-dependent quartic potential and for any order. These rules seem to be different for the quantum and classical case, but we derive both in a similar way and prove that the classical diagrams are a subset of the quantum ones. Also we show a classicality condition extracted from the perturbative expansion.

- **Chapter 5:** We test the validity of classical approximation in several quantum mechanical systems with one degree of freedom, where the exact evolution is available. We start considering time-dependent

potentials where a symmetry breaking occurs, motivated by our inflationary model. We test the assumption of Ref. [33] that approximate the evolution in the mentioned model by two stages: gaussian evolution ($\lambda = 0$) and classical evolution. In addition, we perform a systematic exploratory study for several system in terms of the above defined dimensionless control parameters. We choose two types of Hamiltonian: the anharmonic oscillator and the double well potential.

- **Chapter 6:** We extend the previous analysis to systems with two degrees of freedom. Motivated by the mentioned inflationary model, we use two different systems as toy models to check the criteria used in the above reference. The first system emulate a tachyonic mode of the Higgs coupled to a non-tachyonic mode. We check if the influence of non-tachyonic mode can be indeed neglected. The second system represents a Higgs mode coupled to an Inflaton mode in a way that the effective Higgs mass acquire a linear dependence on t in the first stages of the evolution. We test if the qualitative behavior of the system correspond with the case of 1 degree of freedom.

- **Chapter 7:** We show a review about the fundamental equations in classical field theory (CFT) and quantum field theory (QFT). We show a formal definition of Wigner function and its evolution equation. We describe the evolution for the free theory for time-dependent Hamiltonians. After, we focus in fields with 1+1 dimensions. We extend to this case the perturbative formalism with similar propagators in the quantum and classical case. After, we describe the fields in a Lattice and the corresponding perturbative renormalization. The Loop expansion to fields is also shown.

- **Chapter 8:** In this chapter we present a review about 2PI methods based on the truncation of the 2PI effective action. This is done for QFT and CFT. We focus in the most commonly used approaches: 2PI-Loop to 3 loops and the 2PI-1/N to NLO. These approximations leads to the so-called 2PI classicality condition, that is valid as long as it is the used approximation. Nevertheless, we use our above perturbative expansion to prove that the 2PI classicality condition can be considered as a sufficient condition. Finally, we present a new method that takes advantage of 2PI methods and the classical approximation: the *Hybrid Method*.

- **Chapter 9:** We test the explained 2PI methods in systems with 1 dof. We start with the same time-dependent Hamiltonians used in chapter 5. The results are compared with the exact and the classical evolution. Also, we perform an exploratory study for the same systems of chapter 5, using the mentioned dimensionless control parameters.

- **Chapter 10:** We describe other approach that are usually employed to perform non-linear quantum evolution: the complex Langevin method. We present a review of the method and show the two main problems reported in the literature: the occurrence of instabilities and the wrong convergence to a non-correct state. We test these issues in a system of 1 dof with a quartic Hamiltonian (anharmonic oscillator). Also we implement the method in three different approaches and compare them.

- **Chapter 12:** A new method is presented in this chapter noted as *nQC Method*. We describe the method in the case of QM and after we show how extend it to QFT. We analyze the range of validity and the involved errors. We check how this method works for different quantum mechanical systems. Also we use the method in QFT with 1+1 dimensions and study how the errors and the computational cost increase.

- **Chapter 13:** We show the different conclusions obtained along this thesis.

1.4 Resumen de contenidos

Presentamos una breve descripción de los contenidos incluidos en esta tésis:

- **Capítulo 1:** Presentamos las motivaciones para este trabajo, centrndonos en problemas que se plantean en Cosmologa. En particular, hacemos un resumen acerca de un modelo concreto de Inflación Híbrida, as como de las aproximaciones utilizadas para calcular su evolución. Un importante ingrediente es la *aproximación clásica*, que es descrita a continuación. Este caso sirve para puntualizar las cuestiones importantes y definir los principales objetivos de esta tésis.

- **Capítulo 2:** Mostramos un resumen acerca de la evolución de sistemas físicos en Mecánica Cuántica (QM) y Mecánica Clásica (CM). Definimos la función de Wigner y escribimos sus ecuaciones de evolución

cuántica y clásica. Describimos en particular el caso de potenciales polinómicos motivados por el mencionado modelo de inflación híbrida. En este contexto, estudiamos los estados gaussianos y damos una definición de estado squeezed. Finalmente discutimos la comparación entre la evolución cuántica y clásica, definimos algunos parámetros de control adimensionales que nos serán útiles, y estudiamos el caso ultracuántico.

- **Capítulo 3:** Aquí realizamos un particular desarrollo perturbativo hasta orden λ^2 para un grado de libertad. Nos centramos en un Hamiltoniano cuártico dependiente del tiempo. Este desarrollo utiliza los mismos propagadores para el caso cuántico y clásico. Analizamos los diagramas para diferentes valores esperados, obteniendo que los diagramas clásicos son un subconjunto de los cuánticos.

- **Capítulo 4:** Extendiendo los resultados del capítulo anterior, presentamos un desarrollo perturbativo general cuántico y clásico. Mostramos unas reglas de Feynman que son válidas para cualquier potencial cuártico con dependencia temporal, y a cualquier orden prturbativo. En principio, estas reglas parecen diferentes para el caso cuántico y clásico, pero deducimos otras reglas equivalentes que son similares en ambos casos, y probamos que los diagramas clásicos son un subconjunto de los cuánticos. También presentamos una condición de clasicidad extraída del desarrollo perturbativo.

- **Capítulo 5:** Testamos la validez de la aproximación clásica en varios sistemas mecano-cuánticos con un grado de libertad, donde la solución exacta es calculable. Comenzamos considerando potenciales dependientes del tiempo donde ocurre una ruptura de simetría, motivados por nuestro modelo inflaccionario. Testamos la asunción de la Ref. [33] donde se aproxima la evolución del modelo mencionado en 2 etapas: evolución gaussiana ($\lambda = 0$) y evolución clásica. Además, realizamos un estudio sistemático exploratorio para varios sistemas en términos de los parámetros de control adimensionales mencionados antes. Elegimos 2 tipos de Hamiltonianos: el oscilador anarmónico y el potencial double-well.

- **Capítulo 6:** Extendemos el análisis previo a sistemas con dos grados de libertad. Motivados por nuestro modelo inflaccionario, usamos dos

sistemas diferentes como modelos sencillos donde comprobar los criterios utilizados en la referencia anterior.
El primer sistema emula el comportamiento de un modo taquiónico del Higgs acoplado con un modo no taquiónico. Comprobamos si la influencia del modo no taquiónico puede ser efectivamente despreciada.
El segundo sistema repreenta un modo del Higgs acoplado a un modo del Inflatón, de manera que la masa efectiva al cuadrado del Higgs adquiere una dependencia lineal en t en la primera parte de la evolución. Comprobamos si el comportamiento cualitativo del sistema se corresponde con el caso de 1 grado de libertad.

- **Capítulo 7:** Mostramos un resumen acerca de las ecuaciones fundamentales en Teoría Clásica de Campos (CFT) y Teoría Cuántica de Campos (QFT). Presentamos una definición formal del funcional de Wigner y su ecuación de evolución. Describimos la evolución para la teoría libre con Hamiltonianos dependientes del tiempo. Después, nos centramos en campos en 1+1 dimensiones espacio-temporales. Extendemos para este caso nuestro formalismo perturbativo con iguales propagadores en el caso cuántico y clásico. Después, describimos los campos en un Lattice (retículo) y la correspondiente renormalización perturbativa. La acción efectiva para campos y su expansión en Loops se muestran también.

- **Capítulo 8:** Presentamos un resumen de los métodos 2PI basados en la trncación de la Acción Efectiva 2PI. Esto se hace para QFT y CFT. Nos centramos en las aproximaciones más comunmente utilizadas: 2PI-Loop hasta 3 loops, y 2PI-1/N hasta NLO. Estas aproximaciones conducen a la denominada condición de clasicidad 2PI, que es válida mientras lo sea la aproximación utilizada. Sin embargo, nosotros utilizamos nuestro anterior desarrollo perturbativo que la condición de clasicidad 2PI es realmente una condición suficiente.
  Finalmente, presentamos un nuevo método que saca ventaja de los métodos 2PI y de la aproximación clásica: el *Método Híbrido*.

- **Capítulo 9:** Testamos aquí los anteriores métodos 2PI en sistemas con 1 grado de libertad. Comenzamos con los mismos Hamiltonianos dependientes del tiempo utilizados en el Capítulo 5. Los resultados son comparados con la evolución cuántica exacta y con la eovolución clásica. También realizamos un estudio sistemático exploratorio para

los mismos sistemas del Capítulo 5, usando los mismos parámetros de control adimensionales.

- **Capítulo 10:** Describimos otra aproximación que es usualmente utilizada para realizar evolución cuántica no lineal: el método de Complex Langevin. Presentamos un resumen del método y mostramos los 2 problemas principales mencionados en la literatura: la aparición de inestabilidades y la mala convergencia hacia un estado incorrecto. Testamos estos asuntos en un sistema con 1 grado de libertad con un Hamiltoniano cuártico (oscilador anarmónico). También implementamos el método de tres formas diferentes y las comparamos entre sí.

- **Capítulo 11:** En este capítulo presentamos un nuevo método que hemos denominado *Método nQC*. Decribimos el método en el caso de QM y después lo extendemos al caso de QFT. Analizamos el rango de validez y los errores involucrados. Comprobamos cómo funciona el método para diferentes sistemas mecano-cuánticos. También utilizamos el método en QFT con 1+1 dimensiones espacio-temporales y estudiamos cómo los errores y el coste computacional se incrementan.

- **Capítulo 12:** Mostramos las diferentes conclusiones obtenidas a lo largo de esta tésis.

2 Time-Dependent Quantum and Classical Evolution

We are going to describe the classical and quantum evolution of systems with a generic time dependent Hamiltonian $H(\mathbf{x}, \mathbf{p}, t)$, where $\mathbf{x}, \mathbf{p}$ are vectors that represent generalized coordinates and momenta in any dimension d.

2.1 Classical evolution

In the Hamiltonian formulation, the classical evolution of the system having $H(\mathbf{x}, \mathbf{p}, t)$ as Hamiltonian is given by Hamilton equations of motion

$$\frac{\partial H}{\partial x_i} = -\dot{p}_i \quad ; \quad \frac{\partial H}{\partial p_i} = \dot{x}_i \tag{10}$$

One important property of the classical evolution is given by Liouville theorem, which states that the classical evolution preserves the area in phase space. If we have a system defined by a probability distribution $\rho(\mathbf{x}, \mathbf{p}, t)$ in the phase space, then the classical evolution of this function is given by Liouville equation

$$\frac{\partial \rho}{\partial t} = \{H, \rho\} = \sum_{j=1}^{d} \Big(\frac{\partial H}{\partial x_j} \frac{\partial \rho}{\partial p_j} - \frac{\partial H}{\partial p_j} \frac{\partial \rho}{\partial x_j} \Big) \tag{11}$$

For Hamiltonians of the usual type

$$\hat{H} = \frac{1}{2m} \mathbf{p}^2 + V(\mathbf{x}, t) \tag{12}$$

Hamilton equations take the form

$$\frac{\partial V}{\partial x_i} = -\dot{p}_i \quad ; \quad \frac{p_i}{m} = \dot{x}_i \tag{13}$$

while the Liouville equation is

$$\frac{\partial \rho}{\partial t} = \{H, \rho\} = \sum_{j=1}^{d} \Big(\frac{\partial V}{\partial x_j} \frac{\partial \rho}{\partial p_j} - \frac{p_j}{m} \frac{\partial \rho}{\partial x_j} \Big) \tag{14}$$

2.2 Quantum evolution: Schroedinger picture

2.2.1 Pure state

In the Schroedinger picture the quantum operators that represent observables $\hat{O}_S$ do not evolve and a quantum state $|\psi(t)\rangle$ evolves with the Schroedinger equation

$$i\hbar\frac{\partial}{\partial t}|\psi(t)\rangle = \hat{H}(\hat{\mathbf{x}}, \hat{\mathbf{p}}, t)|\psi(t)\rangle \tag{15}$$

This equation is linear and therefore there exists a linear operator $U(t, t_0)$ (evolution operator) such that

$$|\psi(t)\rangle = U(t, t_0)|\psi(t_0)\rangle \tag{16}$$

and since $|\psi(t_0)\rangle$ is arbitrary then $U(t_0, t_0) = \mathbb{1}$. The evolution operator is an unitary operator that satisfies the equation

$$i\hbar\frac{\partial}{\partial t}U(t, t_0) = \hat{H}(\hat{\mathbf{x}}, \hat{\mathbf{p}}, t)U(t, t_0) \tag{17}$$

2.2.2 Mixed state

If our system is a part of a bigger quantum system, then one has to describe it through the density operator. This operator is defined as

$$\hat{\rho}(t) \equiv \sum_i p_i|\psi_i(t)\rangle\langle\psi_i(t)| \tag{18}$$

where p_i represents the probability that the system is in a pure state $|\psi_i(t)\rangle$, therefore $0 \leqslant p_i \leqslant 1$ and $\sum_i p_i = 1$. So the expectation value of any observable $\hat{O}_S$ is

$$\langle\hat{O}\rangle_\rho(t) = \sum_i p_i\langle\psi_i(t)|\hat{O}|\psi_i(t)\rangle \tag{19}$$

If the system is in a pure state $|\psi_a(t)\rangle$ then $p_i = \delta_{i,a}$ and the density operator has the form $\hat{\rho}_a(t) = |\psi_a(t)\rangle\langle\psi_a(t)|$. In this case, if one chooses an orthonormal basis of the state space $\{|u_n(t)\rangle\}$, then it is easy to deduce that the expectation value of our observable can be written as

$$\langle\hat{O}_S\rangle_{\rho_a}(t) = \langle\psi_a(t)|\hat{O}_S|\psi_a(t)\rangle = \sum_n\langle u_n(t)|\hat{\rho}_a(t)\hat{O}_S|u_n(t)\rangle = \mathrm{Tr}\{\hat{\rho}_a(t)\hat{O}\} \tag{20}$$

Also one can see that $\mathrm{Tr}\{\hat{\rho}_a(t)\} = 1$. For a mixed state, it is straightforward from (19) and (20) that

$$\langle \hat{O}_S \rangle_\rho(t) = \sum_i p_i \langle \hat{O}_S \rangle_{\rho_i} = \sum_i p_i \mathrm{Tr}\{\hat{\rho}_i(t)\hat{O}_S\} = \mathrm{Tr}\{\hat{\rho}(t)\hat{O}_S\} \tag{21}$$

and one can verify that $\mathrm{Tr}\{\hat{\rho}(t)\} = 1$. The evolution of the density operator can be deduced from Schroedinger equation and one gets

$$\frac{d}{dt}\hat{\rho}(t) = \frac{1}{i\hbar}[\hat{H}(\hat{\mathbf{x}}, \hat{\mathbf{p}}, t), \hat{\rho}(t)] \tag{22}$$

2.3 Quantum evolution: Heisenberg picture

In the Heisenberg picture a quantum operator $\hat{O}(t)$ (that represent an observable) evolves in time and the state (represented by the wave function $\psi(t_0)$) remains constant. The expectation value of $\hat{O}(t)$ in any state has to match the expectation value of the same operator in the Schroedinger picture $\hat{O}_S$, therefore

$$\langle \psi(t)|\hat{O}_S|\psi(t)\rangle = \langle \psi(t_0)|U^\dagger(t,t_0)\hat{O}_S U(t,t_0)|\psi(t_0)\rangle = \langle \psi(t_0)|\hat{O}(t)|\psi(t_0)\rangle \tag{23}$$

so the relation with the operator in the Schroedinger picture is

$$\hat{O}(t) = U^\dagger(t,t_0)\hat{O}_S U(t,t_0) \tag{24}$$

The evolution of the operator is governed by the equation

$$\frac{d}{dt}\hat{O}(t) = \frac{i}{\hbar}[\hat{H}(\hat{\mathbf{x}}, \hat{\mathbf{p}}, t), \hat{O}(t)] + \frac{\partial}{\partial t}\hat{O}(t) \tag{25}$$

2.4 Quantum evolution: Wigner Function

A particularly interesting way to describe the quantum system and its similarities and differences with the classical case is the Wigner function formalism to be described below.

2.4.1 Definition

In Quantum Mechanics the expectation values of Weyl-ordered products of operators can be computed in terms of the Wigner function $W(\mathbf{x}, \mathbf{p}, t)$ ($\mathbf{x}, \mathbf{p}$

have dimension d) as follows [65][66]:

$$\langle\Psi|f_W(\hat{\mathbf{x}},\hat{\mathbf{p}})|\Psi\rangle = \int \frac{d\mathbf{x}\,d\mathbf{p}}{\hbar} f(\mathbf{x},\mathbf{p})\,W(\mathbf{x},\mathbf{p},t) \tag{26}$$

where $f_W(\hat{\mathbf{x}},\hat{\mathbf{p}})$ means a Weyl-ordered product of position and momentum operators, whose classical limit is $f(\mathbf{x},\mathbf{p})$. Of course, W depends on the quantum state $|\Psi\rangle$. As an example, for $f(\mathbf{x},\mathbf{p}) = x_i^n p_j^m$ one has

$$f_W(\hat{x_i},\hat{p_j}) = \frac{1}{2^n}\sum_{l=0}^{n}\binom{n}{l}\hat{x}_i^{n-l}\hat{p}_j^n\hat{x}_i^l \tag{27}$$

From this one can calculate a specific quantum expectation value $\langle\hat{x}_i^n\hat{p}_j^m\rangle$ because this value can be expressed as a combination of commutators $[\hat{x}_i,\hat{p}_j]$ and Weyl-ordered expectation values with exponents less or equal than n and m.
For a pure state, given the wave function $\Psi(\mathbf{x},t)$, the expression of the Wigner function is

$$W(\mathbf{x},\mathbf{p},t) \equiv \frac{1}{\pi^d}\int d^d y\,\Psi^*(\mathbf{x}+\mathbf{y},t)\,e^{2i\mathbf{p}\cdot\mathbf{y}/\hbar}\Psi(\mathbf{x}-\mathbf{y},t) \tag{28}$$

This can be extended to mixed states associated to a density operator $\rho(t)$ as follows:

$$W(\mathbf{x},\mathbf{p},t) = \frac{1}{\pi^d}\int d^d y\,\langle\mathbf{x}-\mathbf{y}|\rho(t)|\mathbf{x}+\mathbf{y}\rangle\,e^{2i\mathbf{p}\cdot\mathbf{y}/\hbar} \tag{29}$$

In both cases the Wigner function is real but not necessarily positive definite.

2.4.2 Quantum evolution of $W(\mathbf{x},\mathbf{p},t)$

The Wigner function satisfies an evolution equation in time which depends on the form of the potential. If we consider a Hamiltonian of the usual type (12), then the corresponding Schroedinger equation will be

$$\frac{\partial\Psi(\mathbf{x},t)}{\partial t} = \frac{i\hbar}{2m}\sum_{j=1}^{d}\frac{\partial^2\Psi(\mathbf{x},t)}{\partial x_j^2} - \frac{i}{\hbar}V(\hat{\mathbf{x}},t)\Psi(\mathbf{x},t) \tag{30}$$

Using (30) and (28) we easily obtain

$$\frac{\partial W}{\partial t} = \frac{i\hbar}{2m\pi^d}\int d^d y e^{2i\mathbf{p}\cdot\mathbf{y}/\hbar}\sum_{j=1}^{d}\Big[\Psi^*(\mathbf{x}+\mathbf{y},t)\frac{\partial^2\Psi(\mathbf{x}-\mathbf{y},t)}{\partial x_j^2} - \frac{\partial^2\Psi^*(\mathbf{x}+\mathbf{y},t)}{\partial x_j^2}\Psi(\mathbf{x}-\mathbf{y},t)\Big]+$$
$$+\frac{i}{\hbar\pi^d}\int d^d y\, e^{2i\mathbf{p}\cdot\mathbf{y}/\hbar}\Psi^*(\mathbf{x}+\mathbf{y},t)\Psi(\mathbf{x}-\mathbf{y},t)\Big[V(\mathbf{x}+\mathbf{y})-V(\mathbf{x}-\mathbf{y})\Big] \qquad (31)$$

Now, realizing that $\partial_{x_j} f(\mathbf{x}\pm\mathbf{y}) = \pm\partial_{y_j} f(\mathbf{x}\pm\mathbf{y})$, we can do this change:

$$\frac{\partial^2\Psi(\mathbf{x}-\mathbf{y},t)}{\partial x_j^2} \to \frac{\partial^2\Psi(\mathbf{x}-\mathbf{y},t)}{\partial y_j^2} \qquad (32)$$

and the same for Ψ^*. Then we can integrate by parts and realize that the wave function vanishes in the limit surface of the integral. Both terms with first derivatives cancel out and we get p_j factors from derivating the exponential. If we also Taylor expand the potential in the last term we obtain

$$\frac{\partial W}{\partial t} = \frac{1}{m\pi^d}\int d^d y e^{2i\mathbf{p}\cdot\mathbf{y}/\hbar}\sum_{j=1}^{d} p_j\Big[\Psi^*(\mathbf{x}+\mathbf{y},t)\frac{\partial\Psi(\mathbf{x}-\mathbf{y},t)}{\partial y_j} - \frac{\partial\Psi^*(\mathbf{x}+\mathbf{y},t)}{\partial y_j}\Psi(\mathbf{x}-\mathbf{y},t)\Big]+$$
$$+\frac{2i}{\hbar\pi^d}\int d^d y e^{2i\mathbf{p}\cdot\mathbf{y}/\hbar}\Psi^*(\mathbf{x}+\mathbf{y},t)\Psi(\mathbf{x}-\mathbf{y},t)\sum_{n\ odd}\sum_{i_1+\ldots+i_d=n}\frac{y_1^{i_1}\ldots y_d^{i_d}}{i_1!\ldots i_d!}\frac{\partial^d V(\mathbf{x})}{\partial x_1^{i_1}\ldots\partial x_d^{i_d}} \qquad (33)$$

As we already mentioned, we can substitute $\partial_{y_j} \to \partial_{x_j}$ in the first integral. And in the second integral each factor y_j^k can be obtained through $\left(\frac{-i\hbar}{2}\right)^k \frac{\partial^k}{\partial p_j^k}$. Therefore we can write:

$$\frac{\partial W(\mathbf{x},\mathbf{p},t)}{\partial t} = -\sum_{j=1}^{d}\frac{p_j}{m}\frac{\partial W}{\partial x_j} + \frac{i}{\hbar}\Big[V(\mathbf{x}-\frac{i\hbar}{2}\frac{\partial}{\partial\mathbf{p}}) - V(\mathbf{x}+\frac{i\hbar}{2}\frac{\partial}{\partial\mathbf{p}})\Big]W \qquad (34)$$

This equation is well-known [67] and receives several names in the literature: Moyal equation or quantum Liouville equation.

2.5 Particular case: quadratic Hamiltonians

The case of quadratic Hamiltonians is particularly interesting since it is exactly solvable and serves as an example of the previous concepts. It corresponds to the physical system of a harmonic oscillator. We will start to

describe the one-dimensional time dependent oscillator, whose Hamiltonian is

$$H_0(x,p,t) = \frac{1}{2}(p^2 + w^2(t)x^2) \tag{35}$$

2.5.1 Heisenberg picture evolution

In order to have a uniform notation, we will note the operators that evolve under H_0 as $\hat{O}_0(t)$. In later chapters we will maintain this notation, and for example the subscript 0 will indicates the zero order of the perturbative expansion.
In the Heisenberg picture the quantum evolution equations are

$$\begin{aligned} \dot{\hat{x}}_0 &= i[\hat{H}_0, \hat{x}_0] \Rightarrow \dot{\hat{x}}_0 = \hat{p}_0 \\ \dot{\hat{p}}_0 &= i[\hat{H}_0, \hat{p}_0] \Rightarrow \dot{\hat{p}}_0 + w^2(t)\hat{x}_0 = 0 \end{aligned} \tag{36}$$

which can be combined into a second order evolution equation for $\hat{x}_0$

$$\ddot{\hat{x}}_0 + w^2(t)\hat{x}_0 = 0 \tag{37}$$

Following [33], we are going to rewrite our equation in matrix form to have our results in a compact manner. We consider the vector formed by the position and momentum operators, and an evolution matrix that applied to this vector will give us its time evolution

$$\hat{v}(t) \equiv \begin{pmatrix} \hat{p}_0(t) \\ \hat{x}_0(t) \end{pmatrix} \quad M(t) \equiv \begin{pmatrix} \sqrt{\frac{2}{w}} g_1(t) & \sqrt{2w} g_2(t) \\ -\sqrt{\frac{2}{w}} f_2(t) & \sqrt{2w} f_1(t) \end{pmatrix} \tag{38}$$

where $f(t) = f_1(t) + i f_2(t)$ and $g(t) \equiv i\dot{f}(t) = g_1(t) + i g_2(t)$ will give us the evolution of $\hat{x}_0(t)$ and $\hat{p}_0(t)$. We defined $w \equiv w(t=0)$. From (36) we obtain:

$$\begin{gathered} \hat{v}(t) = M(t)\hat{v}(0); \quad \tfrac{d}{dt}\hat{v}(t) = \begin{pmatrix} 0 & -w^2(t) \\ 1 & 0 \end{pmatrix} \begin{pmatrix} \hat{p}_0(t) \\ \hat{x}_0(t) \end{pmatrix} \Rightarrow \\ \Rightarrow \begin{pmatrix} \sqrt{\frac{2}{w}} \dot{g}_1(t) & \sqrt{2w} \dot{g}_2(t) \\ -\sqrt{\frac{2}{w}} \dot{f}_2(t) & \sqrt{2w} \dot{f}_1(t) \end{pmatrix} = \begin{pmatrix} 0 & -w^2(t) \\ 1 & 0 \end{pmatrix} \begin{pmatrix} \sqrt{\frac{2}{w}} g_1(t) & \sqrt{2w} g_2(t) \\ -\sqrt{\frac{2}{w}} f_2(t) & \sqrt{2w} f_1(t) \end{pmatrix} \end{gathered} \tag{39}$$

so we have the equations:

$$\begin{aligned} \ddot{f}_1 + w^2(t) f_2 = 0 \quad g_1 = -\dot{f}_2 \\ \ddot{f}_2 + w^2(t) f_2 = 0 \quad g_2 = \dot{f}_1 \end{aligned} \tag{40}$$

As clearly $M(t=0) = \mathbb{I}$ then the initial conditions are:

$$\begin{array}{ll} g_1(0) = \sqrt{\frac{w}{2}} & g_2(0) = 0 \\ f_1(0) = \frac{1}{\sqrt{2w}} & f_2(0) = 0 \end{array} \tag{41}$$

To evaluate these functions for arbitrary $w(t)$ we can make a simple program that calculates numerically $f_1(t)$ and $f_2(t)$ for any time range.
Finally, the time evolution will be:

$$\begin{array}{l} \hat{x}_0(t) = \sqrt{2w} f_1(t)\hat{x}_0(0) - \sqrt{\frac{2}{w}} f_2(t)\hat{p}_0(0) \\ \hat{p}_0(t) = \sqrt{2w} g_2(t)\hat{x}_0(0) + \sqrt{\frac{2}{w}} g_1(t)\hat{p}_0(0) \end{array} \tag{42}$$

Note that, since the motion is Hamiltonian (canonical) we have $\det(M(t)) = 1$, and one gets for every time

$$f_1 g_1 + f_2 g_2 = Re(g f^*) = \frac{1}{2} \tag{43}$$

From (42), we can find the magnitudes we are actually interested in, the ones that have information on the quantum system. These are the expectation values of the products of the vector components $v(t)$, i.e., $\Sigma_{ijk\ldots}(t_1, t_2, t_3, \ldots) \equiv < \psi|\hat{v}_i(t_1)\hat{v}_j(t_2)\hat{v}_k(t_3)\ldots|\psi >$ in some state ψ. For instance, we can calculate the two-point functions for $\hat{x}$ and $\hat{p}$. We define the matrix

$$\Sigma_{ij}(t, t') = \langle \psi(t=0)|\hat{v}_i(t)\hat{v}_j(t')|\psi(t=0)\rangle \tag{44}$$

where i, j can represent, as we have seen, $\hat{v}_1 = \hat{p}$ or $\hat{v}_2 = \hat{x}$. To calculate this matrix we need the initial two-point functions

$$\langle \hat{x}_0^2(0)\rangle \equiv A_0 \quad ; \quad \langle \hat{p}_0^2(0)\rangle \equiv B_0 \quad ; \quad \langle \hat{x}_0(0)\hat{p}_0(0)\rangle \equiv C_0 \tag{45}$$

With this, the-two point functions at different times for the evolution with the quadratic potential (35) will be

$$\begin{array}{l} \langle \hat{x}_0(t)\hat{x}_0(s)\rangle = 2wA_0 f_1(t)f_1(s) + \frac{2}{w}B_0 f_2(t)f_2(s) - 2C_0 f_1(t)f_2(s) - 2C_0^* f_2(t)f_1(s) \\ \langle \hat{p}_0(t)\hat{p}_0(s)\rangle = 2wA_0 g_2(t)g_2(s) + \frac{2}{w}B_0 g_1(t)g_1(s) + 2C_0 g_1(t)g_2(s) + 2C_0^* g_2(t)g_1(s) \\ \langle \hat{x}_0(t)\hat{p}_0(s)\rangle = 2wA_0 f_1(t)g_2(s) - \frac{2}{w}B_0 f_2(t)g_1(s) + 2C_0 f_1(t)g_1(s) - 2C_0^* f_2(t)g_2(s) \end{array} \tag{46}$$

2.5.2 Gaussian states

Gaussian states are those having a gaussian Wigner function. For them, Weyl-ordered n-point expectation values $\Sigma_{i_1,\ldots,i_n}$ can be written in terms of two-point functions $\Sigma_{ij}(t,t)$ (Wick's theorem). These states can be present for all Hamiltonians at a given time but, as we said, the quadratic ones preserve this condition at all times.
Pure states with a gaussian wave function

$$\Psi(x) = \frac{1}{(2\pi\sigma^2)^{1/4}} e^{\frac{-x^2}{4\sigma^2}} \tag{47}$$

have the following Wigner function

$$W(x,p) = \frac{1}{\pi} e^{\frac{-x^2}{2\sigma^2}} e^{\frac{-2\sigma^2 p^2}{\hbar^2}} \tag{48}$$

and are therefore gaussian.
The equilibrium state of a time independent quadratic Hamiltonian (harmonic oscillator) at temperature T is also gaussian. Its density operator is

$$\hat{\rho} = \frac{1}{Z(\beta)} e^{-\beta \hat{H}_0} \tag{49}$$

where $\beta = 1/(kT)$ (k Boltzmann's constant) and $Z(\beta) = \mathrm{Tr}(e^{-\beta \hat{H}_0})$. Its corresponding Wigner function is [66]

$$W(x,p) = \frac{1}{\pi} \tanh(\hbar w \beta/2) e^{-\tanh(\hbar w \beta/2)\frac{x^2}{2\sigma^2}} e^{-\tanh(\hbar w \beta/2)\frac{2\sigma^2 p^2}{\hbar^2}} \tag{50}$$

Notice that both cases correspond to a factorizable gaussian in x and p:

$$W(x,p,t=0) = \frac{\hbar}{2\pi\sigma_x\sigma_p} \exp\{-\frac{p^2}{2\sigma_p^2} - \frac{x^2}{2\sigma_x^2}\} \tag{51}$$

In the pure state case the two standard deviations are related as follows:

$$\sigma_x \sigma_p = \frac{\hbar}{2}$$

For a mixed state this condition is relaxed. For example, for the equilibrium state given before one has

$$\sigma_x \sigma_p = \frac{\hbar}{2\tanh(\hbar\omega\beta/2)}$$

which interpolates between $\hbar/2$ at low temperatures and kT/ω at high temperatures.

A particular case of interest is that in which the state at $t = 0$ coincides with the ground state of the $H_0(t = 0)$ Hamiltonian. This case corresponds to a quantum harmonic oscillator of frequency $w \equiv w(t = 0)$. The elements of the matrix $\Sigma(t = 0, t = 0)$ are

$$\langle \hat{p}_0^2(0)\rangle = \tfrac{\hbar w}{2} \quad \langle \hat{x}_0^2(0)\rangle = \tfrac{\hbar}{2w} \quad \langle \hat{x}_0(0)\hat{p}_0(0)\rangle = -\langle \hat{p}_0(0)\hat{x}_0(0)\rangle = \tfrac{i\hbar}{2} \tag{52}$$

and with this

$$\Sigma(0,0) = \hbar \begin{pmatrix} \frac{w}{2} & -\frac{i}{2} \\ \frac{i}{2} & \frac{1}{2w} \end{pmatrix} \tag{53}$$

Now, we can find the matrix Σ for any two equal times t

$$\Sigma(t,t) = M(t)\Sigma(0,0)M^T(t) = \hbar \begin{pmatrix} g_1^2 + g_2^2 & F(t) - \frac{i}{2} \\ F(t) - \frac{i}{2} & f_1^2 + f_2^2 \end{pmatrix} \tag{54}$$

where $F(t) \equiv \mathrm{Im}(f^*(t)g(t)) = f_1(t)g_2(t) - f_2(t)g_1(t)$.

In the Schroedinger picture, the mentioned ground state is

$$\psi(x, t = 0) = e^{i\alpha_0}(w/\pi)^{1/4}e^{-\frac{w}{2}x^2} \tag{55}$$

and from the Schroedinger equation we obtain for every time

$$\psi(x,t) = \frac{e^{i\alpha(t)}}{(2\pi|f(t)|^2)^{1/4}}e^{-\frac{\Omega(t)}{2}x^2} \tag{56}$$

where we have defined

$$\Omega(t) \equiv \frac{g^*(t)}{f^*(t)} = \frac{1 - 2iF(t)}{2|f(t)|^2} \quad ; \quad \dot{\alpha}(t) = -\frac{1}{4|f(t)|^2} \quad ; \quad \alpha(0) = \alpha_0 \tag{57}$$

From $\psi(t)$ we can calculate the Wigner function at all times

$$W(x,p;t) = \frac{1}{\pi}e^{-\frac{x^2}{2|f(t)|^2} - \frac{2|f(t)|^2}{\hbar^2}\left|p - \frac{F(t)}{|f(t)|^2}x\right|^2} \tag{58}$$

Notice that this is gaussian but not factorized and $\sigma_x(t)\sigma_p(t) = \hbar/2$.

Squeezed state condition

The Wigner function is not always positive definite, but in the case of gaussian wave functions it is. As mentioned, for quadratic Hamiltonians the evolution maintains its gaussianity (and then its positivity), and the $2\sigma -$ *contour* represented on the phase space corresponds to an ellipse. We define r'_s (squeezing) as the ratio between the major and the minor axis of the mentioned ellipse. A state that correspond with $r'_s \gg 1$ is so-called *squeezed state*. These states are important because when a system is in a squeezed state, the later non-lineal evolution of the Wigner function can be done with a good accuracy applying the classical Liouville equation [22] (at least for a while).

In order to obtain the squeezing at time t, we must find the semiaxes of the ellipse already mentioned. To achieve that we use the matrix of the expectation values

$$\begin{pmatrix} \langle\Psi(0)|\hat{x}^2(t)|\Psi(0)\rangle & \frac{1}{2}\langle\Psi(0)|\{\hat{x}(t),\hat{p}(t)\}|\Psi(0)\rangle \\ \frac{1}{2}\langle\Psi(0)|\{\hat{x}(t),\hat{p}(t)\}|\Psi(0)\rangle & \langle\Psi(0)|\hat{p}^2(t)|\Psi(0)\rangle \end{pmatrix} \tag{59}$$

where $\Psi(0)$ is the initial state of quantum evolution. If one diagonalize this matrix then the inverse of their eigenvalues will give us the square of the semiaxes.

This calculation is important because the squeezing has been put forward as a classicality condition for several authors [22][23][25]. We plan to test this condition later.

2.6 One dimensional polynomial potentials

One special class of potentials widely used in physics is that of polynomials of degree q. One reason is that in QFT in high dimensions ($d > 2$) they correspond to the renormalizable theories. The $q = 2$ case is the quadratic Hamiltonian studied before. For polynomials of degree $q > 2$ there are no analytic solutions of the Schroedinger equation, and usually one obtains these solutions numerically. However, one can obtain an approximate analytical solution through perturbation theory, as we will see in a later chapter. We will start describing the one-dimensional case.

For a polynomial of degree q the evolution equation of the Wigner function obtained from (34) is

$$\frac{\partial W(x,p,t)}{\partial t} = -\frac{p}{m}\frac{\partial W(x,p,t)}{\partial x} + \frac{\partial V(x,t)}{\partial x}\frac{\partial W(x,p,t)}{\partial p} + \sum_{1<n\ odd\leqslant q} \frac{\hbar^{n-1}}{n!}\frac{1}{(2\mathrm{i})^{n-1}}\frac{\partial^n V(x,t)}{\partial x^n}\frac{\partial^n W(x,p,t)}{\partial p^n} \tag{60}$$

The first two terms on the right-hand side correspond to the evolution with the classical Liouville equation (11). The rest are completely quantum ones. A particularly interesting case for our purposes is the case $q = 4$. Thus, assuming the higher degree term is $(\lambda/24)x^4$, Eq. (60) is expressed as

$$\frac{\partial W(x,p,t)}{\partial t} = -\frac{p}{m}\frac{\partial W(x,p,t)}{\partial x} + \frac{\partial V(x,t)}{\partial x}\frac{\partial W(x,p,t)}{\partial p} - \frac{\hbar^2}{24}\frac{\partial^3 V(x,t)}{\partial x^3}\frac{\partial^3 W(x,p,t)}{\partial p^3} \tag{61}$$

Notice that the first two terms do not contain $\hbar$. As a matter of fact, if we neglect the last term, the solution to this partial differential equation is very simple. It is given by

$$W_0(x_0(x,p,t), p_0(x,p,t))$$

where the functions x_0 and p_0 are obtained by running back in time to time zero the classical equations of motion from a point (x,p) in phase-space at time t.

From (61) one can calculate the evolution of Weyl-ordered expectation values for this quartic potential:

$$\frac{\partial}{\partial t}\langle \hat{x}^n \hat{p}^m \rangle_W = \int dx\, dp\, x^n p^m \frac{\partial W(x,p,t)}{\partial t} =$$
$$w^2(t)\int dx\, dp\, x^{n+1} p^m \frac{\partial W(x,p,t)}{\partial p} + 6\lambda \int dx\, dp\, x^{n+3} p^m \frac{\partial W(x,p,t)}{\partial p} -$$
$$- \int dx\, dp\, x^n p^{m+1} \frac{\partial W(x,p,t)}{\partial x} - \frac{\hbar^2\lambda^2}{24}\int dx\, dp\, x^{n+1} p^m \frac{\partial^3 W(x,p,t)}{\partial p^3} \tag{62}$$

In this case the quantum evolution differs from the classical one on the last term, which has a third order derivative of the Wigner function with respect to the momentum.

2.7 Polynomial potentials with many variables

Consider a polynomial potential of the d variables $x_1, ..., x_d$

$$V(\mathbf{x}, t) = cte + a_{k_1} x_{k_1} + a_{k_1 k_2} x_{k_1} x_{k_2} + a_{k_1 k_2 k_3} x_{k_1} x_{k_2} x_{k_3} + ... \tag{63}$$

where Einstein summation convention is used, $a_{k_1 ... k_n}$ can depend on time, and the number of terms is finite. The previous results for one variable generalize to more than one variable in a fairly straightforward fashion. The equation satisfied by the Wigner function becomes:

$$\partial_0 W(\vec{x}, \vec{p}, t) = -\sum_n \left(\frac{p_n}{m} \frac{\partial W}{\partial x_n} + \frac{\partial V}{\partial x_n} \frac{\partial W}{\partial p_n} \right) - \frac{\hbar^2}{24} \sum_{n,m,r} \frac{\partial^3 V}{\partial x_n \partial x_m \partial x_r} \frac{\partial^3 W}{\partial p_n \partial p_m \partial p_r} \tag{64}$$

and again, the terms without $\hbar$ correspond to the evolution with the classical Liouville equation, and the last term is purely quantum. In the following, we will study this expression for two particularly important cases:

2.7.1 O(N) symmetric potential

The first case to study is an O(N) symmetric potential

$$V = \frac{\mu^2}{2} ||\vec{x}||^2 + \frac{\lambda}{8} \left(||\vec{x}||^2 \right)^2 \tag{65}$$

Here we can note $r \equiv ||\vec{x}||$ and write the potential as a function of r. The Schroedinger equation (15) in generalized polar coordinates include this radial part and the following kinetic term

$$\frac{\hat{p}^2}{2} = -\frac{\hbar^2}{2} \nabla^2 = -\frac{\hbar^2}{2} \Big[\frac{1}{r^{N-1}} \frac{\partial}{\partial r} \Big(r^{N-1} \frac{\partial}{\partial r} \Big) - \frac{\hat{L}^2}{r^2} \Big] \tag{66}$$

where $\hat{L}$ is the angular momentum in N dimensions, which includes the angular dependence. An interesting situation occurs when the initial state is also O(N) invariant, then the angular dependence disappears and gives rise to one-dimensional Schroedinger equation.
With our potential the last term on the right-hand side of the Wigner function equation becomes

$$\frac{\hbar^2 \lambda}{8} \sum_n \sum_m x_n \frac{\partial^3 W}{\partial p_n \partial p_m^2} \tag{67}$$

Again we consider the case in which the initial distribution is O(N) invariant. The Wigner function at all times would only depend on invariants $A = \vec{x} \cdot \vec{p}$, $B = ||\vec{p}||^2$, and $C = ||\vec{x}||^2$. The corresponding equation for $W(\vec{x}, \vec{p}, t) = F(A, B, C, t)$ is given by

$$\begin{aligned}\partial_0 F = (-\tfrac{B}{m} + \mu^2 C + \tfrac{\lambda}{2} C^2)\tfrac{\partial F}{\partial A} - \tfrac{2A}{m}\tfrac{\partial F}{\partial C} + 2A(\mu^2 + \tfrac{\lambda}{2} C)\tfrac{\partial F}{\partial B} - \\ - \tfrac{\lambda\hbar^2}{8}\Big(C^2 \tfrac{\partial^3 F}{\partial A^3} + 6AC\tfrac{\partial^3 F}{\partial A^2 \partial B} + 4(2A^2 + BC)\tfrac{\partial^3 F}{\partial B^2 \partial A} + 8AB\tfrac{\partial^3 F}{\partial B^3} + \\ + (2N+4)C\tfrac{\partial^2 F}{\partial A \partial B} + (4N+8)A\tfrac{\partial^2 F}{\partial B^2}\Big) \qquad (68)\end{aligned}$$

If the initial Wigner function has typical values of A, B and C proportional to N, as in the case of independent variables, and we scale λ to be proportional to $1/N$, the quantum evolution preserves these properties. It is interesting to notice, that in this case the quantum-term in the evolution of the Wigner function is suppressed by one or two powers of N in the denominator. This means that in this particular large N limit, the typical expansion parameters for the quantum evolution is

$$\frac{\hbar^3 \lambda}{16 N \sigma_p^4}$$

This is consistent with the conventional assertion that the large N dynamics is classical. Furthermore, notice that those terms containing third derivatives are suppressed by two powers of N, instead of one. Thus, to leading order in $1/N$ the Wigner function satisfies a simplified equation containing only second derivatives. After some work one can write this leading quantum term as

$$-\frac{\hbar^2 N \lambda}{8(BC - A^2)} \sum_{n,m} x_m (C p_n - A x_n) \frac{\partial^2 F}{\partial p_n \partial p_m} \qquad (69)$$

2.7.2 Hypercubic lattice

The second case which we want to consider is that in which the coordinates are labeled by $\vec{n}$, the points of a d-dimensional hypercubic lattice Λ. The coordinates will be referred as $\phi(\vec{n})$, and the corresponding Hamiltonian is given by

$$H = \sum_{\vec{n} \in \Lambda} \left(\frac{\pi(\vec{n})^2}{2m} + \frac{1}{2a^2} \sum_{\mu} (\phi(\vec{n} + \vec{\mu}) - \phi(\vec{n}))^2 + \frac{\mu^2}{2}\phi^2(\vec{n}) + \frac{\lambda}{24}\phi^4(\vec{n}) \right) \qquad (70)$$

The main property of this family of Hamiltonians is its invariance under the symmetry group of translations in d dimensions. Notice that this corresponds to the discretization of the Hamiltonian of a $\lambda\phi^4$ scalar field theory in d-dimensions on a lattice of spacing a. The quantity $\pi(\vec{n})$ is the conjugate momentum to $\phi(\vec{n})$, satisfying canonical commutation relations among them. If we apply the general formulas to derive the quantum Liouville equation for the Wigner function in this case, we obtain that the quantum term is given by:

$$-\frac{\lambda\hbar^2}{24}\sum_{\vec{n}\in\Lambda}\phi(\vec{n})\frac{\partial^3 W}{\partial\pi(\vec{n})^3} \tag{71}$$

2.8 Comparison with the Classical evolution

In the so-called *Classical Approximation* one performs the evolution of the Wigner function with the classical Liouville equation, instead of the Moyal equation. Moreover, the classical expectation values are directly calculated with the Wigner function, and then the classical position and momentum are now random variables. So, this approximation identify a Weyl-ordered quantum expectation value with a classical expectation value. Therefore, for expectation values that involve position and momentum operators, the classical and quantum calculation are different, even if the Wigner function is the same.

One of our goals is to study the difference between both evolutions, in order to test the validity of classical approximation for different systems. The mentioned evolution of the Wigner function give us a natural framework to study this, because the terms corresponding to classical evolution are clearly identified.

One can see that the quantum evolution (34) and the classical evolution (11) have in common the term which contains the derivatives of W with respect to the coordinates $\partial W/\partial x_j$, and they can differ in the other term which has derivatives with respect to the momenta. For the quantum evolution this last term can be expressed as it was written in (31)

$$\frac{i}{\hbar\pi^d}\int d^d y e^{2i\mathbf{p}\cdot\mathbf{y}/\hbar}\Psi^*(\mathbf{x}+\mathbf{y},t)\Psi(\mathbf{x}-\mathbf{y},t)\Big[V(\mathbf{x}+\mathbf{y})-V(\mathbf{x}-\mathbf{y})\Big] \tag{72}$$

For the classical evolution, from (14), one gets

$$\frac{2i}{\hbar\pi^d}\sum_{j=1}^{d}\frac{\partial V}{\partial x_j}\int d^d y\, y_j e^{2i\mathbf{p}\cdot\mathbf{y}/\hbar}\Psi^*(\mathbf{x}+\mathbf{y},t)\Psi(\mathbf{x}-\mathbf{y},t) \tag{73}$$

Comparing the two expressions, for them to coincide the following condition must be met

$$V(\mathbf{x}+\mathbf{y})-V(\mathbf{x}-\mathbf{y})=\sum_{j=1}^{d}\frac{\partial V}{\partial x_j}2y_j \tag{74}$$

It is easy to prove that to meet this condition necessarily the potential must be quadratic, i.e.

$$V(\mathbf{x},t)=cte+a_{k_1}x_{k_1}+a_{k_1k_2}x_{k_1}x_{k_2} \tag{75}$$

where the coefficients can depend on time. Therefore, for a system that represents a set of coupled (or not) harmonic oscillators the quantum and classical evolution coincide.

2.9 Influence of the quantum term

For simplicity, we will restrict our discussion to one-dimensional case with a quartic potential, but our comments can be extended to more variables and other potentials. So we have

$$V=\frac{1}{2}\mu^2x^2+\frac{\lambda}{24}x^4 \tag{76}$$

where μ can depend on time. For this case the evolution equation for the Wigner function is (61). In this equation, the last term contains all quantum effects and has dramatic consequences. In particular, the Wigner function is not guaranteed to remain positive at all times. Thus, computing expectation values with the Wigner function can be very unstable numerically, because it comes from a cancellation of both positive and negative terms which might be much larger than the overall sum. This is a typical *sign problem*, which might render difficult to compute quantum expectation values by probability methods. However, if we start at $t=0$ from a positive Wigner function it might take some time until the negative part contributes sizably, and expectation values can be determined with reasonable accuracy.

The size of the last term is, in principle, small in macroscopic terms, being proportional to $\hbar^2$. However, this depends very much on the size of the third derivative of the Wigner function. This a time-dependent function, but it is clear that the initial distribution has an important effect on the accuracy of the classical approximation at initial times. This will be tested in some particular cases that we will study, where one can numerically integrate the Schroedinger equation.
If one focuses upon expectation values, the size of quantum effects and the errors committed by numerical integration of the Moyal equation can be quite different. It is to be expected that the accuracy of expectation values is better for operators involving Q alone, than for those involving P.

2.9.1 Control dimensionless parameters

Sticking to the pure state case, and given the scales involved in the problem, one can form dimensionless quantities which control the relative importance of quantum effects and will help us to monitor the validity of the classical approximation.
The first one r_1 is the usual one formed by taking the ratio of a classical quantity with the dimensions of action, divided by $\hbar$. In our present case, this quantity is

$$r_1 = \frac{\sqrt{m}\mu^3}{\lambda\sigma_x\sigma_p} \tag{77}$$

One expects smaller quantum effects for large values of r_1. However, there is another combination which seems more directly related to the size of the quantum term in the equation for the Wigner function. This is given by

$$r_2 = \frac{\sigma_p\mu}{\sigma_x^3\lambda\sqrt{m}} \tag{78}$$

Of course, if μ depend on time we must take the value in $t = 0$.

2.9.2 Ultraquantum case

To get some insight into the structure of the Wigner function, we can study certain limits. For example, one can consider an *ultra-quantum* limit, in which we neglect the classical $\hbar$-independent terms in the equation satisfied by the

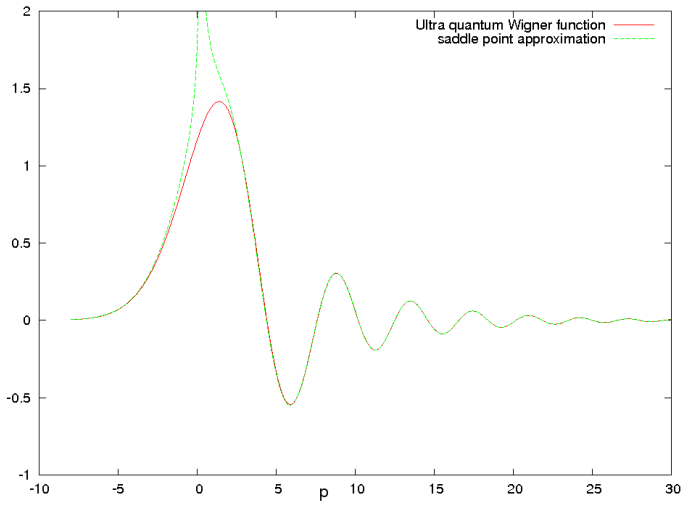

Figure 1: The Wigner function $W_{\rm uq}$ in the ultraquantum limit, for fixed values of x and t.

Wigner function. The equation can be integrated exactly in this case, and the result is a one-dimensional integral:

$$W_{\rm uq}(x,p,t) = \frac{\hbar}{(2\pi)^{3/2}\sigma_x}\, e^{-x^2/(2\sigma_x^2)} \int dz \exp\{ipz - i\lambda Q z^3 - \sigma_p^2 y^2/2\} \quad (79)$$

where $Q \equiv -\lambda\hbar^2 xt/24$. This can be related to Airy functions. The shape of this function is displayed in Fig.1 for $Q = 2$ and $\sigma_p^2 = 2$. Notice the damped oscillations for positive p. It is clear that the Wigner function becomes negative in some regions, but the total integral is finite and positive. As a matter of fact, it is quite easy to understand this oscillatory pattern and its dependence on x and t, by evaluating the integral in the saddle point approximation. The result is also plotted in Fig.1. For small values of p, the approximation breaks down as expected, but it becomes quite precise for large values of $|p|$, which encompasses the oscillatory region. Introducing $\kappa = 3Qp - \sigma_p^2/4$, the approximation is different for positive and negative values of κ. In the first case we have

$$2\sqrt{\pi}\kappa^{-1/4} \cos(2\kappa^{3/2}/(27Q^2) - \pi/4) \exp\{-p\sigma_p^2/(6Q) + \sigma_p^3/(108Q^2)\} \quad (80)$$

while for negative κ we have

$$\sqrt{\pi}|\kappa|^{-1/4} \exp\{-2|\kappa|^{3/2}/(27Q^2) - p\sigma_p^2/(6Q) + \sigma_p^3/(108Q^2)\} \quad (81)$$

Notice that for large p the argument of the cosine is proportional to $p^{3/2}/Q^{1/2}$, so that it broadens for large times. Despite the complicated behavior of the Wigner function in this ultraquantum case, all expectation values of $f(x)$ are time independent.

One can go beyond this approximation by considering also the second term on the right-hand side of the Wigner function equation. This approximation is equivalent to the infinite mass limit $m \longrightarrow \infty$. The new Wigner function is obtained from $W_{\rm uq}(x,p,t)$ by replacing p by $p+V'(x)t$. Again, all expectation values of x are time independent.

3 Perturbative expansion to order 2

For polynomial potentials with degree $q > 2$ there are no exact analytical solutions of the Schroedinger equation. However, one can approximate these solutions through perturbation theory. As we saw in the previous chapter, the quadratic part of the Hamiltonian can be solved analytically. We can consider the non-quadratic part as a perturbation and expand the solution in powers of the coupling. We restrict ourselves to Hamiltonians with $q = 4$ where the quartic term has the usual λ parameter, which will be the parameter involved in the perturbative expansion.

The perturbative expansion that we present here is done for the quantum and classical evolution. We will obtain diagrams with loops for both cases. This is a priori strange for the classical case, but we must remember that the classical approximation that we are using is special, because the classical evolution equations are applied to stochastic variables x, p with an initial distribution function given by the Wigner function.
In this chapter we calculate the perturbative expansion to order 2 for $\langle \hat{x}^2(t) \rangle$ and $\langle \hat{x}^4(t) \rangle$, and we see that it is possible to give the same rules to read the quantum and classical diagrams. In the following chapter we will extend the rules to any order. These rules are different to the usual ones, because we derived them in order to obtain the same propagators in the quantum and classical case. Moreover, the present perturbative expansion is done for time-dependent potentials, unlike the most common time-independent case.

We start considering the case of one degree of freedom. Later we will see how to extend the results to many variables and even to QFT. In fact, the present study was motivated by the case of hybrid inflation in the preheating epoch. In the approach of Ref. [33], the model requires to calculate the quantum evolution in a first stage, and connect with a second stage where one assumes that the system has a classical behavior and the classical approximation can be applied. The evolution in the first stage is usually done with the quadratic part of the Hamiltonian, but this can be improved using perturbation theory. We will test and discuss these aspects in a later chapter.

3.1 Perturbative approach to the quantum evolution

We take the Hamiltonian of a 1-dimensional anharmonic oscillator with an usual quartic term and a time-dependent frequency

$$H = H_0 + H_I = \frac{1}{2}(p^2 + w^2(t)x^2) + \frac{\lambda}{24}x^4 \tag{82}$$

We are going to consider the quartic term as a perturbation and expand the result in powers of λ. This is a technique where the perturbative terms and its corresponding diagrammatization are widely known, although they are usually calculated for a time independent Hamiltonian, unlike our case. So it is interesting to expand the perturbative terms considering the time dependence and take notice of the propagators involved, in order to find the same propagators in the classical case.

Let $\hat{x}(t)$ be the position operator in Heisenberg picture. If ***U(t)*** is the Evolution operator, the relation with the position operator in the Schrödinger picture is

$$\hat{x}(t) = U^\dagger(t)\hat{x}_S U(t) \tag{83}$$

where the evolution operator fulfills the equation

$$\dot{U}(t) = -i\mathbf{H}U(t) \tag{84}$$

with $\mathbf{H}$ representing the whole Hamiltonian, and the dot stands for a time derivative. We can factorize the evolution operator in two factors

$$U(t) = U_0(t)\mathbf{\Omega}(t) \tag{85}$$

where $U_0(t)$ represents the evolution with the unperturbed Hamiltonian H_0, and $\mathbf{\Omega}(t)$ the evolution operator that corresponds to the interaction picture and we can easily deduce from (84) that it fulfills the equation

$$\mathbf{\Omega}'(t) = -iU_0^\dagger(t)\mathbf{H^I}U_0(t)\mathbf{\Omega}(t) = -i\mathbf{H^I_{int}}(\mathbf{t})\mathbf{\Omega} \tag{86}$$

being $\mathbf{H^I_{int}}(\mathbf{t})$ the interaction Hamiltonian in the interaction picture.
It is well known that the solution of the equation is given by a T-exponential.

$$\mathbf{\Omega}(t) = T\exp\{-i\int_0^t ds\mathbf{H^I_{int}}(\mathbf{s})\} \tag{87}$$

and with this, if we call $\hat{x}_0(t)$ to the operator which evolution is given by the unperturbed Hamiltonian (and whose evolution equations we already know), the relation with the same operator in the Heisenberg picture will be

$$\hat{x}(t) = T' \exp\{i \int_0^t ds \mathbf{H}^{\mathbf{I}}_{\mathbf{int}}(\mathbf{s})\} \hat{x}_0(t) T \exp\{-i \int_0^t ds \mathbf{H}^{\mathbf{I}}_{\mathbf{int}}(\mathbf{s})\} \tag{88}$$

where in the T-exponential the times are ordered from right to left, and in the T'-exponential from left to right.

Expanding the T-exponential we obtain the perturbative expansion for $\hat{x}(t)$

$$\begin{aligned} \hat{x}(t) = (I + i \int_0^t ds \mathbf{H}^{\mathbf{I}}_{\mathbf{int}}(\mathbf{s}) - \int_0^t ds \int_0^s ds' \mathbf{H}^{\mathbf{I}}_{\mathbf{int}}(\mathbf{s}') \mathbf{H}^{\mathbf{I}}_{\mathbf{int}}(\mathbf{s}) + ...) \\ \hat{x}_0(t)(I - i \int_0^t ds \mathbf{H}^{\mathbf{I}}_{\mathbf{int}}(\mathbf{s}) - \int_0^t ds \int_0^s ds' \mathbf{H}^{\mathbf{I}}_{\mathbf{int}}(\mathbf{s}) \mathbf{H}^{\mathbf{I}}_{\mathbf{int}}(\mathbf{s}') + ...) \end{aligned} \tag{89}$$

3.1.1 Perturbative terms up to second order

For the particular quartic Hamiltonian (82) that we are studying, the interaction Hamiltonian in the interaction picture is given by

$$\mathbf{H}^{\mathbf{I}}_{\mathbf{int}}(\mathbf{t}) = \frac{\lambda}{24} \hat{x}_0^4(t) \tag{90}$$

We will take into account that the evolution of our operator with the unperturbed Hamiltonian is given by the expression

$$\hat{x}_0(t) = \sqrt{2w} f_1(t) \hat{x}_0(0) - \sqrt{\frac{2}{w}} f_2(t) \hat{p}_0(0) \tag{91}$$

regardless of the initial state. Remember that $w \equiv w(t=0)$

So, from (89), we have:

$$\begin{aligned} \hat{x}(t) = (I + i\frac{\lambda}{24} \int_0^t ds\, \hat{x}_0^4(s) - \frac{\lambda^2}{24^2} \int_0^t ds \int_0^s ds'\, \hat{x}_0^4(s') \hat{x}_0^4(s) + ...) \\ \hat{x}_0(t)(I - i\frac{\lambda}{24} \int_0^t ds\, \hat{x}_0^4(s) - \frac{\lambda^2}{24^2} \int_0^t ds \int_0^s ds'\, \hat{x}_0^4(s) \hat{x}_0^4(s') + ...) \end{aligned} \tag{92}$$

and multiplying and arranging terms we obtain

$$\hat{x}(t) = \hat{x}_0(t) + i\frac{\lambda}{24}\int_0^t ds\,[\hat{x}_0^4(s), \hat{x}_0(t)] + \frac{\lambda^2}{24^2}\int_0^t ds \int_0^t ds'\,\hat{x}_0^4(s)\hat{x}_0(t)\hat{x}_0^4(s') - \\ -\frac{\lambda^2}{24^2}\int_0^t ds \int_0^s ds'\,\hat{x}_0^4(s')\hat{x}_0^4(s)\hat{x}_0(t) - \frac{\lambda^2}{24^2}\int_0^t ds \int_0^s ds'\,\hat{x}_0(t)\hat{x}_0^4(s)\hat{x}_0^4(s') + O(\lambda^3) \quad (93)$$

Now we can expand the commutator that appears in the first order term and rearrange it to be more manageable. To achieve this we will take into account the commutation relations of the position operator and its conjugate momentum at the initial time

$$[\hat{x}_0(0), \hat{x}_0(0)] = [\hat{p}_0(0), \hat{p}_0(0)] = 0 \\ [\hat{x}_0(0), \hat{p}_0(0)] = -[\hat{p}_0(0), \hat{x}_0(0)] = i \quad (94)$$

and we will also make use of (91) to calculate the commutator at different times

$$[\hat{x}_0(s), \hat{x}_0(t)] = [(c(s)\hat{x}_0(0) + d(s)\hat{p}_0(0)), (c(t)\hat{x}_0(0) + d(t)\hat{p}_0(0))] = \\ = i(c(s)d(t) - c(t)d(s)) = -2i(f_2(t)f_1(s) - f_1(t)f_2(s)) = -2iIm(f(t)f^*(s)) \quad (95)$$

If we define a propagator $G_A(t, s)$ by the following expression

$$G_A(t, s) \equiv Im(f(t)f^*(s)) \quad (96)$$

we can calculate the desired commutator:

$$[\hat{x}_0^4(s), \hat{x}_0(t)] = 4[\hat{x}_0(s), \hat{x}_0(t)]\hat{x}_0^3(s) = -8iG_A(t, s)\hat{x}_0^3(s) \quad (97)$$

In this way the first order term in the perturbative expansion is expressed as

$$i\frac{\lambda}{24}\int_0^t ds\,[\hat{x}_0^4(s), \hat{x}_0(t)] = \frac{1}{3}\lambda\int_0^t ds\,G_A(t, s)\hat{x}_0^3(s) \quad (98)$$

We will keep the second order terms as they are, being careful with the integration boundaries and the operator ordering in each one when using them.

We can calculate now the expectation values of operator products that include the self-interaction effect, expressing them in terms of the products of the free operators, using the perturbative expansion.

3.1.2 Initial gaussian states: Wick's theorem

Now we will consider the case of initial gaussian states which will be used in our applications. We have to evaluate expectation values of products of operators $\hat{x}_0(t)$ in those gaussian states. In this case these expectation values will reduce to products of two-point functions according to Wick's theorem. Usually, this theorem is given to expectation values of products of time ordered quantum operators, unlike our case. However, if we consider $A \equiv \langle \hat{x}_0(t_1)....\hat{x}_0(t_n) \rangle$ then we can expand each operator in terms of $\hat{x}_0(0)$ and $\hat{p}_0(0)$ using (42). We obtain a summation of terms involving expectation values of products of $\hat{x}_0(0)$ or $\hat{p}_0(0)$, and then we can apply the Wick's theorem to each term. One can prove that the result is the same as applying Wick's theorem to A, as long as we maintain the initial relative order according to A when applying the theorem.

The same reasoning is valid for any expectation value involving products of operators $\hat{x}_0(t)$ or $\hat{p}_0(t)$. Therefore, in this case one also can apply the Wick's theorem as usually, but being careful of preserving the initial relative order.

3.1.3 Analytical calculation of $< \hat{\mathbf{x}}^{\mathbf{2}}(\mathbf{t}) >$

We have seen that an expectation value of a product operators in the Heisenberg picture can be expressed in terms of the expectation values of products of free operators (interaction representation). If the initial state is gaussian, then the expectation value of a product of free operators can be reduced, using the Wick's theorem, to products of expectation values of pairs of free operators. The two point function of free operators at different times has, in general, the form shown in (46) and we can write

$$\begin{aligned}
&\langle \hat{x}_0(t)\hat{x}_0(s) \rangle \equiv G_S(t,s) + iG_A(t,s) \\
&G_S(t,s) = 2wA_0 f_1(t)f_1(s) + \frac{2}{w}B_0 f_2(t)f_2(s) - 2Re(C_0)(f_2(t)f_1(s) + f_1(t)f_2(s)) = G_S(s,t) \\
&G_A(t,s) = Im(f(t)f^*(s)) = f_2(t)f_1(s) - f_1(t)f_2(s) = -G_A(s,t) \qquad (99)
\end{aligned}$$

where A_0, B_0, C_0 were defined in (45), and G_A is the propagator that we have defined in (96). In the particular case in which the state is the ground state

of the $t = 0$ quadratic Hamiltonian, we have

$$A_0 \equiv \langle \hat{x}_0^2(0) \rangle = \frac{1}{2w} \quad ; \quad B_0 \equiv \langle \hat{p}_0^2(0) \rangle = \frac{w}{2} \quad ; \quad C_0 \equiv \langle \hat{x}_0(0)\hat{p}_0(0) \rangle = \frac{i}{2}$$
$$G_S(t,s) \equiv f_1(t)f_1(s) + f_2(t)f_2(s) = G_S(s,t)$$
$$G_A(t,s) = f_2(t)f_1(s) - f_1(t)f_2(s) = -G_A(s,t) \tag{100}$$

The two point function is complex, but we have separated its real part from the imaginary one with the real functions $G_S(t,s)$ (symmetric with respect to the exchange of the arguments) and $G_A(t,s)$ (antisymmetric).

Going back to the expression we had to second order

$$\hat{x}(t) = \hat{x}_0(t) + \frac{\lambda}{3}\int_0^t ds\, G_A(t,s)\hat{x}_0^3(s) + \frac{\lambda^2}{24^2}\int_0^t ds \int_0^t ds'\, \hat{x}_0^4(s)\hat{x}_0(t)\hat{x}_0^4(s') -$$
$$-\frac{\lambda^2}{24^2}\int_0^t ds \int_0^s ds'\, \hat{x}_0^4(s')\hat{x}_0^4(s)\hat{x}_0(t) - \frac{\lambda^2}{24^2}\int_0^t ds \int_0^s ds'\, \hat{x}_0(t)\hat{x}_0^4(s)\hat{x}_0^4(s') \tag{101}$$

we can multiply it by itself to calculate $< \hat{x}^2(t) >$. Doing this and grouping the terms of the same order (ignoring those greater than two) we obtain:

- Zero order:
$$< \hat{x}^2(t) >_{(0)} = < \hat{x}_0^2(t) > \tag{102}$$

- First order:
$$< \hat{x}^2(t) >_{(1)} = \frac{\lambda}{3}\int_0^t ds\, G_A(t,s)(< \hat{x}_0(t)\hat{x}_0^3(s) > + < \hat{x}_0^3(s)\hat{x}_0(t) >) =$$
$$= 2\lambda \int_0^t ds\, G_A(t,s) < \hat{x}_0^2(s) > Re(f(t)f^*(s)) \tag{103}$$

where we have used the Wick's theorem:

$$< \hat{x}_0(t)\hat{x}_0^3(s) > = 3 < \hat{x}_0^2(s) >< \hat{x}_0(t)\hat{x}_0(s) >$$
$$< \hat{x}_0^3(s)\hat{x}_0(t) > = 3 < \hat{x}_0^2(s) >< \hat{x}_0(s)\hat{x}_0(t) > \tag{104}$$

and we have also taken into account that our operators are hermitian so $< \hat{x}_0(t)\hat{x}_0(s) > = < \hat{x}_0(s)\hat{x}_0(t) >^*$.

- Second order:

$$< \hat{x}^2(t) >_{(2)} = \frac{\lambda^2}{9} \int_0^t ds \int_0^t ds'\, G_A(t,s) G_A(t,s') < \hat{x}_0^3(s) \hat{x}_0^3(s') > +$$
$$\frac{\lambda^2}{24^2} \int_0^t ds \int_0^t ds' \left(< \hat{x}_0(t) \hat{x}_0^4(s) \hat{x}_0(t) \hat{x}_0^4(s') > + < \hat{x}_0^4(s) \hat{x}_0(t) \hat{x}_0^4(s') \hat{x}_0(t) > \right) -$$
$$-\frac{\lambda^2}{24^2} \int_0^t ds \int_0^s ds' \left(< \hat{x}_0(t) \hat{x}_0^4(s') \hat{x}_0^4(s) \hat{x}_0(t) > + < \hat{x}_0^4(s') \hat{x}_0^4(s) \hat{x}_0^2(t) > \right) -$$
$$-\frac{\lambda^2}{24^2} \int_0^t ds \int_0^s ds' \left(< \hat{x}_0^2(t) \hat{x}_0^4(s) \hat{x}_0^4(s') > + < \hat{x}_0(t) \hat{x}_0^4(s) \hat{x}_0^4(s') \hat{x}_0(t) > \right) \quad (105)$$

Here the first term comes from the product of the two operators to first order, and the next three terms come from the product of one to zero order and another to second order. From this last expression we can apply Wick's theorem to reduce each expectation value to products of expectation values of two operators (two-point functions). It is not useful to explicitly write that large expression so we will show later the results coming from it.

3.1.4 Analytic calculation of $< \hat{\mathbf{x}}^{\mathbf{4}}(\mathbf{t}) >$

As in the previous section, we can start from the expression (101), multiply it 4 times by itself and group the terms of the same order to 2 to calculate $< \hat{x}^4(t) >$. Then the following results are obtained:

- Zero order:

$$< \hat{x}^4(t) >_{(0)} = < \hat{x}_0^4(t) > = 3 < \hat{x}_0^2(t) >^2 \quad (106)$$

- First order:

$$< \hat{x}^4(t) >_{(1)} = \frac{\lambda}{3} \int_0^t ds\, G_A(t,s) \{ < \hat{x}_0^3(t) \hat{x}_0^3(s) > + < \hat{x}_0^2(t) \hat{x}_0^3(s) \hat{x}_0(t) > +$$
$$+ < \hat{x}_0(t) \hat{x}_0^3(s) \hat{x}_0^2(t) > + < \hat{x}_0^3(s) \hat{x}_0^3(t) > \} =$$
$$= \frac{\lambda}{3} \int_0^t ds\, G_A(t,s) \{ 36 < \hat{x}_0^2(t) >< \hat{x}_0^2(s) > Re(< \hat{x}_0(t) \hat{x}_0(s) >) +$$
$$+ 12 Re(< \hat{x}_0(t) \hat{x}_0(s) >^3) + 12 \mid < \hat{x}_0(t) \hat{x}_0(s) >^2 \mid Re(< \hat{x}_0(t) \hat{x}_0(s) >) \} \quad (107)$$

where we have used again Wick's theorem to expand it as products of two point functions.

- Second order:

We do not write the long expressions. We will see later the result in a diagrammatic formalism.

3.2 Diagrammatization

We are going to make a diagrammatic representation of the perturbative expansion up to second order, as in the usual case when the unperturbed Hamiltonian does not depend on time. This diagrammatization will involve rules for reading the diagrams that will be the same as for the classical perturbative expansion (although here will appear more diagrams).
We recall the two kinds of propagators that appear in the calculation of the two point function seen in (99)

$$< \hat{x}_0(t)\hat{x}_0(s) >= G_S(t,s) + iG_A(t,s) \tag{108}$$

we already noted that the real part (G_S) is symmetric and the imaginary part (G_A) is antisymmetric with respect to the exchange of arguments.

We have seen in the previous section that for each order we obtain a series of terms composed of products of two point functions, that can be expressed in terms of the two propagators G_S and G_A. Therefore, our perturbative expansion for a concrete expectation value will be a sum of integrals involving G_S and G_A with their corresponding arguments. These integrals can be represented with Feynman diagrams, given some drawing rules. We will show them up to the second order we have calculated, omitting the corresponding combinatorial factors coming from the application of Wick's theorem. We will show how to calculate these factors to any order in the following chapter.

In (105) (and in general for expectation values at second order or higher) the limits of the corresponding integrals appear with certain time ordering (from the expansion of the T-exponentials). But it can be interesting not having to worry about the limits ordering, having everyone of them going from 0 to t (or ∞). To achieve this, we redefine the propagator G_A in such

a way that its arguments are rightly ordered introducing the corresponding functions θ (Heaviside). Then, for any two times t_1, t_2 , we redefine:

$$G_r(t_1, t_2) \equiv \theta(t_1 - t_2)(f_2(t_1)f_1(t_2) - f_1(t_2)f_2(t_1)) \tag{109}$$

Of course this is not mandatory, we can work with the integral limits as obtained from the T-exp expansion using G_A propagators.
These two propagators, G_S y G_r, are going to be represented on the diagrams with two kind of lines, a solid one for G_S and an oriented dotted one for G_r which arguments will keep the ordering of the orientation.
Now we will see the rules needed to represent in diagram form the perturbative contributions using these propagators. These are not general rules, but are only valid to read the diagrams of $\langle \hat{x}^l \rangle$ to second order. However, similar rules will be obtained for the general case that we will present in the following chapter.

3.2.1 Feynman rules to read the diagrams to second order

- The number of internal vertices of the diagram (i.e., the perturbative order) will give us the number of integrals that have to appear, with the limits from 0 to t. We have to multiply these integrals by $\left(\frac{\lambda}{24}\right)^n$ ($n \equiv$ *number of internal vertices* $= 0, 1, 2$) and an additional combinatorial prefactor whose value is obtained from the expansion. I.e., if we have n internal vertices:

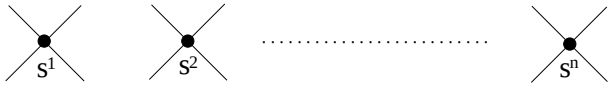

  the related integrals are:

$$\left(\frac{\lambda}{24}\right)^n \text{Prefactor} \int_0^t ds^1 \int_0^t ds^2 ..... \int_0^t ds^n \text{ (arguments)} \tag{110}$$

- With respect to the *arguments* of the integrals, for every solid line that connects two vertices t and s a propagator $G_S(t, s)$ will appear, where the ordering between t, s is irrelevant due to G_S being symmetric under their exchange, so we do not draw any orientation. For every oriented dotted line that connects two vertices t, s a propagator $G_r(t, s)$ will

appear, and in this case the ordering is important and must match the orientation:

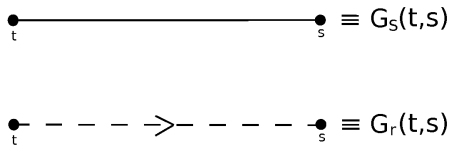

- The value of the *prefactor* for a diagram is calculated similarly to the usual perturbative expansion, but with some differences, and depends on various parameters like the *perturbative order*, the *number of legs of each internal vertex*, the *number of internal vertices*, the *number of external vertices*, *number of oriented dotted lines or solid lines that appear*, etc... We will look to it in detail in the next chapter.

As an example, the contribution from the diagram:

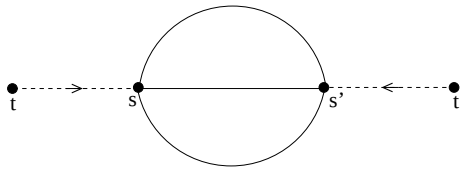

Figure 2: Example diagram for $< \hat{x}^2(t) >$

will be an expression with the following form

$$\text{prefactor} \left(\frac{\lambda^2}{24^2}\right) \int_0^t ds \int_0^t ds' \, G_r(t,s) G_S^3(s,s') G_r(t,s') \tag{111}$$

3.2.2 Diagrams for $< \hat{x}^2 >$

Next we will present the diagrams obtained expanding the expressions shown above in terms of our two real propagators and considering only the connected ones:

Zero order:

We have only one diagram:

corresponding to the expression:

$$G_S(t,t) \tag{112}$$

First order:

It also has only one diagram:

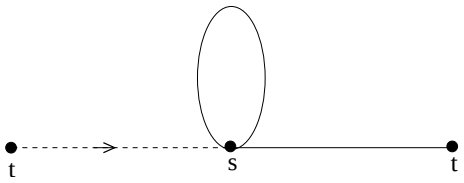

corresponding to the expression:

$$2\lambda \int_0^t ds\, G_r(t,s) G_S(s,s) G_S(t,s) \tag{113}$$

Second order:

Here we have three kinds of topologically different diagrams. We already explained how to read them.

First kind:

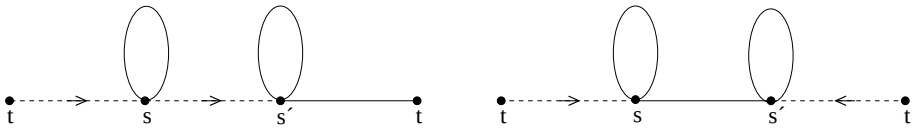

Second kind:

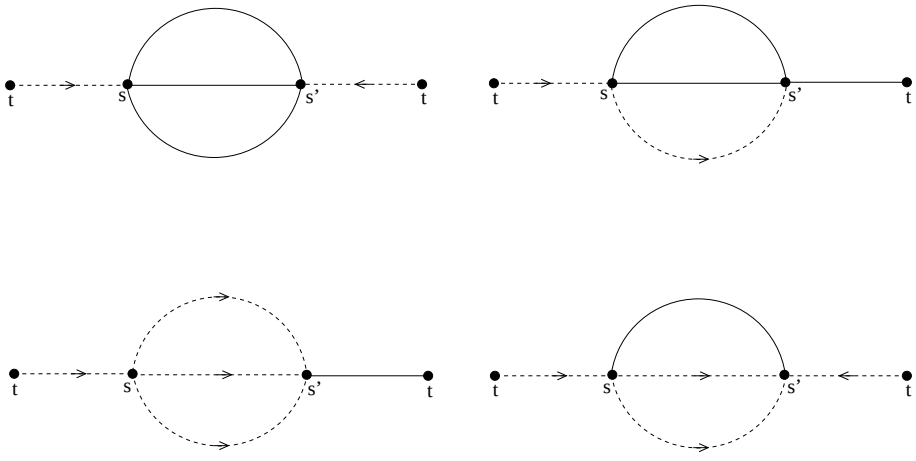

Third kind:

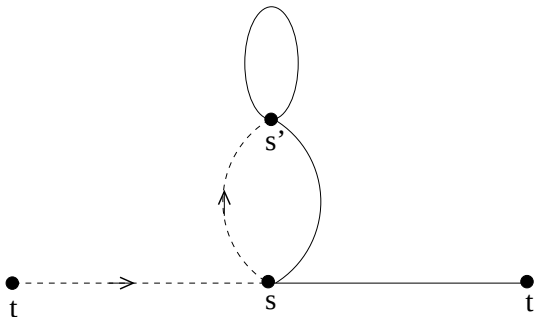

As an example and considering that only one diagram of this third kind exists, we will show the expression corresponding to it

$$prefactor\ \frac{\lambda^2}{24^2}\int_0^t ds \int_0^t ds'\, G_S(t,s)G_r(t,s)G_r(s,s')G_S(s,s')G_S(s',s') \quad (114)$$

We have implemented in FORTRAN a group of programs that calculate all these contributions, defining the corresponding propagators and integrating numerically the expressions shown.

3.2.3 Diagrams for $< \hat{x}^4(t) >$

We are going to show the diagrams corresponding to $< \hat{x}^4(t) >$ too. They are read the same as the previous case. These diagrams have also been calculated analytically expanding expression (89).

Zero order:

We have three diagrams:

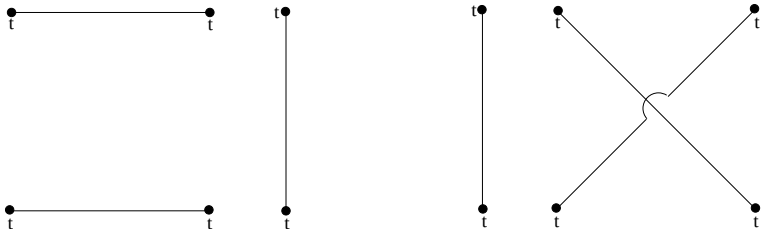

corresponding to the expression:

$$3(G_S^2(t,t))^2 \tag{115}$$

As we are only interested in the connected diagrams (that contribute to the cumulants), we are going to ignore this contribution.

First order:

There are two diagrams, and the prefactor for both is the same.

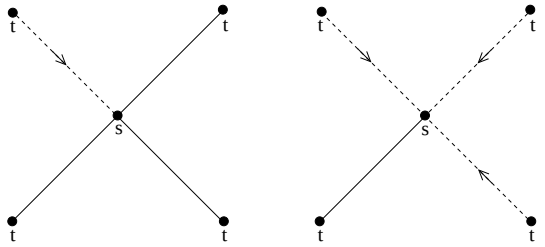

Concerning the signs, the first one is $+1$ and the second one is -1. Therefore they represent the following contribution:

$$\text{prefactor}\frac{\lambda}{24}\int_0^t ds\ \left(G_S^3(t,s)G_r(t,s) - G_S(t,s)G_r^3(t,s)\right) \tag{116}$$

Second order:

Here we have two different topologies, and we will show them separately.

First kind:

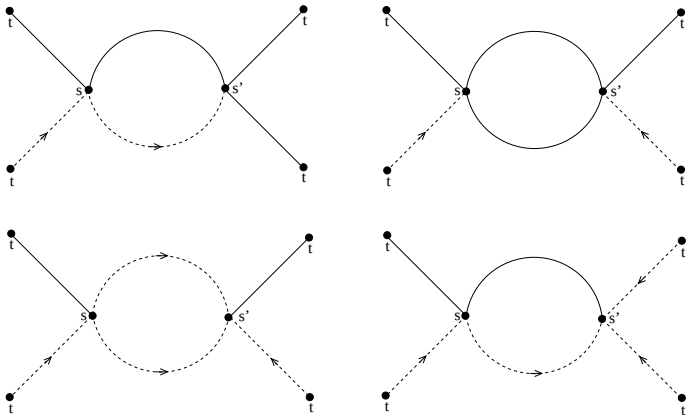

Second kind:

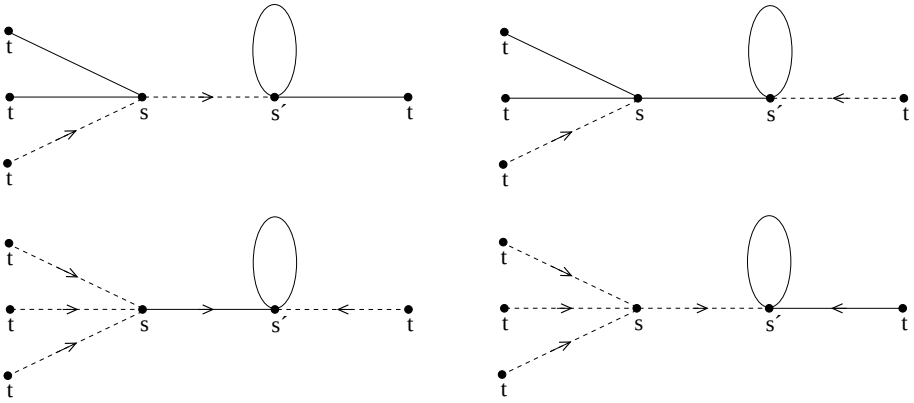

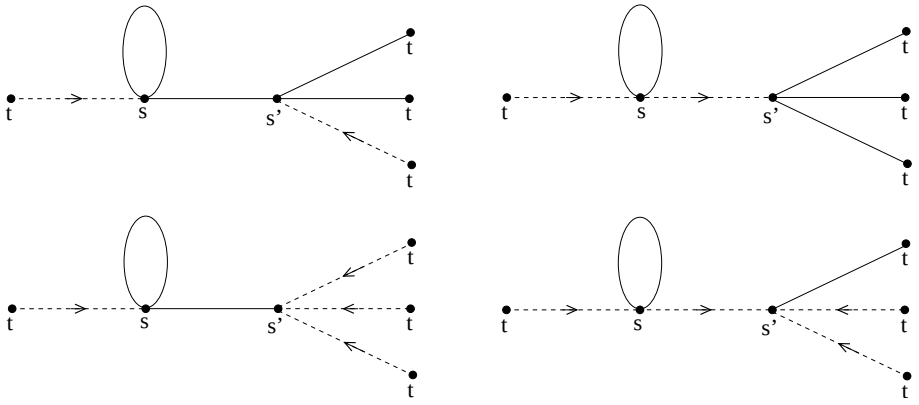

The contribution of these connected diagrams is known as *Cumulant*, and for $< \hat{x}^4(t) >$ we will call it C_4. It follows the expression

$$< \hat{x}^4(t) >= C_4 + 3 < \hat{x}^2(t) >^2 \tag{117}$$

Therefore, if we want to calculate $< \hat{x}^4(t) >$ perturbatively up to *second order*, calculating just C_4 up to that order is not enough, we also have to use the results corresponding to the diagrams of the previous section to sum the term $3 < \hat{x}^2(t) >^2$.

3.2.4 Application to diagrams involving $\hat{p}$

If we calculate expectation values that include the momentum operator $\hat{p}$, we can obtain a Feynman rules in a similar way to we have done above. However, this is a priori a more difficult case, because involve two-point functions of type $\langle \hat{p}_0(t)\hat{x}_0(s)\rangle$, whose real and imaginary parts do not have any symmetry with respect to the exchange of their arguments (unlike G_S and G_A).
Actually, it is not necessary to perform all this, because we can take into account that $\hat{p}_0(t) = \partial_t \hat{x}_0(t)$ and then it is enough to the explained in the previous section. For instance, we can write

$$\langle \hat{p}(t)\hat{p}(t')\rangle = \partial_t \partial_{t'} \langle \hat{x}(t)\hat{x}(t')\rangle \tag{118}$$

and also a similar expression can be written for a product of four operators $\hat{p}(t)$. In fact, this is valid for a general product of n operators.

3.3 Classical evolution with perturbative treatment

We want to compare the quantum and classical evolution, so that it will be useful to perform a perturbative expansion in λ for the classical case. Thus, we are going to consider our one-dimensional variable x as classical one, and solve its classical evolution equation perturbatively.

3.3.1 System description

Evolution equation

As we just said, we consider a one-dimensional classical variable x that evolves using the classical equation of motion. The Hamiltonian is the same that was written in (82) and therefore we have the following evolution equation

$$\ddot{x}(t) + w^2(t)x(t) = -\frac{\lambda}{6}x^3(t) \tag{119}$$

If we take $\lambda = 0$, then the evolution correspond to a quadratic Hamiltonian and is the same than in the quantum case. We have already calculated this evolution analytically. Thus, we will consider that the cubic term of the equation can be considered a perturbation in order to obtain an expansion in λ.

Initial conditions

Analogous to the quantum perturbations case, we will consider that initially our variable has a gaussian distribution function. The zero order will be the evolution of the unperturbed Hamiltonian ($\lambda = 0$) and will correspond with $x_0(t)$ and $p_0(t) = \dot{x}_0(t)$. For this zero order we start from the full initial state so that, if $x(t)$ and $p(t)$ correspond with the complete evolution, then we have

$$x(0) = x_0(0) \qquad p(0) = p_0(0) \tag{120}$$

3.3.2 Perturbative expansion

We take the cubic term as a perturbation, and expand $x(t)$ as a series in powers of λ

$$x(t) = \sum_{n=0}^{\infty} \lambda^n x_n(t) \tag{121}$$

We introduce this in the equation (119) and equate both sides of it order by order. We will see what we obtain up to second order.

Zero order

Being the right hand side of (119) multiplied by λ, there will not be any independent term of such λ and therefore for zero order we have

$$\ddot{x}_0(t) + w^2(t)x_0(t) = 0 \tag{122}$$

To solve the equation given some initial values $x_0(0)$ and $\dot{x}_0(0) = p_0(0)$ we can use what was explained in the chapter 2. Thus, our solutions can be expressed in terms of $f(t)$ and $g(t)$ defined in (38) and whose components fulfill (40) with the initial conditions (41). In this case the solutions are given by (42) replacing the operators to the corresponding classical variables.

First order

Equalizing the terms that have only one λ we obtain, introducing the perturbative series in (119), the following equation

$$\ddot{x}_1(t) + w^2(t)x_1(t) = \eta_1(t) \tag{123}$$

where in this case $\eta_1(t) = -x_0^3(t)$. As we already mentioned, initially (121) is fulfilled and that means

$$x_n(0) = 0 \quad p_n(0) = \dot{p}_n(0) = 0 \tag{124}$$

for every $n = 1, 2, ...$. Particularly this will be true for $x_1(0), p_1(0)$ and both will be zero. We have then the initial conditions and we can solve the equation. To do this we use the parameter variation approach, taking advantage of our knowledge of the solution of the homogeneous equation (that corresponds with zero order). So, from (38) and (39), if we consider the $M(t)$ defined there and we identify it for this case

$$v_0(t) \equiv \begin{pmatrix} p_0(t) \\ x_0(t) \end{pmatrix} \quad A(t) \equiv \begin{pmatrix} 0 & -w^2(t) \\ 1 & 0 \end{pmatrix} \tag{125}$$

we obtain, from (39)

$$v_0(t) = M(t)v_0(0) \;\; \dot{v}_0(t) = A(t)v_0(0) \;\Rightarrow\; \dot{M} = AM \tag{126}$$

Now we introduce two time arbitrary functions and we force them to satisfy the complete equation. I.e., we define

$$v_1(t) \equiv \begin{pmatrix} p_1(t) \\ x_1(t) \end{pmatrix} \quad u(t) \equiv \begin{pmatrix} u_1(t) \\ u_2(t) \end{pmatrix} \tag{127}$$

satisfying $v_1(t) = M(t)u(t)$ and equation (123). Therefore we have

$$\dot{v}_1(t) = A(t)v_1(t) + \begin{pmatrix} \eta_1(t) \\ 0 \end{pmatrix} \Leftrightarrow \dot{M}u + M\dot{u} = AMu + \begin{pmatrix} \eta_1(t) \\ 0 \end{pmatrix} \tag{128}$$

and taking into account $\dot{M} = AM$ it results

$$\dot{u}(t) = M^{-1} \begin{pmatrix} \eta_1(t) \\ 0 \end{pmatrix} \tag{129}$$

In fact, due to the initial conditions for $x_n(t), p_n(t)$ are the same for any other n, this equation (129) is valid for every n adapting in each case the corresponding $\eta(t)_n$ (that will differ from case to case).
Therefore, we have obtained:

$$\begin{aligned} \dot{u}_1 &= \sqrt{2w} f_1(t)\eta(t) \\ \dot{u}_2 &= \sqrt{2/w} f_2(t)\eta(t) \end{aligned} \tag{130}$$

and taking into account (124) for $n = 1$ and $v_1 = Mu$, the initial conditions for (130) results

$$u_1(0) = u_2(0) = 0 \tag{131}$$

so we have at last:

$$u_1(t) = \sqrt{2w}\int_0^t f_1(s)\eta_1(s)ds \quad u_2 = \sqrt{2/w}\int_0^t f_2(s)\eta_1(s)ds \tag{132}$$

With all this, and taking into account that $v_1(t) = M(t)u(t)$, we can find the following expressions for $x_1(t)$ and $p_1(t)$

$$\begin{aligned} p_1(t) &= -2\int_0^t (g_1(t)f_1(s) + g_2(t)f_2(s))\eta_1(s)ds \\ x_1(t) &= -2\int_0^t (f_2(t)f_1(s) - f_1(t)f_2(s))\eta_1(s)ds = -2\int_0^t G_A(t,s)\eta_1(s)ds \end{aligned} \tag{133}$$

where we have identified $G_A(t,s) \equiv Im(f(t)f^*(s))$ (Green's function obtained inverting the differential operator that represents the first part of the equation (123)). This G_A coincides with the one defined for the quantum case. Therefore, taking into account that $\eta_1(t) = -x_0^3(t)$ we have

$$x_1(t) = 2\int_0^t G_A(t,s)x_0^3(s)ds \tag{134}$$

Second order

As we already said, the equations (133) are valid for any n only considering the corresponding $\eta_n(t)$. In the second order case, the equation to solve is

$$\ddot{x}_2(t) + w^2(t)x_2(t) = \eta_2(t) \tag{135}$$

that has the same form than the first order equation (and it will remain for any higher order) and the same initial conditions (124). Nevertheless, now $\eta_2(t) = -3x_0^2(t)x_1(t)$. So, from (133), after substituting the $x_1(t)$ obtained previously

$$x_2(t) = 12\int_0^t ds\int_0^s ds' G_A(t,s)G_A(s,s')x_0^2(s)x_0^3(s') \tag{136}$$

3.3.3 Perturbative calculation of $< x^2(t) >$

If we expand to second order

$$x(t) = x_0(t) + \lambda x_1(t) + \lambda^2 x_2(t) \tag{137}$$

and we substitute it in the expression $< x^2(t) >$ with the x_0, x_1, x_2 obtained in the previous section, we can express this expectation value in terms of the expectation values which only have variables to zero order x_0. To these variables (that have a gaussian distribution) we can apply the Wick's theorem analogously to the quantum case and have everything in terms of two point functions $< x_0(t)x_0(s) >$. Then we have only to calculate these functions. In order to do this, it is worth remembering that the initial state is the same to quantum and classical evolution, and correspond to a gaussian Wigner function $W(x, p; 0)$ at $t = 0$. The quantum expectation values obtained from this W correspond to the quantum ones Weyl-ordered, and are directly the classical ones. This means that we have

$$\begin{aligned} &< x_0^2(0) >=< \hat{x}_0^2(0) >= A_0 \ ; \ < p_0^2(0) >=< \hat{p}_0^2(0) >= B_0 \\ &< x_0(0)p_0(0) >=< p_0(0)x_0(0) >= \frac{1}{2}(< \hat{x}_0(0)\hat{p}_0(0) > + < \hat{p}_0(0)\hat{x}_0(0) >) = Re(C_0) \end{aligned} \tag{138}$$

With this, and taking into account (42) (where we have to replace the operators $\hat{x}_0, \hat{p}_0$ to the classical variables x_0, p_0), one obtain for this classical case

$$< x_0(t)x_0(s) >= G_S(t, s) \tag{139}$$

where $G_S(t, s)$ is real and symmetric respect to argument swapping and coincides with the same propagator defined for the quantum case in (99) (which take the form seen in 100) for the ground state). This result implies that every two point function (that involves variables x_0) can have its arguments swapped, unlike the quantum case where this swapping led to a complex conjugation.

Now we will use all this and we will calculate the contribution of the different orders

- *Zero order*:

We have:

$$< x^2(t) >_{(0)} = < x_0^2(t) > = G_S(t,t) \tag{140}$$

- *First order*:

This order can come from two contributions, $< x_1(t)x_0(t) >$ or $< x_0(t)x_1(t) >$. But both, after using Wick's theorem, give the same terms, with the arguments of some two point functions exchanged. Nevertheless, we already said that the order of such arguments is irrelevant, so the two contributions are the same. The sum of both gives:

$$< x^2(t) >_{(1)} = 2\lambda \int_0^t G_A(t,s) G_S(s,s) G_S(t,s) ds \tag{141}$$

that coincides with the first order contribution in the quantum case.

- *Second order*:

Now the contributions can come from various terms. We can have the two variables to first order $< x_1(t)x_1(t) >$, or the first one to second order and the second one to zero order $< x_2(t)x_0(t) >$, or vice versa $< x_0(t)x_2(t) >$. Anyway the last two give the same results as they only differ in the arguments exchange of the two point functions.

The whole sum gives a very large expression so we will not show it here. However, we will mention that all the terms in this case also appeared in the quantum case and with the same factors too, although in the quantum one there were additional terms. We are going to represent all of them as diagrams in the next section.

3.3.4 Perturbative diagrams

Propagators

We have obtained the two propagators G_0 and G_A identical to the quantum ones, and just like then we can include the corresponding function θ to redefine $G_A \to G_r$. Thus we can have the integral limits from 0 to t without

worrying for the time ordering. Therefore we have

$$G_r(t,s) \equiv \theta(t-s)G_A(t,s) \tag{142}$$

To draw the contributions with Feynman-like diagrams we are going to represent these two propagators with two different kinds of lines, as we did in the quantum case. G_S corresponds with an unoriented solid line (because its arguments ordering is irrelevant) and G_r corresponds with an oriented dashed line according the ordering

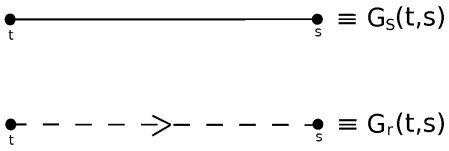

Feynman rules

It has been checked that in this case the Feynman rules to read the diagrams are exactly the same as the quantum case. The propagators are identical, even the calculated *prefactors* are also the same.
In fact, as we already mentioned, all the terms obtained for $< x^2(t) >$ were included in the quantum expectation value, among others. This means that there are fewer diagrams but they have the same expressions.

This has been checked not only for $< x^2(t) >$, but also for $< x^4(t) >$. So it seems that the quantum case includes the classical case, at least up to second order.

Diagrammatization for $< x^2(t) >$

Next we show the diagrams that appear for each order in the calculation of $< x^2(t) >$

- *Zero order*:

- *First order*:

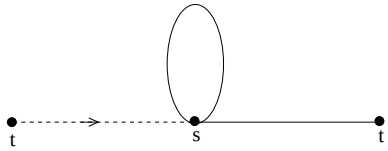

- *Second order*:

First kind

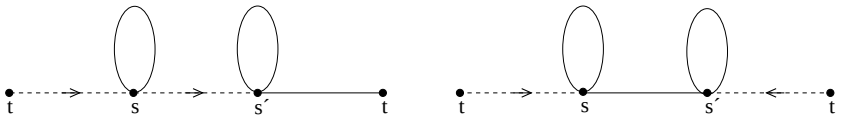

are the same as in the quantum case.

Second kind

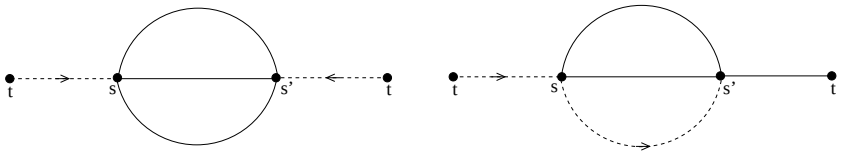

there are two less than in the quantum case.

Third kind

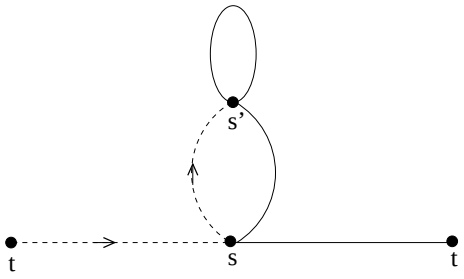

is the same that in the quantum case.

Thus, we see that till *First order* the classical and quantum case are identical.

Diagrammatization for $< x^4(t) >$

We also show the connected diagrams that appear for each order in the calculation of $< x^4(t) >$:

- *Zero order*:

They are the same as the quantum case, and being disconnected we will not show them here.

- *First order*:

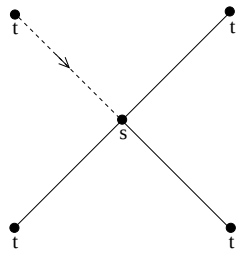

There is one less than in the quantum case.

- *Second order*:

First kind

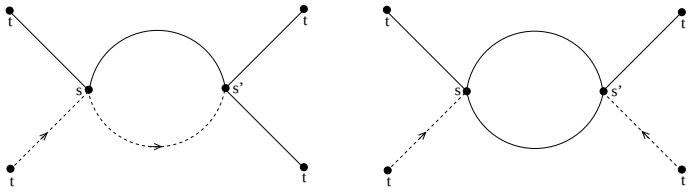

there are two less than in the quantum case.

Second kind

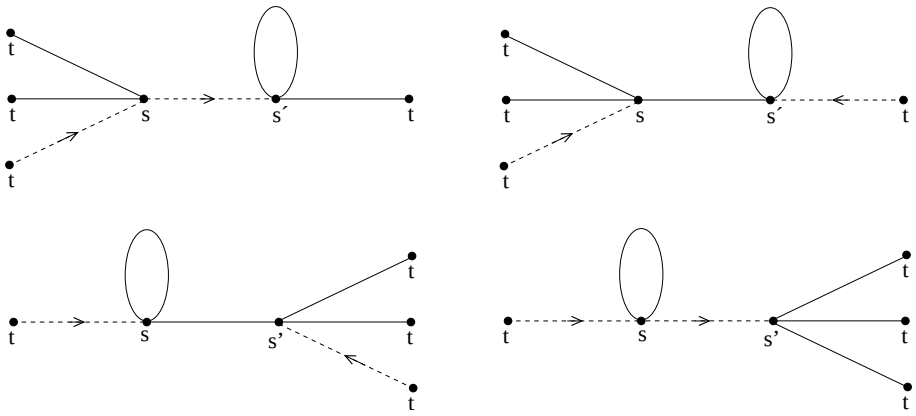

there are four less than in the quantum case.

3.3.5 Classical vs. quantum diagrams

If we study the diagrams obtained and compare them with the quantum ones, we notice that the ones that appear in the classical case are those that have a number of oriented dotted lines (i.e., a number of propagators G_r) equal to the order of the diagram. For them it has been checked that the combinatorial prefactors are the same. Thus, it seems (up to second order at least) that the building rules of the diagrams are the same than in the quantum case, but only the diagrams that satisfy the previous rule are considered. It would be important to check if this is true for any order, so we will do it in the following chapter .

3.3.6 Comparison with the case of $< \hat{x}^2(t) >$

We take the Hamiltonian of an anharmonic oscillator with a time dependent frequency of the form

$$H(x,t) = \frac{1}{2}p^2 + \frac{1}{2}(c_0 - u_0 t)x^2 + \frac{\lambda}{24}x^4 \tag{143}$$

with the values of parameters: $c_0 = 8, u_0 = 2, \lambda = 0.12$. The initial state is gaussian and corresponds with the following Wigner function

$$W(x,p) = \frac{1}{\pi} e^{\frac{-x^2}{2\sigma^2}} e^{\frac{-2\sigma^2 p^2}{\hbar^2}} \tag{144}$$

with the value $\sigma = 0.5$. This system will be studied later, when we test the classical approximation.

We have seen that to second order in perturbation theory there are two diagrams more appearing in the quantum case than in the classical case. We can draw both contributions as a function of time to estimate the difference.

We expect the difference to be very small at first, since the quantum and classical expectation values are equal to order λ. The difference should increase as the second order contribution start start to play a role. This is shown in Fig. 3, where we have represented the difference between the classical and the quantum values of $< \hat{x}^2(t) >$ up to second order in perturbation theory divided by square root of quadratic sum of both (to avoid dividing by one of the two that becomes zero at some points)

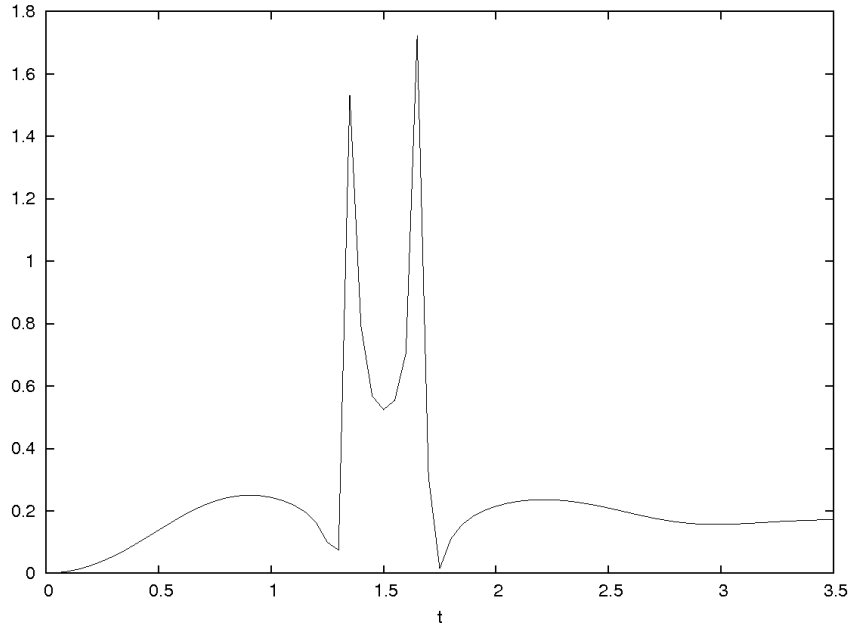

Figure 3: Relative differences between the classical and the quantum perturbative values of $< \hat{x}^2(t) >$ up to second order in perturbation theory.

We notice there is a region where the value rockets. This is because in that zone the second order contribution approaches zero and has very small values, smaller than the difference between the classical and quantum second order values. After that the contribution increases again, and the difference reach the 20%.

This means that the differences for the whole value up to order 2 of $< \hat{x}^2 >$ between the classical and the quantum case are very small at first (about $\lambda^2/24^2$), but they will grow as the system evolves. We can see those differences in Fig. 4.
Therefore, the perturbative evolution from the beginning is described correctly in a certain range of times, as one expects.

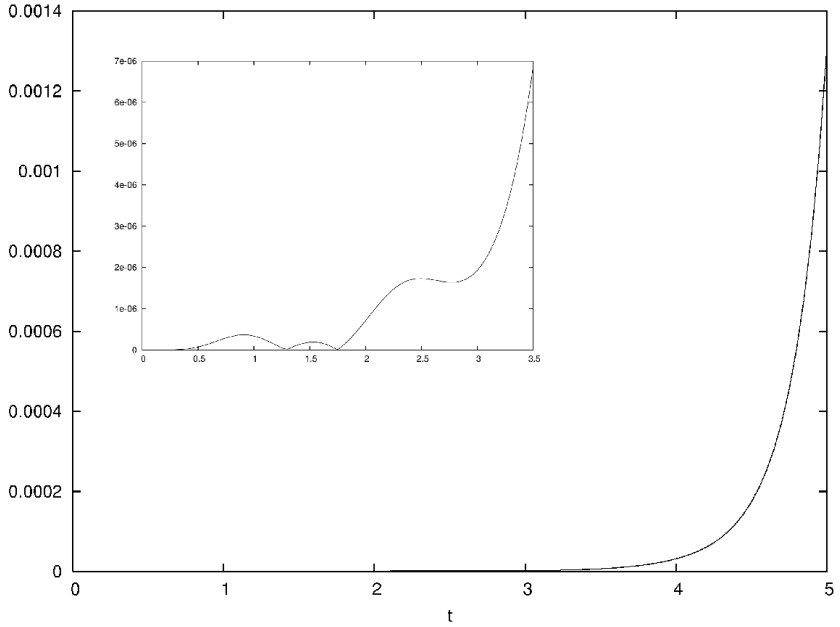

Figure 4: Absolute differences for $< x^2 >$ between the classical and the quantum perturbative calculations.

4 General Perturbative Expansion

In the previous chapter we have shown a particular perturbative expansion that uses the same propagators in the quantum and classical case, and leads to similar Feynman rules to draw the diagrams. With this formalism, the obtained classical diagrams to second order are a subset of the quantum diagrams. This allows us to monitor the difference between quantum and classical evolution to second order.
It would be convenient to obtain general Feynman rules that allow us to build perturbative diagrams to any order, for the case of time dependent potentials, in QM (Quantum Mechanics) and CM (Classical Mechanics). Moreover, if one can draw these diagrams with lines that correspond to propagators G_S and G_A, we can compare both cases to find the diagrams that differ. With this, we can split the perturbative expansion into that appearing in the classical expansion and that appearing in the quantum corrections.

Thus, we will start showing a general time-dependent perturbative expansion for QM that uses the operator formalism, following Ref. [55]. This leads to Feynman rules with a concrete propagators that are not our G_S, G_A, and therefore are not convenient for our purposes. After, we show the general perturbative expansion for CM, deriving the corresponding Feynman rules that use our mentioned propagators G_S and G_A. In order to reach similar rules for the quantum case, we express the mentioned propagators of the quantum perturbative expansion as functions of G_S and G_A, obtaining new Feynman rules. These rules are, a priori, different from the Feynman rules obtained in the classical case. However, we will prove that equivalent rules can be derived for the quantum case that are similar to the rules of the classical case, and allow us to compute the diagrams that differ to any order.

4.1 Quantum Mechanics

4.1.1 Perturbation Theory for time-dependent potential

Consider the potential

$$V(x,t) = \frac{1}{2}w^2(t)x^2 + \frac{\lambda}{24}x^4 \tag{145}$$

Let $\hat{x}(t)$, $\hat{p}(t)$ stand for the position and momentum operators in the Heisenberg picture that evolve with the above potential, and $\hat{Q}(t)$ any product of

these operators at the same time. If $\hat{x}_0(t)$, $\hat{p}_0(t)$ are the operators in the interaction picture evolving with the quadratic potential ($\lambda = 0$), the expectation value of $\hat{Q}(t)$ from some initial state has a time-dependent perturbative series in λ

$$\langle \hat{Q}(t) \rangle = \langle \hat{Q}(t) \rangle_0 + \langle \hat{Q}(t) \rangle_1 + \langle \hat{Q}(t) \rangle_2 + ... \tag{146}$$

where the sub-index indicates the λ-order. Each term can be calculated using the well-known expression from the T-exponential

$$\langle \hat{Q}(t) \rangle_N = \sum_{n+m=N} \frac{1}{n!m!} \int_0^t ds_1...ds_n ds'_1...ds'_m$$
$$\langle \hat{T}'\{i\frac{\lambda}{4!}\hat{x}_0^4(s_1)...i\frac{\lambda}{4!}\hat{x}_0^4(s_n)\}\hat{Q}(t)\hat{T}\{(-i)\frac{\lambda}{4!}\hat{x}_0^4(s'_1)...(-i)\frac{\lambda}{4!}\hat{x}_0^4(s'_m)\}\rangle \tag{147}$$

with $n, m = 0, ..., N$ (as long as $n + m = N$). $\hat{T}$ means time-ordering and $\hat{T}'$ anti-time-ordering. Assuming a Gaussian initial state, it is possible to apply Wick's theorem, thus the integral factorizes into products of pairs. For each pair we have to keep the same relative order as in (147) . Reading from left to right, if the pair involves s_i, s_j then the ordering is in increasing times, if the pair involves s'_i, s'_j then the ordering is in decreasing times and if it involves s_i, s'_j then the pair is $\langle \hat{x}_0(s_i)\hat{x}_0(s'_j)\rangle$. The pair can also involve s_i, t (t indicates an external vertex) and then we get $\langle \hat{x}_0(s_i)\hat{v}_0(t)\rangle$, or t, s'_j and consequently we get $\langle \hat{v}_0(t)\hat{x}_0(s'_j)\rangle$. Here $\hat{v}_0(t)$ can be $\hat{x}_0(t)$ or $\hat{p}_0(t)$.

4.1.2 Diagrammatic formalism

The previous expansion leads to a set of diagrammatic rules [55], but one that is more complicated than ordinary Feynman rules. A Nth-order diagram has N vertices. We are going to distinguish between *left* and *right* vertices, arising respectively from the anti-time-ordered and time-ordered product in (147). Each left or right vertex contributes a factor $i\lambda/24$ or $-i\lambda/24$ respectively. Furthermore, if we apply Wick's theorem then we obtain several types of propagators depending on the kind of vertices involved (left, right or external), as explained before. A line is associated with one of this propagators according to its two vertices. We must consider also all possible connections between the vertices that give equivalent diagrams, and then we get a combinatorial factor for each diagram. We are going to focus in these factors.

–In the usual Feynman rules for a time-independent potential with a quartic

interaction term as in (145), the final factor for any Nth-order diagram comes from the computation of all allowed vertices and legs permutations that give equivalent diagrams, the $1/N!$ which appears in the exp, and from the $1/24^N$ originating of the interaction term. The resulting value for the final factor is $1/s$, where s is the diagram symmetry factor. A priori, it could seem that the number of equivalent diagrams is the product of 24^N (permutations of 4 legs on every vertex) times $N!$ (permutations of N vertices), but this is an over-counting with respect to the actual number coming from Wick's theorem application. The ratio between this over-counting and the actual number of equivalent terms is indeed the symmetry factor:

$$s = \frac{24^N N!}{\text{number of equivalent terms}} \tag{148}$$

Of course, when we replace diagrams by integrals, we have to multiply the final factor $1/s$ by λ^N coming from the N internal vertices.

–Return now to our case and consider a diagram D with n left vertices and m right vertices. The number of equivalent diagrams is not as in (148) because all $N!$ vertices permutations do not represent equivalent terms. The interchanges between left and right vertices do not give the same contribution. Nevertheless, the permutation of the n left vertices among themselves and/or the permutation of the m right vertices among themselves give the same contribution (it is straightforward to see this from (147)). Therefore, we have $\binom{N}{n}$ different ways to place the n left vertices inside the total N vertices, resulting diagrams that are not, in principle, equivalent. And there are $n!m!$ forms to permute separately the left and right vertices that give equivalent diagrams. This last factor cancels the $1/(n!m!)$ that appeared in (147). Notice that $\binom{N}{n}n!m! = N!$ and we have considered all permutations of the N vertices.
The additional factor 24^N coming from leg permutations produces the mentioned over-counting and cancels the $1/24^N$ of the interaction term. It is necessary to divide by the diagram symmetry factor to eliminate the over-counting and obtain the final correct factor.
There also exists a factor i^{n-m}, as follows from (147).
Consequently, our diagram D actually represents $\binom{N}{n}$ different diagrams, and the final global factor for each diagram is i^{n-m}/s. Every term in (147) corresponds to a value of n, m and we have to consider the $N+1$ possible values. Thus, the total number of diagrams that we have to count is $\sum_{n=0}^{N}\binom{N}{n} = 2^N$,

and this is exactly the 2^N ways of choosing each internal vertex to be *left* or *right*. Of course, the integral that corresponds with each diagram has to be multiplied by λ^N.
We will not consider vacuum diagrams because:

$$\left\langle \left[\text{T-exp}\left(i\int_0^t ds \frac{\lambda}{4!}\hat{x}_0^4(s) \right) \right] \left[\text{T'-exp}\left(-i\int_0^t ds \frac{\lambda}{4!}\hat{x}_0^4(s) \right) \right] \right\rangle = \hat{1} \qquad (149)$$

With the previous considerations we can already give a set of rules to calculate $\langle \hat{Q}(t) \rangle$ with a gaussian initial state [55]. We note them by *A rules* because later we will give other set of rules with other propagators.

A Rules:

- We consider the ordinary Feynman diagrams. For a diagram with N (internal) vertices we have 2^N ways of choosing each vertex to be *left* or *right*, giving 2^N, a priori, different diagrams. Each one has a global factor $i^{n-m}\lambda^N/s$, where n, m are respectively the number of left and right vertices, and s is the diagram symmetry factor.

- A line connecting a left vertex s_i to a right vertex s'_j contributes a propagator $\langle \hat{x}_0(s_i)\hat{x}_0(s'_j) \rangle$.

- A line connecting a left vertex s_i to a left vertex s_j contributes a propagator $\langle \hat{T}'\{\hat{x}_0(s_i)\hat{x}_0(s_j)\} \rangle$.

- A line connecting a right vertex s'_i to a right vertex s'_j contributes a propagator $\langle \hat{T}\{\hat{x}_0(s'_i)\hat{x}_0(s'_j)\} \rangle$.

- A line connecting a external vertex t to a left vertex s_i contributes a propagator $\langle \hat{x}_0(s_i)\hat{v}_0(t) \rangle$, where $\hat{v}_0$ can be $\hat{x}_0$ or $\hat{p}_0$.

- A line connecting a external vertex t to a right vertex s'_j contributes a propagator $\langle \hat{v}_0(t)\hat{x}_0(s'_j) \rangle$.

- We must integrate over all variables $..., s_i, ..., s'_j, ...$ from 0 (or t_0) to t.

- It is not necessary to consider vacuum diagrams.

Notice that if a diagram is transformed by transforming a left vertex into a right vertex (or vice versa) then the resulting global factor is the same but multiplied by -1 (although the new diagram contribution can be different). In the case $\hat{Q}(t) = \hat{x}^l(t)$ (also $\hat{p}^l(t)$), if for a diagram the n left vertices are transformed into right and the m right vertices into left, then the new diagram is the complex conjugate of the previous one. So, each diagram has his complex conjugate and the total sum is real (the zero order is real), as it is expected.

We can see an example of this with $\hat{Q}(t) = \hat{x}^2(t)$. For this case (and, in general, for $\hat{Q(t)} = \hat{x}^l(t)$) we can define three kinds of propagators:

$$\begin{aligned} G_>(s,s') &\equiv \langle \hat{T}\{\hat{x}_0(s)\hat{x}_0(s')\}\rangle = G_>(s',s) \\ G_<(s,s') &\equiv \langle \hat{T}'\{\hat{x}_0(s)\hat{x}_0(s')\}\rangle = G_<(s',s) = G^*_>(s,s') \\ G(s,s') &\equiv \langle \hat{x}_0(s)\hat{x}_0(s')\rangle = G^*(s',s) \end{aligned} \tag{150}$$

with $s, s' \in [0,t]$. We assign a different line to each propagator:

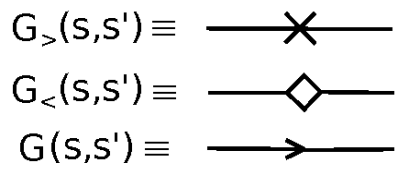

G needs an oriented line because it changes if we interchange its arguments. Consider the second order diagram

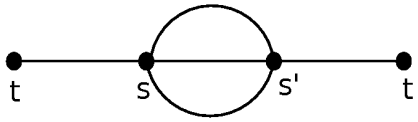

there are $2^2 = 4$ different terms with the contributions

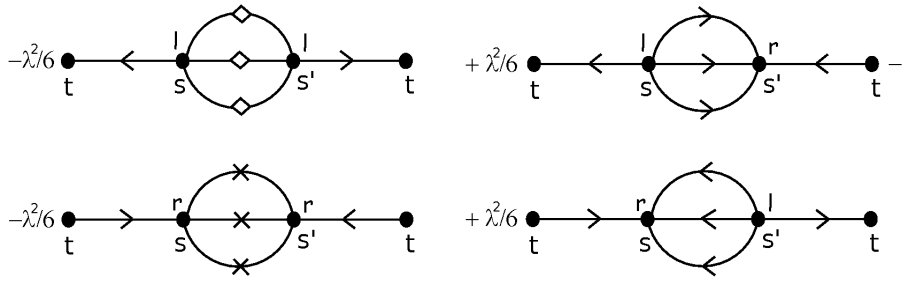

The last two diagrams are the complex conjugate of the previous two ones and we can write the final contribution as

$$2Re\Big[-\frac{\lambda^2}{6}\int_0^t dsds' G(s,t)G^3_<(s,s')G(s',t)+\frac{\lambda^2}{6}\int_0^t dsds' G(s,t)G^3(s,s')G(t,s')\Big] \tag{151}$$

The A Rules do not include the propagators G_S and G_A that will appear in the classical perturbation theory (as we will see in the following section), and then are not useful to compare the quantum and classical case.

4.2 Time-dependent perturbation theory in Classical Mechanics

We are going to perform a perturbative expansion in CM along the lines of the previous chapter. After, we will return to the quantum case in order to obtain, from the A Rules shown in the previous section, a new rules that are similar to the Feynman rules for classical evolution.
From (145), the classical equations of motion are

$$\begin{aligned}\ddot{x}(t)+w^2(t)x(t) &= -\frac{4\lambda}{24}x^3(t)\\ \dot{x}(t) &= p(t)\end{aligned} \tag{152}$$

Let us perform a perturbative expansion in λ

$$\begin{aligned}x(t) &= x_0(t)+\lambda x_1(t)+\lambda^2 x_2(t)+...\\ p(t) &= p_0(t)+\lambda p_1(t)+\lambda^2 p_2(t)+...\end{aligned} \tag{153}$$

choosing the initial conditions

$$\begin{aligned} x(0) = x_0(0) &\longrightarrow x_n(0) = 0 \quad for \quad n > 0 \\ p(0) = p_0(0) &\longrightarrow p_n(0) = 0 \quad for \quad n > 0 \end{aligned} \tag{154}$$

We can put this into the equation of motion and match order by order to obtain

$$\begin{aligned} &\ddot{x}_n(t) + w^2(t)x_n(t) = \eta_n(t) \\ &\eta_n(t) \equiv -\frac{4}{24}(x^3(t))_{n-1} \end{aligned} \tag{155}$$

where $(x^3(t))_{n-1}$ are all terms in $(x_0(t) + \lambda x_1(t) + ...)^3$ having a λ^{n-1} factor (because the right hand side of the first line in (152) has already a λ factor). The first values of η_n are:

$$\begin{aligned} &\eta_0(t) = 0 \\ &\eta_1(t) = -\frac{4}{24}x_0^3(t) \\ &\eta_2(t) = -\frac{4}{24}3x_0^2(t)x_1(t) \\ &\eta_3(t) = -\frac{4}{24}(3x_0(t)x_1^2(t) + 3x_0^2(t)x_2(t)) \\ &..... \end{aligned} \tag{156}$$

We can solve the zero order similarly to above chapters. The equation is

$$\ddot{x}_0(t) + w^2(t)x_0(t) = 0 \tag{157}$$

and we find the solution

$$x_0(t) = \sqrt{2w}f_1(t)x_0(0) - \sqrt{\frac{2}{w}}f_2(t)p_0(0) \tag{158}$$

Now we can solve the nth order in the perturbative expansion in terms of previous orders. In fact, one can write any other order as a function of zero order, and it is enough to solve this one. The solution from eq. (155) for any n-order is

$$\begin{aligned} x_n(t) &= -2\int_0^t ds(f_2(t)f_1(s) - f_1(t)f_2(s))\eta_n(s) = -2\int_0^t dsG_A(t,s)\eta_n(s) \\ p_n(t) &= -2\int_0^t ds(\dot{f}_1(t)f_2(s) - \dot{f}_2(t)f_1(s))\eta_n(s) \end{aligned} \tag{159}$$

We show next the first orders for $x_n(t)$

$$x_1(t) = \frac{8}{24}\int_0^t ds G_A(t,s)x_0^3(s)$$
$$x_2(t) = \frac{8^2 3}{24}\int_0^t ds_1 G_A(t,s_1)x_0^2(s_1)\int_0^{s_1} ds_2 G_A(s_1,s_2)x_0^3(s_2)$$
$$x_3(t) = \frac{8^3 3}{24}\left[\int_0^t ds_1 G_A(t,s_1)x_0(s_1)\int_0^{s_1} ds_2 G_A(s_1,s_2)x_0^3(s_2)\int_0^{s_1} ds_3 G_A(s_1,s_3)x_0^3(s_3) + \right.$$
$$\left. +3\int_0^t ds_1 G_A(t,s_1)x_0^2(s_1)\int_0^{s_1} ds_2 G_A(s_1,s_2)x_0^2(s_2)\int_0^{s_2} ds_3 G_A(s_2,s_3)x_0^3(s_3)\right]$$
$$.....$$ (160)

4.2.1 Classical diagrammatic formalism

As in the quantum case, we assume a Gaussian initial state and calculate $\langle x^l(t)\rangle$.
We associate an oriented dotted line to G_A propagator, as in QM. Each loose leg of a vertex s_i represents a function $x_0(s_i)$.
Thus, the integrals in (160) can be drawn as branches containing vertices, dotted lines and loose legs. Next, we show these branches for $x_n(t)$ up to order 3

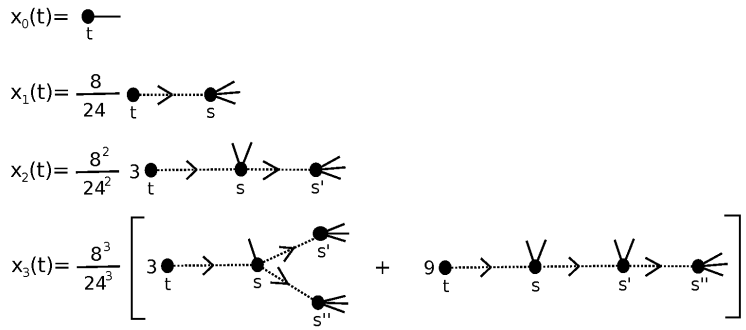

We will discuss later how to get the integration volume. The expression for $x_1(t)$ contains a G_A propagator. If we consider any (n-1)-order and increase one order, we have to place a new G_A propagator and a new integration

variable s_n (directly connected to the external vertex) into solution (159). Thus, when we calculate $x_n(t)$ involving only $x_0(s_i)$ functions by iteration, we get a sum of branches, and every branch contains n G_A propagators and n internal vertices, because η_n includes triple products of $x_0, ..., x_{n-1}$ functions whose orders sum $(n-1)$. By the same arguments, we find a global factor $8^n\lambda^n/24^n$ in each branch. This means that the graphical expression for $x_n(t)$ is a sum of *branches*, defined as in the previous section. Moreover, if one wants to make a complete Nth-order diagram, one has to join several of these branches. Clearly, in the resulting diagram, each internal vertex is connected to an external vertex traveling along dotted lines (coming from the same original branch).
From (159), it is straightforward that the dotted lines orientations in every branch flows from the external vertex to internal vertices.

Now, let us analyze the $\eta_n(s)$ term. This one is the sum of all possibles products $x_ix_jx_k$ with $i+j+k=n-1$. Each term has a coefficient that indicates the number of ways to obtain the same product. If $i \neq j \neq k \neq i$ there are a factor 6 coming from the six terms that give the same product, which represents three different subbranches starting from s vertex or two different subbranches and one lose leg. If there are two equal indices and another different, the coefficient is 3, and start two equal subbranches and another different (or lose leg) from the s vertex, or one subbranch and two lose legs. If $i=j=k$ we have a coefficient 1 and three equal subbranches (or lose legs). After, the different choices in each subbranch give several drawings with additional coefficients calculated in the same way. We shall do the last one step by step, following the example (156):
–We begin with $\eta_1(s)$, whose term has three equal indices (coefficient=1) and leads to one branch associated to $x_1(t)$.
–$\eta_2(s)$ has one term also with two equal indices (coefficient=3), and $x_2(t)$ has one branch.
–$\eta_3(s)$ has two terms, both with coefficient=3. But the term with factor x_2 contains, at the same time, another coefficient=3 and corresponds to a branch with a total coefficient=9.
–Up to now, each term in $\eta_n(s)$ was a subbranch with only one element. But for $\eta_4(s)$ there are terms, as for example $x_0x_0x_3$, where a subbranch has two elements. This leads to a greater number of total branches in $x_4(t)$. Moreover, we have to consider other cases. Let us focus in $\eta_7(s)$, involving the term $x_0x_3x_3$. The initial coefficient is 3, but the subbranch associated to x_3

contains two subbranches that we shall label A and B. We can choose for both factors x_3 the AA, AB, BA, BB combinations. However, the AB and BA ones lead to two branches with the same contribution, because the associated integrals are equal if one renames the integration variables. Thus, in this case we can sum AB+BA and the initial coefficient becomes 6, reflecting the fact that actually there are two different subbranches starting from s and they can be set from 6 different ways.

Thus, these coefficients have to be evaluated in each vertex according to subbranches starting from it. The value 1, 3 or 6 depends on the number of equal subbranches. A similar counting will be obtained in the quantum case.

On the other hand, if 1,2 or 3 subbranches (not loose legs) start from an internal vertex s of a branch, the successive 1,2 or 3 vertices directly connected to s correspond to variables that have their integral limits from 0 to s. We can see this for $x_3(t)$ in (160). Thus, about the integration limits, there is an implicit ordering in each branch: *if we travel along any path in the branch, from the external vertex to internal vertices, each variable has to be smaller than the previous ones*. Therefore, if we want to integrate over the reduced volume, we have to choose a definite ordering $s_N \leqslant ... \leqslant s_1$ that agrees with the above implicit ordering and perform all possible permutations that do not violate this implicit ordering. This means that we only can permute variables from different branches or excluding-subbranches. For example, in (160), we can focus on the first integral of $x_3(t)$, and write

$$\int_0^t ds_1 \int_0^{s_1} ds_2 \int_0^{s_1} ds_3 f(t,s_1,s_2,s_3) = \\ = \int_0^t ds_1 \int_0^{s_1} ds_2 \int_0^{s_2} ds_3 \Big[f(t,s_1,s_2,s_3) + f(t,s_1,s_3,s_2) \Big] \qquad (161)$$

Now, we can make complete Nth-order diagrams belonging to $\langle x^l(t) \rangle$ joining l branches that sum a total N order. Of course, we have to consider all different ways to perform these junctions to obtain equivalent diagrams. This leads to the factor $l!/(l_1!l_2!...l_k!)$.
Finally, due to Wick's theorem, we must do all the possible connections between the loose legs that contain every diagram. These connections only involve the G_S propagator because in the classical case one has

$$\langle x_0(t) x_0(t') \rangle = f_1(t) f_1(t') + f_2(t) f_2(t') = G_S(t,t') \qquad (162)$$

where we have taken into account that $\langle x_0(0)p_0(0)\rangle = 0$. So, if we build any diagram, the remaining lose legs lead only to solid lines, and the number of dotted lines is equal to diagram order.

4.2.2 Quantum perturbative expansion in terms of G_S and G_A propagators

Now, we want to find Feynman rules for the quantum perturbative expansion that are similar to those derived in the classical case. Thus, we need to obtain new rules equivalent to A Rules that involve our propagators G_S and G_A.
We will restrict to the case $\hat{Q}(t) = \hat{x}^l(t)$ from now on. In this case, when one solves the evolution equations for the potential (145) with $\lambda = 0$, one obtains that the free two point function $\langle \hat{x}_0(s)\hat{x}_0(s')\rangle$ can be written in terms of two propagators with a definite symmetry, as we have seen in the previous chapter

$$\langle \hat{x}_0(s)\hat{x}_0(s')\rangle = G_S(s,s') + iG_A(s,s') \tag{163}$$

The expressions for G_S and G_A were shown in (99), as well as their symmetry properties.
Our aim is to express the three propagators appearing in A Rules that we shown in (150) in terms of the two propagators G_S and G_A. Next, we want to obtain the set of rules that give all diagrams and associated factors belonging to $\langle \hat{x}^l(t)\rangle$, where the lines symbolize the new propagators. This is necessary because we want to compare the quantum and classical evolution, and when one performs classical perturbation theory the resulting diagrams are functions of the same propagators G_S and G_A. Furthermore, as we will see, the classical perturbative terms have different integral limits and, in order to compare, we are going to modify these limits in our present case.

The integrals in (147) run over a N-dimensional hypercube. We are going to rename the integration variables as $s_1, ..., s_n, s_{n+1}, ..., s_N$. So that there are $N!$ separate volumes inside our hypercube with a definite ordering between the variables s_i, i. e., $s_{i_1} \leqslant s_{i_2} \leqslant ... \leqslant s_{i_N}$. Inside each of these volumes, the perturbative diagrams coming from Wick's theorem have fixed orderings in all their lines, and the integrals only contain propagators $G(s_{i_a}, s_{i_b})$ with $i_a \leqslant i_b$. Of course, for different volumes, the arguments of G are exchanged. However, the integral over any of these volumes can be calculated on a particular volume renaming the integration variables. Indeed, let $f(s_1, ..., s_N)$ be

any integrable function, and σ the set of N-elements permutations, we can always write

$$\int_0^t ds_1, ..., ds_N f(s_1, ..., s_N) = \int_0^t ds_1 \int_0^{s_1} ds_2 ... \int_0^{s_{N-1}} ds_N \sum_\sigma f(s_{\sigma_1}, ..., s_{\sigma_N}) \tag{164}$$

Thus, we shall select a definite ordering of the variables

$$s_N \leqslant s_{N-1} \leqslant ... \leqslant s_1 \tag{165}$$

and denote the volume in which the variables satisfy the previous ordering as *reduced volume*

$$\int_0^t ds_1 \int_0^{s_1} ds_2 ... \int_0^{s_{N-1}} ds_N \tag{166}$$

So, one can consider the ordering (165), select a definite ordinary Nth-order diagram D, consider the 2^N different diagrams (with their global factors) arising from taking into account that each internal vertex can be left or right, perform in every of these diagrams all $N!$ permutations between the variables $s_1, ..., s_N$ but without changing the left or right character of each vertex, and then integrate the expressions belonging to all these $2^N N!$ diagrams over the reduced volume (166). All these operations have to be equivalent to applying the *Rules A* to diagram D, although we now have many more diagrams. Nevertheless, we already have all integrals over the reduced volume and in their arguments only appear propagators $G(s_i, s_j)$, which we can write as functions of G_S and G_A using (163).
We shall do this with the previous example

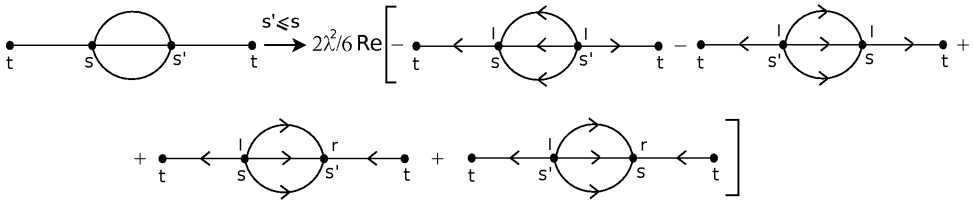

and the 4 diagrams have to be integrated over the *reduced volume*.

In short, for any Nth-order ordinary diagram D, with L lines, we select an

ordering for the integration variables and obtain $2^N N!$ diagrams (and their factors) with oriented lines symbolizing the propagator G. These diagrams represent $2^N N!$ integrals over the reduced volume. So, if we replace each propagator G by $G_S + iG_A$ then we get $2^N N! 2^L$ total integrals, that can be also represented by diagrams defining two new lines symbolizing G_S and G_A

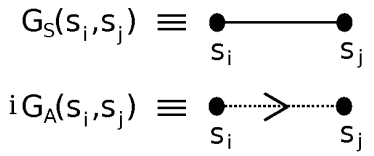

G_A is antisymmetric with respect to the interchange of its arguments, and it must be denoted by an oriented line.
It is convenient to give also an example of this

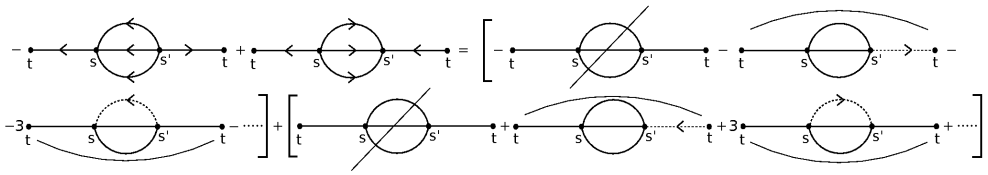

where we have seen that some diagrams can be grouped. In fact, the enormous number $2^N N! 2^L$ of new diagrams that correspond with a Nth-order ordinary diagram will be reduced, because there are many cancellations or groupings between themselves. In order to study these cancellations we will see some interesting properties.

First, since the $\langle \hat{x}^l(t) \rangle$ is real and a Nth-order diagram has N $\pm i$ factors from the vertices, we can derive the following property:

–***Property 1:*** In a Nth-order diagram, the number of dotted lines has to be even if N is even, and odd if N is odd.

This property is necessary because, otherwise, the diagram contribution is a purely imaginary number, and cancels the complex conjugate diagram resulting from exchanging the left and right character of each vertex.

Second, we consider any diagram, select any internal vertex s_i and flip its character from left to right (or vice-versa). Each dotted line connecting s_i to another successive vertex s_j can or cannot change its orientation. If $s_i \leqslant s_j$ according to ordering (165) or $s_j = t$ (external vertex) the dotted line flips it orientation. If $s_j \leqslant s_i$ the orientation remains the same. One can check the four possibilities to be convinced of it.
The s_i flipping gives a (-1) global factor. Each dotted line that changes the orientation also gives a (-1) factor due to antisymmetry of G_A. So, if the product of these factors is negative, both diagrams sum up to zero. Thus, the number of orientation flippings have to be odd to take into account the diagram contribution. This leads to the following property:

–***Property 2:*** The number of dotted lines connecting any internal vertex to either posterior or external vertices, have to be an odd number. Of course, a line connecting an external vertex to another external vertex can only be a solid line, because $G_A(t,t) = 0$
This property also implies that an internal vertex cannot be connected to anterior vertices.

Third, if a internal vertex is only attached to solid lines, the diagram contribution will be zero. To prove this, suppose that we flip the vertex type (left o right), them we obtain another diagram with the same contribution (it has the same lines with the same orientations) but with opposite sign, and the two diagrams add up to zero. We will extend this to a more general property:

–***Property 3:*** For each diagram, there always exists a path connecting any internal vertex to some external vertex, traveling along dotted lines.

To prove it, suppose that a diagram does not satisfy the property 3, then there is a subset of internal vertices D' surrounded by solid lines only:

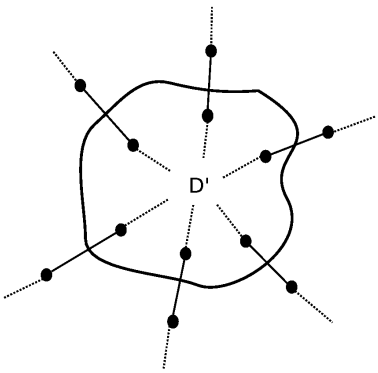

Let s_a be the highest vertex of D'. It is straightforward that all dotted lines arising from s_a connect this vertex to lower vertices and the diagram does not satisfy *property 2*, having zero contribution.
Notice that, by property 3, *the minimum number of dotted lines for a Nth-order diagram is indeed* N, because each internal vertex has a dotted line that connects it with the next vertex along the path to an external vertex. We denote this diagrams with N dotted lines by ***minimal diagrams***.

There is an interesting ***corollary*** from the previous properties: if a Nth-order diagram satisfies properties 1, 2 and 3, the 2^N diagrams obtained by taking each vertex to be left or right give the same contribution.
To prove this corollary imagine a left vertex that flips to right (or vice-versa) in a diagram, by property 2, the global sign change is compensated by an argument interchange in an odd number of G_A propagators, and the contribution is the same.

So, the diagrams that do not satisfy the set of properties above cancel themselves and they give vanishing contribution. For the remaining diagrams we can choose a vertex configuration (each one either left or right) that gives the G_A propagators orientation and the factor $i^{n-m}\lambda^N/s$, and multiplied by 2^N. Thus, we can now summarize all this with a new set of rules for the new diagrams made with G_S and G_A:

B Rules:

- We consider the ordinary Feynman diagrams. We select any diagram D with N (internal) vertices and L lines. We set a definite ordering

$s_N \leqslant s_{N-1} \leqslant ... \leqslant s_1$. There are 2^L ways of choosing each line to be either solid or dotted, and each one has $N!$ possibles permutations between the variables s_i that label the vertices. Many of these $2^L N!$ diagrams give zero sum and it is not necessary to consider all, but only the diagrams satisfying properties 1,2 and 3. Some of these diagrams are equivalent and can be grouped. Notice that, up to now, we do not need to place any orientation in the dotted lines.

- In every diagram of these, we have to fix a definite vertex configuration, choosing each vertex to be left or right. Each Nth-order diagram has a global factor $2^N i^{A+n-m} \lambda^N / s$, where n, m are respectively the number of vertices left, right, A is the number of dotted lines and s the symmetry factor of D. The orientation of the dotted lines depend of the vertices kind following our ordering, as we will see next.

- A dotted line connecting a left vertex s_i to a right vertex s_j contributes a propagator $G_A(s_i, s_j)$.

- A dotted line connecting a left vertex s_i to a left vertex s_j, with $s_i \leqslant s_j$, contributes a propagator $G_A(s_i, s_j)$.

- A dotted line connecting a right vertex s_i to a right vertex s_j, with $s_i \leqslant s_j$, contributes a propagator $G_A(s_j, s_i)$.

- A dotted line connecting an external vertex t to a left vertex s_i contributes a propagator $G_A(s_i, t)$.

- A dotted line connecting an external vertex t to a right vertex s_j contributes a propagator $G_A(t, s_i)$.

- Of course, a line connecting a vertex s_i to itself contributes a propagator $G_S(s_i, s_i)$, where s_i can be t.

- We must integrate in all variables $s_1, ..., s_N$ over the *reduced volume* shown in (166).

- It is not necessary to consider vacuum diagrams.

Let's apply this to our example:

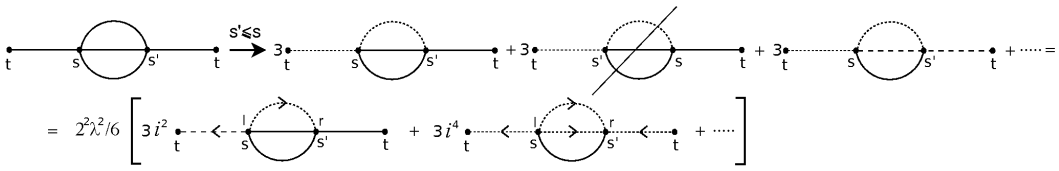

Maybe, some diagrams can still be grouped, depending on the form of each one. Moreover, notice that ***all not minimal diagrams can be obtained from minimal ones by selecting some pairs of solid lines that end up in the same lower vertex and converting two*** G_S ***propagators into two*** G_A ***propagators***. It is straightforward from property 2 that solid lines have to be taken in pairs and that the final vertex must be lower.

These rules already include the G_S and G_A propagators, but still are not similar to the rules obtained in the classical perturbation theory, and not are useful to compare quantum and classical case. From B Rules, we will find an equivalent rules that are similar to the classical case.

4.2.3 Alternative diagrammatic formalism similar to classical one

In order to compare quantum and classical perturbation theory, it is convenient to show an alternative set of diagrammatic rules equivalent to B Rules that are similar to those obtained in the classical case.
We have defined *minimal diagrams* as the diagrams that have a number of dotted lines equal to their order. We are going to do an analysis of B Rules for any *Nth-order minimal diagram* D. We select a definite configuration having n left and m right vertex. In this case $A = N$ and the factor $i^{A+n-m} = (-1)^n$. The factor $2^N\lambda^N$ remains the same. The remaining factor $1/s$ avoids the double-counting coming from the interchange of (internal) vertices and legs. In fact, as we saw earlier, the interchange of vertices plus the possible choices of vertex type (left or right) leads to 2^N factor, and the 24^N legs interchanges cancel the $1/24^N$ coming from interaction term.
Now we are going to perform our counting in a different way. We consider the interchange of vertices, but not the interchange of legs in each vertex (therefore we cannot cancel the $1/24^N$). Let us give a convenient definition:
branch: is a set containing all vertices that are connected to the same external vertex by dotted lines, including the external vertex itself and the

mentioned dotted lines. A branch can be formed by an external vertex only. The branch involves the vertices and the dotted lines, and the remaining lines have to be loose in each vertex.
With this, we can take a minimal $Nth-order$ diagram D with l external vertices and split it in l branches whose vertices are only connected by dotted lines. There is a single way to do this, grouping in each branch all vertices that are connected with the same external vertex through dotted lines. It is convenient to give an example

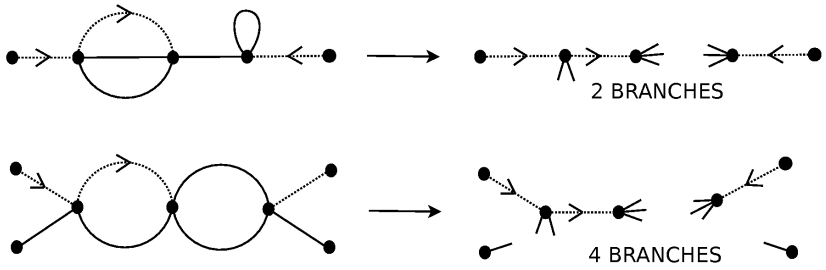

Now we focus in the calculation of the number of equivalent diagrams. We consider an ordinary Nth-order diagram D' with l external vertices. In the expression (148), the factor $24^N N!$ corresponds to interchange of internal vertices and legs. This factor can give an over-counting that is avoided by the symmetry factor s. However, it can have other equivalent diagrams that have to be considered, coming from the interchange among the l external vertices. We give an example of this by labeling external vertices in the following diagram

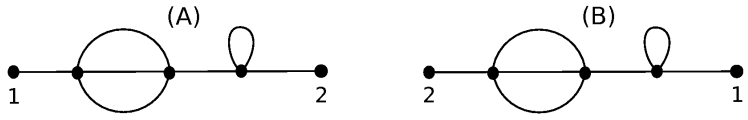

In the (A) diagram the $24^N N!$ permutations involve an over-counting (avoided by s), but do not contain the (B) equivalent diagram.

With this in mind, we return to our minimal diagram D with l external vertices. We consider all vertices as right vertices. Then, from properties 2

and 3, the orientation in each dotted line flows toward the lower vertex. This means that the allowed permutations of variables s_i included in B Rules must be consistent with this orientations, according with the selected ordering $s_1 \leqslant s_2 \leqslant ... \leqslant s_N$. Moreover, we get $i^{A+n-m} = 1$.

Thus, we have l branches to construct our minimal diagram D, and we need to calculate its global factor. We have already considered the internal vertices permutations. We also take into account the 2^N factor coming from the possible choices of the kind of the internal vertices. Now we have to calculate all possibilities that lead to our diagram keeping fixed the location of the vertices in the branches.

We start calculating all possibilities to construct a branch. In each internal vertex we can choose that the incoming dotted line correspond to any of their four legs, obtaining a factor 4^N. Then, we must evaluate all possible connections between the selected *dotted leg* in each internal vertex and the solid loose legs of the corresponding predecessor vertex (that can be an external vertex). One must be careful here, because if the mentioned predecessor vertex is attached to several lower vertices, an interchange of their legs could be equivalent to an interchange of internal vertices, and this have already taken into account. Notice that we cannot connect two dotted lines between themselves because we would not obtain a valid diagram (we would violate property 3).

Now, we do all possible connections between loose legs leading to diagram D, and again ruling out possible over-countings coming from the interchange of internal vertices. Now, as mentioned, we have to consider if a possible interchange of external vertices can generate equivalent diagrams, taking care not generate over-counting if some of these interchanges are already considered when we have connected the loose legs.

This method give us the total number of diagrams equivalent to D, and it is necessary to state it step by step:

Rules C1 for Minimal Diagrams:

- We split our diagram D in l branches involving all dotted lines, whose orientations are from out to in (all internal vertices are right vertices).

We consider all internal vertex permutations and choose one dotted line in each of them, obtaining a factor 8^N. Of course, in this case we have also the factor $\lambda^N/24^N$ from the interaction term, because we are not taking into account the leg permutations in each internal vertex.

- Now, we focus on the possible permutations between external vertices. It could seem that there are $l!$ possibilities but we can have over-counting. If there are m equal branches, to permute their external vertices is the same than to interchange collectively the internal vertices between the branches, which we have already considered. Therefore, it is necessary a factor $1/m!$ to avoid the over-counting. We show an example for $m = 2$

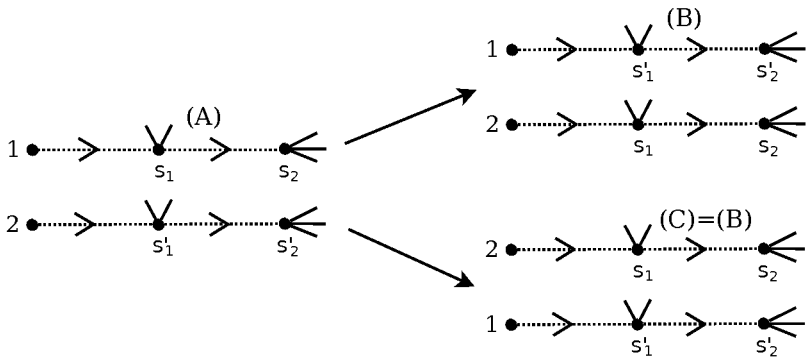

Thus, if we have k groups with l_i equal branches inside each one so that $l_1 + ... + l_k = l$, then the resulting factor is $l!/(l_1!l_2!...l_k!)$.

- Once the places of the vertices (internal and external) in a branch are chosen, we must connect their dotted lines in every possible way in order to construct the branch, ruling out the possible over-countings from internal vertices interchange. Let a *subbranch* be a part of a branch from an internal vertex to internal endpoints. To construct the branch, we can put $0, 1, 2$ or 3 subbranches in each internal vertex, because it contains 3 loose legs. The 0 value means that the internal vertex is an endpoint, and there is no extra factor. If we connect only one subbranch, we can choose any of three loose legs, and it appears a

factor 3. We can connect two subbranches in 6 different ways, but we can have over-counting if the subbranches are equal, because to transpose the subbranches is the same than to interchange collectively their vertices, and then we would have a factor 3. For the same reason, although we can connect three subbranches in 6 different ways it can have over-countings if there are two or three equal branches, obtaining a factor 3 or 1 respectively. We give an example with different branches

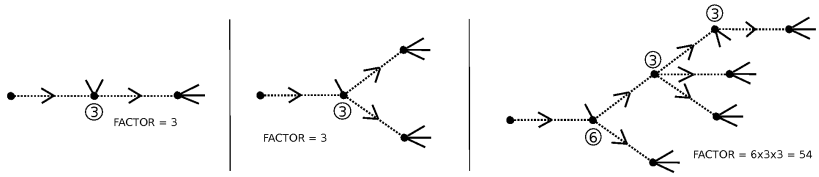

- We already have all branches, and we have to perform all possible connections between loose legs that lead to D, again leaving out possible over-countings from (internal or external) vertices interchange.

- We define *excluding-subbranches* as two subbranches that do not have any common vertex At the moment, the s_i variables that label the internal vertices do not have any ordering, but there is an implicit ordering according with the dotted lines orientations. In each branch, the orientations must point to lower vertices, otherwise one violates property 2 and the diagram give zero contribution. However, if s_a, s_b belong to different branches or excluding-subbranches, then can be $s_a \leqslant s_b$ or $s_b \leqslant s_a$. Thus, to integrate over the reduced volume we have to impose an ordering, but this ordering has to agree with the location of vertices in the branches. Therefore, we set a definite ordering $s_N \leqslant s_{N-1} \leqslant ... \leqslant s_1$ and perform all possible permutations between the variables s_i that are in agreement with the dotted lines orientations, i.e., we only can permute variables of different branches or excluding-subbranches. This lead to diagrams, in principle, with different contributions.

- Finally, we must integrate all variables $s_1, ..., s_N$ over the *reduced volume*.

These C1 Rules are equivalent to B Rules for minimal diagrams. The non-minimal diagrams have more dotted lines than N, but not any number. As we said above, we can obtain non-minimal diagrams from minimal ones converting solid lines pairs into dotted lines pairs. Each solid lines pair can come from different (external or internal) vertices or from the same internal vertex, but must finalize in the same lower internal vertex. This ensures that property 2 is not violated.
Clearly, in a minimal diagram each internal vertex is connected to one (and only one) greater vertex by a dotted line. This implies that a non-minimal diagram can only come from one minimal one. To see this, think that if two minimal diagrams D_1, D_2 lead to the same non-minimal diagram D', then both D_1 and D_2 must have some internal vertex connected to three greater vertices by dotted lines, and therefore they cannot be minimal diagrams.
With this, we can give new rules for non-minimal diagrams.

Rules C2 for non-minimal diagrams:

- We consider a not minimal diagram D'. This diagram arises from a minimal diagram D (only one). D' has the same factor as D ($\equiv minimal factor$), and additional factors. We can obtain D' from D if we convert solid lines pairs into dotted lines pairs. If D' is a valid diagram (satisfies properties 1,2,3), each solid lines pair to convert can come from different (external or internal) vertices or from the same internal vertex, but have to finalize in the same lower internal vertex. Each pair contributes a factor $i^2 = -1$. Moreover, one has to consider if several ways exist to select one pair, or otherwise, if the possible selections included in the minimal factor have to be reduced. This possible factors can be summarized in 6 cases, as we are going to show:

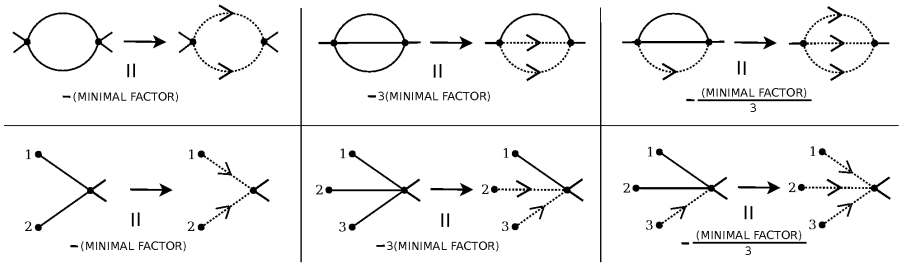

The vertices labeled with numbers can be internal or external ones.

The C1 and C2 Rules are equivalent to B Rules. And if one compare with the classical perturbation theory then one can state the following proposition: ***the rules to obtain the classical diagrams are indeed the Rules C1 for minimal diagrams.***
The classical diagrams are the quantum minimal diagrams with the same propagators and the same factors. This conclusion will allow us to compare the quantum and classical evolution for $\langle x^l(t)\rangle$.

4.3 Classical limit

The quantum diagrammatic formalism has to agree with the classical limit, i.e., if $\hbar \to 0$ then it has to be equivalent to classical diagrammatic formalism. To prove this we are going to recover the $\hbar$ factors involved in the perturbative expansion.
We have shown in (87) the expression for the evolution operator in the interaction picture $\Omega(t)$. This operator with $\hbar$ factors is

$$\mathbf{\Omega}(t) = \text{T-exp}\Big\{-\frac{i}{\hbar}\frac{\lambda}{24}\int_0^t ds\hat{x}_0^4(s)\Big\} \tag{167}$$

This means that each internal vertex have a new factor $1/\hbar$ in the perturbative diagrams. Thus, an order N diagram have a new $1/\hbar^N$ factor.
On the other hand, from (42) we can obtain the free two point function (163) with the corresponding $\hbar$ factors. We have to take into account that $[\hat{x}_0(0), \hat{p}_0(0)] = i\hbar$ and then we find

$$\langle \hat{x}_0(s)\hat{x}_0(s')\rangle = G_S(s,s') + i\hbar G_A(s,s') \tag{168}$$

and then we have an $\hbar$ factor in each G_A propagator (dotted line).

In the minimal diagrams the number of dotted lines is equal to the order of the diagram, and the $\hbar$ factors cancel each other. Thus, as expected, the minimal diagrams do not have any $\hbar$ factor.
The non-minimal diagrams have additional dotted lines that provide extra $\hbar$ factors. The number of additional dotted lines is always even so the not-minimal diagrams have $\hbar^n$ factors where n is even.

Therefore, if $\hbar \to 0$ all non-minimal diagrams vanish, leaving only the minimal (classical) ones.

4.4 Perturbative Classicality Condition

The perturbative expansion allow us to calculate the first orders and check when the evolution with the quadratic Hamiltonian fails. Also, we can use the shown diagrammatic expansion in order to calculate quantum corrections from classical evolution, taking into account non-minimal diagrams. Moreover, we are going to present a classicality condition based on our perturbative expansion, which we will note PCC.

We want to sum the infinite series S_{Cl} and S_Q that we can see in the following Figure

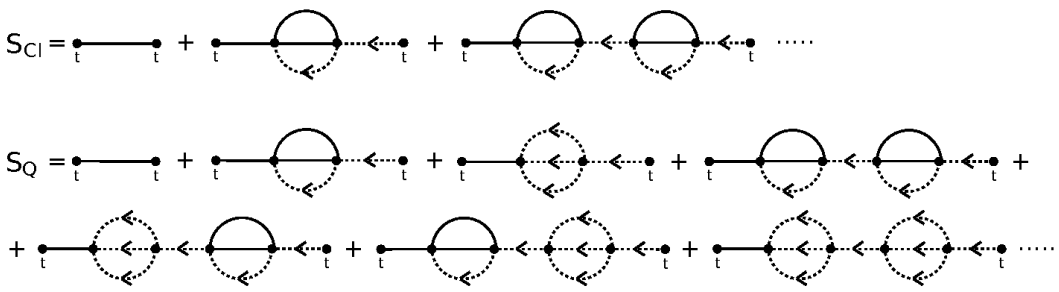

To achieve these sums of sunset diagrams we define

$$
\begin{aligned}
C(s,s') &\equiv \frac{2}{3}\lambda^2 G_S^2(s,s') G_A(s,s') = -C(s',s) \\
D(s,s') &\equiv -\frac{2}{9}\lambda^2 G_A^3(s,s') = -D(s',s) \\
A(s,s') &\equiv (CG_A)(s,s') = \int du C(s,u) G_A(u,s') \\
B(s,s') &\equiv (DG_A)(s,s') = \int du D(s,u) G_A(u,s')
\end{aligned}
\tag{169}
$$

and then we can write the series in a formal way, as we show in the following

expressions

$$S_1 \equiv G_S + G_S A + G_S A^2 + G_S A^3 + ... = \frac{G_S}{\mathbb{I} - A}$$
$$S_2 \equiv G_S + G_S(A-B) + G_S(A-B)^2 + G_S(A-B)^3 + ... = \frac{G_S}{\mathbb{I} - A + B}$$
$$S_{Cl}(t) = S_1(t,t) \quad ; \quad S_Q(t) = S_2(t,t) \tag{170}$$

We would like to draw attention to the extra factor $1/3$ that appears in the definition of $D(s,s')$. This is due to the fact that we have only one way to choose three internal dotted lines in each sunset, compared with the three ways to choose one internal dotted line. We choose these series because the total factor in a chain of n sunsets is the product of individual factors in each sunset.
Now, we can discretize the time with Δt, set a value of t and calculate the functions $f_1(t), f_2(t)$ for a concrete system. With this, we can compute the matrices $G_S, G_A, A, B, (\mathbb{I}-A)^{-1}, (\mathbb{I}-A+B)^{-1}$ and calculate $S_{Cl}(t)$ and $S_Q(t)$. If $S_Q(t) \approx S_{Cl}(t)$ then the classical approximation has to be valid. We will perform these calculations in the following chapter and we will see that indeed this condition works well.

5 Test of the Classical Approximation: 1 DoF

We will test the classical approximation performing the classical evolution of several quantum mechanical systems with one degree of freedom where the solution of the Schroedinger equation is available. In this chapter we focus upon systems with one degree of freedom. In a first stage we take time-dependent potentials motivated by the hybrid inflation model shown in chapter 1. After we take a time-independent single well and double well quartic potential and perform a systematic study for several values of the dimensionless control parameters r_1 and r_s presented in chapter 2.
Let us remember that the classical approximation corresponds to taking points in phase space that follow an initial distribution ρ and evolving them using the classical equations of motion. This is a deterministic evolution and the randomness is produced by the initial distribution. In our systems, this distribution is the Wigner function, and we always start from a gaussian state.

5.1 Stages of approximate evolution for time-dependent potentials

In order to mimick the behavior at the preheating epoch in the hybrid inflation model shown in chapter 1, we will take time-dependent quartic potentials where the coefficient of quadratic term changes from positive to negative, causing a symmetry breaking. After this, one expects that the system reaches a classical behavior and the classical approximation is a good approximation. However, in the case of QFT, one needs to calculate the quantum evolution in an initial stage up to the time in which the system acquires the classical behavior (squeezed state). This is done in Ref. [33] calculating the evolution with the quadratic Hamiltonian to a connection time t_{con}, and after connecting with the classical approximation. We note the evolution with the quadratic Hamiltonian as *gaussian approximation* (because it maintains the gaussianity of the Wigner function).
We plan to test how this approximate evolution, with the two mentioned stages, works in QM where the exact evolution is available.

Thus, we have two different evolution stages:

–In the first one we start taking a gaussian state (that can or cannot be the

ground state of the quadratic Hamiltonian) and perform the quantum evolution with the gaussian or perturbative approximation to a time at which the system is already classical (t_{con}). In the gaussian evolution the wave function of each degree of freedom maintains its gaussianity. In the perturbative evolution we also consider gaussian states at t_{con} but their widths are modified by the perturbative expectation values. Thus, from the two-point correlation functions at t_{con} we derive the Wigner function $W(x, p; t_{con})$, that serves as the initial state of the subsequent classical evolution. This stage corresponds with the quantum-classical transition of the system.

–In the second stage we consider the degrees of freedom in the phase space as random variables, whose distribution are the mentioned Wigner function, and perform the full classical evolution taking into account the complete Hamiltonian.

To test this method we focus on systems with few degrees of freedom and compare the classical with the exact quantum evolution. We can also check if at the connection time the Wigner function is a squeezed state.
We show the mentioned two stages of the evolution in Fig. 5.

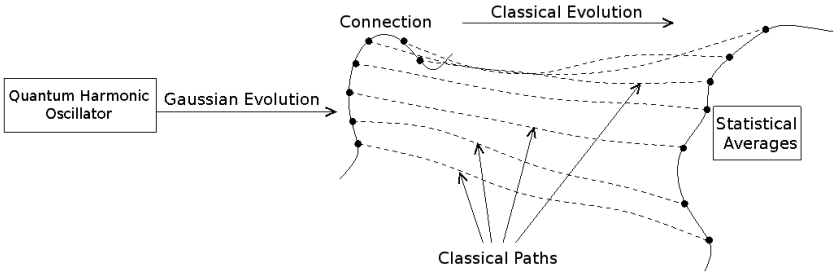

Figure 5: In this approach the initial conditions for the classical equations have a certain distribution function. Subsequently all these paths evolve classically and averages on those are calculated later.

To perform all this numerically, we need to generate a sample of the Wigner function in t_{con} and evolve each sample-point with the classical equations of motion. After, the expectation values are calculated as statistical averages over the sample at any time.

5.1.1 Classical evolution equation

We will consider systems with a Hamiltonian of the form

$$H(x,p,t) = \frac{1}{2m}p^2 + \frac{1}{2}mw^2(t)x^2 + \frac{\lambda}{24}x^4 \tag{171}$$

The corresponding classical evolution equation will be

$$m\ddot{x} + mw^2(t)x + \frac{\lambda}{6}x^3 = 0 \tag{172}$$

If we consider more degrees of freedom, then we will have an equation for each. We will study cases with 2 degrees of freedom in the following chapter.

5.1.2 Numerical quantum-classical connection

We are going to explain how to make the connection between the quantum and classical stages. In other words, how to use the data given by the quantum evolution to obtain the initial conditions needed for the later classical treatment.

When in the quantum evolution we arrive to the moment t_{con} in which the system reaches a classical behavior, we get the *probability distribution* $W(\mathbf{x},\mathbf{p},t_{con})$ (Wigner function). Then we can make a numerical program that generate a sample of W, and do the evolution with the classical equations for each of the sample-points up to the time at which we are interested. The expectation values in this second time will be the statistical average over the evolved sample.
Thus, we have two random variables x, p, with a distribution function $W(x,p;t_{con})$. To obtain this distribution we use the two-point functions coming from the initial quantum evolution under the gaussian or perturbative approximation

$$\langle\hat{x}^2(t_{con})\rangle \quad ; \quad \langle\hat{p}^2(t_{con})\rangle \quad ; \quad \frac{1}{2}\langle\{\hat{x},\hat{p}\}(t_{con})\rangle \tag{173}$$

where the operators are in the Heisenberg picture and the expectation values are calculated in the initial state of quantum evolution. So we have at t_{con} a gaussian distribution W and we can generate easily a sample using the known expression that from two uniform random variables θ, φ generates a normal distribution (of width unity):

$$\cos(\theta)\sqrt{-2\log(2\pi\varphi)} \tag{174}$$

Then we can multiply the generated values by the width we want.

From now on, x, p will be operators or functions depending on the context. This is convenient because we are going to treat the quantum and classic evolution together. Also, let us remember that we have natural units ($\hbar = c = 1$).

5.2 Case $w^2(t) = c_0 - u_0 t$

We consider a linear dependence for $w^2(t)$ that cause the above mentioned symmetry breaking. This illustrates the case of Hybrid Inflation, where the Inflaton is decaying so that the Higgs effective mass square turn from positive to negative. We can expand this dependence around the bifurcation point up the linear order, because close to this point the quantum-classical transition take place.

5.2.1 Description of the system

We have a linear $w^2(t)$ in the potential that is positive initially but turn to negative along time. Therefore we consider the next Hamiltonian

$$H(x,p,t) = \frac{1}{2m}p^2 + \frac{1}{2}(c_0 - u_0 t)x^2 + \frac{\lambda}{24}x^4 \tag{175}$$

As usual, it is convenient to redefine our quantities and parameters in order to make them dimensionless, using the mass m. Thus, from now on, all quantities and parameters will be dimensionless and we show their correspondence with those with dimensions next

$$\begin{gathered} x \to mx \quad ; \quad p \to \frac{p}{m} \quad ; \quad t \to mt \\ c_0 \to \frac{c_0}{m^3} \quad ; \quad u_0 \to \frac{u_0}{m^4} \quad ; \quad \lambda \to \frac{\lambda}{m^5} \end{gathered} \tag{176}$$

We have to choose an appropriate values for c_0 u_0 and λ. Firstly, we want that λ is small compared to coefficient of quadratic term (initially), because in the first stage we would like that the gaussian and the perturbative evolution are valid. Moreover, we want to see a time interval before the bifurcation point ($w^2(t_b) = 0$) and also after this point, showing the sufficient interval to appreciate the quantum-classical transition and the later behavior. So t_b does not

have to be very small, but if we choose t_b very large then computation time increases unnecessarily (especially for the case of more degrees of freedom, which we show later). With this, we have chosen a suitable prototype-model with the next parameters

$$c_0 = 8.0 \qquad u_0 = 2.0 \qquad \lambda = 0.12 \tag{177}$$

So initially $w(0) = \sqrt{8}$. The bifurcation point is $t_b = 4.0$.

Initial conditions

Initially, if we neglect λ (and use dimensionless quantities) then we have an harmonic oscillator potential with $w = \sqrt{2c_0}$. We choose the initial wave function $\Psi(x, t = 0)$ as the ground state of this harmonic oscillator

$$\Psi(x, 0) = \left(\frac{w}{\pi}\right)^{\frac{1}{4}} e^{-\frac{w}{2}x^2} \tag{178}$$

Numerical solution of Schroedinger equation

In order to calculate the exact quantum evolution we have to solve the time dependent Schroedinger equation. We can do this very accurately if we discretize the equation and use computational methods. We have implemented in FORTRAN a program that solves the equation by the finite difference method.

Numerical evolution of the wave function

When one performs the numerical evolution one can see that shortly after the bifurcation point ($t_b = 4.0$) the wave function (and then the Wigner function) is still about gaussian. This justifies the use of gaussian approximation that we will do later. We show in Fig. 6 the wave function for three different values of t.

Beyond these times the system becomes highly non-linear and the wave function moves away of the gaussian shape. We display an example of this in Fig. 7 for $t = 6.5$.

The numerical program also allow us to calculate expectation values. As an example we display $< x^2(t) >$ in Fig. 8. We see a fast growth after the bifurcation point. After this transition, the wave function is very squeezed and we hope a classical behavior. We will show this behavior later.

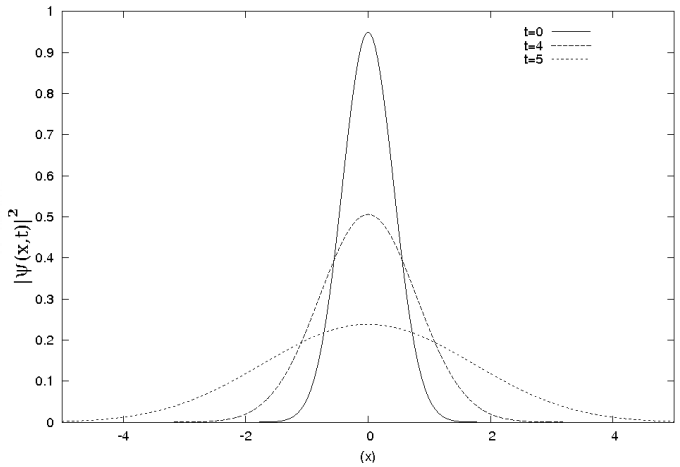

Figure 6: $|\Psi(x,t)|^2$ for $t = 0$, $t = t_b = 4$ (bifurcation point), $t = 5$ (one already hopes a classical behavior at this time).

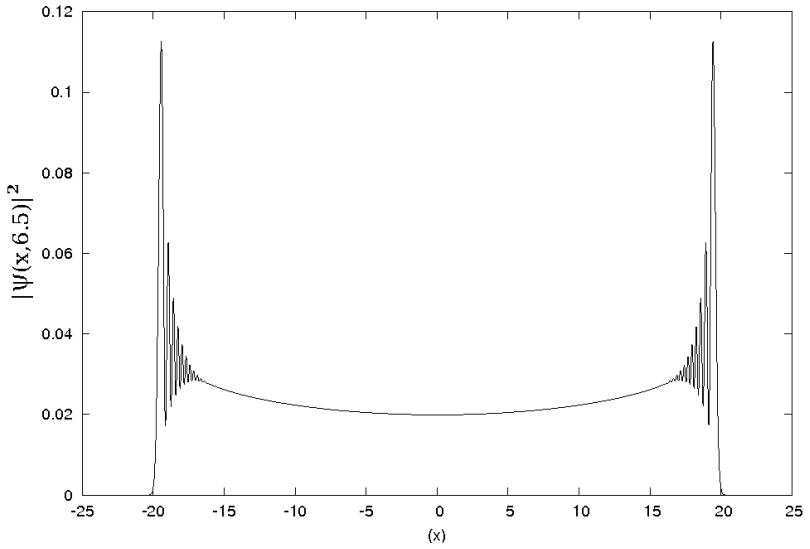

Figure 7: $|\Psi(x,t)|^2$ at $t = 6.5$. This function is not gaussian.

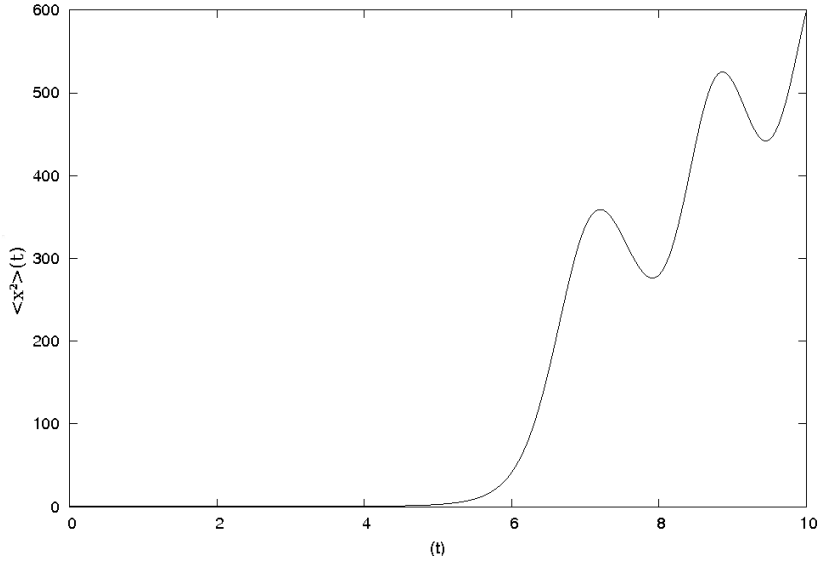

Figure 8: Numerical exact evolution of $< x^2(t) >$.

Here we have shown the results for exact numerical evolution. But in many interesting cases one have a lot of degrees of freedom and it is impossible to reach the exact solution. Therefore, it is necessary to consider some approximations.
We will perform the classical approximation in two different ways:
–Using the gaussian evolution in the first stage to connection time t_c (gaussian connection).
–Using the perturbative evolution to t_c (perturbative connection).

5.2.2 Gaussian evolution

We note the interval time from $t = 0$ to connection time t_c by *quantum zone*. We will show the evolution in this zone neglecting the value the quartic term of potential ($\lambda = 0$). This is justified because λ is small compared to c_0, and also because in this zone the width of $|\Psi(x,t)|^2$ is small and the values of x that contribute to the expectation values are $0 < x < 3$ approximately (see Fig. 6), so the quartic term of potential is small compared to quadratic term. Thus, with $\lambda = 0$ the evolution equation for the operators $x(t), p(t)$ in the Heisenberg picture is linear and can be solved analytically as explained in

chapter 2. Te solution depends on functions $f(t), g(t)$, which for linear $w^2(t)$ are Airy-like functions [33]. These functions can be obtained from software as *Mathematica* or *Maple*, although we have preferred to implement a FORTRAN program to solve numerically the differential evolution equation. This equation (37) for linear dependence is

$$\ddot{x} + (c_0 - u_0 t)\, x = 0 \tag{179}$$

With this one can calculates the evolution matrix (38) and the expectation values on which we are interested, using the functions $f_1(t)$, $f_2(t)$ and their derivatives (40) (41). In this case the evolution equations for $f_1(t)$ and $f_2(t)$ are

$$\ddot{f}_1 + \left(w^2 - 2t\right) f_1 = 0 \quad \ddot{f}_2 + \left(w^2 - 2t\right) f_2 = 0 \tag{180}$$

with $w^2 = \sqrt{c_0} = \sqrt{8}$. The initial conditions are

$$f_1(0) = \frac{1}{\sqrt{2w}} \quad \dot{f}_1(0) = 0 \quad f_2(0) = 0 \quad \dot{f}_2(0) = -\sqrt{\frac{w}{2}} \tag{181}$$

The expectation values take the form (see chapter 2)

$$|f|^2(t) \equiv f_1^2(t) + f_2^2(t) =< x^2(t) > \tag{182}$$

$$|g|^2(t) \equiv g_1^2(t) + g_2^2(t) =< p^2(t) > \tag{183}$$

$$F(t) \equiv f_1(t)g_2(t) - f_2(t)g_1(t) =< \frac{1}{2}(xp + px)(t) > \tag{184}$$

An example of gaussian evolution in this zone is shown in Fig. 9 for the $< x^2(t) >$.

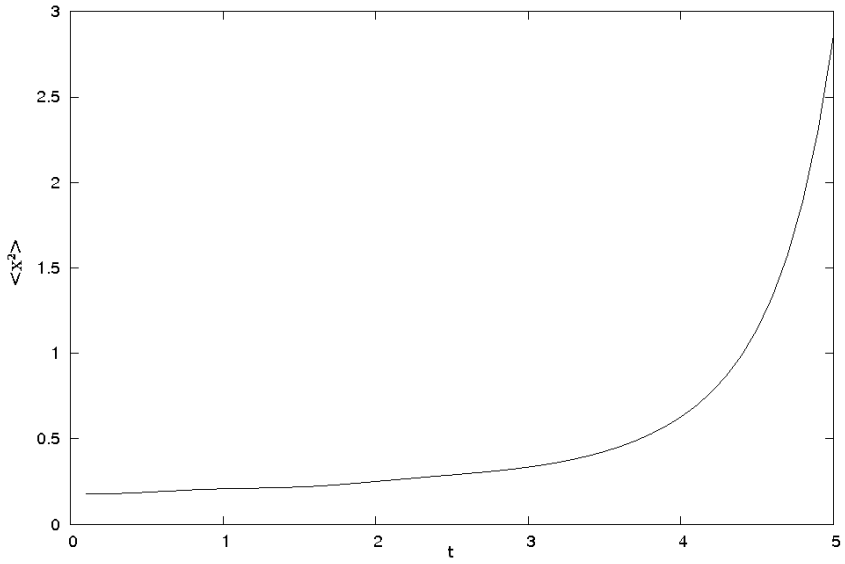

Figure 9: $< x^2(t) >$ for gaussian evolution.

As one hopes, after the bifurcation point the value grows indefinitely because if $\lambda = 0$ the potential is decreasing monotonously. Later the system will notice the influence of quartic term and we cannot neglect λ.
We can solve analytically the Schroedinger equation to obtain the wave function and it square modulus (probability distribution for x) at any time

$$|\Phi(x,t)|^2 = \frac{1}{\sqrt{\pi}|f|^2(t)} e^{-\frac{x^2}{|f|^2(t)}} \tag{185}$$

We will compare later this function to that obtained from numerical exact evolution.

5.2.3 Quantum perturbative evolution

We have seen in chapter 4 the perturbative expansion (to order λ^2) for potentials whose interaction term is the same as we are using here. Therefore we can apply all diagrams and expressions that are read from them.

With perturbation theory we obtain results closer to the true values than

in the case of gaussian evolution. This allow us to reach the connection time in a status nearer to the real one. With this we hope to improve the later classical evolution.
In addition, the perturbative expansion involve analytical expressions that we can implement and evaluate in a computer with a much lower computational cost than in the case of Schroedinger equation.

To see the improvement we show in the next table the value of $< x^2 >$, $< p^2 >$ and $\frac{1}{2} < xp+px >$ at $t_c = 5.0$ for the considered value of $\lambda = 0.12$. In the table we include the results for gaussian evolution, perturbative evolution and numerical exact evolution.

$\lambda = 0.12$ / $t = 5.0$	Gaussian	Perturbative	Exact
$< x^2 >$	2.90	2.74	2.71
$< p^2 >$	3.65	3.10	3.19
$1/2 < xp + px >$	3.21	2.92	2.89

With these expectation values we can calculate the Wigner function assuming that it is gaussian.

5.2.4 Classical evolution. Transition zone

Transition zone

With the gaussian and perturbative evolution we obtain the wave function and the expectation values to connection point. Now we want to detect if there is a *transition zone* in which the system already has a classical behavior but the influence of quartic term is still small. This zone can exists or not depending on the chosen parameters. If the zone exists then within it the gaussian or at least the perturbative evolution is still valid and we can reach a suitable connection time. In our case the zone exists and we can do the gaussian or perturbative connection.

Now we consider how to detect the transition zone. We cannot do different connections and take those closest to the numerical exact value, because as mentioned when we need to work with some approximation then we do not have the exact solution. The right way is to consider a range of connection times after the bifurcation point and perform the classical approximation for each one. If exists an interval time in which the evolution is similar and outside it one obtain remarkable differences then this interval is our transition

zone. We can see this in Fig. 10, where we employed gaussian connections. Let us remember that the Wigner function at each connection time is extracted from the two-point correlation functions (coming for the gaussian or perturbative evolution) at this time. If one recall our hybrid inflation model, we would be applying the gaussian or perturbative evolution for each mode separately.

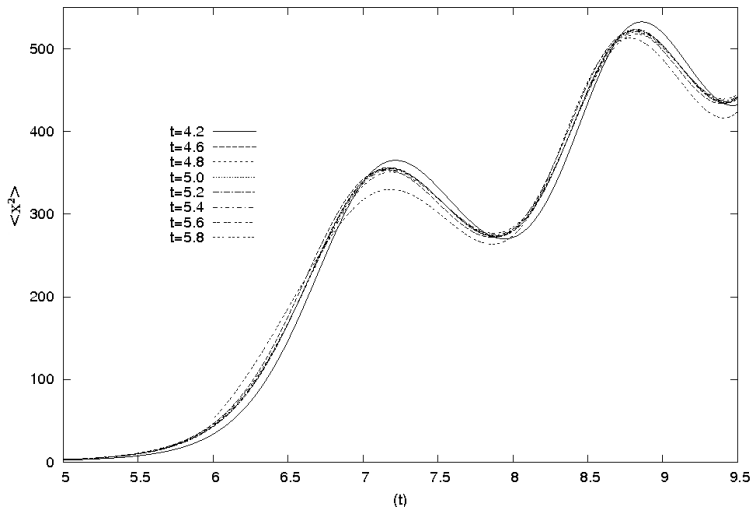

Figure 10: Classical evolution of $< x^2 >$ for several connection times. We can see a zone where the result is similar.

Thus we found our transition zone for $4.6 \leqslant t \leqslant 5.4$. We can take the connection time inside this zone.

Parameters

As mentioned before, at the connection time we assume a gaussian wave function and we can calculate it from expectation values. Also we can calculate the Wigner function (gaussian) in the same way. This Wigner function will be our probability distribution at the connection time.

So we generate at t_c a sample according to our gaussian distribution. Then

we take each point inside the sample x_i, p_i and perform the classical evolution with the equation of motion (172). Once this is done we have a set of trajectories that allow us to calculate any expectation value (at any time) as statistical averages.

In this case it is not necessary that the time step is very small because only appears derivatives respect to the t (and not respect to the x as in Schroedinger equation).
About the number of sample points N, has to be enough so that the result changes little if N increases.
The connection time t_c has been chosen approximately at the midpoint of transition zone.
Thus, we have chosen

- Time step: $\Delta t = 0.0005$
- Number of sample points: $N = 200000$
- Connection time: $t_c = 5.0$

5.2.5 Comparison: quantum zone

In this section our goal is to verify the validity of classical approximation in time-dependent quantum mechanical systems where we can solve numerically the Schroedinger equation, to compare both evolutions.
Now we want to show the results, on the quantum zone, for the gaussian and perturbative evolution compared with the numerical exact evolution.

Gaussian vs numerical exact evolution

We compare here the gaussian evolution with the full evolution (numerical exact evolution). We display in Fig. 11 the wave function in two different times. At the bifurcation point the wave functions are very similar, and at the connection time $t_b = 5.0$ one can see more difference. In Figs. 12-14 we compare the expectation values. We see that the relative differences up $t = 5.0$ are small (although we will show that the perturbative evolution work better).

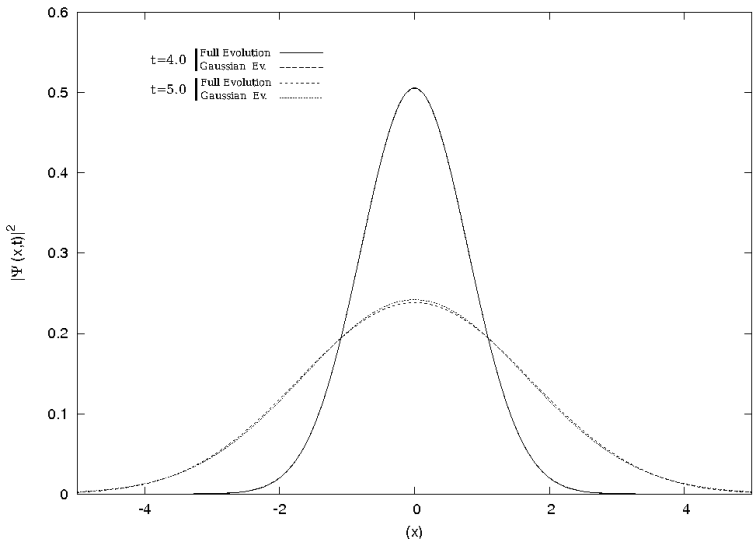

Figure 11: Comparison of $|\Psi(x,t)|^2$ for two different times. One can see that at $t = 4.0$ (bifurcation point) they are practically the same. At $t = 5.0$ the difference is slightly higher.

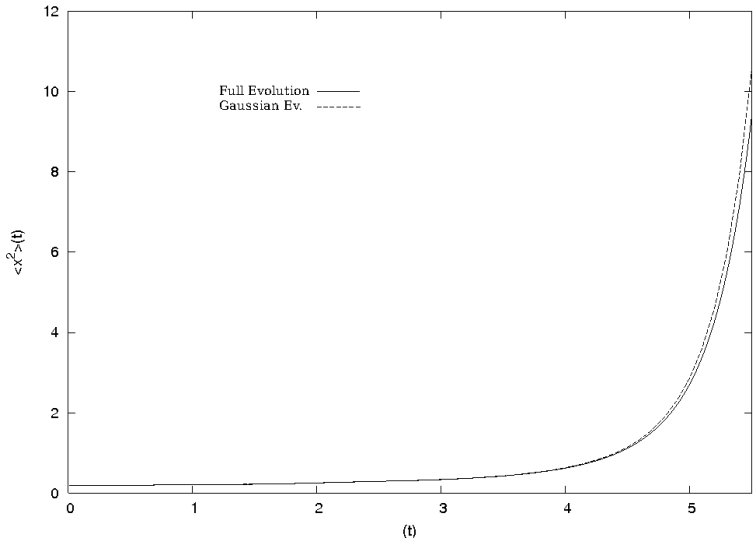

Figure 12: Comparison of $< x^2(t) >$

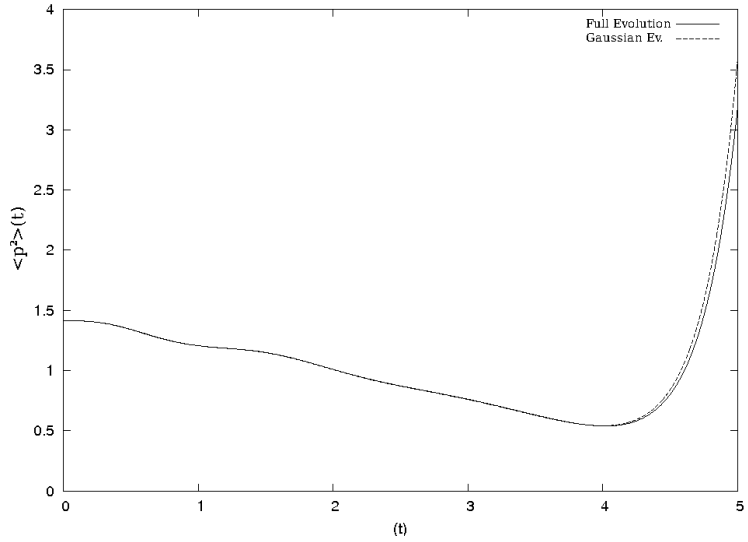

Figure 13: Comparison of $< p^2(t) >$

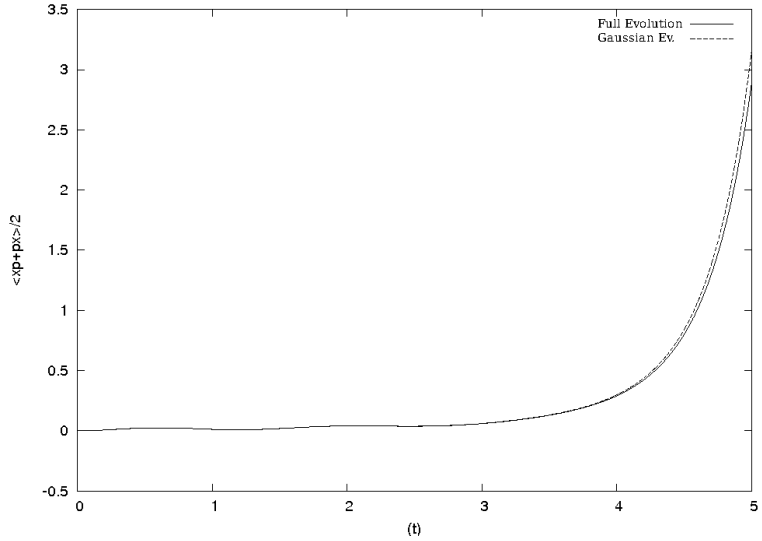

Figure 14: Comparison of $\frac{1}{2} < (xp + px)(t) >$

5.2.6 Classical zone

In all quantities drawn, the relative errors do not exceed 0.1 %. Otherwise we will mention it.

Gaussian connection

We will compare the numerical exact evolution with classical evolution taking initial conditions at t_c coming from gaussian evolution in the previous zone (quantum zone). We want see how the classical approximation work and display in Figs. 15-17 the same expectation values that for the quantum zone. Again we have $t_c = 5.0$. We can see that the classical evolution work well.

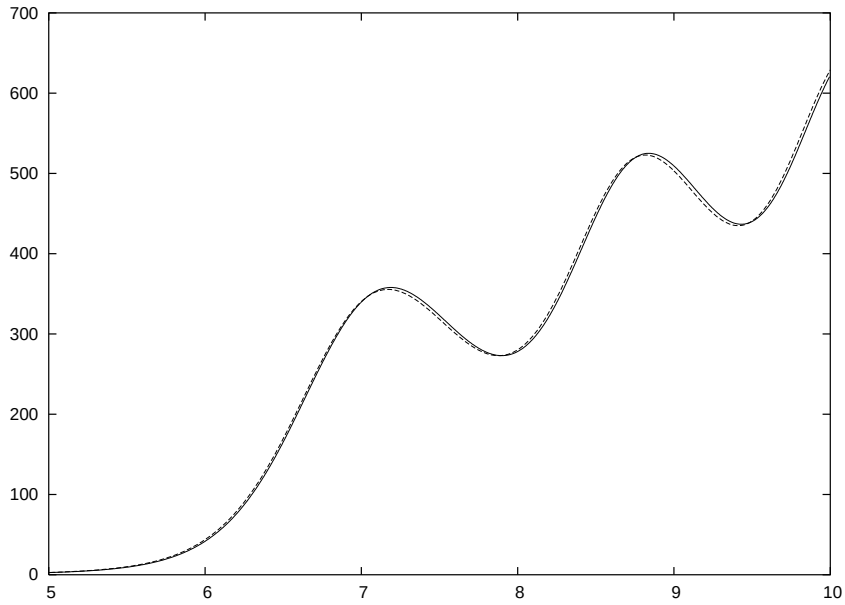

Figure 15: Quantum and classical evolution for $< x^2(t) >$ with gaussian connection.

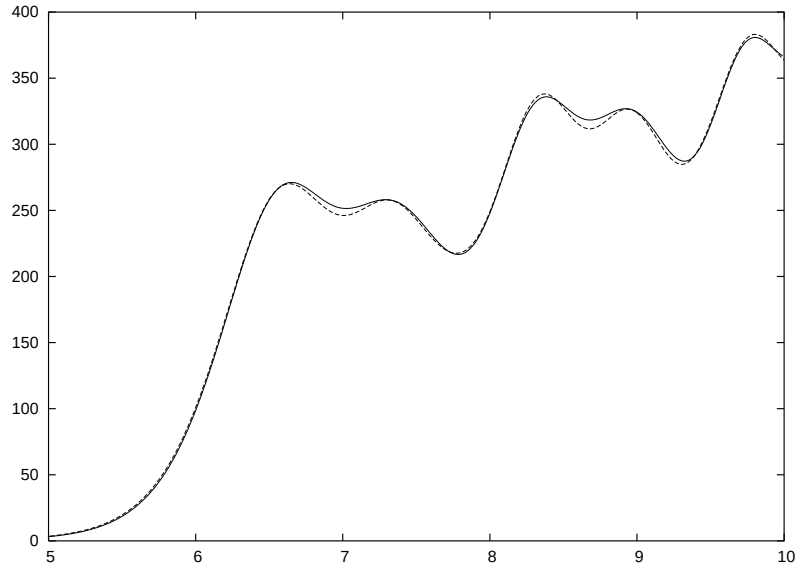

Figure 16: The same as in Fig. 15 for $< p^2 > (t)$

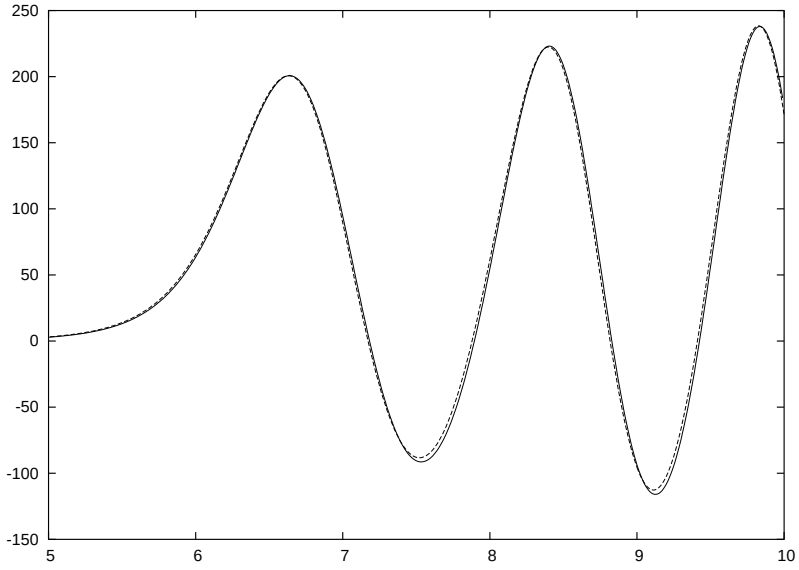

Figure 17: The same as in Fig. 15 for $\frac{1}{2} < xp + px >$

Perturbative connection

Here the initial condition at t_c for classical approximation comes from a previous perturbative evolution to order two. We compare this evolution with quantum and gaussian evolution and display it for $< x^2(t) >$.

In Fig. 18 we show the comparison among the three cases. We see that the main differences correspond to time shifts with respect to the quantum curve, which is not important to extracting average properties over time. Thus, we shifted the curves to match the value at maxima and display the absolute differences in Fig. 19. We observe an improvement in the case of perturbative connection.

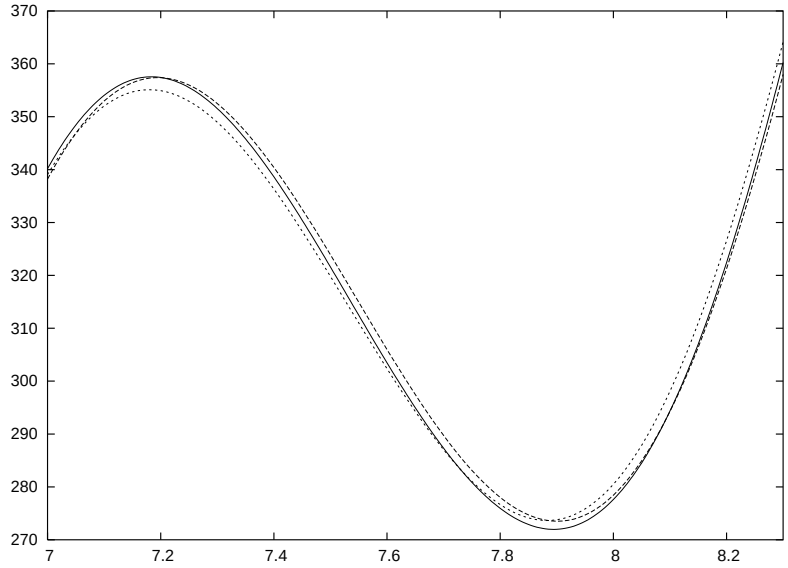

Figure 18: Quantum evolution (solid line) vs perturbative (dashed line) and gaussian (dotted line) evolution, for $< x^2(t) >$.

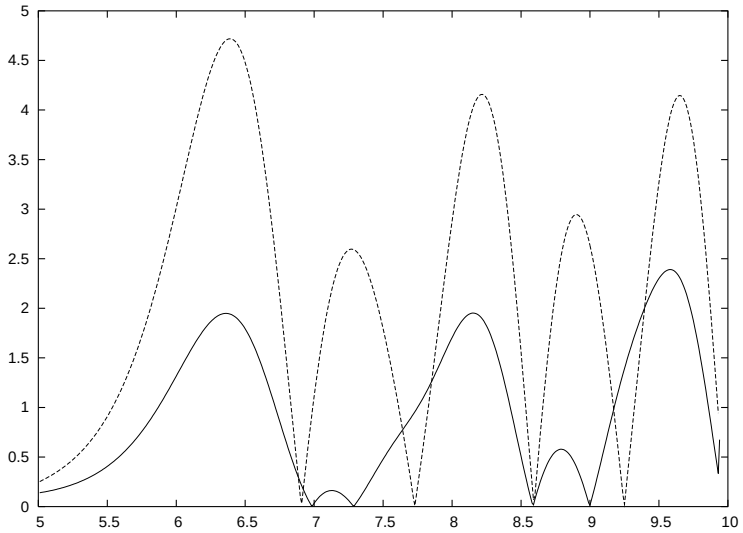

Figure 19: Absolute differences with respect to the quantum curve for perturbative (solid line) and gaussian (dashed line) connection.

5.2.7 Quantum zone for $< x^4(t) >$

With the same parameters we have calculated the numerical exact evolution of $< x^4(t) >$. Also we performed the perturbative and gaussian evolution and the subsequent classical evolution. We are going to compare these results.

Gaussian evolution

We show in Fig. 20 the numerical exact evolution vs gaussian evolution (115). Here the difference is greater than in the case of $< x^2(t) >$, which is logical because this value is larger (is approximately the square of the other). However, we have verified that the relative difference is twice that in the other case, so we can say that in this case the gaussian approximation works worse.

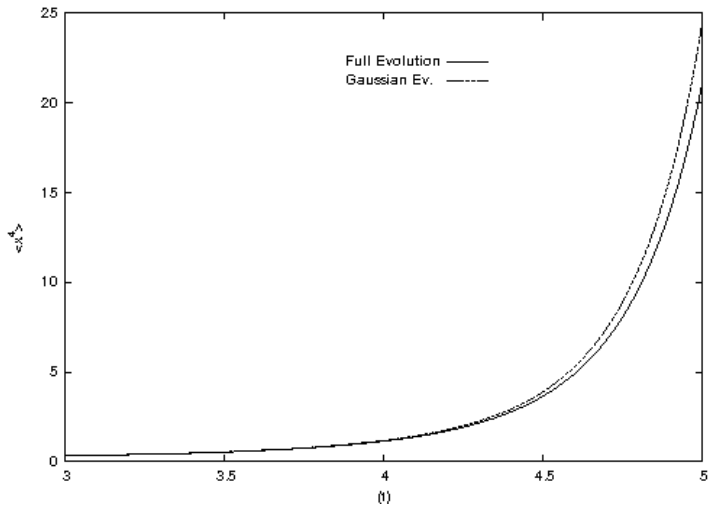

Figure 20: Numerical exact and gaussian evolution for $< x^4(t) >$ (errors $\leq 0.3\,\%$).

Perturbative evolution

In Fig. 21 we compare the quantum evolution with the gaussian and perturbative evolution for $< x^4(t) >$. The perturbative calculation is a significant improvement. Also we have calculated the *cumulant* to order 2, ie, the contribution of connected diagrams to order two. This measures the deviation from gaussian behavior, since for a gaussian distribution all cumulants are zero. We note this cumulant as C_4 and it has the following expression

$$C_4(t) =< x^4(t) > -3 < x^2(t) >^2 \tag{186}$$

We display in Fig. 22 the value of C_4 from numerical exact evolution (Schroedinger equation) vs the connected diagrams sum to order two. The curves are very similar, and is logical that there is little difference between them because the perturbative calculation is truncated to order 2. For the same reason is natural that the difference is increasing along the time, because the contribution of higher orders (non considered in the perturbative evolution) becomes more and more relevant.

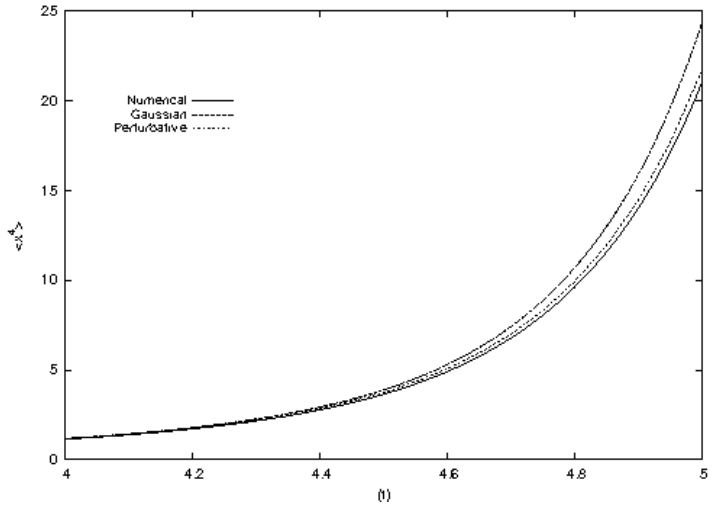

Figure 21: Numerical exact value vs gaussian and perturbative for $< x^4(t) >$ (errors $\leq 0.3\,\%$).

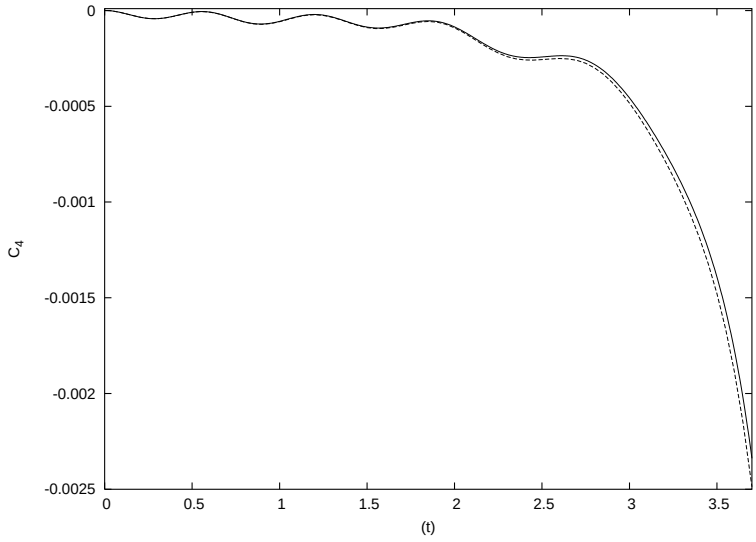

Figure 22: Numerical exact evolution for C_4 vs sum of connected diagrams to order two (errors $\leq 0.3\,\%$).

As in the case of $< x^2(t) >$, we want to test here the validity of perturbative diagrams obtained for $< x^4(t) >$. We do this for the connected diagrams. So we perform a least squares fit from the numerical exact calculation of C_4 in order to obtain the contribution of each order to cumulant. Once this done, we compare the results with the sum of perturbative diagrams for each order.

- *Comparison to order 0*:

The zero order diagram is disconnected and therefore the contribution of this order to C_4 is null. Indeed we can see in Fig. 23 that the contribution of zero order is compatible with zero.

- *Order 1*:

We show the result in Fig. 24. Both curves are compatible.

- *Order 2*:

The result is displayed in Fig. 25. Also we obtain compatible curves.

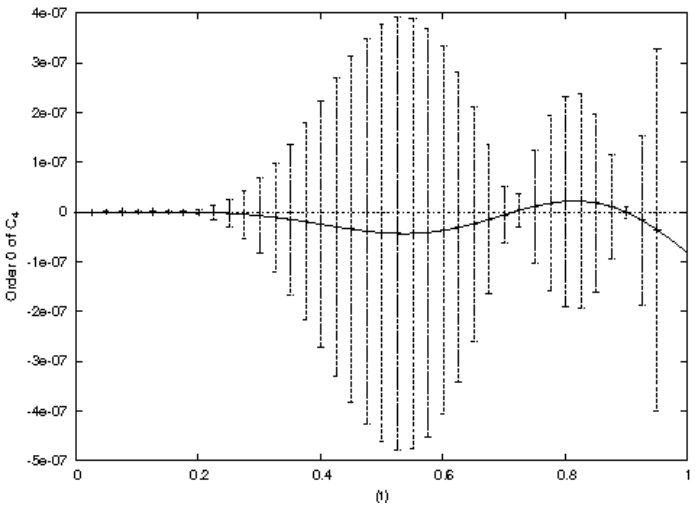

Figure 23: The zero order contribution to C_4 is compatible with zero.

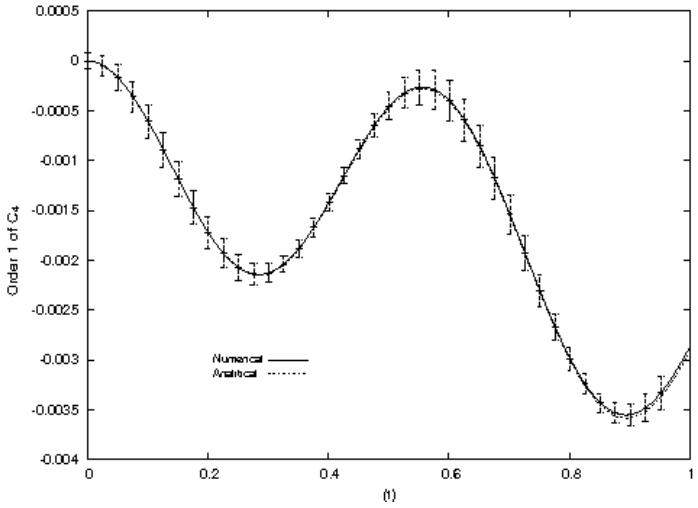

Figure 24: Contribution of one order to C_4. The curves are compatible.

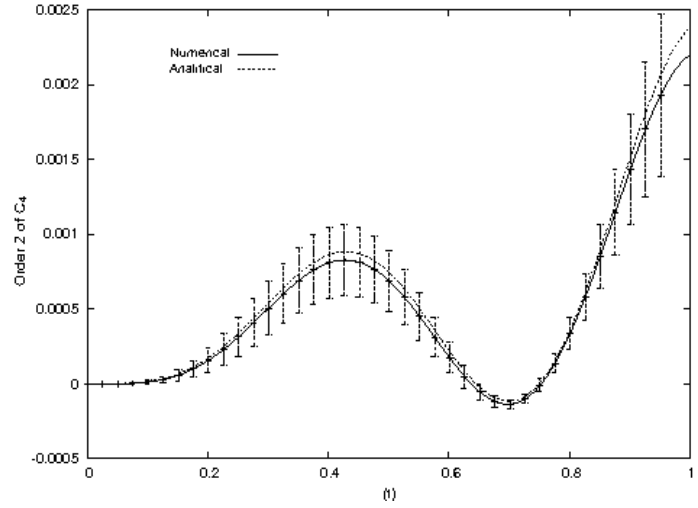

Figure 25: Contribution of two order to C_4. The curves also are compatible.

5.2.8 Classical zone for $< x^4(t) >$

Now we have to do the connection at $t_c = 5.0$ and perform the later classical evolution. We found the values of $< x^4 >$ at the connection time and display the result in the next Table. The perturbative calculation is a remarkable improvement.

$\lambda = 0.12$ / $t = 5.0$	Gaussian	Perturbative	Exact
$< x^4 >$	24.42	21.71	21.02

We use this data to obtain a better distribution at the connection time. We take the gaussian width that correspond to $< x^4(t_c) >$ and the value obtained from $< x^2(t_c) >$ and calculate the mean value between them. This is done for gaussian and perturbative connection. We display in Fig. 26 the relative differences (%) between the numerical exact evolution and the classical evolution with gaussian and perturbative connection.

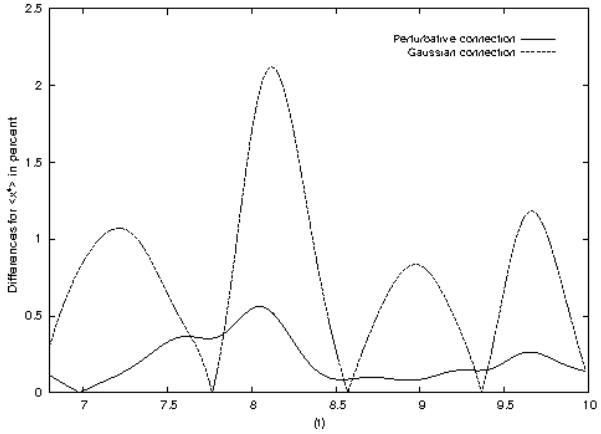

Figure 26: Relative differences (%) between the numerical exact evolution of $< x^4(t) >$ and the classical evolution with gaussian and perturbative connection.

Initially (connection time $t = 5$) the differences are about 2.8% (perturbative) and 14.2% (gaussian) and are not included. After decrease, as can be seen in the figure. Clearly the perturbative connection work better. However, the effect of the perturbative diagrams is only a shift in the evolution.

5.2.9 Squeezing condition

Squeezing of initial state is one of the conditions that are taken to justify (at least for a time) the use of the classical approximation. This approximation works well in our system and we want to check if the initial state is squeezed, and if remains so on the subsequent evolution. So we have calculated the Wigner function W at the connection time $t_c = 5.0$ and also in later times. We define the Squeezing Ratio as

$$r_s \equiv \frac{major\ axis}{minor\ axis} \tag{187}$$

where the axes correspond to elliptical $2\sigma - contour$ assuming that W is gaussian. We display in Fig. 27 the Wigner function at the connection time. It is practically a Gaussian and is very squeezed. In this case $r_s = 11.4$ and the integral of the negative part W_- is close to zero.
We show in Fig. 28 the Wigner function at $t = 6.0$ and it is not more a gaussian. This function has a very squeezed central zone and we can extract from here a value $r_s = 92.0$. However it has non-negligible negative values at other zones, and now the integral of positive part is $W_+ = 2.08$ and the integral of negative part is $W_- = 1.08$. So the negative part has a significant value.

In the later evolution we have verified that the central zone is more and more squeezed (and less gaussian). Also that the negative part is increasing, although grow more slowly from $t \approx 8.0$. The waving fan that one can see in Fig. 28 are spreading more and more.

Thus the squeezing condition is not maintained in the evolution, only in the central zone that is becoming less gaussian. It seems that the waving fan arising out of the central zone are such that they do not contribute to expectation values with low exponents. This explains why the classical approximation work better for $\langle x^2 \rangle$ than for $\langle x^4 \rangle$. We also have verified that for larger exponents (as $\langle x^6 \rangle$) the approximation works worse.

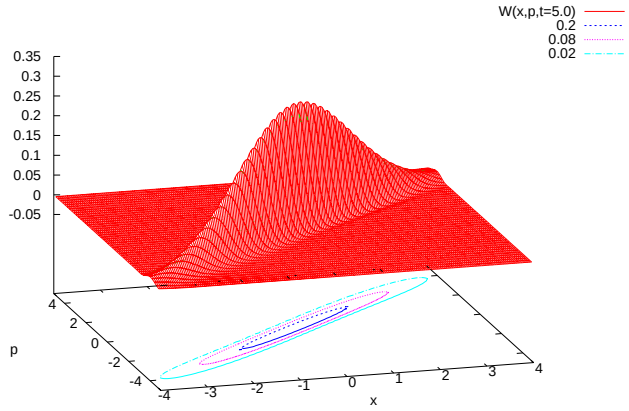

Figure 27: Wigner function at $t = 5.0$.

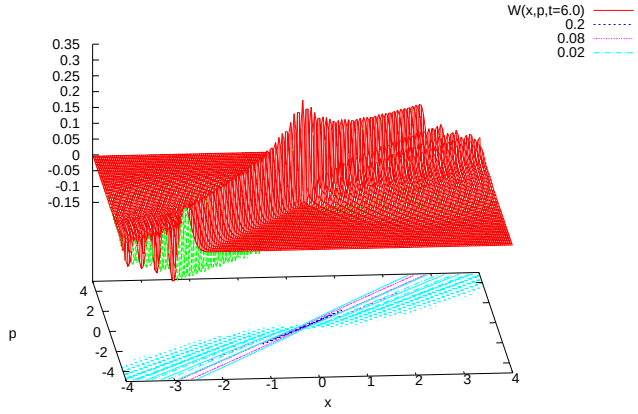

Figure 28: Wigner function at $t = 6.0$.

5.3 Case $w^2(t) = 4\tanh(c_0 - u_0 t)$

5.3.1 Description of the system

We will calculate the same quantities as in previous section, but now $w^2(t)$ is

$$w^2(t) = 4\tanh(c_0 - u_0 t) \tag{188}$$

and therefore we have the next potential

$$V(x,t) = \frac{1}{2}4\tanh(c_0 - u_0 t)x^2 + \frac{\lambda}{24}x^4 \tag{189}$$

For the same reasons that in the case of linear dependence we have chosen the following parameters

$$c_0 = 2.0 \quad u_0 = 0.5 \quad \lambda = 0.02 \tag{190}$$

Therefore $w = w(t=0) = \sqrt{8\tanh(4.0)}$ and the bifurcation point is $t_b = 4.0$.

The initial state will be as in (178) but with the w just described.

5.3.2 Evolution equations

Numerical exact evolution

We perform the numerical exact evolution with the discretized Schroedinger equation, but with the new potential (189). In the case of linear dependence for $w^2(t)$ the value of potential minimum growing indefinitely. So $< x^2 > (t)$ also increasing indefinitely and oscillating around the x^2_{min} (being x_{min} the position of the minimum). Now the potential minimum is become stabilized and we expect the same behavior to $< x^2(t) >$. Indeed we can see in Fig. 29 that this expectation value reaches a maximum value and remains oscillating around x^2_{min}.

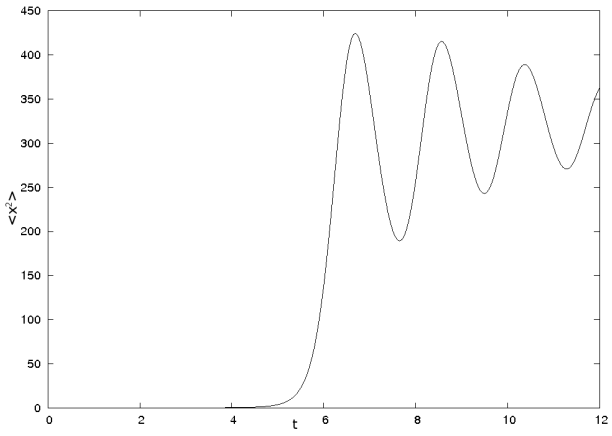

Figure 29: Numerical exact evolution for $< x^2 > (t)$. Do not grow indefinitely.

Gaussian evolution

The evolution equation for gaussian approximation ($\lambda = 0$) is now

$$\ddot{x} + 8\tanh(c_0 - u_0 t)x = 0 \tag{191}$$

With this equation one calculates the evolution matrix $M(t)$ (38) with the same initial conditions as in (41) but using the new $w = \sqrt{8\tanh(4.0)}$. So now we have new functions $f(t)$, $g(t)$, $F(t)$ obtained from equation (191). With this we can calculate the two point functions and then the matrix $\Sigma(t)$. In fact, still being valid the expressions (182), (183) (184) and (185) (with the new mentioned functions).

Perturbative evolution

In our system the quadratic Hamiltonian has been modified but the interaction Hamiltonian is the same as for the case of linear dependence. Therefore all expressions for the different perturbative orders are valid here, although now the propagators include new functions $f(t)$, $g(t)$.

5.3.3 Transition zone

We also will evolve the system with the classical approximation using different connection times. So one can test if there is a transition zone in which the

curves are compatible.
From (189), the classical evolution equation is

$$\ddot{x} + 8\tanh(c_0 - u_0 t)x + \lambda x^3 = 0 \tag{192}$$

The parameters for this discretized equation are

- Time step $\Delta t = 0.0005$
- Number of sample points $N = 200000$
- Connection time $t_c = 5.0$

We have verified that the transition zone is similar to that found in the case of linear dependence. So we have here a time interval $4.5 \leqslant t \leqslant 5.4$ where the curves are compatible. We display this in Fig. 30 (without errors) and Fig. 31 (with errors).

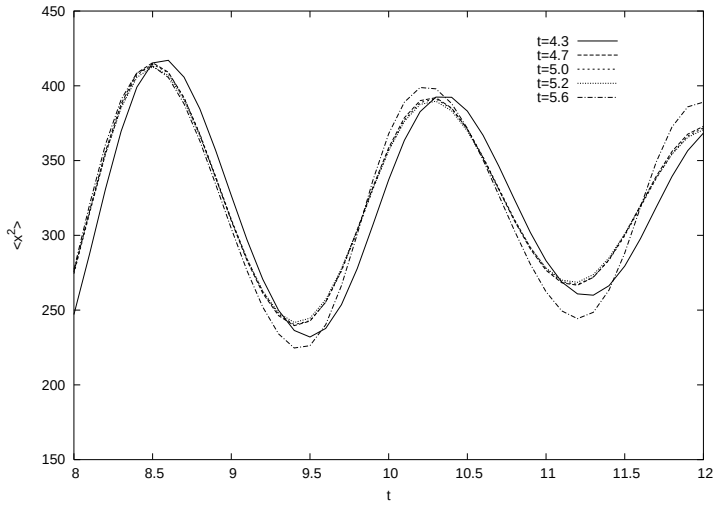

Figure 30: Classical evolution of $< x^2(t) >$ for several connection times. We have perturbative connections.

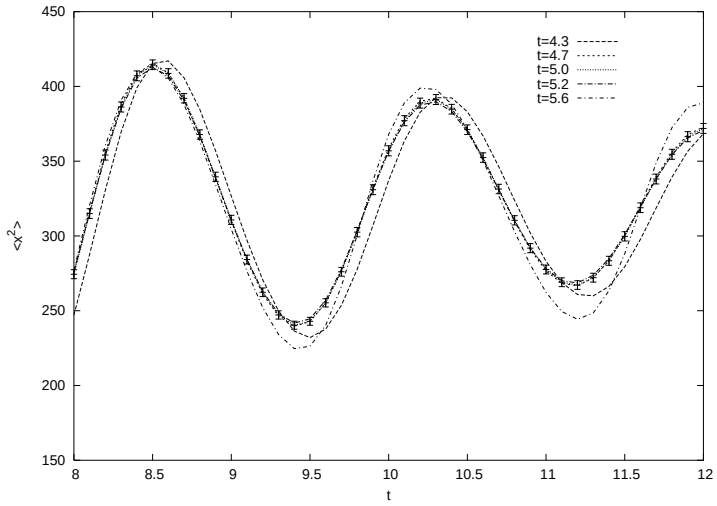

Figure 31: The same as in previous Figure with errors.

5.3.4 Quantum vs classical evolution

Quantum zone

We show in the next table the expectation values $< x^2 >$, $< p^2 >$ and $\frac{1}{2} < xp + px >$ at the connection time $t_c = 5.0$ calculated with the full quantum evolution, the gaussian evolution and the perturbative evolution. Clearly the perturbative approximation is an improvement over the gaussian approximation.

$\lambda = 0.02$ / $t = 5.0$	Gaussian	Perturbative	Exact
$< x^2 >$	4.049	3.897	3.863
$< p^2 >$	10.57	10.015	9.660
$< xp + px > /2$	6.51	6.215	6.098

Classical zone

We show the comparison between the numerical exact evolution and the classical evolution with perturbative connection for the two-point functions in Figs. 32, 33 and 34. The curves are compatible and then the classical approximation work well.

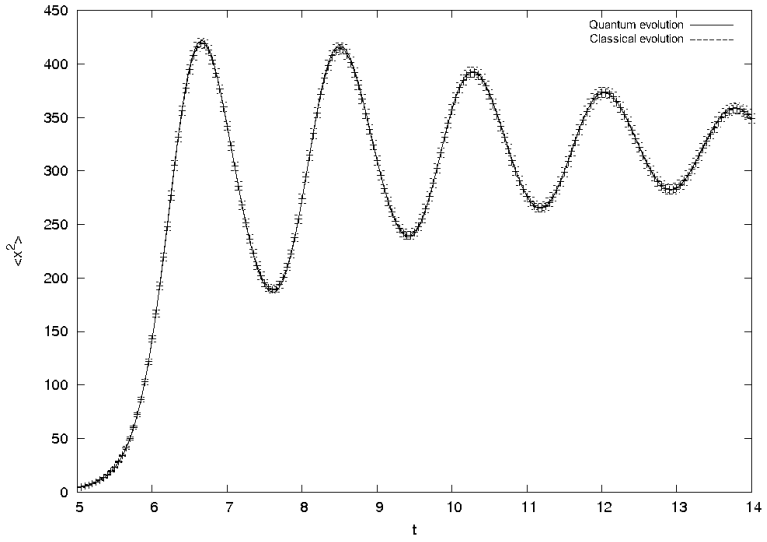

Figure 32: Numerical exact evolution vs classical evolution (with perturbative connection) for $< x^2(t) >$.

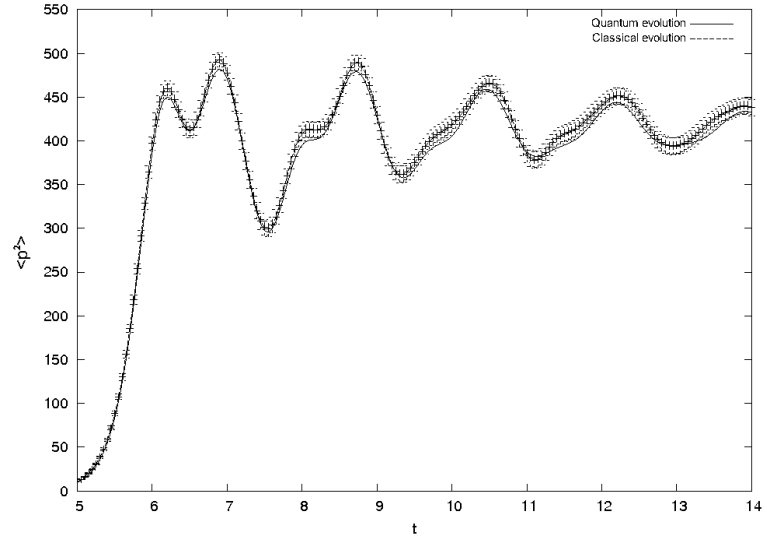

Figure 33: As in Fig. 32 for $< p^2(t) >$.

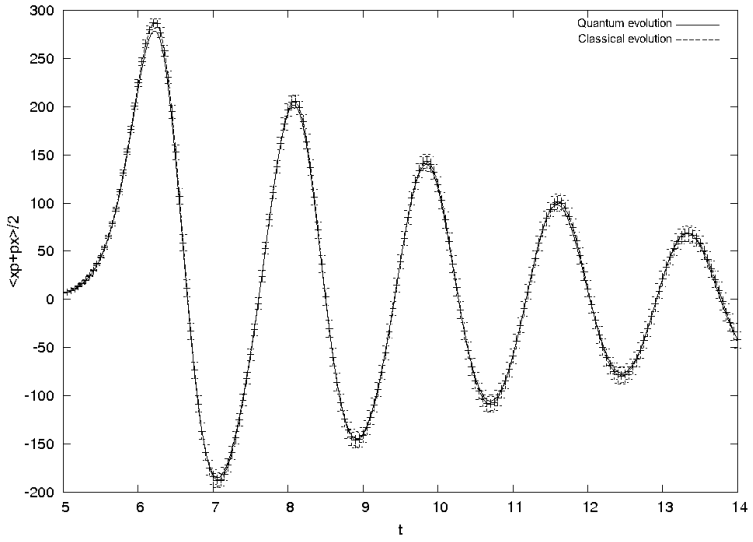

Figure 34: As in Fig. 32 for $\frac{1}{2} < (xp + px)(t) >$.

To see the differences between gaussian and perturbative connection we display in Fig. 35 the relative difference respect to the full evolution for $< x^2(t) >$ with both approximations. The perturbative connection is a remarkable improvement compared with the gaussian connection.

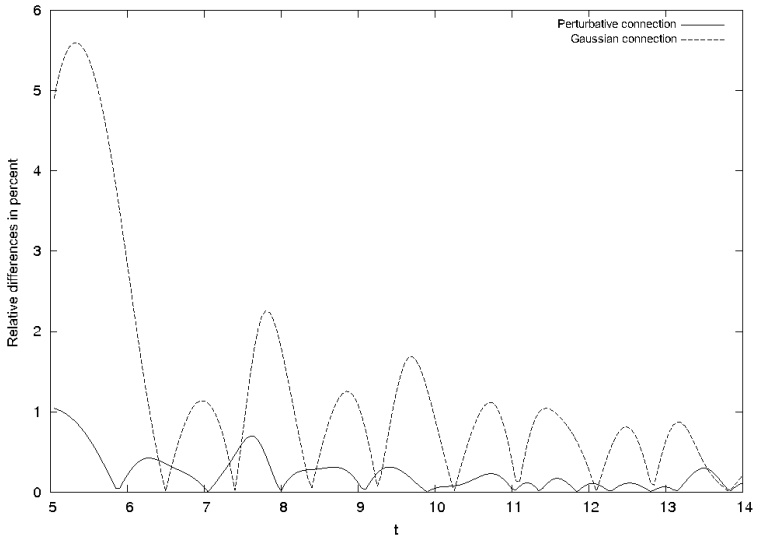

Figure 35: Relative differences (%) for $< x^2(t) >$ between the exact and the classical evolution with gaussian and perturbative connection.

5.3.5 Squeezing condition

The classical approximation works well here, and we will test if the state at the connection time is a squeezed state. Also if along time the state remains squeezed. With this purpose we display in Fig. 36 the Wigner function at $t = t_c = 5.0$, which is close to gaussian and very squeezed. In this case $r_s = 22.4$. The integral of positive part is almost zero.
In Fig. 37 we show the Wigner function at $t = 6.0$ and it is not gaussian. This function has a central zone very squeezed and we can extract from here a value $r_s = 201$. The integral of positive part is $W_+ = 4.43$ and of negative part is $W_- = 3.43$. So the contribution of negative part is important.
We have verified that the central zone is more and more squeezed. The negative part grows and later becomes stabilized. The waving fun seen in Fig. 37 spread more and more. So the behavior is similar as the previous case.
Thus the squeezing condition is not maintained along the evolution for the full Wigner function, but only for the central zone. The contribution to expectation values with low exponent of waving fun outside the central zone is almost null. We also have verified that for larger exponents the classical approximation work worse.

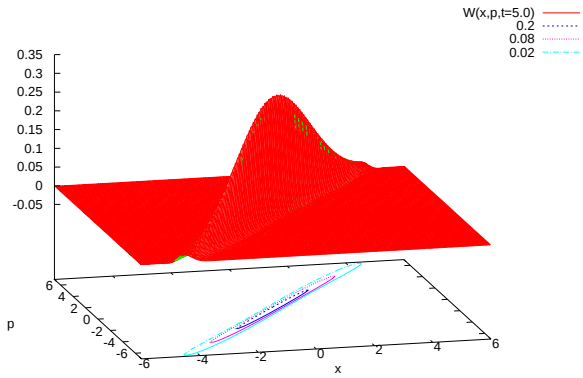

Figure 36: Wigner function at $t = 5.0$.

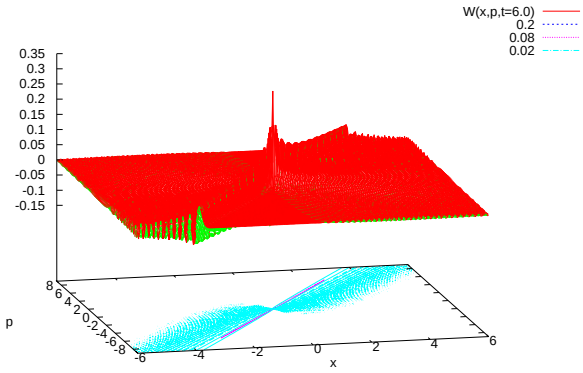

Figure 37: Wigner function at $t = 6.0$.

5.4 Systematic study of time-independent quartic quantum-mechanical systems

In the previous sections we had small values of λ and also a squeezed state in the connection time. Thus, the classical approximation works very well. Now we want to study several systems varying the parameters of the Hamiltonian and of the initial state, to see when it stops working the approximation. The time-independent Hamiltonian is

$$H = \frac{1}{2m}p^2 + \frac{1}{2}mw^2x^2 + \frac{\lambda}{24}x^4 \tag{193}$$

We take a gaussian initial state with a wave function

$$\psi(x, t = 0) = \frac{1}{\sqrt{2\pi\sigma_x^2}} e^{-\frac{1}{4\sigma_x^2}x^2} \tag{194}$$

that corresponds to the following Wigner function

$$W(x, p, t = 0) = \frac{1}{\pi} e^{-\frac{1}{2\sigma_x^2}x^2} e^{-2\sigma_x^2 p^2} \tag{195}$$

and clearly we have $\sigma_x\sigma_p = 1/2$.
We will use the dimensionless control parameters r_1, r_2 defined in chapter 2. Also we define a new parameter r_S that depends on the other two. These parameters are

$$r_1 \equiv \frac{m^2w^3}{\lambda\sigma_x\sigma_p} \quad ; \quad r_2 \equiv \frac{w\sigma_p}{\lambda\sigma_x^3} \quad ; \quad r_S \equiv \frac{m^2\sigma_x}{\sigma_p} \tag{196}$$

The r_1 parameter encoding the relative importance between the quadratic and quartic term in the potential. r_2 is more directly related to the size of quantum term in the evolution equation of the Wigner function (61). r_S gives us an idea of the squeezing in the initial state. As mentioned, the three parameters are not independent.
For simplicity, we will consider time-independent potentials ($w \neq w(t)$), because the conclusions can be extrapolated to the time-dependent case evaluating these parameters at any time.

5.4.1 Single well quartic potential

We assume that the coefficient of the quadratic term is greater than zero and then the potential has only one minimum. Thus, the expectation values

oscillate around a particular value. We have calculated the system evolution for a range of values of the r_1, r_2 parameters, and the corresponding r_S. The squeezed state condition is valid for $r_S \gg 1$ ($\sigma_x \gg \sigma_p$) and also for $r_S \ll 1$ ($\sigma_x \ll \sigma_p$). Therefore, inside our table, we will write the r_S value when $r_S > 1$ and the $(1/r_S)$ value (in brackets) when $r_S < 1$. After, we have extracted the expectation values in order to compare quantum and classical evolution.
The curves show an oscillatory pattern and one can identify the successive minima and maxima. We note each maximum as M_i (starting from $i = 1$ for the first maximum), and consider the first few maxima to test the differences with respect to the exact quantum evolution.
We focus on $\langle x^2 \rangle$ and define new useful quantities that we will use to compare the cumulative differences between quantum and classical evolution. We start with the following definition

$$I(t) \equiv 100 \frac{\int_0^t ds |\langle x^2(s) \rangle_Q - \langle x^2(s) \rangle_{Cl}|}{\int_0^t ds \langle x^2(s) \rangle_Q} (\%) \tag{197}$$

From this, we define $I_{tr} \equiv I(t_{tr})$ where t_{tr} is the time on first oscillation. Also we define t_1 as the time for which $I(t_1) = 0.5\%$, and t_2 satisfies that $I(t_2) = 1\%$. T is the period of quadratic Hamiltonian.
We show these quantities in Table 1, and also the relative difference (in %) between the quantum and classical evolution. These differences are measured at the maxima $M_1, M_2, ...$ ruling out the time shifts.
We have estimated the following errors:

$$\begin{aligned} &\nabla M_1 = \nabla M_2 = \nabla M_3 = \pm 0.05\% \quad ; \quad \nabla M_4 = \nabla M_5 = \pm 0.06\% \\ &\nabla(2t_1/T) = \pm 0.07 \quad ; \quad \nabla(2t_2/T) = \pm 0.1 \end{aligned} \tag{198}$$

From Table 1, we can see that the most important influence correspond to factor r_1. If r_1 is small then the classical approximation do not work well. To intermediate values ($r_1 \sim 10$) the classical approximation work well. And for large values ($r_1 > 20$) the classical approximation is very good.
Since r_1 is chosen, the r_S values establish the range of validity for classical approximation. The squeezing is very important and the classical approximation improves when r_S is growing. However, we see that this approximation also improves for $r_S \approx 1$, but this is so because if $r_S = 1$ then we are in the ground state of quadratic Hamiltonian. We show this in Fig. 38 for $(2t_1/T)$, with $r_1 = 10$ and different values of r_S.

To notice some influence in the evolution, the variation range of r_2 is too large with respect to the variation range of r_S.

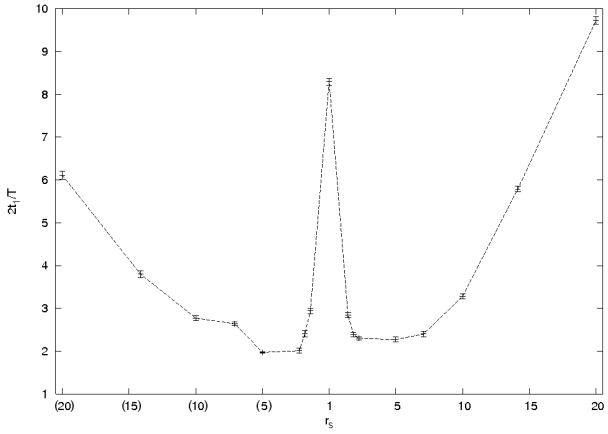

Figure 38: $2t_1/T$ vs r_s with $r_1 = 10$. The classical approximation improves when r_s is growing or $r_s \approx 1$.

For our systems, the quantum and classical curves are smooth. The main difference among them is a damping in classical curve. Also there is a temporal shift. We show an example in Fig. 39.

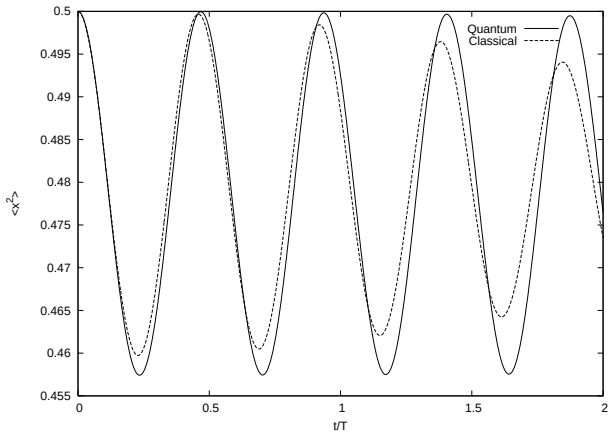

Figure 39: $< x^2 > (t)$ for quadratic term > 0, $r_1 = r_2 = 5.0$. The quantum and classical curve are smooth.

r_1	r_2	r_S	M_1	M_2	M_3	M_4	M_5	I_{tr}	$\frac{2t_1}{T}$	$\frac{2t_2}{T}$
0.4	0.4	1.00	4.14	11.9	18.3	21.1	20.3	2.65	0.30	0.3
0.4	2.0	(2.24)	2.25	10.3	22.8	28.1	28.7	4.83	0.30	0.4
0.4	5.0	(3.53)	1.29	13.4	29.9	37.9	39.7	4.28	0.32	0.4
0.4	10.0	(5.00)	0.88	11.6	29.7	39.5	42.7	3.24	0.33	0.4
0.4	20.0	(7.07)	0.64	7.35	27.3	37.6	43.0	2.15	0.34	0.5
0.4	50.0	(11.18)	0.45	0.25	22.8	31.6	39.3	1.22	0.37	0.5
2.0	0.4	2.24	2.48	8.17	14.2	19.6	26.1	0.87	0.69	0.9
2.0	2.0	1.00	0.51	1.91	3.65	5.23	6.44	0.73	0.55	1.4
2.0	5.0	(1.58)	0.80	2.14	6.89	12.0	16.4	1.27	0.55	0.7
2.0	10.0	(2.24)	0.62	3.46	9.99	16.9	23.1	1.42	0.56	0.7
2.0	20.0	(3.16)	0.51	3.62	10.1	16.9	23.9	1.34	0.57	0.8
2.0	50.0	(5.00)	0.41	2.90	7.79	13.48	20.6	1.06	0.59	0.8
5.0	0.4	3.53	0.76	2.67	4.93	7.37	9.66	0.28	1.28	1.8
5.0	2.0	1.58	0.64	2.42	4.96	7.82	10.6	0.27	1.39	2.2
5.0	5.0	1.00	0.06	0.28	0.64	1.09	1.56	0.32	2.42	6.0
5.0	10.0	(1.41)	0.44	0.38	1.90	3.90	6.16	0.49	1.63	2.6
5.0	20.0	(2.00)	0.39	0.87	3.15	6.11	9.38	0.60	0.82	1.9
5.0	50.0	(3.16)	0.35	0.98	3.30	6.18	9.19	0.62	0.81	1.8
10.0	0.4	5.00	0.26	0.94	1.79	2.64	3.60	0.10	2.27	3.4
10.0	2.0	2.24	0.26	1.00	2.15	3.56	5.11	0.12	2.30	3.3
10.0	5.0	1.41	0.17	0.68	1.50	2.56	3.80	0.15	2.84	4.3
10.0	10.0	1.00	0.00	0.03	0.09	0.173	0.285	0.21	8.30	>25.1
10.0	20.0	(1.41)	0.34	0.04	0.54	1.35	2.37	0.30	2.94	4.8
10.0	50.0	(2.24)	0.32	0.14	1.02	2.24	3.72	0.37	2.01	3.4
20.0	0.4	7.07	0.06	0.31	0.62	0.92	1.19	0.04	4.45	8.7
20.0	2.0	3.16	0.08	0.32	0.71	1.22	1.81	0.05	3.92	5.9
20.0	5.0	2.00	0.07	0.28	0.63	1.10	1.68	0.08	4.36	6.4
20.0	10.0	1.41	0.05	0.19	0.43	0.77	1.18	0.12	5.42	8.3
20.0	20.0	1.00	0.01	0.014	0.013	0.01	0.00	0.17	¿25.1	≫25.1
20.0	50.0	(1.58)	0.12	0.10	0.02	0.35	0.76	0.25	5.31	7.9
50.0	0.4	11.18	0.02	0.05	0.14	0.24	0.32	0.01	17.10	>25.1
50.0	2.0	5.00	0.02	0.06	0.14	0.24	0.38	0.02	9.42	15.7
50.0	5.0	3.16	0.01	0.06	0.13	0.23	0.36	0.04	9.39	14.2
50.0	10.0	2.24	0.01	0.05	0.12	0.21	0.33	0.06	9.96	14.8
50.0	20.0	1.58	0.01	0.04	0.09	0.16	0.25	0.10	11.93	17.9
50.0	50.0	1.00	0.01	0.02	0.02	0.03	0.03	0.16	>25.1	≫25.1

Table 1: Relative difference ratio (%) in maxima and $(2t_i/T)$ for $\langle x^2(t)\rangle$. Quadratic term > 0

5.4.2 Double-well quartic potential

Now the coefficient of the quadratic term (w^2) is less than zero and then the potential is a double-well with two minima. We hope that expectation values pass through a transition zone and after they oscillate around a value.
Like in the previous section, the differences between quantum and classical evolution for $\langle x^2 \rangle$ are showed in Table 3 for several values of r_1, r_2, r_s. From intermediate values of r_1 there exists a transition time where the expectation values are increasing, and after they oscillate around a certain value. Now, the period of quadratic Hamiltonian expanded around a minimum is twice as above.
The expectation values shape is smoother in classical case. We show the $\langle x^2 \rangle$ for $w^2 < 0$ in Fig. 41 and Fig. 42. We see that in the quantum curve appear secondary oscillations and there is no clear correspondence between the maxima of quantum and classical curves, except for the first maximum which appears in the transition zone. For this first maximum the differences are very small, with values of the order of the error, and it is not an useful quantity. Therefore we will not use here the difference at the maxima. We will focus to the other amounts considered in the previous section. We define $I(t)$ as in (197), but now the differences are larger and we have taken t_1 as the time for which $I(t_1) = 5\%$, and t_2 satisfies that $I(t_2) = 10\%$. In Table 3 appear $2t_i/T$, where T is the new period (double of the previous one).
We have estimated next errors:

$$\nabla 2t_1/T = \pm 0.04 \quad ; \quad \nabla 2t_2/T = \pm 0.06 \tag{199}$$

From Table 3, it is clear that again the most important influence corresponds to r_1. We can see that in this case it is necessary to take greater values of this parameter in order to obtain a good approximation. This can be due to two causes:
– If we expand the potential around the minimum ($x_{min} = \sqrt{6m^3w^2/\lambda}$ dimensionless) then the quadratic term is twice, but it appears a cubic term containing m, w^2, λ that also contributes. Therefore, after the transition, when compared to the previous case now we have an extra non lineal term.
– Moreover, after the transition, the tunneling influence will decrease with larger x_{min} (smaller λ).

We found that on transition zone the classical approximation work very well for intermediate values of r_1 ($r_1 \sim 10$), although after the differences are

significant. The result is better when r_1 is growing. This can be seen in Fig. 41 and Fig. 42. Hence r_1 is fixed the r_s parameter has a clear relevance for the validity of classical approximation. Great r_s or $(1/r_s)$ values lead to an improvement of the approximation. However, unlike what we found in the previous section, the $r_s \sim 1$ value is the worst of all, especially after the transition zone, because now this value do not represent initially the ground state of quadratic Hamiltonian. We show an example of this in Fig. 40 for $r_1 = 100$.

Like above, to see the influence of r_2 it is necessary a too large variation range.

We have also calculated another quantity to see the behavior in transition zone. We show in Table 2 $I(T)$ (T new period) for small values of r_1 (for greater values it is of order of the error). The estimated error is $\nabla I(T) = \pm 0.2\%$. When r_1 is growing then $I(T)$ decreases and the classical approximation work better. For a fixed r_1 value, the approximation work well for great values of r_s or $(1/r_s)$, and the worse behavior seems to be around $(1/r_s) = (2.24)$.

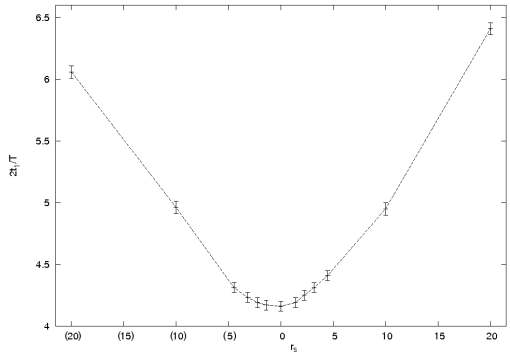

Figure 40: $2t_1/T$ vs r_s with $r_1 = 100$. The classical approximation improves when r_s is growing.

r_1	r_2	r_s	$I(T)$ (%)
0.4	0.4	1	28.0
0.4	2	(2.24)	29.4
0.4	5	(3.53)	26.7
0.4	10	(5)	23.3
0.4	20	(7.07)	19.9
0.4	50	(11.18)	15.3
2	0.4	2.24	5.6
2	2	1	5.9
2	5	(1.58)	7.4
2	10	(2.24)	7.9
2	20	(3.16)	7.6
2	50	(5)	6.7

Table 2: $I(t_r)$ for several values of r_1, r_2, r_s. Quadratic term < 0.

r_1	r_2	r_s	$\frac{2t_1}{T}$	$\frac{2t_2}{T}$
0.4	0.4	1	0.50	0.62
0.4	10	(5)	1.03	1.14
0.4	50	(11.18)	1.13	1.34
10.0	0.4	5	3.08	4.28
10.0	10	1	2.98	3.78
10.0	50	(2.24)	2.96	3.77
50	0.5	11.18	4.87	8.61
50	10	2.24	3.91	5.16
50	50	1	3.79	4.17
50	100	(1.41)	3.81	4.69
50	5000	(10)	4.77	7.92
100	1	10	4.95	8.73
100	5	4.47	4.41	6.58
100	20	2.24	4.25	5.48
100	100	1	4.16	5.03
100	500	(2.24)	4.19	5.25
100	2000	(4.47)	4.31	7.26
100	10000	(10)	4.96	8.57
200	50	2	4.52	5.55
200	100	1.41	4.50	5.44
200	200	1	4.49	5.39
300	100	1.73	4.70	5.69
300	200	1.22	4.68	5.57
300	300	1	4.67	5.55
500	1.25	20	6.16	13.96
500	5	10	5.66	9.73
500	25	4.47	5.08	8.29
500	500	1	4.93	5.81
500	10000	(4.47)	5.06	8.33
500	50000	(10)	5.64	9.74
500	200000	(20)	6.10	14.38

Table 3: Relative difference ratio (%) for $\langle x^2 \rangle$. Quadratic term < 0.

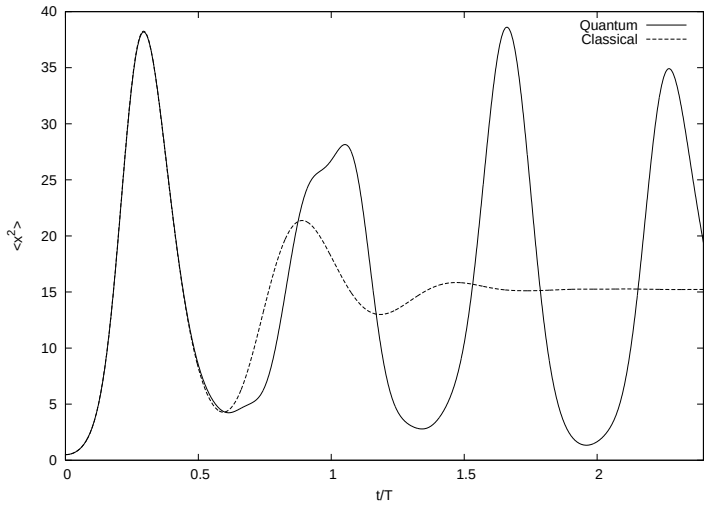

Figure 41: $< x^2 > (t)$ for quadratic term < 0, $r_1 = r_2 = 10.0$. The curves are very different.

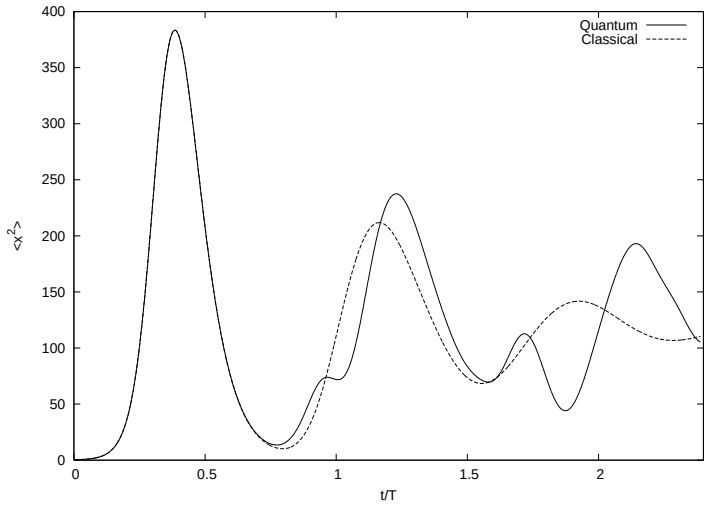

Figure 42: $< x^2 > (t)$ for quadratic term < 0, $r_1 = r_2 = 100.0$. The quantum curve have secondary oscillations.

5.5 Check for PCC

Now we are going to verify the *Perturbative Classicality Condition* shown in chapter 4 for several values of parameters.
Once we have discretized the time we can use numerical methods to compute $S_Q(t)$ and $S_{Cl}(t)$ over a range of t. We need to invert the matrices $(\mathbb{I} - A)$ and $(\mathbb{I} - A + B)$. This can take a high computational cost for large values of t, although in our systems we will can perform the calculations without problems.
We have to include a factor $(\Delta t)^2$ in definitions of matrices C, D, so the integrals appearing in (170) are now usual products of matrices. Therefore, if $s_j = j\Delta t$ with $0 \leqslant s_j \leqslant t$ then we have

$$C(i,j) \equiv \frac{2}{3}\lambda^2(\Delta t)^2 G_S^2(s_i,s_j)G_A(s_i,s_j) = -C(j,i)$$
$$D(i,j) \equiv -\frac{2}{9}\lambda^2(\Delta t)^2 G_A^3(s_i,s_j) = -D(j,i)$$
$$A \equiv CG_A \quad ; \quad B \equiv DG_A \tag{200}$$
$$\tag{201}$$

5.5.1 Single well potential

We return to our case of single well potential in order to test PCC. In this case the functions $f_1(t), f_2(t)$ are bounded and have the form that we saw in (247). We have verified PCC for many values of r_1, r_s and show some of them in Tables 4-9. As above, we calculate the relative difference ratio (%) between $\langle x^2(t)\rangle_Q$ and $\langle x^2(t)\rangle_{Cl}$, and will note this as rdr(t). Similarly we define $S_{rel}(t)$ as the relative difference ratio (%) between $S_Q(t)$ and $S_{Cl}(t)$. These differences are calculated in $t_1, t_2, t_3, ...$, where t_i is the time of the maximum M_i. Also we have considered appropriate to define (analogous to $I(t)$)

$$I_p(i) \equiv 100\frac{\int_{t_i}^{t_i+T_i/2} ds|\langle x^2(s)\rangle_Q - \langle x^2(s)\rangle_{Cl}|}{\int_{t_i}^{t_i+T_i/2} ds\langle x^2(s)\rangle_Q}(\%) \tag{202}$$

where $T_i/2$ is the time between t_i and next minimum. We will obtain $I_p(i)$ and compare with $S_{rel}(t_i + T_i/4)$.
The values of $\mathrm{rdr}(t_i), S_{rel}(t_i)$ and $I_p(i), S_{rel}(t_i + T_i/4)$ are presented in Tables

4-9. The estimated errors are

$$\nabla rdr(t_i) = \pm 0.05\% \ for \ t_i \leqslant t_3 \ ; \ \nabla rdr(t_i) = \pm 0.06\% \ otherwise$$
$$\nabla I_p = \pm 0.2\% \ ; \ \nabla S_{rel} = \pm 0.1\% \quad (203)$$

In some Tables we have discarded the first values because they are of error order.
After our calculations, we can write the following conclusions:
–The true relative difference between the quantum and classical evolution is of the same order as the relative difference between $S_Q(t)$ and $S_{Cl}(t)$.
–If $S_{rel}(t) < 1.0\%$ then CPP give us at least the 33% of the true difference $(rdr(t))$.
–If $S_{rel}(t) > 3.0\%$ then CPP give us at least the 50% of the true difference.
–The data work better when we compare $I_p(i)$ and $S_{rel}(t_i + T_i/4)$, instead of to compare in the maxima.

	M_1	M_2	M_3	M_4	M_5
$rdr(t_i)$	2.10	10.44	22.85	28.08	28.71
$S_{rel}(t_i)$	1.1	20.2	22.7	28.3	28.7
$I_p(i)$	8.7	16.3	25.6	29.3	27.7
$S_{rel}(t_i + T_i/4)$	5.8	25.4	23.6	26.9	30.2

Table 4: Relative differences for $r_1 = 0.4$ and $r_s = (2.24)$. Quadratic term > 0.

	M_1	M_2	M_3	M_4	M_5
$rdr(t_i)$	0.61	3.46	9.97	16.91	23.15
$S_{rel}(t_i)$	0.2	3.6	8.7	13.3	16.8
$I_p(i)$	2.4	5.9	12.0	18.9	25.7
$S_{rel}(t_i + T_i/4)$	0.8	4.6	9.8	14.6	18.3

Table 5: Relative differences for $r_1 = 2.0$ and $r_s = (2.24)$. Quadratic term > 0.

	M_2	M_3	M_4	M_5	M_6
$rdr(t_i)$	0.39	1.90	3.90	6.17	8.48
$S_{rel}(t_i)$	0.7	2.1	4.1	6.6	9.5
$I_p(i)$	1.4	2.7	4.5	6.5	8.6
$S_{rel}(t_i + T_i/4)$	1.1	2.6	4.7	7.2	10.2

Table 6: Relative differences for $r_1 = 5$ and $r_s = (1.41)$. Quadratic term > 0.

	M_3	M_4	M_5	M_6
$rdr(t_i)$	0.54	1.35	2.37	3.54
$S_{rel}(t_i)$	0.6	1.1	1.9	2.8
$I_p(i)$	1.0	1.7	2.6	3.7
$S_{rel}(t_i + T_i/4)$	0.7	1.3	2.1	3.1

Table 7: Relative differences for $r_1 = 10.0$ and $r_s = (1.41)$. Quadratic term > 0.

	M_4	M_5	M_6	M_7	M_8
$rdr(t_i)$	0.92	1.19	2.16	2.4	2.6
$S_{rel}(t_i)$	0.3	0.5	1.0	1.2	1.4
$I_p(i)$	1.0	1.2	1.8	2.0	2.1
$S_{rel}(t_i + T_i/4)$	0.4	0.5	1.0	1.2	1.3

Table 8: Relative differences for $r_1 = 10.0$ and $r_s = 5.0$. Quadratic term > 0.

	M_4	M_5	M_6	M_7	M_8	M_9	M_{10}
$rdr(t_i)$	0.35	0.76	1.84	2.49	3.18	3.92	4.7
$S_{rel}(t_i)$	0.3	0.5	1.0	1.4	1.7	2.2	2.6
$I_p(i)$	0.7	1.1	2.1	2.6	3.3	4.0	4.7
$S_{rel}(t_i + T_i/4)$	0.3	0.6	1.1	1.4	1.8	2.3	2.7

Table 9: Relative differences for $r_1 = 20.0$ and $r_s = (1.58)$. Quadratic term > 0.

5.6 Time-dependent studied cases

We have analyzed two cases for $w^2(t)$: *linear dependence* and *tanh dependence* on t.

In the case of *linear dependence* we have taken the connection time ($t = 5.0$) and we have calculated the widths σ_x, σ_p from expectation values matrix showed in (59). With this, we have found the values

$$r_1 = 47.14 \quad ; \quad r_2 = 3222 \quad ; \quad r_s = 8.27 \tag{204}$$

The value of $|w^2(t)|$ is growing along the evolution and r_1 will increase. The potential minimum is moved away more and more and the tunneling influence is decreasing. Therefore, the classical approximation work very well.

We have done the same calculations in the case of *tanh dependence*. For the connection time ($t = 5.0$) we found

$$r_1 = 118.47 \quad ; \quad r_2 = 23447 \quad ; \quad r_s = 14.07 \tag{205}$$

Also r_1 is increasing along the evolution and the tunneling influence is decreasing. The value of r_s is already large enough at the connection time. Thus, the classical approximation is also valid.

6 Test of the Classical Approximation: 2 DoF

In this chapter we extend the test of classical approximation to systems with two degrees of freedom. If we recall the example of Hybrid Inflation presented in chapter 1 then the new degree of freedom would be a new Higgs mode. This new mode can be coupled with the zero Higgs (and/or Inflaton) mode and also can have an auto-interaction term. We will consider different systems with these possibilities.
As above, all quantities and parameters are dimensionless.

6.1 Constant coupling

We start considering the case of two coupled degrees of freedom, where one of them has a time-dependent coefficient of quadratic term that changes from positive to negative. In the mentioned Hybrid Inflation model this emulates the case of a Higgs mode whose coupling with the Inflaton is not enough to acquire by itself a classical behavior, but this mode can acquire this behavior if is coupled to other Higgs mode that becomes classical. In all presented Figures the errors are less than 0.2 %.

6.1.1 Description of the system

We want to study the influence of a new degree of freedom y over the old one x when there is a constant coupling among them. We consider the Hamiltonian

$$H(x,y,t) = \frac{1}{2}p_x^2 + \frac{1}{2}w_x^2(t)x^2 + \frac{1}{2}p_y^2 + \frac{1}{2}w_y^2y^2 + \frac{\lambda}{24}x^4 + \frac{\mu}{24}x^2y^2 \qquad (206)$$

where clearly p_x, p_y are the conjugate momenta of x, y. Notice the new coupling μ for the interaction between x and y.
In this Hamiltonian x still has an $w_x^2(t)$ that will become from positive to negative. The mass of y is constant. We want to see if the influence of y delay or advance the classical behavior of x. Also we want to test if y can reach a classical behavior driven by x. Now the interaction Hamiltonian is

$$H_I(x,y,t) = \frac{\lambda}{24}x^4 + \frac{\mu}{24}x^2y^2 \qquad (207)$$

We choose the potential so that $w_x^2(t)$ is linear with t

$$w_x^2(t) = c_0 - u_0t \qquad (208)$$

For the same reasons that in the previous chapter, a suitable choice of parameters is

$$c_0 = w_y^2 = 8.0 \quad u_0 = 2.0 \quad \lambda = 0.3 \quad \mu = 0.6 \tag{209}$$

The initial state corresponds to ground state of two decoupled harmonic oscillators with $w_x = w_y = \sqrt{8}$. Therefore the initial wave function is

$$\Psi(x, y, t) = \left(\frac{w_x w_y}{\pi^2}\right)^{\frac{1}{4}} \exp\left\{-\frac{1}{2} w_x x^2 - \frac{1}{2} w_y y^2\right\} \tag{210}$$

6.1.2 Numerical exact evolution

We solve numerically the Schroedinger equation for two dimension with the given values of parameters. We use a standard discretization and obtain the numerical solution with the finite difference method.

Results

In this case, to understand the results one must reason from two points of view:

- from the point of view of x, it effective mass is increased by the coupling with y

  $$w_x^2(t) x^2 \longrightarrow (w_x^2(t) + \frac{\mu}{2} y^2) x^2 \tag{211}$$

  As $< y^2 >$ will not grow but is kept in the first moments and decreases later (as we will see), then the effective mass for x has an additional positive contribution that is bounded. In the evolution, this leads to a delay respect to the case of one degree of freedom. We compare both cases in Fig. 43 and we can see the mentioned delay.

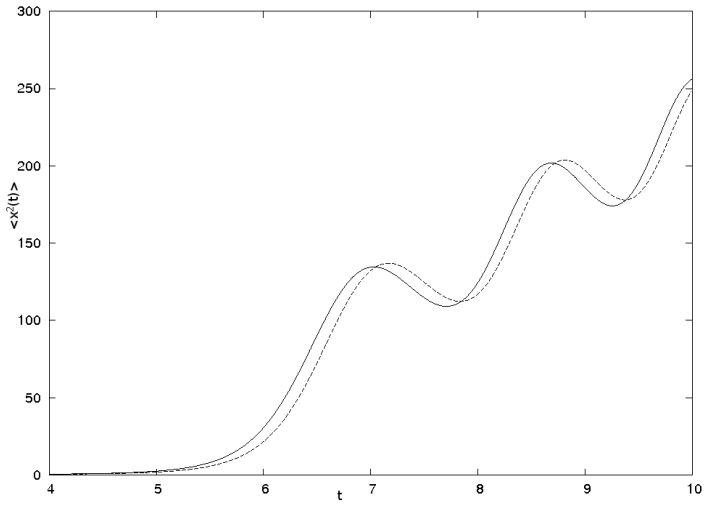

Figure 43: Full evolution of $< x^2(t) >$ for $\mu = 0$ (solid line) and $\mu \neq 0$ (dashed line). In both cases we have $\lambda = 0.3$.

- from the point of view of y, it receives a little influence in the first moments from the coupling with x, because the values of $< x^2(t) >$ and $< y^2(t) >$ are small. But later $< x^2(t) >$ is growing and then the effective mass for y is increasing because it has an additional contribution

$$w_y^2(t)y^2 \longrightarrow (w_y^2(t) + \frac{\mu}{2}x^2)y^2 \tag{212}$$

This means that the effective quadratic potential for y is a parabola more and more narrow and then the value of $< y^2(t) >$ has to decrease, especially when $< x^2(t) >$ grows quickly. We can see this in Fig. 44.

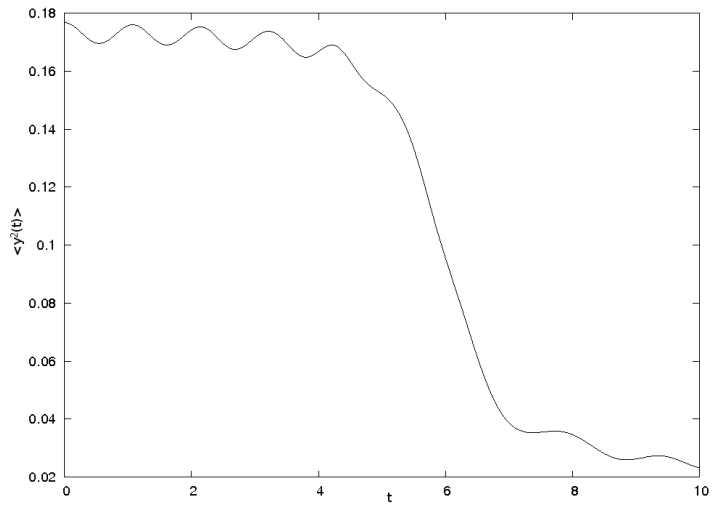

Figure 44: Numerical exact evolution for $< y^2(t) >$ with $\lambda = 0.3$ and $\mu = 0.6$. We see that the zone of greatest decreasing match the zone where $< x^2(t) >$ grows quickly (see previous Figure).

6.1.3 Gaussian approximation

If we take $\lambda = 0$ and $\mu = 0$ then x, y evolve independently. x evolve as we have seen in chapter 2 using the functions $f_{x,1}(t), f_{x,2}(t)$. y remains in the ground state of an harmonic oscillator with frequency w_y, and then we have in this case $\langle y^2(t)\rangle_0 = 1/(2w_y) = cte$.

6.1.4 Perturbative expansion

As we have done in the case of one degree of freedom, we will perform a perturbative expansion in order to obtain a more accurate evolution to connection time. We will extend the study presented in chapter 4 to the case of two degrees of freedom. Now the interaction Hamiltonian (207) has an additional term respect to the case of one degree of freedom. This Hamiltonian in the interaction picture is

$$\mathbf{H^I_{int}(t)} = \frac{\lambda}{24}x_0^4(t) + \frac{\mu}{24}x_0^2(t)y_0^2(t) \tag{213}$$

So the evolution operator takes the form

$$\Omega(t) = \mathrm{T}\ \exp\{-i\int_0^t ds\mathbf{H}^{\mathbf{I}}_{\mathbf{int}}(\mathbf{s})\} = I - i\frac{\lambda}{24}\int_0^t ds x_0^4(s) - i\frac{\mu}{24}\int_0^t ds y_0^2(s)x_0^2(s) + ... \tag{214}$$

where we have shown the expression to *order 1.*
As we mentioned, in this case the operator $y_0(s)$ (under the free potential) remains in the same state and the two point function at equal times remains constant

$$< y_0^2(s) >=< y_0^2(0) >= \frac{1}{2w_y} \tag{215}$$

Moreover, initially one has

$$\begin{array}{l}[x_0(0), y_0(0)] = [x_0(0), p_{y,0}(0)] = [p_{x,0}(0), y_0(0)] = [p_{x,0}(0), p_{y,0}(0)] = 0 \\ \langle x_0(0)y_0(0)\rangle = 0 \ \ ; \ \ \langle x_0(0)p_{y,0}(0)\rangle = \langle p_{x,0}(0)y_0(0)\rangle = 0 \ \ ; \ \ \langle p_{x,0}(0)p_{y,0}(0)\rangle = 0\end{array} \tag{216}$$

With this, and taking into account that here one has for $x_0(t), y_0(t)$ similar expressions to (42), one find

$$[x_0(t), y_0(t')] = 0 \quad ; \quad \langle x_0(t)y_0(t')\rangle = 0 \tag{217}$$

which simplifies the perturbative expansion.
Thus, we can expand the Texp shown in (214) and apply the Wick theorem, ruling out the pairings $\langle x_0(s)y_0(s')\rangle$. We have done this to order two for $\langle x^2(t)\rangle$ in order to calculate the perturbative contribution at the connection time that we choose.
Of course, we can perform a diagrammatic expansion with the next propagators

$$\begin{array}{l}\langle x_0(t)x_0(t')\rangle = G_S(t,t') + iG_A(t,t') \\ G_S(t,t') = f_{x,1}(t)f_{x,1}(t') + f_{x,2}(t)f_{x,2}(t') = G_S(t',t) \\ G_A(t,t') = f_{x,2}(t)f_{x,1}(t') + f_{x,1}(t)f_{x,2}(t') = -G_A(t',t) \\ \langle y_0(t)y_0(t')\rangle = K_S(t,t') + iK_A(t,t') \\ K_S(t,t') = \dfrac{1}{2w_y}\cos(w_y(t-t')) = K_S(t',t) \\ K_A(t,t') = -\dfrac{1}{2w_y}\sin(w_y(t-t')) = -K_S(t',t)\end{array} \tag{218}$$

We assign a different type of line to each propagator, as for example

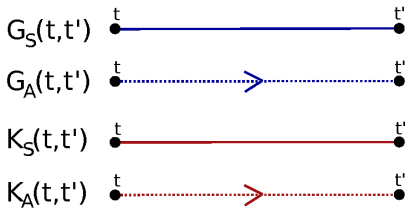

where clearly the blue legs correspond to x_0 and the red legs to y_0. We also have two types of internal vertices (see (206)) and we can represent them as

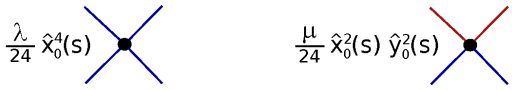

With this we can draw the obtained diagrams from the expansion of $\langle x^2(t)\rangle$ to order two. As an example, we will show the expression to order one and draw the corresponding diagrams. We start from expression

$$\langle x^2(t)\rangle = \langle \Omega^\dagger(t) x_0(t)\Omega(t)\Omega^\dagger(t)x_0(t)\Omega(t)\rangle = \langle \Omega^\dagger(t)x_0^2(t)\Omega(t)\rangle \tag{219}$$

and expand (214) to order one. We obtain

$$\langle x^2(t)\rangle_1 = \frac{1}{24}\int_0^t ds\Big[48\lambda G_S(t,s)G_S(s,s)G_A(t,s)+8\mu G_S(t,s)K_S(s,s)G_A(t,s)\Big] \tag{220}$$

This expression corresponds to the next diagrams

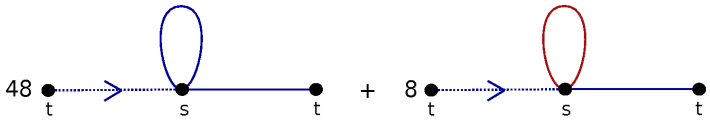

It is not difficult to deduce Feynman rules for this stage.

•In the case of $\langle x^l(t)\rangle$ the rules are a priori the same as in chapter 4, for

example the *B rules*, although with some modifications. The K_S, K_A propagators have the same symmetry properties than G_S, G_A, and therefore remain valid the arguments of chapter 4 about the properties of diagrams with not null contribution. Here the diagrams are the same, with the same topology, the same solid lines, the same dashed lines with equal orientations, and the same sign in the prefactors. But now we have two possible colors for each line, and one has to consider all possibilities taking into account two conditions:
–In each internal vertex it can only have two red lines.
–The red legs only can join among themselves. Therefore each red line join two vertices of two-type according to (206). So in this case ($\langle x^l(t)\rangle$) the red legs cannot join to external legs.
This means that now we have additional diagrams that mix both colors. About the prefactors, we have seen in (148) that the symmetry factor s rectified the over-counting coming from 4! possible permutations between the legs in each internal vertex. Now we have to take into account that in each internal vertex of two-type we only can permute the legs with the same color to obtain equivalent diagrams, and therefore the factor is 4. So the old prefactor must be divided by 6^m, where m is the number of two-type vertices in the diagram under consideration.
Moreover the symmetry factor s can be smaller because now one only can shuffle the legs with the same color among themselves. So if the old s has to be divided by k then we have to multiply the new prefactor by k.
In brief, the new prefactor ($prefactor'$) respect to the old prefactor ($prefactor$) is $prefactor' = prefactor\, k/6^m$. We show some examples in Fig. 45, where if we change the vertex from one-type to two-type then we have to change the coupling $\lambda \to \mu$.

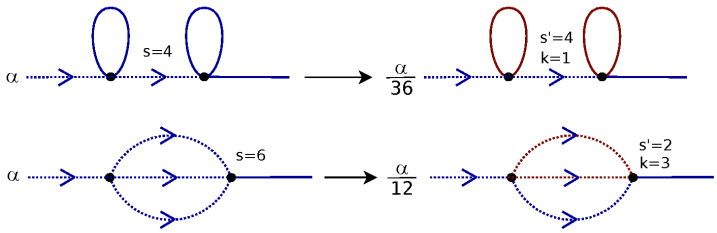

Figure 45: Example about the calculation of prefactors for new diagrams.

• In the case of $\langle y^l(t)\rangle$ the rules are similar. One solely has to take into ac-

count that the external legs only can be joined to vertices of two-type.

These arguments can be generalized to more types of internal vertices or more degrees of freedom, but this is not our goal. We have verified the rules to order 2 and we have calculated the expectation values up the connection time (in order to do the later classical evolution).

6.1.5 Comparison of results

We will compare the obtained results for $< x^2(t) >$ using the numerical exact evolution and the classical evolution with gaussian and perturbative connection. We display these results in Fig. 46. Also we show the absolute differences respect to full quantum evolution in Fig. 47. The classical approximation work well in this case. Moreover we can see that the perturbative connection represents a significant improvement respect to the gaussian connection.

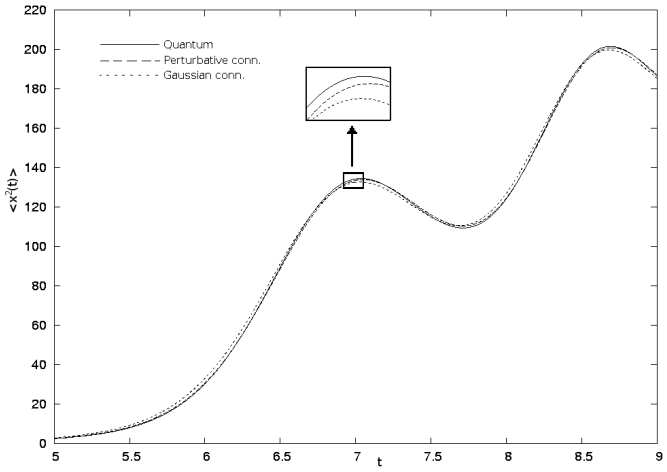

Figure 46: Quantum evolution of $< x^2(t) >$ vs classical evolution with gaussian and perturbative connection.

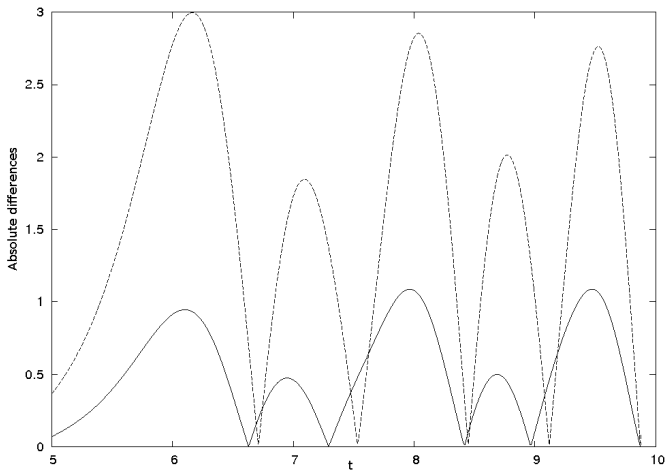

Figure 47: Absolute differences for $< x^2(t) >$ between the quantum evolution and the classical evolution with perturbative (solid line) and gaussian (dashed line) connection.

Now we focus on y. This degree of freedom will not reaches a classical behavior. We have calculated the numerical exact evolution of $< y^2(t) >$ and also the classical evolution with perturbative connection. The results are very different, and for y is not valid the classical approximation.

6.1.6 Connection zone

We want to see if in this case also exists an interval time where we can choose the connection time and the later classical evolution lead to compatible curves.
We have detected this zone around $t = 5.0$ (as in the case of one degree of freedom). For this, we observed that the main differences between quantum and classical evolution are little time shifts, as one can see in Fig. 48.

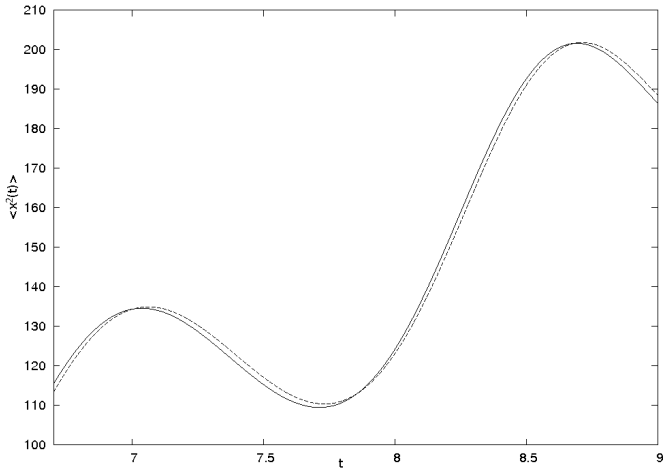

Figure 48: Quantum (solid line) and classical (dashed line) evolution for $< x^2(t) >$. Here we have $t_c = 4.9$

We are interested in the global behavior, irrespective of small shifts that do not change the time scale. So we can rectify the shift and the curves are similar, as we show in Fig. 49..

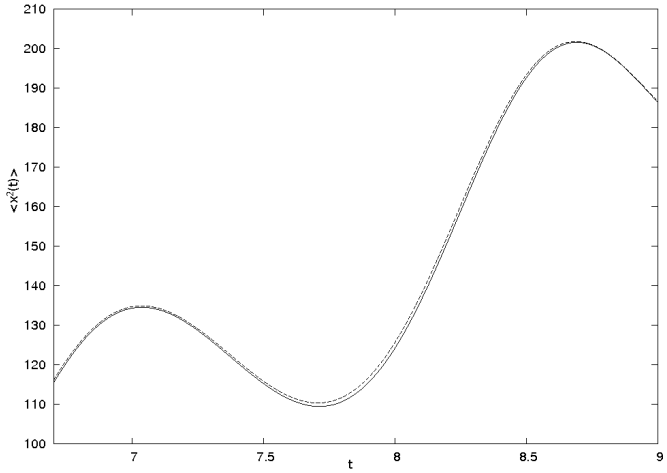

Figure 49: The same as in Fig. 48 but with the shift rectified.

So we evolve the system with classical approximation from several connection

times and rectify the shifts. We display in Fig. 50 the absolute differences for these connection times respect to the quantum evolution. We see that for a concrete time interval the difference become stabilized, and outside this interval the difference is growing. This interval is our transition zone. Of course, in more realistic cases we will not have the numerical exact evolution, but we can detect the transition zone as the interval in which the classical curves are compatible (as in the previous sections). We have verified that outside the transition zone the curves are very sensitive to the connection point, and this makes it easier the detection.

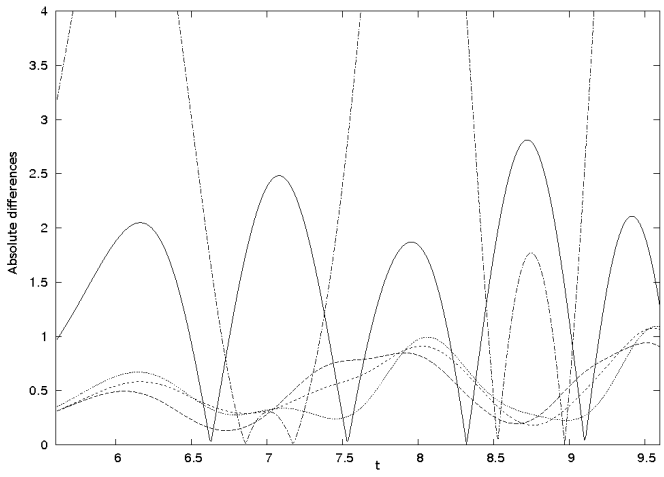

Figure 50: Absolute differences respect to quantum evolution for $< x^2(t) >$ with several connection times. The outermost lines correspond to $t_c = 4.2$ (solid line) and $t_c = 5.6$ (alternating line). The remaining lines correspond to $t_c = 4.8, 5.0, 5.2$.

Thus, we found a transition zone on the time interval $[4.6, 5.2]$.

Influence of w_y

Up now we have taken $w_y = w_x$. However we also want to study the case in which the frequencies are not equal. If we consider that w_y is less than w_x then we hope that the influence of y over the behavior of x also decrease. As we seen this influence lead to a delay for the evolution of $< x^2(t) >$ respect to the case of one degree of freedom. Then the delay should decrease for

smaller values of w_y, as we can see in Fig. 51. As we said the delays are not

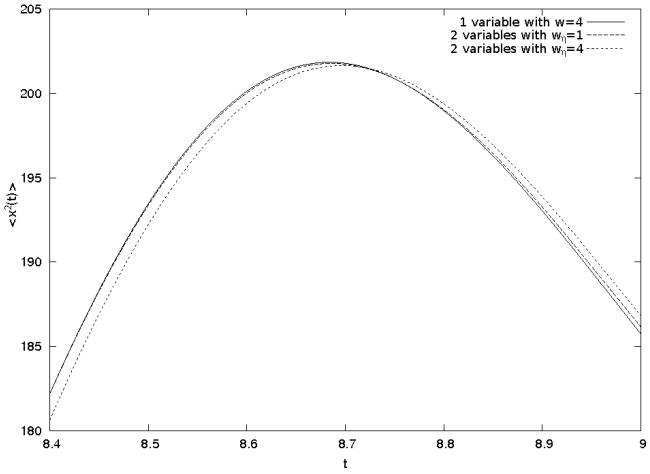

Figure 51: $< x^2(t) >$ for one degree of freedom vs two degrees of freedom with different values of w_y.

significant in the global behavior. So it seems that in the case of fields we can neglect the influence of non-classical modes, as long as the coupling with them is relatively small.

6.2 Inflaton as a quantum variable

Up to now, motivated by our hybrid inflation model presented in chapter 1, we have shown the evolution of a quantum degree of freedom with a time dependent mass term. In the mentioned model, the coupling of the inflaton (considered as a classical background field) to the Higgs zero mode, results in a time dependent effective mass. We have supposed this mass linear with t.

Now we are going to consider a degree of freedom x representing the Higgs zero mode coupled to other degree of freedom y that will represent the inflaton. And we will choose a model so that the coupling produces a negative effective mass square for the Higgs, at least at for a while. This effective mass has to evolve similarly to the 1 dof with linear dependence case.

6.2.1 System description

Potential election

Reminding our hybrid inflation model, we are going to consider a potential:

$$V(x,y) = \frac{1}{2}\left(g^2y^2 - \mu^2\right)x^2 + \frac{\lambda}{4}x^4 \tag{221}$$

that is time independent. But if $< y^2 >$ vary with time, the effective mass for x will have a dependence on t. Our goal is that this effective mass square behaves linearly from the bifurcation point to the connection time, in a equivalent way to the case of 1 dof.

Initial conditions

We are going to start the evolution exactly at the bifurcation point. At this point, if we ignore the coupling ($g = 0$), the effective potential for y can be considered null. So we are going to find the evolution of this variable from the bifurcation point to the connection point under a null potential. Then we will demand this evolution to behave linearly in this period of time.

We choose as initial wave function a normalized gaussian wave packet with three parameters w, δ, p_0 that we can tune at our convenience

$$\Psi(y) = \left(\frac{w}{\pi}\right)^{\frac{1}{4}} e^{-\frac{w}{2}(y+\delta)^2 + ip_0(y+\delta)} \tag{222}$$

this wave function fulfills

$$< p_y >= p_0 \qquad < y >= -\delta \qquad < y^2 >= \frac{1}{2w} + \delta^2 \tag{223}$$

For x, we choose the wave function obtained from the numerical evolution without approximations in the case of 1 dof, evolving it up to the bifurcation point ($t = 4.0$). The complete wave function will be the product of the two we have just described.

Linearity conditions

We want that the following condition be fulfilled at least up to the connection point

$$\frac{1}{2}\left(g^2 < y^2(t) > -\mu^2\right) \approx \frac{1}{2}(c_0 - u_0 t) \tag{224}$$

So we need to know how $< y^2(t) >$ evolves. Solving the Schrödinger equation for y with the initial condition (222) and a null potential, the normalized wave function is obtained:

$$\Psi(y,t) = \frac{\sqrt{w/\pi}}{\sqrt{1+iwt}} e^{\frac{-w(y+\delta)^2 + 2ip_0(y+\delta) - ip_0^2 t}{2+2iwt}} \tag{225}$$

and with this wave function, it can be calculated:

$$< y^2(t) >= \frac{1}{2w} + \delta^2 - 2\delta p_0 t + \left(\frac{w}{2} + p_0^2\right)t^2 \tag{226}$$

It is required than the linear term with t of (226) be quite larger than the quadratic term. We will suppose that it will be K times larger. This and (224) lead us to the following linearity conditions:

$$\begin{aligned} &\frac{g^2}{2w} + g^2\lambda^2 - \mu^2 = c_0 \\ &2g^2\delta p_0 = u_0 \\ &2\delta p_0 = K\left(\frac{w}{2} + p_0^2\right)\Delta t \end{aligned} \tag{227}$$

Clearly (225) is not the exact solution, because the potential is only zero at the beginning, but it is useful for estimating what happens in the first moments. Of course the exact evolution must be checked numerically to see if is roughly linear in this period of time.

Parameters election

Here c_0, u_0 and λ have the same values than in the case of 1 dof

$$c_0 = 0.0 \qquad u_0 = 1.0 \qquad \lambda = 0.02 \tag{228}$$

Furthermore, as the connection time was taken at $t = 5.0$, the period between the bifurcation and the connection time will be $\Delta t = 1.0$. Therefore we must only choose K and p_0 values to obtain the three parameters g, δ and w from the equations (227). In this manner we will have completely defined both the potential (221) and the wave function (225). It is advisable that the p_0 value will be similar to the u_0 value (as they represent the initial speed), so we have made them equal.

With respect to the other parameters, we can infer from (223) that δ represents the initial movement of the inflaton with respect to the origin. We do not want it to be very large because we do not want to expand our lattice too much. But the last equation of (227) means that choosing a large K is the same as choosing a large δ, and this cannot be compensated by reducing w value as it has to be always positive. Therefore we must look for a compromise. After these considerations we have chosen the following values:

$$\begin{cases} c_0 = 0.0 & u_0 = 1.0 & \lambda = 0.02 & p_0 = 1.0 & \Delta t = 1.0 \\ K = 10.0 & \mu^2 = 10.0 & g^2 = 0.10025 & \delta = 9.975 & w = 1.989924 \end{cases} \tag{229}$$

With them we can find what approximation fulfills (224). Of course, for the analytical value of $< y^2(t) >$ given by (226) the variation in the first stage $\Delta t = 1$ will be roughly 10%, as we have chosen it so. But we have to check it for the exact quantum evolution. Fig. 52 shows the separation respect to the linear behavior is about a 27% lower. This suits us because our goal is to see if these systems become classical and the faster the effective mass value that x generates over y is reduced, the faster the classical behavior will manifest. In fact, we will take advantage of this, and in order to compare it with the linear coupling we will take $t = 4.8$ as the connection time.

6.2.2 Classical versus quantum evolution

In the case of many variables systems, to calculate the Wigner function at the connection point, some approximations should be taken (gaussian ap-

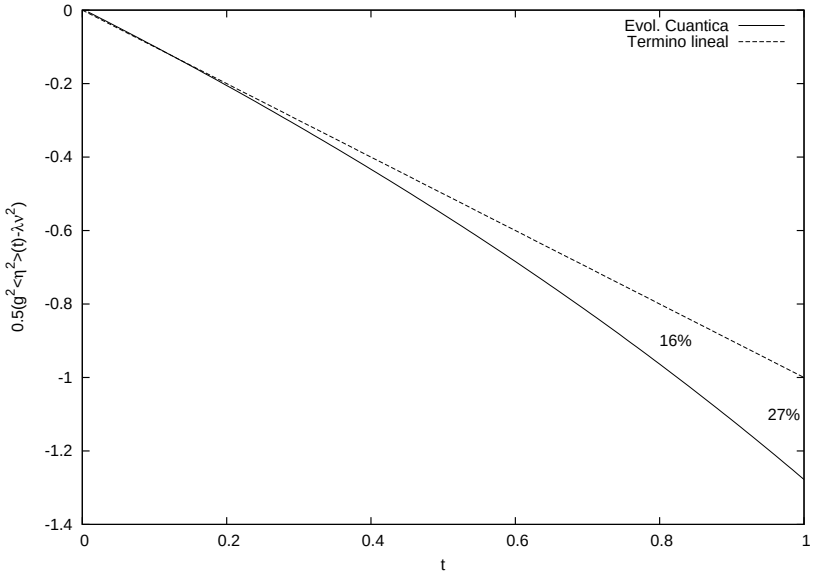

Figure 52: Evolution of the linear term and $g^2 < y^2(t) > -\lambda\nu^2$ with the chosen parameters

prox., perturbative approx.,...). But in our two variables case it can be calculated without any approximation (except the numerical one), obtaining $W(x, y, p_x, p_y)$ in $t = 0.8$.

Classical approach for $W(x, p_x)$ and $W(y, p_y)$

If we integrate the whole Wigner function in y, p_y we obtain $W(x, p_x)$ at the connection point. Integrating in x, p_x we obtain $W(y, p_y)$. Both are positive definite and their shapes are shown in Fig. 53 and Fig. 54 respectively.
Now we can generate configurations with these two functions considering them as independent, and subsequently do the classical evolution. If our analogy with the 1 dof case is right, then the classical evolution of the expectation values must coincide with the quantum evolution. We compare it for $\langle x^2 \rangle$ in Fig. 55. The differences are apparent and the analogy do not seem valid.

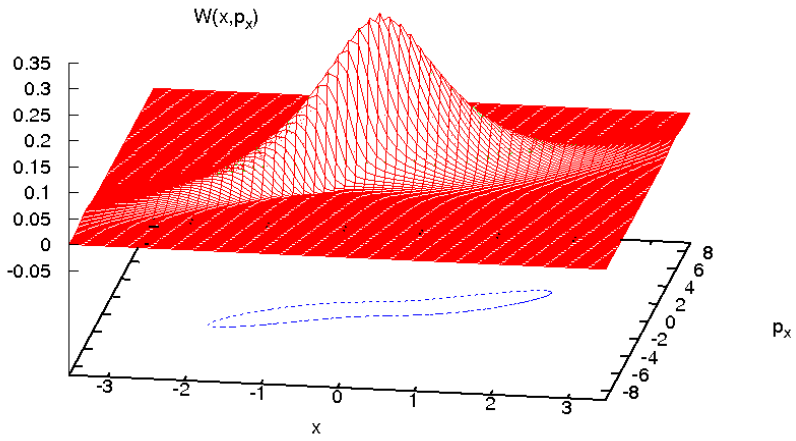

Figure 53: $W(x, p_x, t)$ para $t = 4.8$.

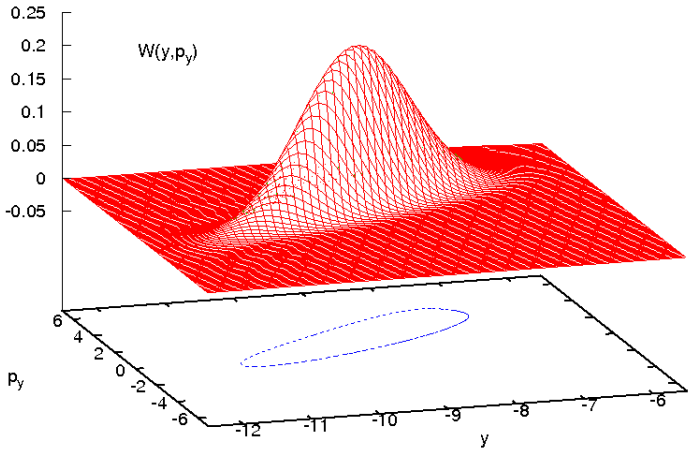

Figure 54: Integrated Wigner function $W(y, p_y, t)$ at the connection point.

Classical evolution with the positive full Wigner function

Maybe x has acquired a classical behavior and the differences come from considering $W(x, p_x)$ and $W(y, p_y)$ as independent in the complete Wigner function. So we are going to use now $W(x, y, p_x, p_y)$ to generate the initial

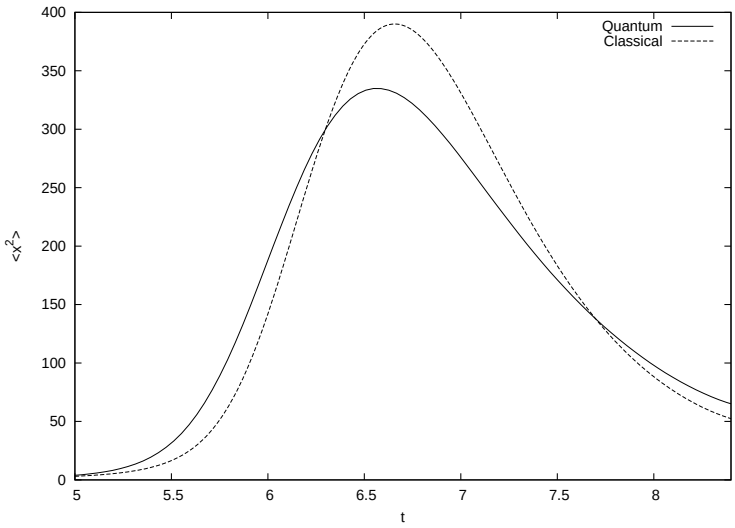

Figure 55: Classical and quantum $\langle x^2 \rangle$. The initial configurations for the classical evolution are generated from $W(x, p_x)$ and $W(y, p_y)$ considered as independent.

configurations (x, y, p_x, p_y) and we will evolve it classically. We suppose that if this complete function has a negative part, it is negligible and we can safely ignore it. Then we represent $< x^2 > (t)$ for the classical and quantum evolution in Fig. 56. Notice that even if the curves are closer there is still a significant difference between them. It is advisory to check the Wigner function squeezing for x.

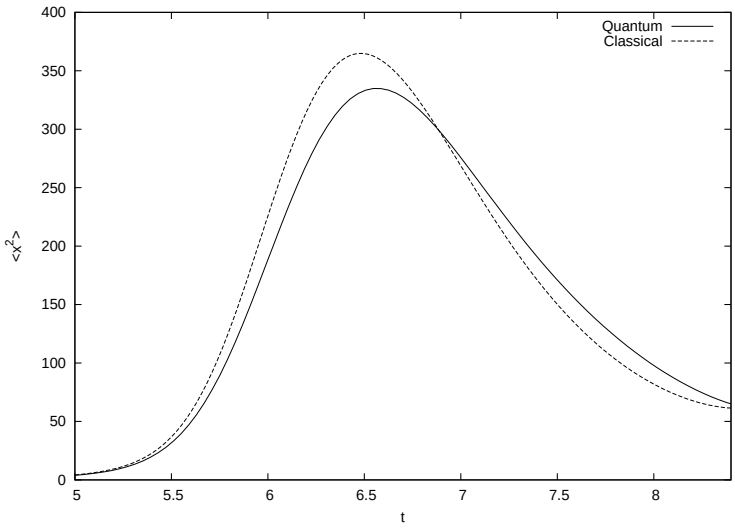

Figure 56: Classical and quantum evolution from $< x^2(t) >$.

Squeezed condition

We have seen the function $W(x, p_x)$ in Fig. 53, where the boundary 2σ is also drawn. It has been estimated that the axis ratio for this boundary is approximately $r_s = 6.7$. This value is roughly more than half of the one obtained from the 1 dof case, but a priori, it seems that the classical approximation should work better with that value. Besides, the negative part of $W(x, p_x)$ is negligible and the difference cannot come from that.

Quantum vs. mixed classical evolution

In other systems that we have studied, the Wigner functions at the connection time used for the classical approximation were positive definite, though W is generally not. In our current case, the fact of having negligible negative parts of $W(x, p_x)$ and $W(y, p_y)$ is what leaded us to think that the negative part of the complete Wigner function $W(x, y, p_x, p_y)$ can be ignored. But this is not true, as we have checked that, although initially the complete Wigner function is practically positive definite, at the connection time has a significant negative part. For $t = 0.8$ (connection time) the numerical integral

of both positive and negative parts results:

$$\mathrm{V}_+(t=0.8) \equiv \int W_+(x,p_x,y,p_y,t=0.8)dxdp_xdydp_y = 1.329$$
$$\mathrm{V}_-(t=0.8) \equiv \int W_-(x,p_x,y,p_y,t=0.8)dxdp_xdydp_y = 0.329 \qquad (230)$$

Thus, comparing with the 1 dof case, we have for x a Wigner function at the connection time virtually gaussian and definite positive (Fig. 53), with a seemingly good enough squeezing to obtain a good classical approximation. But this is hiding the fact that the complete function has a significant negative volume. This makes this system substantially different to the 1 dof case, where we have considered that the influence of a possible coupled degree of freedom y over x becomes in a linear dependence with t in the coefficient of the quadratic term.
Up to now we have done the classical evolution generating configurations at the connection time ignoring the negative part, while in the quantum evolution the complete Wigner function is considered implicitly. So we are going to study how to account this negative part for a classical evolution.

We know that the classical evolution using Liouville equation conserves the distribution volume, which is always positive definite. In the studied 1 dof cases the negative part of W is almost stabilized, and since the connection time it grew very slowly. We are going to check if this happens in our current case. In order to do this, the integrals appeared in (230) are calculated from the initial time beyond the connection time. These results are shown in Fig.57.

Effectively, the volume stabilize before the connection time and then increase slowly. Therefore, we are going to consider the positive partW_+ and the negative one W_- separately, in which we will call *Mixed classical evolution*. We will generate configurations with the distribution W_+ and we will evolve them classically as usual, obtaining the evolution of the expectation values we are interested in, which we will denote as $\langle ... \rangle_{cl+}$. Then we will do the same with the distribution $|W_-|$ and we will also evolve it classically obtaining the expectation values $\langle ... \rangle_{cl-}$. Finally, for each time, we have to subtract the negative part from the positive part contribution, but weighting each one with their corresponding volume, to obtain the final classical values

$$\langle ... \rangle_{cl}(t) = \mathrm{V}_+(t)\langle ... \rangle_{cl+}(t) - \mathrm{V}_-(t)\langle ... \rangle_{cl-}(t) \qquad (231)$$

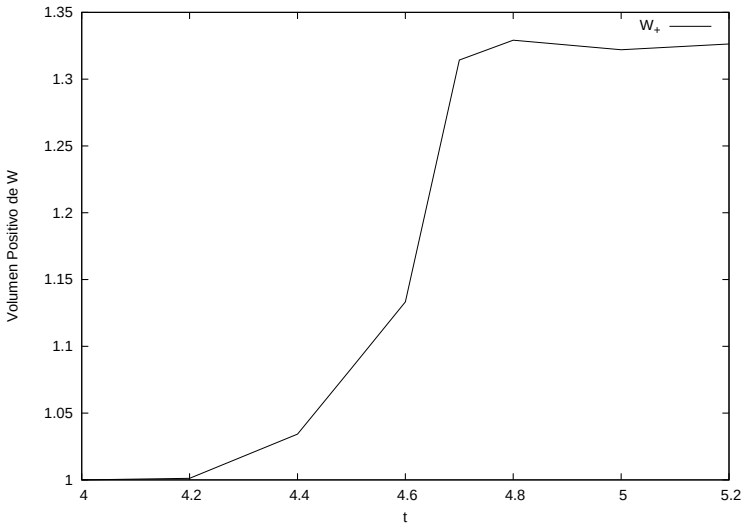

Figure 57: Evolution of the positive volume of the Wigner function

The evolution of $\langle x^2 \rangle$ is shown in Fig.58 and the evolution of $\langle p_x^2 \rangle$ in Fig.59. Now the classical and the quantum evolution actually coincide.

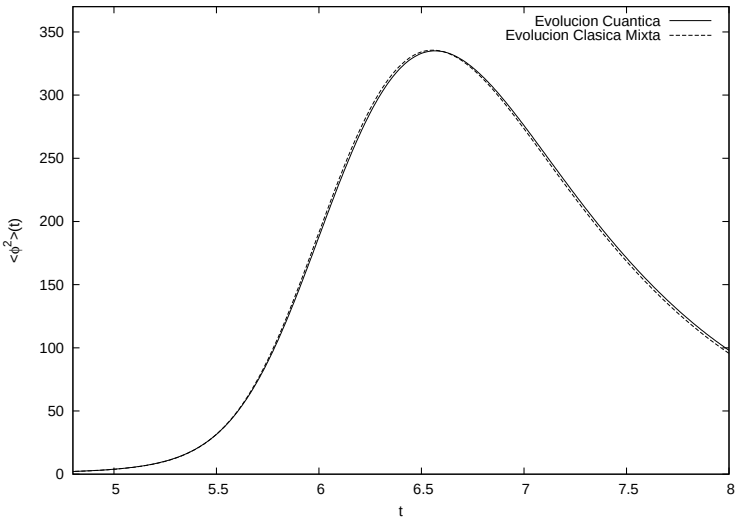

Figure 58: Quantum evolution versus mixed classical evolution of $\langle x^2 \rangle$

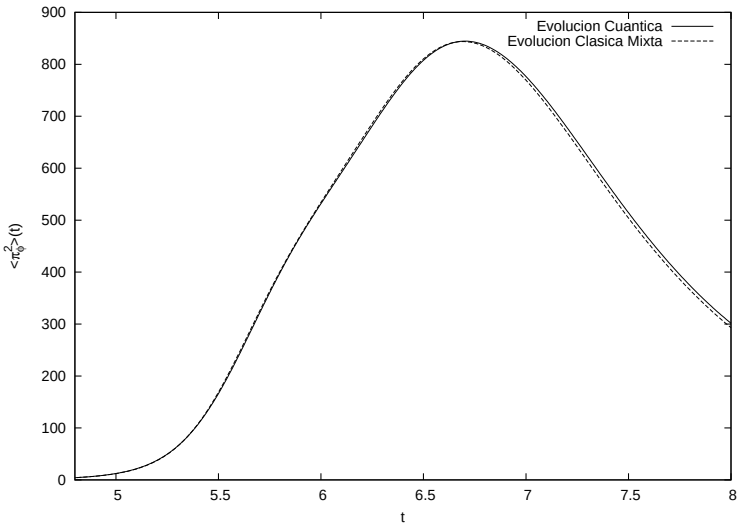

Figure 59: Quantum evolution versus mixed classical evolution of $\langle p_x^2 \rangle$

Of course, we have tweaked our system to emulate similar conditions over x as the one-dimensional case, so we expect a classical behavior for x. For y this same behavior is not expected. In fact, we have calculated the evolution of $\langle y^2 \rangle$ and we showed in Fig.60. As we can see the quantum and mixed classical evolution do not coincide.
Furthermore, it can be checked for y how the integrated part of the Wigner function $W(y, p_y)$ is not squeezed enough in the connection time. This is shown in Fig.54 where we can also observe the 2σ-contour that gives an axis ratio of about $r_s = 3.2$.

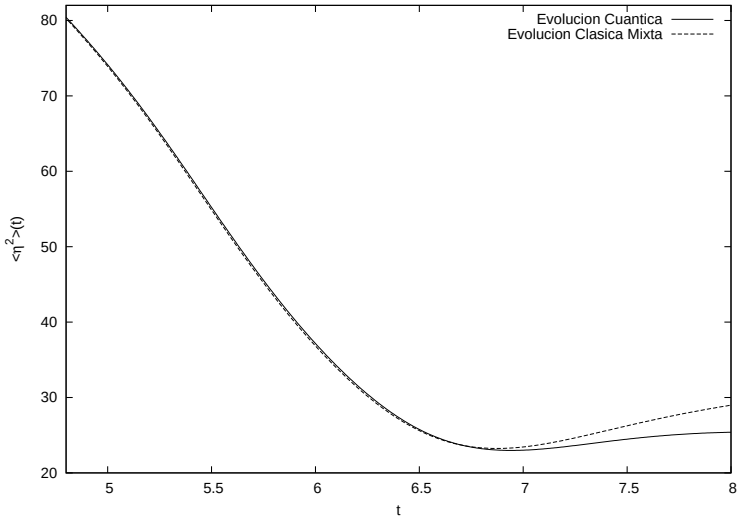

Figure 60: Quantum evolution versus mixed classical evolution of $\langle y^2 \rangle$

In summary, x seems to have become classical, as it is possible to calculate its expectation values evolution with the classical approximation, but only taking into account the negative part of the Wigner function. But it is not correct the analogy between this system and the one which has only 1 dof, where the influence of y translated into a linear dependence for $w^2(t)$. Thus, both are substantially different.

6.2.3 Back-Reaction

We are now interested in studying the influence of the *Back-Reaction* with respect to the case of 1 dof, where this did not exist. So we have to tweak the evolution of $< y^2 >$ in order to produce a mass term for x similar to the 1 dof case (once we have taken the same initial conditions for x in both cases). For that we add a negative quadratic term for y in the potential

$$V(x,y) = \frac{1}{2}\left(g^2y^2 - \mu^2\right)x^2 + \frac{\lambda}{4}x^4 - \frac{1}{2}d_0y^2 \tag{232}$$

This allows us to further reduce the difference between the terms of (224) up to roughly a 3% for the first stage $\Delta t = 1$, as it is shown in Fig.61.

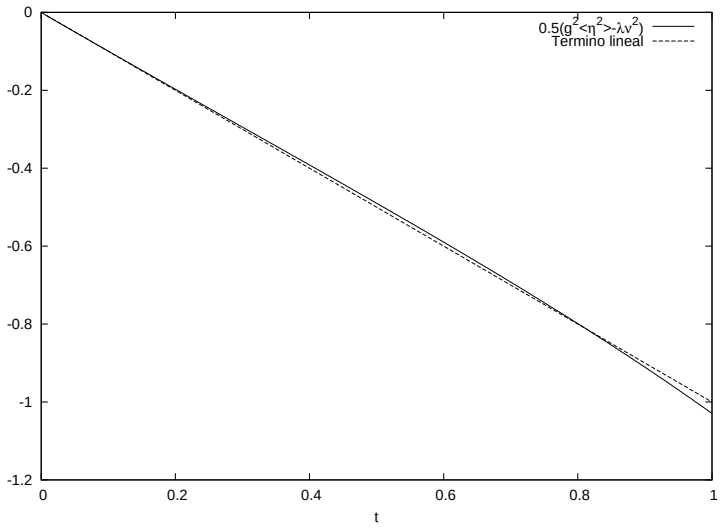

Figure 61: Evolution of $g^2 < y^2(t) > -\lambda\nu^2$ respect to the linear term for an optimal $d_0 = 0.007$

With this adjustment, there is a clear discrepancy in the first moments between the quantum evolution in our current case and the 1 dof case, due to the *back-reaction* (because the influence of y results in both cases in a similar quadratic term on x). This discrepancy is shown in Fig.62 for $< x^2 >$, that in the first stage is already larger than 50%. We have verified that for $< p_x^2 >$ is even larger.
So the *Back-Reaction* has a large influence on the evolution. This confirms again that this system, seen only from the point of view of x, is essentially different to the 1 dof case.

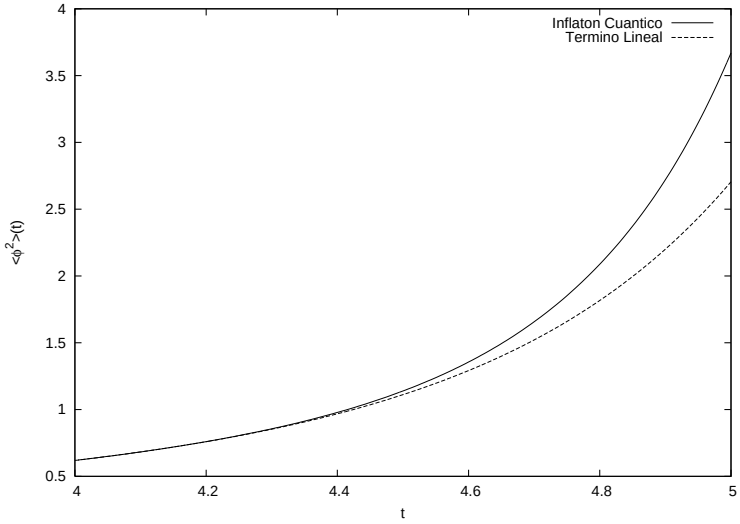

Figure 62: Evolution of $< x^2(t) >$ for the quantum inflaton case versus the linear term case

7 Time Evolution in CFT and QFT

Our main goal is to test the methods that are usually employed to calculate the approximate evolution of quantum fields. This evolution is important in different areas of the Physics. For instance, in Cosmology, the evolution of quantum fields is necessary to study several epochs in the early universe.
As we have done in the previous chapters, we can test the approximations in quantum-mechanical systems where the exact quantum evolution is available. Quantum mechanics is a particular case of QFT with the spatial dimension equal to zero, and then one can adapt the different methods to this case. However, we present the methods for the general case of QFT and after particularize it for the case of QM, as in the case of classical approximation shown before. Moreover, in a later chapter we will perform explicitly the evolution in QFT and CFT. Thus, it is appropriate to devote a chapter to give an overview of the features, about the evolution in QFT and CFT, that are useful to us.

We restrict to the case of scalar fields, not only for simplicity, but also because they are used in the description of the early universe, as in the model of hybrid inflation explained in chapter 1. However, the methods can be easily extended to study other types of fields, and this has been done by many authors. About the systems, we focus upon polynomial quartic Hamiltonians, that are widely used. In fact, in QFT for 3+1 dimensions the Hamiltonian has to be at most quartic, for the theory to be renormalizable [6].

At a classical level, a field theory is equivalent to study a system with an infinite number of degrees of freedom. At a quantum level, a similar treatment leads to ultraviolet divergences, which have to be cured through renormalization. We will discuss these aspects in this chapter.

7.1 Brief review of classical field theory

A classical system of fields has an infinite number of degrees of freedom. The Lagrangian L is now the spatial integral of the Lagrangian density $\mathcal{L}$. This Lagrangian density is a function of one or more fields and their derivatives. We consider for simplicity a single scalar real-valued field $\phi(x)$ in $d+1$

dimensions, and the action S is

$$S = \int dt\, L = \int dt \int d^d\mathbf{x}\, \mathcal{L}(\phi, \partial_\mu \phi) \tag{233}$$

The principle of least action leads to the Euler-Lagrange equation of motion for a field

$$\partial_\mu \Big(\frac{\partial \mathcal{L}}{\partial(\partial_\mu \phi)} \Big) - \frac{\partial \mathcal{L}}{\partial \phi} = 0 \tag{234}$$

In the Hamiltonian formulation one introduces the conjugate momentum $\pi(x) \equiv \partial \mathcal{L}/\partial \dot{\phi}(x)$. The Hamiltonian is obtained by the corresponding Legendre transformation

$$H = \int d^d\mathbf{x}\, [\pi(x)\dot{\phi}(x) - \mathcal{L}] \equiv \int d^d\mathbf{x}\, \mathcal{H} \tag{235}$$

where $\mathcal{H}$ is the Hamiltonian density. The Hamilton equations are

$$\dot{\phi} = \frac{\partial \mathcal{H}}{\partial \pi} \quad ; \quad \dot{\pi} = -\frac{\partial \mathcal{H}}{\partial \phi} + \partial_n \Big(\frac{\partial \mathcal{H}}{\partial(\partial_n \phi)} \Big) \tag{236}$$

where there is an implicit sum over $n = 1, 2, ..., d$.

We will restrict ourselves to the case of quartic Lagrangian densities. So we have

$$\mathcal{L}(x) = \frac{1}{2}\partial^\mu \phi(x) \partial_\mu \phi(x) - \frac{1}{2}\mu^2 \phi^2(x) - \frac{\lambda}{24}\phi^4(x) \tag{237}$$

where μ^2 may depend on time. In this case the conjugate momentum is $\pi(x) = \partial_0 \phi(x)$. The corresponding Hamiltonian takes the form

$$H = \int d^d\mathbf{x} \Big[\frac{1}{2}\pi^2(x) + \frac{1}{2}(\nabla \phi(x))^2 + \frac{1}{2}\mu^2 \phi^2(x) + \frac{\lambda}{24}\phi^4(x) \Big] \tag{238}$$

Instead of working with the fields $\phi(x)$ one can work in Fourier space. With the following Fourier transform

$$\phi(\mathbf{x}, t) = \int \frac{d^d\mathbf{k}}{(2\pi)^{d/2}} \phi(\mathbf{k}, t) \exp(i\mathbf{k} \cdot \mathbf{x}) \tag{239}$$

one obtains

$$\begin{aligned} H = & \int d^d\mathbf{k}\, \frac{1}{2} \Big[|\pi(\mathbf{k}, t)|^2 + (\mathbf{k}^2 + \mu^2) |\phi(\mathbf{k}, t)|^2 \Big] + \\ & + \frac{\lambda}{24} \frac{1}{(2\pi)^d} \int d\mathbf{k}\, d\mathbf{k}'\, d\mathbf{k}''\, \phi(\mathbf{k}, t) \phi(\mathbf{k}', t) \phi(\mathbf{k}'', t) \phi(-\mathbf{k} - \mathbf{k}' - \mathbf{k}'', t) \end{aligned} \tag{240}$$

As we have considered a real-valued field, we have $\phi(-\mathbf{k},t)=\phi^*(\mathbf{k},t)$. In this case, if one neglects the contribution of the quartic term ($\lambda=0$), then the field modes are independent and can be treated separately.

For simplicity, and to make later the comparison with QM easier, we will consider the fields as living in a box of size L^d with periodic boundary conditions. Now we have an infinite discrete set of modes labeled as $\mathbf{k}=(2\pi/L)\mathbf{j}$, where each component of $\mathbf{j}$ run over all integers. The discrete Fourier transform is

$$\phi(\mathbf{x},t)=\frac{1}{L^{d/2}}\sum_{\mathbf{k}}e^{i\mathbf{k}\cdot\mathbf{x}}\phi(\mathbf{k},t) \tag{241}$$

The Hamiltonian the Fourier space becomes

$$H=H_0+H_I=\sum_{\mathbf{k}}\left[\frac{1}{2}|\pi_{\mathbf{k}}(t)|^2+\frac{1}{2}(\mathbf{k}^2+\mu^2)|\phi_{\mathbf{k}}(t)|^2\right]+H_I \tag{242}$$

where we noted $\phi_{\mathbf{k}}(t)\equiv\phi(\mathbf{k},t)$ and the interaction Hamiltonian is

$$H_I=\frac{\lambda}{24L^d}\sum_{\mathbf{k}_1,\mathbf{k}_2,\mathbf{k}_3}\phi_{\mathbf{k}_1}(t)\phi_{\mathbf{k}_2}(t)\phi_{\mathbf{k}_3}(t)\phi_{-\mathbf{k}_1-\mathbf{k}_2-\mathbf{k}_3}(t) \tag{243}$$

7.2 Quantum Field Theory

The quantization of classical fields is performed in a similar way to the case of QM. So, in QFT, the field and its conjugate momentum have to be considered as operators. We take from now on natural units ($\hbar=c=1$), otherwise we will say it explicitly. Now, ϕ and π are operators that fulfill the following commutation relations at equal times

$$[\phi(\mathbf{x},t),\pi(\mathbf{y},t)]=i\delta^d(\mathbf{x}-\mathbf{y})\ ;\ [\phi(\mathbf{x},t),\phi(\mathbf{y},t)]=[\pi(\mathbf{x},t),\pi(\mathbf{y},t)]=0 \tag{244}$$

There exist some difficulties when one quantizes the classical Hamiltonian simply considering ϕ,π as operators and maintaining the same form. For instance, the quadratic Hamiltonian H_0 leads to an infinite vacuum energy (although this is not an observable), that can be avoided taking H_0 in normal order. Moreover, the full Hamiltonian leads to divergences in perturbation theory, that have to be cured through renormalization. We will discuss this later; for the moment, we consider the Hamiltonian (238) where ϕ and π are considered as operators.

In the Heisenberg picture, one uses the evolution operator $U(t)$ as usually

$$\phi(\mathbf{x},t) = U^\dagger(t)\phi(\mathbf{x},0)U(t) \tag{245}$$

The Heisenberg equation of motion for any operator $\mathcal{O}$ is

$$i\frac{\partial}{\partial t}\mathcal{O} = [\mathcal{O}, H] \tag{246}$$

and can be applied to ϕ or π.

In the Interaction picture, we note $\phi_0(x), \pi_0(x)$ as the operators that evolve with H_0. Then we have

$$\phi(\mathbf{x},t) = \Omega^\dagger(t)\phi_0(\mathbf{x},t)\Omega(t) \tag{247}$$

where $\Omega(t)$ is the evolution operator in the interaction picture, that satisfies the equation

$$\dot{\Omega}(t) = -i\mathbf{H_I}(t)\Omega(t) \quad ; \quad \Omega(0) = 1 \tag{248}$$

being $\mathbf{H_I}(t)$ the interaction Hamiltonian in the interaction picture. The solution is

$$\Omega(t) = \mathrm{T}\ \exp\Big[-i\int_0^t ds\, \mathbf{H_I}(s)\Big] \tag{249}$$

7.3 Free theory

The free field theory corresponds to fields with the quadratic Hamiltonian H_0. In position space this Hamiltonian corresponds to (238) but taking $\lambda = 0$. Both the classical Euler-Lagrange equation and the quantum Heisenberg equation lead to the same equation of motion, the Klein-Gordon equation

$$(\partial_t^2 - \nabla^2 + \mu^2)\phi_0 = 0 \tag{250}$$

where, as mentioned, μ^2 generally depends on t. In Fourier space, as can be seen from (242), the Fourier modes can be treated as independent harmonic oscillators. Therefore, we can deal separately with each one of them and calculate the evolution of a generic mode $\mathbf{k}$. So the equation of motion is

$$\ddot{\phi}_{0,\mathbf{k}}(t) + w_k^2(t)\phi_{0,\mathbf{k}}(t) = 0 \tag{251}$$

where we have defined $w_{\mathbf{k}}^2(t) \equiv k^2 + \mu^2(t)$ ($k \equiv |\mathbf{k}|$). We solve this equation in a similar way to the case of Quantum Mechanics. Let us remember the functions $f_i(t), g_i(t)$, here we define similar real valued functions

$$\begin{aligned} & f_k(t) = f_{k,1}(t) + i f_{k,2}(t) \quad ; \quad g_k(t) = i\dot{f}_k(t) \\ & \ddot{f}_k + w_k^2(t) f_k = 0 \\ & f_{k,1}(0) = \frac{1}{\sqrt{2w_k}} \quad ; \quad f_{k,2}(0) = 0 \\ & g_{k,1}(0) = \sqrt{\frac{w_k}{2}} \quad ; \quad g_{k,2}(0) = 0 \end{aligned} \tag{252}$$

where $w_k \equiv w_k(t=0)$. With these functions we have

$$\begin{aligned} \phi_{0,\mathbf{k}}(t) &= \sqrt{2w_k} f_{k,1}(t)\phi_{0,\mathbf{k}}(0) - \sqrt{\frac{2}{w_k}} f_{k,2}(t)\pi_{0,\mathbf{k}}(0) \\ \pi_{0,\mathbf{k}}(t) &= \sqrt{2w_k} g_{k,2}(t)\phi_{0,\mathbf{k}}(0) + \sqrt{\frac{2}{w_k}} g_{k,1}(t)\pi_{0,\mathbf{k}}(0) \end{aligned} \tag{253}$$

7.3.1 Initial Gaussian state

We consider initially a general gaussian state, where each mode has a Wigner function $W_{\mathbf{k}}(\phi_{\mathbf{k}}, \pi_{\mathbf{k}})$ in which $\phi_{\mathbf{k}}$ and $\pi_{\mathbf{k}}$ are independent gaussian random variables with widths $\sigma_{k,\phi}$ and $\sigma_{k,\pi}$. This state can be parametrized using two independent parameters w'_k, n_k in the following form

$$\begin{aligned} & \langle \phi_{0,\mathbf{k}}(0) \rangle = 0 \quad ; \quad \langle \pi_{0,\mathbf{k}}(0) \rangle = 0 \\ & \langle \phi_{0,\mathbf{k}}(0)\phi_{0,\mathbf{k}'}(0) \rangle = \frac{1}{w'_k}\Big(n_k + \frac{1}{2}\Big)\delta_{\mathbf{k},-\mathbf{k}'} \\ & \langle \pi_{0,\mathbf{k}}(0)\pi_{0,\mathbf{k}'}(0) \rangle = w'_k\Big(n_k + \frac{1}{2}\Big)\delta_{\mathbf{k},-\mathbf{k}'} \\ & \langle \phi_{0,\mathbf{k}}(0)\pi_{0,\mathbf{k}'}(0) \rangle = \frac{i}{2}\delta_{\mathbf{k},-\mathbf{k}'} \end{aligned} \tag{254}$$

Clearly, n_k represents the mean number of particles. However, this state is only eigenstate of the Hamiltonian H_0 for $w'_k = w_k$ and $n_k = 0$ $\forall k$. In this case we are in the ground state.
These initial values can be reproduced by the following gaussian Wigner function for each mode

$$W(\phi, \pi, t=0) \propto \exp\Big[- \frac{w_k'^2 \phi_{0,-\mathbf{k}}(0)\phi_{0,\mathbf{k}}(0) + \pi_{0,-\mathbf{k}}(0)\pi_{0,\mathbf{k}}(0)}{2w'_k(n_k + 1/2)} \Big] \tag{255}$$

With the chosen initial state, from (253), one can derive the two-point functions

$$\langle\phi_{0,\mathbf{k}}(t)\phi_{0,\mathbf{k}'}(t')\rangle = 2\Big(n_k+\frac{1}{2}\Big)\Big(\frac{w_k}{w_k'}f_{k,1}(t)f_{k,1}(t')+\frac{w_k'}{w_k}f_{k,2}(t)f_{k,2}(t')\Big)\delta_{\mathbf{k},-\mathbf{k}'}+$$
$$+\,i(f_{k,2}(t)f_{k,1}(t')-f_{k,1}(t)f_{k,2}(t'))\delta_{\mathbf{k},-\mathbf{k}'}\equiv[G_{k,S}(t,t')+iG_{k,A}(t,t')]\delta_{\mathbf{k},-\mathbf{k}'} \tag{256}$$

where we have defined the propagators $G_{k,S}, G_{k,A}$ in a similar way to QM. From (253), is clear that $f_k = f_{-k}$ and $g_k = g_{-k}$, therefore $G_{k,S} = G_{-k,S}$ and $G_{k,A} = G_{-k,A}$ (because n_k only depends on $|\mathbf{k}|$). Thus, we have the following symmetry properties (like in QM)

$$\begin{aligned} G_{k,S}(t,t') &= G_{k,S}(t',t) \\ G_{k,A}(t,t') &= -G_{k,A}(t',t) \end{aligned} \tag{257}$$

For the sake of completeness, we write the Wigner function that corresponds to an eigenstate of $H_0(\mathbf{k})$

$$W_{\mathbf{k},n_k}(\phi,\pi,t=0)\propto\exp\Big[-\frac{2H_0(\mathbf{k})}{w_k}\Big]L_{n_k}(4H_0(\mathbf{k})/w_k) \tag{258}$$

where $H_0(\mathbf{k})$ is the term of H_0 that depends on $\mathbf{k}$, and L_{n_k} is the n_kth Laguerre polynomial.

We consider a particular case widely used, that correspond to taking the initial state as a thermal state. In this case, from (254), this state is an equilibrium state of a Hamiltonian $H_0'(\mathbf{k})$ with the form

$$H_0'(\mathbf{k}) = \frac{1}{2}(|\pi_{\mathbf{k}}|^2 + w_k'^2|\phi_{\mathbf{k}}|^2) \tag{259}$$

where $w_k'^2 = k^2 + \mu'^2$. If the state has a temperature T_k, then n_k take the following form

$$n_k = \frac{1}{2}\Big(1-\frac{1}{\tanh(w_k'\beta_k/2)}\Big) \tag{260}$$

where $\beta_k = 1/(\kappa T_k)$ (κ is the Boltzmann constant). This can easily be derived from the expression of the Wigner function for a thermal state, which can be consulted in Ref. [66]. Thus, for $k\to\infty$ we have that n_k tends exponentially to zero.

7.3.2 Time-independent potential

Most Hamiltonians frequently used in QFT do not depend on time, and we are going to show this case explicitly. If $w_k(t) = w_k = constant$ then we find

$$f_{k,1}(t) = \frac{1}{\sqrt{2w_k}}\cos(w_k t) \quad ; \quad f_{k,2}(t) = -\frac{1}{\sqrt{2w_k}}\sin(w_k t)$$
$$g_{k,1}(t) = \sqrt{\frac{w_k}{2}}\cos(w_k t) \quad ; \quad g_{k,2}(t) = -\sqrt{\frac{w_k}{2}}\sin(w_k t) \tag{261}$$

and from (256) we obtain

$$G_{k,S}(t,t') = \Big(n_k + \frac{1}{2}\Big)\Big[\frac{1}{w'_k}\cos(w_k t)\cos(w_k t') + \frac{w'_k}{w_k^2}\sin(w_k t)\sin(w_k t')\Big]$$
$$G_{k,A}(t,t') = -\frac{1}{2w_k}\sin(w_k(t-t')) \tag{262}$$

If we take a similar Hamiltonian but with the coefficient of quadratic term less than zero, then we would have $w_k^2 = |k^2 - \mu^2|$. For a mode $\mathbf{k}$ with $k^2 < \mu^2$, one has to replace in the last expressions $\sin, \cos$ by $\sinh, \cosh$.

As a particular case, we consider that the initial state correspond with the equilibrium thermal state of Hamiltonian H_0, i.e., $w'_k = w_k$, which is a stationary state. One gets

$$G_{k,S}(t,t') = \frac{1}{w_k}\Big(n_k + \frac{1}{2}\Big)\cos(w_k(t-t'))$$
$$G_{k,A}(t,t') = -\frac{1}{2w_k}\sin(w_k(t-t')) \tag{263}$$

In this case, $G_{k,S}(t,t)$ is time-independent, as corresponds with a stationary state.

7.4 Wigner functional for Fields

We are going to show for QFT a similar formalism than the one used for QM with the Wigner function. This will be a formal description. We will follow the same steps as [70]. In this section we will recover the $\hbar$ factors, because this will be convenient for a future chapter. Consider a scalar real-valued quantum field with the following Lagrangian density

$$\mathcal{L}(x,t) = \frac{1}{2}\partial^\mu\phi(x,t)\partial_\mu\phi(x,t) - \frac{1}{2}m^2\phi^2(x,t) - \frac{\lambda}{24}\phi^4(x,t) \tag{264}$$

Let us remember the definition for the Wigner function in the QM case for a general mixed state

$$W(\mathbf{x},\mathbf{p},t) \equiv \frac{1}{\pi^d}\int d^d y e^{2i\mathbf{p}\cdot\mathbf{y}/\hbar}\langle \mathbf{x}+\mathbf{y}|\rho(t)|\mathbf{x}-\mathbf{y}\rangle \tag{265}$$

where $\rho(t)$ is the density operator. In analogy with this, the Wigner functional is defined for QFT in this manner

$$W(\phi,\pi,t) \equiv \int \mathcal{D}\phi' \, \exp\Big\{\frac{2i}{\hbar}\int dx\, \pi(x)\phi'(x)\Big\}\langle \phi+\phi'|\rho(t)|\phi-\phi'\rangle \tag{266}$$

With this functional we can calculate directly the Weyl-ordered expectation values [70]. So, if we have an expectation value of the form

$$\langle \phi^n \pi^n\rangle = \frac{1}{Z} Tr[\rho(t)\phi^n\pi^n] \quad ; \quad Z = Tr[\rho(t)] \tag{267}$$

then the corresponding Weyl-ordered expectation value ($\langle ...\rangle_W$) is obtained

$$\langle \phi^n \pi^n\rangle_W = \frac{1}{2\pi Z}\int \mathcal{D}\phi\, \mathcal{D}\pi\, \phi^n\pi^m W(\phi,\pi,t) \tag{268}$$

7.4.1 Evolution equation

From the motion equation for the density operator

$$i\hbar\frac{\partial\rho(t)}{\partial t} = [H,\rho(t)] \tag{269}$$

the evolution equation for $W(\phi,\pi,t)$ can be obtained

$$\frac{\partial W}{\partial t} = \int dx\Big[-\pi(x)\frac{\delta W}{\delta\phi(x)} + \big(m^2\phi(x) - \nabla^2\phi(x) + \frac{\lambda}{6}\phi^3(x)\big)\frac{\delta W}{\delta\pi(x)} - \frac{\hbar^2\lambda}{24}\phi(x)\frac{\delta^3 W}{\delta\pi^3(x)}\Big] \tag{270}$$

It is similar to the QM case. If we ignore the $\hbar^2$ term, then (270) can be written as the classical Liouville equation for functionals

$$\frac{\partial W}{\partial t} = \int dx\Big[\frac{\delta H}{\delta\pi(x)}\frac{\delta W}{\delta\phi(x)} - \frac{\delta H}{\delta\phi(x)}\frac{\delta W}{\delta\pi(x)}\Big] \tag{271}$$

7.5 Perturbative expansion for QFT

The traditional formalism of Quantum Field Theory is done in perturbation theory. One can consult any textbook on the subject [6][7]. For illustrative purposes and for comparison with the quantum mechanical case we will give below the explicit calculation of several observables for the theory with Lagrangian (237) in 1+1 space-time dimensions. We will work in Fourier space. In the interaction picture we have

$$\phi_k(t) = \Omega^\dagger(t)\phi_{0,k}(t)\Omega(t) \tag{272}$$

This operator satisfies the differential equation

$$\begin{aligned} &\dot{\Omega}(t) = -i\mathbf{H_I}(t)\Omega(t) \\ &\Omega(0) = 1 \end{aligned} \tag{273}$$

where $\mathbf{H_I}$ is the interaction Hamiltonian in the interaction picture. The solution is

$$\Omega(t) = T\exp\Big[-i\int_0^t ds\mathbf{H_I}(s)\Big] \tag{274}$$

and from (243) we have

$$\mathbf{H_I}(s) = \frac{\lambda}{24L}\sum_{k_1,k_2,k_3}\phi_{0,k_1}(s)\phi_{0,k_2}(s)\phi_{0,k_3}(s)\phi_{0,-k_1-k_2-k_3}(s) \tag{275}$$

Thus, as the initial state is gaussian, we can calculate $\langle|\phi_k(t)|^n\rangle$ in a similar way to QM using Wick's theorem. The rules to build the diagrams are the same that in QM but now we have summations over all modes. We are going to give an example with two-point functions:

$$\begin{aligned} &\langle|\phi_k(t)|^2\rangle = \langle \mathrm{T'}\exp\Big[i\int_0^t ds\mathcal{H}_I(s)\Big]\phi_{0,k}(t)\phi_{0,-k}(t)\mathrm{T}\exp\Big[-i\int_0^t ds\mathcal{H}_I(s)\Big]\rangle = \\ &= G_{k,S}(t,t) + \frac{\lambda}{12L}\int_0^t dsIm\Big[\sum_{i,j,l}\langle\phi_{0,k}(t)\phi_{0,-k}(t)\phi_{0,i}(s)\phi_{0,j}(s)\phi_{0,l}(s)\phi_{0,-i-j-l}(s)\rangle\Big] + O(\lambda^2) = \\ &= D_0 + D_1(vacuum) + \frac{2\lambda}{L}\int_0^t dsG_{k,S}(t,s)G_{k,A}(t,s)\sum_i G_{i,S}(s,s) + O(\lambda^2) \end{aligned} \tag{276}$$

where i, j, l run over all modes (they are not integers). We neglect vacuum diagrams for the same reason as in (149). The order 1 diagram has the same factor and shape as for QM, but there appears a new sum over all modes in the tadpole

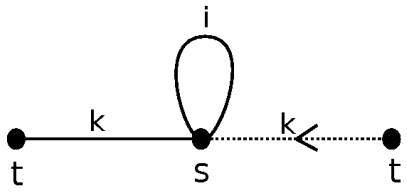

This sum is divergent, as we will see. In general, from (256) we have

$$\sum_i G_{i,S}(s,s) = \sum_i 2\Big(n_i + \frac{1}{2}\Big)\Big[\frac{w_i}{w_i'} f_{i,1}^2(s) + \frac{w_i'}{w_i} f_{i,2}^2(s)\Big] \tag{277}$$

The tadpole is divergent for non-zero spatial dimension. As we said, the following orders contain the same diagrams that in QM with equal factors. The summations over all modes can cause divergences, according to the considered dimension of space-time.

As a particular case, we will analyze a system with any time-independent potential. This will be useful later. We obtain from (262)

$$\begin{aligned}\sum_i G_{i,S}(s,s) = \sum_i \frac{1}{2}\Big\{\Big(n_i + \frac{1}{2}\Big)\Big[\frac{1}{w_i'} + \frac{w_i'}{w_i^2}\Big] + \\ + \frac{1}{2}\Big(n_i + \frac{1}{2}\Big)\Big[\frac{1}{w_i'} - \frac{w_i'}{w_i^2}\Big]\cos(2w_i t) Big\}\end{aligned} \tag{278}$$

A priori, the second term of the right hand side is convergent (because $\sum_n \cos(an)/n$ is convergent), but this depends of n_k. If n_k does not increases with k from a certain value k_0, then the mentioned second term is convergent. This will happen in all cases that we will consider. For instance, this happens in the case of a thermal state that we explained above, where n_k tends exponentially to zero as k grows. About the first term, it is divergent for any value of n_i (even when $n_i = 0 \ \ \forall i$). In any other sub-diagram that involves

one internal vertex s and its neighbors s_1, s_2, s_3, s_4 we can have independent sums of the types

$$\sum_{i,j,l} G_i(s,s_1)G_j(s,s_2)G_l(s,s_3)G_{i+j+l}(s,s_4)$$
$$\sum_{i,j} G_i(s,s_1)G_j(s,s_2)G_{i+j+q}(s,s_3)$$
$$\sum_{i} G_i(s,s_1)G_{i+q}(s,s_2) \tag{279}$$

where q is fixed and G_i can be $G_{i,S}$ or $G_{i,A}$. In these sums, the number of factors $1/w_m$ (with m any running mode) is always greater than the number of summation indices, therefore they are convergent.
For example, the following two-order diagram

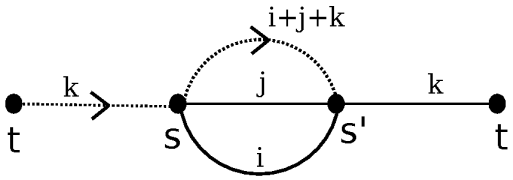

represents the contribution

$$-4\int_0^t ds\int_0^s ds' G_{k,A}(t,s)G_{k,S}(t,s)\sum_{i,j}\frac{1}{w_i}\frac{1}{w_j}\frac{1}{2w_{i+j+k}}\Big(n_i+\frac{1}{2}\Big)\Big(n_j+\frac{1}{2}\Big)$$
$$\cos(w_i(s-s'))\cos(w_j(s-s'))\sin(w_{i+j+k}(s-s')) \tag{280}$$

Here we have three factors $1/w_m$ with $m = i, j, i+j+k$ and two summation indices i, j, consequently the result is convergent.
Thus, we have seen that the only divergent sub-diagrams are the tadpoles. This is not true for 3+1 dimensions, where there are other diagrams that generate divergences.

Return now to the general case of time-dependent potentials. A priori, the expression (277) can be divergent or not, depending of the behavior with too large values of k. But, if one recalls the evolution equation (276) for f_k, is clear that when k is too large then the equation correspond to the case

of time independent potential, because $w_k(t) \approx k$ when k has an enormous value. Thus, the divergence in this case is the same that we shown in (278) for time-independent potentials. Therefore, the previous discussion is valid for this case and the only divergent subdiagram is the tadpole.

7.6 Lattice regularization of QFT

In QFT, as we have seen, one has to deal with divergent quantities. This is done by regularizing the system in order to eliminate the divergences, and after taking the limit of the cut-off going to infinity with a suitable dependence of the bare parameters on the cut-off. This last procedure is called Renormalization. This is usually described in the framework of perturbation theory, where the renormalization of the parameters eliminates the divergences to all perturbative orders. Nevertheless, this is not adequate when studding non-perturbative phenomena. One of the most successful procedures to define and renormalize a quantum field theory at a non-perturbative level, is the Lattice approach. This consists in discretizing space-time and replacing it by a space-time lattice. The role of the cut-off is played by the inverse lattice spacing (a). After, one has to take the continuum limit ($a \to 0$) with a suitable dependence of the bare parameters. We will discuss about this in the present section. Again, to illustrate the discussion, we will take the case of the fields in 1+1 space-time dimensions.

We have a system with the following Hamiltonian

$$H = \int dx \Big[\frac{1}{2}\pi^2(x,t) + \frac{1}{2}(\nabla\phi(x,t))^2 + \frac{1}{2}\mu^2\phi^2(x,t) + \frac{\lambda}{24}\phi^4(x,t)\Big] \qquad (281)$$

In natural units, the field ϕ and his conjugate momentum π have the following dimensions

$$[\phi(x,t)] = dimensionless \quad ; \quad [\pi(x,t)] = [t^{-1}] = [l^{-1}] \qquad (282)$$

We get a discrete space considering the fields in a lattice with L volume and a lattice spacing. We have $N = L/a$ sites in the spatial direction, so that we label $x_n = na$ for $n = 0, 1, ..., N-1$ and we note $\phi_n(t) \equiv \phi(na,t)$, $\pi_n(t) \equiv \pi(na,t)$. We choose periodic boundary conditions in the lattice. The Hamiltonian is now

$$H = \sum_{n=0}^{N-1} a\Big[\frac{1}{2}\pi_n^2 + \frac{1}{2}(\nabla\phi_n)^2 + \frac{1}{2}\mu^2\phi_n^2 + \frac{\lambda}{24}\phi_n^4\Big] \qquad (283)$$

As usual, we label field modes with $k = (2\pi/L)j$ for $j = -N/2+1, -N/2+2, ..., N/2$ and write the discrete Fourier transform

$$\phi_k(t) = \frac{\sqrt{L}}{N} \sum_{n=0}^{N-1} e^{-i\frac{2\pi}{N}nj} \phi_n \tag{284}$$

where clearly $\phi_k(t) \equiv \phi((2\pi/L)j, t)$ and similarly for π_k. As $\phi(x)$ is real, we have $\phi_k^*(t) = \phi_{-k}(t)$ and equal for π_k. We have the following dimensions

$$[\phi_k(t)] = [\sqrt{a}] = [\sqrt{l}] \quad ; \quad [\pi_k(t)] = [1/\sqrt{a}] = [1/\sqrt{l}] \tag{285}$$

The inverse Fourier transform is

$$\phi_n(t) = \frac{1}{\sqrt{L}} \sum_{j=-N/2+1}^{N/2} e^{i\frac{2\pi}{N}nj} \phi_k \tag{286}$$

Therefore, if we transform the Hamiltonian then we get

$$H = H_0 + H_I = \sum_{j=-N/2+1}^{N/2} \Big[\frac{1}{2}|\pi_k|^2 + \frac{1}{2}(c_k^2 + \mu^2)|\phi_k|^2\Big] + H_I \tag{287}$$

where $c_k \equiv 2\sin(ka/2)/a = 2\sin((\pi/L)ja)/a$ and the interaction Hamiltonian is

$$H_I = \frac{\lambda}{24L} \sum_{j_1,j_2,j_3=-N/2+1}^{N/2} \phi_{k_1}\phi_{k_2}\phi_{k_3}\phi_{-k_1-k_2-k_3} \tag{288}$$

with $k_i = (2\pi/L)j_i$. From now on we denote $w_k^2(t) \equiv c_k^2 + \mu^2(t)$ and $w_k \equiv w_k(t=0)$.

A useful quantity is the two point function in position space. We write its expression in terms of the modes

$$\int dx\, \langle\phi(x,t)\phi(x+y,t)\rangle \to \sum_{n=0}^{N-1} a\langle\phi_n(t)\phi_{n+m}(t)\rangle = \sum_k e^{ikma}\langle|\phi_k(t)|^2\rangle \tag{289}$$

7.6.1 Renormalization

We start with the case of time-independent potential. Now we have a finite number of modes, and if we recover the expression of the first order in the perturbative expansion then we get

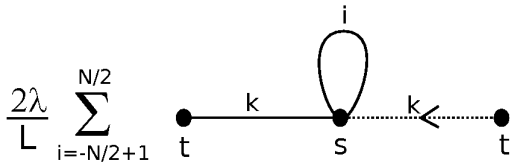

When the lattice spacing tends to zero ($N \to \infty$), this summation over i gives

$$\sum_i G_{i,S}(s,s) = \sum_i \frac{1}{2}\Big(n_i + \frac{1}{2}\Big)\Big[\frac{1}{w_i'} + \frac{w_i'}{w_i}\Big] + (\text{convergent}) \xrightarrow{N\to\infty} \frac{L}{2\pi} ln\Big(\frac{2\pi}{a\mu}\Big) \tag{290}$$

and the tadpole has a logarithmic divergence for $N \to \infty$ ($a \to 0$) even when $n_i = 0 \ \ \forall i$.
As is well known, in $1+1$ dimensions we only have to renormalize the mass parameter μ. We replace

$$\mu^2 = m^2 + \delta m \tag{291}$$

where m is the renormalized mass and δm is the counterterm. We will calculate this counterterm and prove that all tadpoles are eliminated. In general we would write $\delta m = b_1\lambda + b_2\lambda^2 + ...$ but in this case it is enough with the first term. So, we get $\delta m = b\lambda$ and we can consider that the free Hamiltonian is the same as before replacing $\mu^2 \to m^2$, thus we have a new interaction Hamiltonian $H_I + \delta H_I$ with

$$\delta H_I = \frac{1}{2}\delta m \sum_k |\phi_k|^2 \tag{292}$$

Now we have two types of interaction vertices

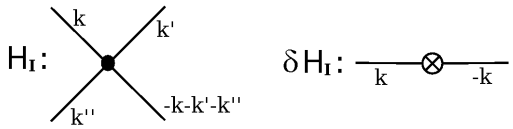

If $\delta m = b\lambda$ then it is enough to calculate the first perturbative order to obtain δm. After, we will prove that the result is valid for the remaining orders. It is convenient to define $[\langle ...\rangle ...\langle ...\rangle]_{\bar{v}}$ ($\bar{v} \equiv$ *not vacuum diagrams are considered*) as the application of Wick's theorem over all expectation values to obtain the corresponding diagrams but ruling out the vacuum diagrams. With this, the first order is

$$\langle|\phi_k|^2\rangle_1 = 2\int_0^t dsIm\Big\{\frac{\lambda}{24L}\sum_{i,j,l}\langle\phi_{0,k}(t)\phi_{0,-k}(t)\phi_{0,i}(s)\phi_{0,j}(s)\phi_{0,l}(s)\phi_{0,-i-j-l}(s)\rangle +$$
$$+\frac{\delta m}{2}\sum_j\langle\phi_{0,k}(t)\phi_{0,-k}(t)\phi_{0,j}(s)\phi_{0,-j}(s)\rangle\Big\} = \{D_1 + D_2 + ...\}(vacuum) +$$
$$+\int_0^t dsIm\Big\{\frac{6\lambda}{24L}[\sum_i\langle\phi_{0,i}(s)\phi_{0,-i}(s)\rangle\sum_j\langle\phi_{0,k}(t)\phi_{0,-k}(t)\phi_{0,j}(s)\phi_{0,-j}(s)\rangle]_{\bar{v}} +$$
$$+\frac{\delta m}{2}[\sum_j\langle\phi_{0,k}(t)\phi_{0,-k}(t)\phi_{0,j}(s)\phi_{0,-j}(s)\rangle]_{\bar{v}}\Big\} \tag{293}$$

Thus, in order to eliminate the tadpole divergence, we have to subtract the part of $(\lambda/(2L))\sum_i\langle\phi_{0,i}(s)\phi_{0,-i}(s)\rangle$ that becomes divergent when $N \to \infty$. Therefore we get

$$\delta m = -\frac{\lambda}{2L}\sum_i\frac{1}{2}\Big(n_i + \frac{1}{2}\Big)\Big[\frac{1}{w_i'} + \frac{w_i'}{w_i^2}\Big] \tag{294}$$

Here we have considered that n_k does not increases indefinitely as k grows, and then the last term in (278) is convergent. Actually, as we said above, the divergence depends of the behavior for very large values of k, where one can take $w_k \approx w_k' \approx k$. Thus, the counterterm can be chosen as

$$\delta m = -\frac{\lambda}{2L}\sum_i\Big(n_i + \frac{1}{2}\Big)\frac{1}{k_i} \tag{295}$$

where $k_i = (2\pi/L)i$. This expression depend on the initial state through n_k. However, in the mentioned cases in which n_k is bounded above, one can eliminate n_k of the counterterm δm, and then we would not have any dependence on the initial state. This last choice corresponds to taking the Hamiltonian in normal order.

Let us see that the tadpoles are eliminated to all orders. We consider the following expression

$$\begin{aligned}\langle|\phi_k|^2\rangle_N &= \int ...ds_n...ds_N \sum_{...,i,j,l,...} \langle...\phi_{0,i}(s_n)\phi_{0,j}(s_n)\phi_{0,l}(s_n)\phi_{0,-i-j-l}(s_n)...\rangle = \\ &= 6\int ...ds_n...ds_N \sum_{...,i,j,...} \langle\phi_{0,i}(s_n)\phi_{0,-i}(s_n)\rangle[\langle...\phi_{0,j}(s_n)\phi_{0,-j}(s_n)...\rangle]_{\bar{v}} + ...\end{aligned} \tag{296}$$

therefore we have the equivalence

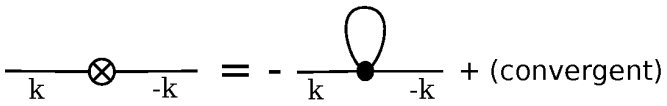

From (293) one can see that where there is a tadpole one can place a new cross-vertex, and vice versa. For other sub-diagrams one cannot do this. Moreover, when we include δH_I in the T-exp (274) is clear that if we have a diagram with n tadpoles, then there will be many other diagrams with new cross-vertices located in those positions over all possible combinations. When the number of cross-vertices is odd then the global sign is different from the initial diagram without cross-vertices. This means that the global contribution, coming from the cross-vertices and the divergent part of the tadpoles, has the following factor

$$\binom{n}{0} - \binom{n}{1} + \binom{n}{2} - \binom{n}{3} + ... + (-1)^n\binom{n}{n} = (1-1)^n = 0 \tag{297}$$

and indeed the counterterm (294) eliminates all divergent parts of the tadpoles. Of course, a priori, there remains the convergent contributions of the tadpoles.

7.7 Perturbative expansion in CFT

From Hamiltonian (287) and following the same arguments that in (152)-(160), we can do the perturbative expansion for Classical Field Theory. The classical equation of motion are

$$\ddot{\phi}_k(t) + w_k^2(t)\phi_k(t) = -\frac{4\lambda}{24L}\sum_{i,j}\phi_i(t)\phi_j(t)\phi_{-i-j-k}(t)$$
$$\pi_k(t) = \dot{\phi}_k(t) \tag{298}$$

and we expand in λ

$$\phi_k(t) = \phi_{0,k}(t) + \lambda\phi_{1,k}(t) + \lambda^2\phi_{2,k}(t) + ... \tag{299}$$

(similarly for π_k). Choosing the initial conditions for any order like in (154) we obtain

$$\ddot{\phi}_{n,k}(t) + w_k^2(t)\phi_{n,k}(t) = \eta_{n,k}(t)$$
$$\eta_{n,k}(t) = -\frac{4}{24L}\sum_{i,j}(\phi_i(t)\phi_j(t)\phi_{-i-j-k}(t))_{n-1} \tag{300}$$

where $(...)_{n-1}$ means all possible three-field products that lead to order λ^{n-1}, like in (155). The first values are

$$\eta_{0,k}(t) = 0$$
$$\eta_{1,k}(t) = -\frac{4}{24L}\sum_{i,j}\phi_{0,i}(t)\phi_{0,j}(t)\phi_{0,-i-j-k}(t)$$
$$\eta_{2,k}(t) = -\frac{4}{24L}3\sum_{i,j}\phi_{1,i}(t)\phi_{0,j}(t)\phi_{0,-i-j-k}(t)$$
$$\eta_{3,k}(t) = -\frac{4}{24L}\sum_{i,j}(3\phi_{1,i}(t)\phi_{1,j}(t)\phi_{0,-i-j-k}(t) + 3\phi_{2,i}(t)\phi_{0,j}(t)\phi_{0,-i-j-k}(t))$$
$$..... \tag{301}$$

The zero order evolution agrees with the QFT case shown in (253). The initial conditions are the same as in (254) with the gaussian distribution (255). Therefore, the solution of (298) to any order involves the same functions f_k, g_k that we have seen in QFT and we find

$$\phi_{n,k}(t) = -2\int_0^t dsG_{k,A}(t,s)\eta_{n,k}(s) \tag{302}$$

This leads to the same branches as in (160) but now we have summations over all modes. For example the first and second orders are

$$\phi_{1,k}(t) = \frac{8}{24L}\int_0^t dsG_{k,A}(t,s)\sum_{i,j}\phi_{0,i}(s)\phi_{0,j}(s)\phi_{0,-i-j-k}(s)$$

$$\phi_{2,k}(t) = \frac{8^2}{24^2L^2}3\int_0^t ds\int_0^s ds' G_{k,A}(t,s)\sum_{i,j,l,m}\phi_{0,j}(s)\phi_{0,-i-j-k}(s)G_{i,A}(s,s')$$

$$\phi_{0,l}(s')\phi_{0,m}(s')\phi_{0,-l-m-i}(s') \tag{303}$$

Hence, the branches and the factors are the same as in CM (with $\lambda \to \lambda/L$), and there appear sums over running modes. The sum of the modes in each internal vertex has to be equal to zero. When we build diagrams with this branches we can only connect loose legs with solid lines, because the zero order two-point function is

$$\langle\phi_{0,k}(t)\phi_{0,k'}(t')\rangle = 2\Big(n_k+\frac{1}{2}\Big)\Big[\frac{w_k}{w'_k}f_{k,1}(t)f_{k',1}(t') + \frac{w'_k}{w_k}f_{k,2}(t)f_{k',2}(t'))\Big]\delta_{k,-k'} =$$

$$= G_{k,S}(t,t')\delta_{k,-k'} \tag{304}$$

and then, for any diagram, the number of dashed lines is equal to the order of the diagram.

Thus, for CFT we have the *C1 Rules* with the corresponding mode sums. The perturbative expansion involve the minimal diagrams of QFT case, and we can renormalize the tadpole divergences in the same way.

7.8 Path integral and generating functionals

We will show a brief review about the formalism with functional integrals [6]. Consider a Hamiltonian H for a scalar field theory in d space-time dimensions, the n-point correlation function is defined as

$$\langle\Omega|T\{\phi(x_1).....\phi(x_n)\}|\Omega\rangle \tag{305}$$

where $|\Omega\rangle$ is the vacuum state of H, and T is the time ordering operator. The fields are operators in the Heisenberg picture. These functions can be obtained through the formalism of the *path integral*. If $S(\phi)$ represents the

action, the path integral Z is the following functional

$$Z = \int D\phi \, e^{\frac{i}{\hbar}S(\phi)} \tag{306}$$

From Z, one can obtain the n-point functions

$$\langle \Omega | T\{\phi(x_1).....\phi(x_n)\}|\Omega\rangle = \frac{1}{Z}\int D\phi \, \phi(x_1).....\phi(x_n) e^{\frac{i}{\hbar}S(\phi)} \tag{307}$$

where the fields in the right hand side are functions. In the free theory, we can express any n-point function in terms of two-point functions (Wick's theorem). We note the free two point function as usually $\langle 0|T\{\phi_H(x_1)\phi_H(x_2)\}|0\rangle \equiv D_F(x_1 - x_2)$, where $|0\rangle$ is the vacuum of the free Hamiltonian. Then, one can expands the interaction part in the exponential appearing in (307) in order to express any n-point function in terms of products of free two-point functions. Thus, we can derive the Feynman rules to express any n-point function as a sum of diagrams whose lines represent the free propagator D_F.

A similar approach can be done for any state different to $|\Omega\rangle$ using the Schwinger-Keldysh formalism [15] [16] [17]. This involves a different integration path for the action $S(\phi)$. Thus, we can maintain the formal expressions considering this path when it be necessary. This is also valid for the rest of this chapter. We will apply this formalism in the following chapter to define the 2PI effective action.

Generating functional of correlation functions

One can introduce a more formal method to calculate correlation functions. The generating functional of the correlation functions $Z(J)$ is defined as

$$Z(J) \equiv \int D\phi \, e^{\frac{i}{\hbar}\{S(\phi) + \int d^dx \, J(x)\phi(x)\}} \tag{308}$$

where we have added in the exponent a source term $J(x)\phi(x)$. Clearly, we can obtain the correlation functions by variations of this functional with respect to $J(x)$

$$\langle \Omega | T\{\phi(x_1).....\phi(x_n)\}|\Omega\rangle = \Big[\frac{1}{Z(J)}(-i\hbar)^n \frac{\delta^n Z(J)}{\delta J(x_1).....\delta J(x_n)}\Big]_{J=0} \tag{309}$$

Generating functional of connected diagrams

The above formalism allow us to calculate any n-point correlation function as the contribution of an infinite number of diagrams. These diagrams can or cannot be connected. A connected n-point function is defined as the contribution of all connected diagrams. One can also construct a generating functional that give us these connected correlation functions in a similar way to (309). This functional $W(J)$ is defined from $Z(J)$ in the following form [6] [7]

$$Z(J) = e^{\frac{i}{\hbar}W(J)} \tag{310}$$

The variations of this functional with respect to $J(x)$ give us the connected correlation functions (which can be consulted in textbooks, as the mentioned above).

1PI diagrams

A diagram is considered as 1PI (one particle irreducible) if we can cut any of its internal lines and the resulting diagram remains connected. From this, one can define the n-order vertex function as the contribution of all 1PI diagrams belonging to n-point correlation function. There exist also a generating functional for the vertex functions, the effective action Γ. We will discuss about the effective action in the following section.

7.9 Effective Action

We are going to make a brief review of the Effective Action and its Loop Expansion, since several expressions from it will be useful in the following chapter where we will define the 2PI effective action. We define $\bar{\phi}(x)$ as

$$\bar{\phi}(x) \equiv \frac{\delta W(J)}{\delta J(x)} \tag{311}$$

From this, the effective action Γ is defined by a Legendre transform of $W(J)$

$$\Gamma(\bar{\phi}) = W(J(\bar{\phi})) - \bar{\phi}J(\bar{\phi}) \tag{312}$$

7.9.1 Effective Action in terms of $\hbar$

We will calculate the effective action with the technique of background field. We want to obtain a suitable expression for Γ in order to perform a perturbative expansion in powers of $\hbar$. For the sake of simplicity, we consider again a scalar real-valued field ϕ with a single component. The extension to several components is straightforward and will be presented at the end of this section.
We start with the path integral $Z(J)$ for a field $\phi(x)$ with an action $S(\phi)$ and an external source $J(x)$

$$Z(J) = e^{\frac{i}{\hbar}W(J)} = \int D\phi \; e^{\frac{i}{\hbar}\{S(\phi)+\phi J\}} \tag{313}$$

We aim to get another functional from which obtain the effective action directly, that is, whose derivatives allow to find the vertex functions (in the same way as the n-th derivatives of the $W(J)$ allow to find the n-point connected functions). To that propose, we make a variable change in the $Z(J)$

$$\bar{\phi}(x) \equiv \frac{\delta W(J)}{\delta J(x)} \;\longrightarrow\; \phi = \bar{\phi} + \phi' \tag{314}$$

i.e. we get $\bar{\phi} = \bar{\phi}(J)$. The change of variables in the functional integral does not affect the $Z(J)$, which remains the same. Performing the change we obtain:

$$\begin{aligned} Z(J) = e^{\frac{i}{\hbar}W(J)} &= \int D\phi' \; e^{\frac{i}{\hbar}\{S(\bar{\phi}+\phi')+\bar{\phi}J+\phi' J\}} = \\ &= e^{\frac{i}{\hbar}\bar{\phi}J} \int D\phi' \; e^{\frac{i}{\hbar}\{S(\bar{\phi}+\phi')+S(\bar{\phi})-S(\bar{\phi})+\phi' J\}} = \\ &= e^{\frac{i}{\hbar}\bar{\phi}J} e^{\frac{i}{\hbar}S(\bar{\phi})} \int D\phi' \; e^{\frac{i}{\hbar}\{S(\bar{\phi}+\phi')-S(\bar{\phi})+\phi' J\}} \end{aligned} \tag{315}$$

Let us remember here the expression (312) for the effective action. Differentiating this expression we get the well known expression

$$\frac{\delta\Gamma(\bar{\phi})}{\delta\bar{\phi}(x)} = \int dy \; \frac{\delta W(J)}{\delta J(y)} \frac{\delta J(y)}{\delta\bar{\phi}(x)} - J(x) - \int dy \; \bar{\phi}(y) \frac{\delta J(y)}{\delta\bar{\phi}(x)} = -J(x) \tag{316}$$

where (314) was taken into account. This equation can be rewritten in compact notation as:

$$\frac{\delta\Gamma(\bar{\phi})}{\delta\bar{\phi}} = -J \tag{317}$$

a simpler form to work with. In fact, from now on we will make use of this compact notation except when the explicit show of the dependences is mandatory. The second variation of effective action leads to the inverse of full connected propagator $G^{-1}(x,y)$. To see this we do

$$\int dz\, \frac{\delta^2 W(J)}{\delta J(x)\delta J(z)} \frac{\delta^2 \Gamma(\bar{\phi})}{\delta\bar{\phi}(z)\delta\bar{\phi}(y)} = \int dz\, \frac{\delta\bar{\phi}(z)}{\delta J(x)} \frac{\delta J(y)}{\delta\bar{\phi}(z)} = -\frac{\delta J(y)}{\delta J(x)} = -\delta(x-y) \tag{318}$$

and then

$$\frac{\delta^2 W(J)}{\delta J(x)\delta J(y)}\Big|_{J=0} = i\hbar G(x,y) \rightarrow \frac{\delta^2 \Gamma(\bar{\phi})}{\delta\bar{\phi}(x)\delta\bar{\phi}(y)}\Big|_{\bar{\phi}(J=0)} = i\hbar G^{-1}(x,y) \tag{319}$$

In fact, the effective action is the functional generator of the n-vertex functions, that are the ressumation of all 1PI diagrams with n external legs [6]. Remember that a diagram is 1PI when one can cut any line and the diagram remains connected.

Now, in (315), we can move the exponential multiplying the integral to the other side and, taking into account (312), we get

$$e^{\frac{i}{\hbar}\{W(J)-\bar{\phi}J\}} = e^{\frac{i}{\hbar}\Gamma(\bar{\phi})} = e^{\frac{i}{\hbar}\{S(\bar{\phi})+\hbar\Gamma_1(\bar{\phi})\}} \tag{320}$$

where we have defined

$$e^{i\Gamma_1(\bar{\phi})} \equiv \int D\phi'\; e^{\frac{i}{\hbar}\{S(\bar{\phi}+\phi')-S(\bar{\phi})+\phi' J\}} \tag{321}$$

The expression (320) establishes:

$$\Gamma(\bar{\phi}) = S(\bar{\phi}) + \hbar\Gamma_1(\bar{\phi}) \tag{322}$$

With the aim of getting an expression that allows us to make a perturbative expansion in terms of $\hbar$,in the following we are going to perform several transformations in the exponent of the integrand of (321). From (322) and (317) it is deduced

$$\frac{\delta S(\bar{\phi})}{\delta\bar{\phi}} = -J - \hbar\frac{\delta\Gamma_1(\bar{\phi})}{\delta\bar{\phi}} = -J - \hbar\Gamma_{1\bar{\phi}}(\bar{\phi}) \tag{323}$$

where subindex $\bar{\phi}$ stands for variations with respect to $\bar{\phi}$. We now see how the exponent of the integrand in (321) behaves under the Taylor expansion of $S(\bar{\phi}+\phi')$:

$$S(\bar{\phi}+\phi') - S(\bar{\phi}) + \phi' J = \frac{\delta S(\bar{\phi})}{\delta \bar{\phi}}\phi' + \frac{1}{2}\phi' S_{\bar{\phi}\bar{\phi}}\phi' + S_{int}(\bar{\phi},\phi') + \phi' J \quad (324)$$

where $S_{int}(\bar{\phi},\phi')$ is at least cubic in ϕ'. Making use of (323) the $\phi' J$ term in the right hand side of (324) vanishes and the expression (321) is

$$e^{i\Gamma_1(\bar{\phi})} = \int D\phi' \; e^{\frac{i}{\hbar}\{\frac{1}{2}\phi' S_{\bar{\phi}\bar{\phi}}\phi' + S_{int}(\bar{\phi},\phi') - \hbar\Gamma_{1\bar{\phi}}(\bar{\phi})\phi'\}} \quad (325)$$

as mentioned, we are making use of the compact notation. In usual notation it reads as

$$\begin{aligned} \phi' S_{\bar{\phi}\bar{\phi}}\phi' &= \int dx\; dy\; \phi'(x)\frac{\delta^2 S(\bar{\phi})}{\delta\bar{\phi}(x)\delta\bar{\phi}(y)}\phi'(y) \\ \Gamma_{1\bar{\phi}}(\bar{\phi})\phi' &= \int dx\; \frac{\delta\Gamma_1(\bar{\phi})}{\delta\bar{\phi}(x)}\phi'(x) \end{aligned} \quad (326)$$

Actually, (325) can be considered as the *path-integral* of a theory where the action, call it $\tilde{S}$, has a quadratic term $(1/2)\phi' S_{\bar{\phi}\bar{\phi}}\phi'$, an interaction term $S_{int}(\bar{\phi},\phi')$ and where a external source $-\Gamma_{1\bar{\phi}}(\bar{\phi})$ is considered. With respect to this action $\tilde{S}(\bar{\phi},\phi')$, the inverse of the free propagator will clearly be

$$i\hbar G_0^{-1}(x,y) = \frac{\delta^2 S(\bar{\phi})}{\delta\bar{\phi}(x)\delta\bar{\phi}(y)} \quad (327)$$

and the perturbative diagram vertices will be obtained from $S_{int}(\bar{\phi},\phi')$.
Thus, from (319) (322) and (327) one obtains

$$i\hbar G^{-1}(x,y) = i\hbar G_0^{-1}(x,y) + \hbar\frac{\delta^2\Gamma_1(\bar{\phi})}{\delta\bar{\phi}(x)\delta\bar{\phi}(y)} \quad (328)$$

and taking into account the Schwinger-Dyson equation we reach

$$\frac{\delta^2\Gamma_1(\bar{\phi})}{\delta\bar{\phi}(x)\delta\bar{\phi}(y)}\Big|_{\bar{\phi}(J=0)} = -i\Sigma(x,y) \quad (329)$$

where $\Sigma(x,y)$ is the *self-energy*, i.e., the ressumation of all $1PI$ diagrams with two external legs and lines associated to G_0.
Therefore, $\Gamma_1(\bar{\phi})$ is precisely the contribution of every 1PI vacuum diagram with propagator $G_0(x,y)$ and vertices corresponding to $S_{int}(\bar{\phi},\phi')$.

7.9.2 Expansion of $\Gamma(\bar{\phi}(x))$ in powers of $\hbar$: Loop Expansion

Now the target is to write the exponent in (325) in terms of powers of $\hbar$ and then find an iterative method that return us all diagrams of a given order in $\hbar$.

We start removing the $\hbar$ in the denominator of the exponent of (325). To that propose we re-define the field as

$$\phi'' \equiv \frac{\phi'}{\sqrt{\hbar}} \;\rightarrow\; \phi' = \sqrt{\hbar}\phi'' \;\rightarrow\; D\phi' = \sqrt{\hbar}D\phi'' \tag{330}$$

The $\sqrt{\hbar}$ in the Jacobian gives a constant in the expansion of Γ and does not play any role in the dynamics. So we can always re-define Γ to re-absorb it, not taking it into account any more. With that change it results

$$e^{i\Gamma_1(\bar{\phi})} = \int D\phi''\; e^{i\left[\frac{1}{2}\phi'' S_{\bar{\phi}\bar{\phi}}\phi'' + \frac{1}{\hbar}S_{int}(\bar{\phi},\sqrt{\hbar}\phi'') - \sqrt{\hbar}\Gamma_{1\bar{\phi}}(\bar{\phi})\phi''\right]} \tag{331}$$

This expression allow us to perform a perturbative expansion in powers of $\hbar$ (in a similar manner as it is usually done in powers of the λ coupling) and calculate $\Gamma_1(\bar{\phi})$ up to an given order. And from this we can find $\Gamma(\bar{\phi})$ by using (322).

We consider a single component field ϕ with the $\lambda\phi^4$ theory usual action:

$$S(\phi) = \int dz\; \left[\frac{1}{2}\partial_\mu\phi(z)\partial^\mu\phi(z) - \frac{1}{2}m^2\phi^2(z) - \frac{\lambda}{4!}\phi^4(z)\right] \tag{332}$$

With this, we can calculate the propagator G_0^{-1} from (327):

$$i\bar{h}G_0^{-1} = \frac{\delta^2 S(\bar{\phi})}{\delta\bar{\phi}(x)\delta\bar{\phi}(y)} = -\left[\Box_x + m^2 + \frac{\lambda}{2}\bar{\phi}^2(x)\right]\delta(x-y) \tag{333}$$

In the following, we calculate some orders in the expansion of $\Gamma(\bar{\phi})$ in powers of $\hbar$:

-Zero Order

In this case, making $\hbar = 0$,, from (322) we directly get

$$\Gamma^{(0)}(\bar{\phi}) = S(\bar{\phi}) \tag{334}$$

so, considering (327) it is obtained at this order:

$$i\hbar G^{-1}(x,y) = i\hbar G_0^{-1}(x,y) \iff G(x,y) = G_0(x,y) \tag{335}$$

-$\hbar$ Order

Up to order $\hbar$ the effective action has the form

$$\Gamma^{(1)}(\bar{\phi}) = S(\bar{\phi}) + \frac{1}{2} i\hbar \, Tr \; ln(S_{\bar{\phi}\bar{\phi}}) \tag{336}$$

-$\hbar^2$ Order

It could seem that the next order would be $\hbar^{3/2}$, but a closer look shows that the next order appearing is two. The effective action to order $\hbar^2$ is

$$\begin{aligned}
&\Gamma^{(2)}(\bar{\phi}) = S(\bar{\phi}) + \frac{i}{2} Tr \; ln\big(S_{\bar{\phi}\bar{\phi}}\big) + \\
&+\frac{1}{12}\hbar \int dxdydzdsdvdw S^{-1}_{\bar{\phi}(x)\bar{\phi}(s)} S_{\bar{\phi}(x)\bar{\phi}(y)\bar{\phi}(z)} S^{-1}_{\bar{\phi}(y)\bar{\phi}(v)} S_{\bar{\phi}(s)\bar{\phi}(v)\bar{\phi}(w)} S^{-1}_{\bar{\phi}(z)\bar{\phi}(w)} - \\
&-\frac{1}{8}\hbar \int dxdydzds \; S^{-1}_{\bar{\phi}(x)\bar{\phi}(y)} S_{\bar{\phi}(x)\bar{\phi}(y)\bar{\phi}(z)\bar{\phi}(s)} S^{-1}_{\bar{\phi}(z)\bar{\phi}(s)}
\end{aligned} \tag{337}$$

or in diagrammatic form

$$\Gamma^{(2)}(\bar{\phi}) = S(\bar{\phi}) \; + \; \frac{i}{2} Tr \; ln\big(S_{\bar{\phi}\bar{\phi}}\big) \; +$$

where subscripts $\bar{\phi}$ stand for variation respect to $\bar{\phi}$.

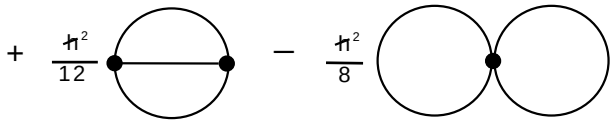

7.9.3 $\Gamma_{(2)}$ calculation for a Multicomponent Field

We compute the effective action up to order $\hbar^2$ for a N component real scalar field, whose action is given in the form

$$S(\phi) = \int dx \; \left(\frac{1}{2} \partial_\mu \phi_a(x) \partial^\mu \phi_a(x) - \frac{m^2}{2} \phi_a(x) \phi_a(x) - \frac{\lambda}{4!\, N} (\phi_a(x) \phi_a(x))^2 \right) \tag{338}$$

where there is a sum over repeated indices. After some computation and having in mind that our action (338) has a $O(N)$ symmetry and we can

consider the propagator diagonal with respect to the field components thus, we obtain

$$S^{-1}_{\bar{\phi}_a(x)\bar{\phi}_b(y)} = \delta_{ab}\; S^{-1}_{\bar{\phi}(x)\bar{\phi}(y)} \tag{339}$$

so the corresponding summation over the components can be performed, resulting

$$\Gamma_{(2)}(\bar{\phi}) = S(\bar{\phi}) + \frac{i}{2}Tr\; ln\big(S_{\bar{\phi}\bar{\phi}}\big) + \frac{\hbar\lambda^2(N+2)}{36N}\int dxdy\; \bar{\phi}(x)\bar{\phi}(y)\left(S^{-1}_{\bar{\phi}(x)\bar{\phi}(y)}\right)^3 + \\ + \frac{\hbar\lambda(N+2)}{24}\int dx\; \left(S^{-1}_{\bar{\phi}(x)\bar{\phi}(x)}\right)^2 \tag{340}$$

We can write this in terms of the free propagator as defined in (327)

$$\Gamma_{(2)}(\bar{\phi}) = S(\bar{\phi}) + \frac{i}{2}Tr\; ln\big(i\hbar G_0^{-1}(x,y)\big) + \tag{341}$$
$$+ i\frac{\hbar\lambda^2(N+2)}{36N}\int dxdy\; \bar{\phi}(x)\bar{\phi}(y)\left(\frac{G_0(x,y)}{\hbar}\right)^3 - \frac{\hbar\lambda(N+2)}{24}\int dx\; \left(\frac{G_0(x,x)}{\hbar}\right)^2$$

So far, we have seen that when we write the corresponding diagrams, we can consider that each vertex of n legs carries a factor $\hbar^{n/2}$ and each propagator line carries a factor $\frac{1}{\hbar}$. In this way, the right $\hbar$ order for each diagram will be stated by the number of loops of the diagram.

8 2PI Approximation

8.1 Introduction

An important technique to study real-time quantum evolution of fields, that has been widely used in the last years, is the 2PI approximation. This method gives rise to different levels of approximation based on the resummation of (finite or not) series of perturbative diagrams. These series involve only two-particle irreducible (2PI) diagrams, which are diagrams where one can cut any two lines and the diagram remains connected.
In this technique the evolution equations are restricted to two-point functions, and use integrals with memory that take into account the history of the previous evolution. In the following sections we will describe these methods for the two usual approximations: 2PI-Loop approximation and 2PI-1/N approximation. Similar approximations can be implemented for the classical evolution, and we will also show this case.

The 2PI approximation is based in the called 2PI effective action $\Gamma_2(G)$ [49][50] that is the contribution of all two-particle irreducible vacuum diagrams where the lines represent to full propagator G. So the variation of $\Gamma_2(G)$ respect to $G(x,y)$ represents the contribution of all 1PI diagrams with two external legs, which is precisely the self-energy $\Sigma(x,y)$. The evaluation of Γ_2 for a closed path time (CPT) was presented in [76] and leads to a Schwinger-Dyson equation that relates the full propagator G with the free propagator G_0 and the self-energy Σ, obtaining from it the corresponding evolution equation for G (see also [77]). Then one can define [78] the statistical two-point function $F(x,y) \equiv \langle\{\phi(x)\phi(y)\}\rangle/2$ (anti-commutator) and the spectral function $\rho(x,y) \equiv i\langle[\phi(x)\phi(y)]\rangle$ (commutator) and so one can write G as

$$G(x,y) = F(x,y) - \frac{i}{2}\rho(x,y)\text{sign}_{\mathcal{C}}(x^0 - y^0) \tag{342}$$

where $\mathcal{C}$ indicates that the sign function has to be evaluated along the CPT. The evolution equation for G, obtained from the Schwinger-Dyson equation, leads to two causal evolution equations for F and ρ (366) where only real quantities are involved (*2PI evolution equations* [78]). It is remarkable the causal nature of the 2PI equations because it is feasible to discretize it in order to perform numerical computations.
The 2PI equations are exact but in practice it is necessary to make some

approximation for the self-energy. Usually one chooses a (infinite or not) subset of all diagrams that contribute to Γ_2, and therefore a subset of all diagrams that contribute to Σ.
So, in the 2PI-Loop Expansion we cut the diagrammatic expansion to a concrete number of loops. One can see the self-energy to 3-loops in [77] as a function of the full propagator, and in [78] in a more computationally useful way as a function of F and ρ. The diagrams that contribute to 3-loops can be seen in Fig. 64.
Also the so-called 2PI-1/N expansion is used. Here the chosen subset of diagrams that contribute to Γ_2 can be infinite depending on the selected order. To leading order (LO) we take only one diagram and this correspond with the so-called Hartree approximation. To Next to Leading Order (NLO) we have an infinite subset of diagrams and the expressions for the components of self-energy can be found in [79].
Thus, in the 2PI approximation only the evolution of two-point functions are computed, although there are other approximation schemes based on the nPI effective action for the evolution of n-point functions. A comprehensive review of all this can be accessed in [17].
There is also a similar method for Classical Field Theory that we note 2PI-Cl method. In fact, the evolution equations are the same than in the quantum case, although the definition of self-energy components is different. We will analyze this method later and one can find a complete description in [17].
In recent years, many results have been provided from the use of this 2PI effective action techniques to study real time quantum evolution. The out-of-equilibrium dynamics of quantum fields and the subsequent approach to equilibrium states has been studied by several authors. So the 2PI-Loop formalism to 3 loops is numerically implemented for a scalar field in 1+1 dimensions in order to study thermalization in [77] or the nonequilbrium time evolution of spectral function in [78]. Also one can find in [51] a complete study of nonequilibrium real-time evolution of a O(N)-symmetric scalar quantum field in 1+1 dimensions using the 2PI-1/N approximation. The author investigates two different initial conditions (*quench* and *tsunami*) frequently used in the context of heavy-ion collisions. The evolution is obtained for LO and NLO and the corresponding results are compared. Moreover the behavior at late times and the approach to equilibrium is also shown. As mentioned above, another interesting study for 1+1 dimensions that compare the evolution in the 2PI-1/N approximation at NLO with the evolution in the classical approximation can be seen in [42], where also the evolution from the 2PI-Cl

method is calculated. Similar issues are presented in [80] for 2+1 dimensions computing the evolution from 2PI-Loop expansion to 3 loops. Results for 3+1 dimensions can be found for fermions and scalars in [81][82]. An analytical study also for scalars and fermions to see how the calculation of transport coefficients is organized in the framework of 2PI effective action it is shown in [83], starting from the 2PI-Loop expansion to 3 loops and from the 2PI-1/N approximation to NLO. Also for 3+1 dimensions, a numerical computation using the 2PI-Loop approximation to 2 and 3 loops allows the calculation of several thermodynamic quantities and its dependence on renormalization in [84]. Another study to 2 loops of ϕ^4 scalar theory at finite temperature can be seen in [85].In these studies one may expect scattering to result in equilibration of the system, but this does not happen in the Hartree (LO) approximation. Nevertheless it has been verified that the inclusion of the NLO diagrams indeed leads to thermalization.

The 2PI approximation is also used in the area of cosmology. The process of resonant preheating was studied in [86] from the 2PI-1/N approximation at NLO. In [87] the authors present an interesting study in a O(4) model of tachyonic preheating of scalar fields in 3+1 dimensions similar to the Higgs sector in the SM, using the 2PI-1/N expansion at LO and NLO an compare it with the classical approximation. It is found that for reasonable couplings the classical approximation agree so well with the quantum case for not too long times. More recently, in [88], the authors investigate the fermion production during the preheating epoch after inflation. They use the 2PI-1/N expansion and compare the LO with the NLO, obtaining remarkable differences between the two evolutions. About the properties of convergence for the 2PI evolution techniques, one can see a complete study in [89], where the behavior of different approximations is calculated in quantum-mechanical systems where it is possible the comparison with the exact evolution. Here the authors calculate the evolution on the 2PI-1/N approximation to LO (Hartree), NLO and also with some contributions of NNLO and compare it with the exact quantum evolution. It is found that the qualitative change in the nonequilibrium evolution when going from LO to NLO is enormous, but the impact when changing from NLO to NNLO is reassuringly small. Another interesting study is presented in [90] on the 2PI-1/N expansion for the O(N) model in 1+1 dimensions. Here it is investigated convergence properties including LO, NLO and also some diagrams of NNLO, as well as the classical approximation. The expansion is convergent (the evolution from the different approximations match) even at large coupling as N increased. At

fixed N one found convergence as the coupling is reduced.

8.2 2PI Effective Action (Γ_2)

We will consider $\hbar = c = 1$ units. In order to define the *2PI Effective Action* we ought to consider a *path-integral* with 2 sources, a local one $J(x)$ and a bilocal $K(x, y)$. For a real N component scalar field, using the sum-over-repeated-index prescription, we obtain

$$\begin{aligned} Z(J,K) &= e^{iW(J,K)} = \\ &= \int D\phi \; exp\Big(i\Big[S(\phi) + \int dx \; J_a(x)\phi_a(x) + \\ &\quad + \frac{1}{2}\int dxdy \, \phi_a(x) K_{ab}(x,y)\phi_b(y)\Big]\Big) \end{aligned} \tag{343}$$

We are using the Schwinger-Keldysh formalism [15][16] and the shorthand notation $\int dx \equiv \int d^d\mathbf{x} \int_{\mathcal{C}} dt$ where $\mathcal{C}$ is a *Closed Path Time* (CPT) [17] along the real axis as we show in the next figure:

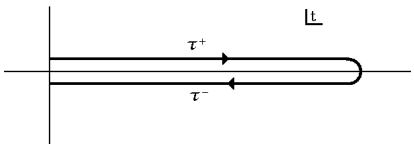

Figure 63: Closed Path Time contour. One has time-ordering along τ^+ and anti-time ordering along τ^-.

Now we define the expectation value of the field $\bar{\phi}_a$ and the 2 point connected function G_{ab} by means of variations of W with respect to the sources and in the presence of them

$$\begin{aligned} \frac{\delta W(J,K)}{\delta J_a(x)} &= \bar{\phi}_a(x) \\ \frac{\delta W(J,K)}{\delta K_{ab}(x,y)} &= \frac{1}{2}[\bar{\phi}_a(x)\bar{\phi}_b(y) + G_{ab}(x,y)] \end{aligned} \tag{344}$$

The effective action is obtained by means of a double Legendre transform, in

a manner that the conjugate variables of J, K will be $\bar{\phi}, G$

$$\Gamma(\bar{\phi}, G) = W(J,K) - \int dx \bar{\phi}_a(x) J_a(x) - \frac{1}{2}\int dx\, dy K_{ab}(x,y)\bar{\phi}_a(x)\bar{\phi}_b(y) - \frac{1}{2}Tr(KG) \tag{345}$$

taking derivatives, the resulting equations are

$$\begin{aligned} \frac{\delta\Gamma(\bar{\phi}, G)}{\delta\bar{\phi}_a(x)} &= -J_a(x) - \int d^4y\, K_{ab}(x,y)\bar{\phi}_b(y) \\ \frac{\delta\Gamma(\bar{\phi}, G)}{\delta G_{ab}(x,y)} &= -\frac{1}{2}K_{ab}(x,y) \end{aligned} \tag{346}$$

and since the physical processes correspond with the removal of the sources J y K, this also represents the derivation of the stationary equations for $\bar{\phi}$ and G.

We define a new quantity $\Gamma_2(\bar{\phi}, G)$ from $\Gamma(\bar{\phi}, G)$, which is written in compact matrix notation as

$$\Gamma(\bar{\phi}, G) = S(\bar{\phi}) + \frac{i}{2}Tr(lnG^{-1}) + \frac{i}{2}Tr(G_0^{-1}(\bar{\phi})G) + \Gamma_2(\bar{\phi}, G) \tag{347}$$

If variations with respect to $G(x,y)$ are made, the so called *Schwinger-Dyson equation* follows

$$G^{-1}_{ab}(x,y) = G^{-1}_{0,ab}(x,y) - iK_{ab}(x,y) - \Sigma_{ab}(x,y;\bar{\phi}, G) \tag{348}$$

where it was defined

$$\Sigma_{ab}(x,y;\bar{\phi}, G) \equiv 2i\frac{\delta\Gamma_2(\bar{\phi}, G)}{\delta G_{ab}(x,y)} \tag{349}$$

Actually, this Σ_{ab} is the self-energy, that is the contribution of all the 1PI diagrams built with the propagator $(G^{-1}_{0,ab} - iK_{ab})^{-1}$. Later on, it will coincide with the traditional self-energy when all sources will be equal to zero, but having in mind that $G^{-1}_{0,ab}$ is in this case:

$$i\hbar G^{-1}_{0,ab}(x,y) = \frac{\delta^2 S(\bar{\phi})}{\delta\bar{\phi}_a(x)\delta\bar{\phi}_b(y)} \tag{350}$$

The traditional Schwinger-Dyson equation allow us to write the full propagator G as an infinite series in terms of the free propagator G_0 and the self-energy Σ

$$G = G_0 + G_0\Sigma G_0 + G_0\Sigma G_0\Sigma G_0 + ... \tag{351}$$

Σ is the contribution of all 1PI diagrams with two external legs and lines associated to free propagator G_0. But we can interchange the roles of G and G_0 in the Schwinger-Dyson equation

$$G_0^{-1} = G^{-1} + \Sigma \tag{352}$$

and then we would have a series similar to (351) but exchanging $G_0 \leftrightarrow G$ and replacing $\Sigma \to -\Sigma$. Therefore the contribution of all 1PI diagrams with lines equal to free propagator (self-energy) is the same than the contribution of all 1PI diagrams with lines equal to full propagator, with a sign change. In our case Σ_{ab} has been built with the full propagator G_{ab} and represents the contribution of all 1PI diagrams with lines associated to G_{ab}. This means, from (349), that Γ_2 is made by all 2PI diagrams with lines representing the full propagator G and vertices corresponding to the $S_{int}(\bar{\phi}, \phi')$ defined in (324) (it was obtained by displacing the field around its expectation value).

8.2.1 Evolution equations

We consider the symmetric case ($\bar{\phi} = 0$) and we take an action with a $O(N)$ symmetry in addition. In this case the propagator can be taken as diagonal in the field components

$$G_{ab}(x, y) = G(x, y)\delta_{ab} \tag{353}$$

With this, the equation (348) reads

$$G^{-1}(x, y) = G_0^{-1}(x, y) - iK(x, y) - \Sigma(x, y; G) \tag{354}$$

If we make the convolution of this equation with G, by means of

$$\int dx\, G^{-1}(x, z)G(z, y) = \delta(x - y) \tag{355}$$

then we get the equations of motion for the propagator G

$$(\Box_x + m^2)G(x, y) + i \int dz\, [\Sigma(x, z; G) + iK(x, y)]G(z, y) = -i\delta(x - y) \tag{356}$$

where we took into account that the inverse of the propagator G_0 in the case $\bar{\phi} = 0$ is given by

$$G_0^{-1}(x, y) = i(\Box_x + m^2)\delta(x - y) \tag{357}$$

It is remarkable that the equation (356) is exact. Furthermore in order to get it, we have taken derivatives with respect to several functions as the field, G, etc, but never with respect to the coordinates. So the equation remains valid in the case $m^2 = m^2(t)$.

Now we rather prefer the evolution equation in a more useful manner, in the way it allows to perform calculations with the help of a computer. For that purpose we start by defining the *spectral component* ρ and the *statistical component* F as

$$\begin{aligned} \rho(x,y) &\equiv i\big\langle[\phi(x),\phi(y)]\big\rangle \\ F(x,y) &\equiv \frac{1}{2}\big\langle\{\phi(x),\phi(y)\}\big\rangle \end{aligned} \tag{358}$$

It can be shown that following this definition, all equal-time commutation relations are included into $\rho(x,y)$, satisfying

$$\rho(x,y)|_{x^0=y^0} = 0 \quad ; \quad \partial_{x^0}\rho(x,y)|_{x^0=y^0} = \delta(x-y) \tag{359}$$

and it is straightforward to show that $F(x,y)$ is symmetric under argument interchange and $\rho(x,y)$ is anti-symmetric

$$F(x,y) = F(y,x) \quad ; \quad \rho(x,y) = -\rho(y,x) \tag{360}$$

Moreover it is easy to obtain the equation that relates these two quantities with the whole propagator $G(x,y)$

$$G(x,y) = F(x,y) - \frac{i}{2}\rho(x,y)sign(x^0 - y^0) \tag{361}$$

We also separate the self-energy in a local and a non-local component in the following form

$$\Sigma(x,y;G) = -i\Sigma^{(0)}(x;G)\delta(x-y) + \bar{\Sigma}(x,y;G) \tag{362}$$

As $\Sigma^{(0)}$ corresponds to a coordinate dependent mass term, we include it in the former mass term and we have

$$M^2(x;G) \equiv m^2 + \Sigma^{(0)}(x;G) \tag{363}$$

With respect to the non-local part of the self-energy, we decompose it in another two quantities Σ_ρ and Σ_F in a similar way as the G decomposition that we made in (361)

$$\bar{\Sigma}(x,y) = \Sigma_F(x,y) - \frac{i}{2}\Sigma_\rho(x,y) sign(x^0 - y^0) \tag{364}$$

As F and ρ, Σ_F is symmetric under argument interchange and Σ_ρ is anti-symmetric

$$\Sigma_F(x,y) = \Sigma_F(y,x) \quad ; \quad \Sigma_\rho(x,y) = -\Sigma_\rho(y,x) \tag{365}$$

With all this, starting from the evolution equation (356), making use of the definitions (361) and (364), and with the CPT shown in Fig. 63, we obtain a computer friendly set of exact evolution equations for ρ and F useful for numerical computation [17]

$$\begin{aligned}
\left[\Box_x + M^2(x)\right] \rho(x,y) &= -\int_{y^0}^{x^0} dz\, \Sigma_\rho(x,z)\rho(z,y) \\
\left[\Box_x + M^2(x)\right] F(x,y) &= -\int_0^{x^0} dz\, \Sigma_\rho(x,z)F(z,y) + \int_0^{y^0} dz\, \Sigma_F(x,z)\rho(z,y)
\end{aligned} \tag{366}$$

8.3 2PI-Loop Approximation

Consider a real scalar field with N components and action

$$S(\phi) = \int dx \left(\frac{1}{2}\partial_\mu\phi_a(x)\partial^\mu\phi_a(x) - \frac{m^2}{2}\phi_a(x)\phi_a(x) - \frac{\lambda}{4!\,N}(\phi_a(x)\phi_a(x))^2\right) \tag{367}$$

we come back to the previous section case of 2 sources, whose *path-integral* is given by (343). The free propagator is obtained as indicated in (350) being

$$iG^{-1}_{0,ab}(x,y) = -\left(\Box_x + m^2 + \frac{\lambda}{6N}\bar{\phi}_c(x)\bar{\phi}_c(x)\right)\delta_{ab}\delta(x-y) - \frac{\lambda}{3N}\bar{\phi}_a(x)\bar{\phi}_b(x)\delta(x-y) \tag{368}$$

As done in the first section, it is possible to expand the 2PI effective action Γ_2 in powers of $\hbar$, in a way that the $\hbar$ order is represented by the number of loops in each diagram. We know that such expansion only contains 2PI diagrams and lines representing the whole propagator G. If we stop the expansion at a certain order, we are actually making an approximation to Γ_2.

This approximation is known as *2PI Approximation on Loop Expansion*.

We consider from now on the symmetric case, $\bar{\phi} = 0$, with just a single diagram at each order contributing to Γ_2 up to order 3 in $\hbar$. This is shown in Fig. 64.

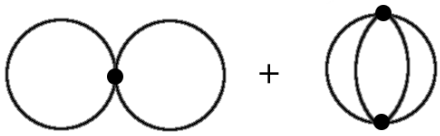

Figure 64: Diagrams contributing to Γ_2 up to order 3 in $\hbar$

We know that the lines represent G_{ab} in these diagrams, for any possible value of a and b, but since the action is $O(N)$ symmetric, we have $G_{ab} = \delta_{ab}G$, and any line in the diagram will represent G. We have the 4-leg vertices obtained by differentiating 4-times the action $S(\bar{\phi})$ with respect to $\bar{\phi}$. In this way, the contributions of the 2 diagrams in Fig. 64 to the 2PI effective action can be easily computed

$$\begin{aligned}
\Gamma_2^{(3loop)} &= \Gamma_2^{(2)} + \Gamma_2^{(3)} \\
\Gamma_2^{(2)} &= -\frac{\lambda(N+2)}{24} \int dx\, G^2(x,x) \\
\Gamma_2^{(3)} &= \frac{i\lambda^2(N+2)}{144N} \int dx\, dy\, G^4(x,y)
\end{aligned} \tag{369}$$

8.3.1 Evolution of Γ_2 up to Order 3 in $\hbar$

The equations of evolution (366) are consistent, which means that they can be discretized in a way that, starting with some initial conditions, the evolution up to time t can be performed by means of the data of previous times. So although non-linear, the equations are feasible to be solved by a computer.

In order to apply the equations, initial values for F and ρ are mandatory. Also $\Sigma^{(0)}$, Σ_F and Σ_ρ must be expressed in terms of them. In fact, it is precisely in the value of these 3 quantities obtained from the self-energy, where the different approximations to the 2PI effective action apply. This is due to

the fact that the self-energy is directly obtained from the Γ_2, which is the one accordingly approximated.

In our case, we are approximating by taking a cut in the Loop-Expansion at order 3 in $\hbar$. The form of Γ_2^{3loop} at this order is given by (369). The quantities of interest are obtained in terms of F and ρ from it:

$$\begin{aligned}
\Sigma^{(0)}(x) &= \lambda \frac{N+2}{6N} F(x,x) \\
\Sigma_\rho(x,y) &= -\lambda^2 \frac{N+2}{6N^2} \rho(x,y) \left[F^2(x,y) - \frac{1}{12}\rho^2(x,y) \right] \\
\Sigma_F(x,y) &= -\lambda^2 \frac{N+2}{18N^2} F(x,y) \left[F^2(x,y) - \frac{3}{4}\rho^2(x,y) \right]
\end{aligned} \tag{370}$$

Thus, we got all necessary elements to discretize the evolution equations (366) and obtain the values of later times by means of previous times. In fact, if we discretize with a time step a_t, we need to specify as initial values the following quantities

$$F(x,y)|_{x^0=0,\,y^0=0} \quad ; \quad F(x,y)|_{x^0=1,\,y^0=0} \quad ; \quad F(x,y)|_{x^0=1,\,y^0=1} \tag{371}$$

where the value of the temporal coordinates is given by the number of a_t steps. We must also set the initial values for $\rho(x,y)$, but they are given by the anti-symmetry of ρ and by relations (359) obtained from the equal-time commutation of fields. Thus

$$\rho(x,y)|_{x^0=y^0} = 0 \qquad ; \qquad \rho(x,y)|_{x^0=t+a_t,\,y^0=t} = a_t \tag{372}$$

and then the requested initial values of ρ are

$$\rho(x,y)|_{x^0=0,\,y^0=0} = 0 \;\; ; \;\; \rho(x,y)|_{x^0=1,\,y^0=0} = a_t \;\; ; \;\; \rho(x,y)|_{x^0=1,\,y^0=1} = 0 \tag{373}$$

with this the initial values for $\Sigma^{(0)}$, Σ_F and Σ_ρ can be found by means of (370). Then we discretize the evolution equations (366) and we are ready for their numerical implementation.

Hence having the values for F and ρ we can compute expectation values of products of the field $\phi(x)$ by itself or by its conjugate momentum $\pi(x)$. It

is clear for instance:

$$\begin{aligned}
&\big\langle\phi(x)\phi(y)\big\rangle|_{x^0=y^0} = F(x,y)|_{x^0=y^0} \Rightarrow \big\langle\phi^2(x)\big\rangle = F(x,x) \\
&\frac{1}{2}\big\langle\{\pi(x),\phi(y)\}\big\rangle|_{x^0=y^0} = \partial_{x^0}F(x,y)|_{x^0=y^0} \Rightarrow \frac{1}{2}\big\langle\{\pi(x),\phi(x)\}\big\rangle = \partial_{x^0}F(x,x) \\
&\big\langle\pi(x)\pi(y)\big\rangle|_{x^0=y^0} = \partial_{x^0}\partial_{y^0}F(x,y)|_{x^0=y^0} \Rightarrow \big\langle\pi^2(x)\big\rangle = \partial_{x^0}\partial_{y^0}F(x,x) \quad (374)
\end{aligned}$$

8.4 2PI-1/N Approximation

As previously shown, the 2PI effective action can not be exactly computed in the interacting theory. The obtained evolution equations from the Schwinger-Dyson one are usually solved by means of any sort of approximation over the self-energy components (as the approximation on Loop Expansion that we made before). Now we will perform a $1/N$ expansion, where N is the number or field components.

8.4.1 1/N expansion of Γ_2 at LO

The Leading Order (LO) is found by considering diagrams where the sum over internal lines gives just a factor greater or equal than N^l, where l is the number of loops in the diagram. This LO is also called Hartree Approximation. In the Next to Leading Order (NLO) the diagrams give a factor N^{l-1}. And so on.

We are going to consider in the following a symmetric regime $\bar{\phi} = 0$, and hence we have $\Gamma(\bar{\phi} = 0, G) \equiv \Gamma(G)$. Thus we write:

$$\Gamma_2(G) = \Gamma_2^{LO}(G) + \Gamma_2^{NLO}(G) + ... \quad (375)$$

As previously stated, the contribution to LO comes from a single diagram, which is shown in Fig. 65

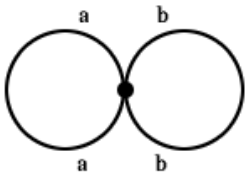

Figure 65: LO contribution to the 2PI effective action

following this figure, the contribution is

$$\Gamma_2^{LO}(G) = -\frac{\lambda}{24N}\sum_{a,b}\int_{\mathcal{C}} d^4x\; G_{aa}(x,x)\, G_{bb}(x,x) \tag{376}$$

where, as mentioned, $\mathcal{C}$ stands for a Closed Time Path (CTP) [15][16][79].

8.4.2 NLO of 1/N expansion of Γ_2

Omitting combinatorial factors, Fig. 66 shows the diagrams contributing to $\Gamma_2(G)$ at NLO

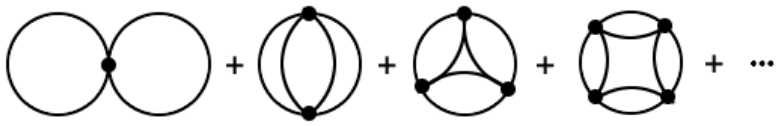

Figure 66: NLO contribution to the 2PI effective action

The first diagram in the series corresponds to the one shown in Fig. 64 and is

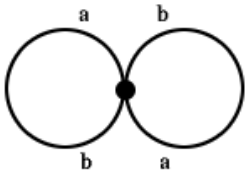

Figure 67: NLO double bubble contribution

The next diagram is a 3 loop one, and the subsequent diagrams can be built from their previous one by introducing a new vertex and an extra loop. This contribution can be interpreted as a 3-loop diagram with an effective tetra-vertex containing all *bubble chain* contributions. Thus, the double bubble and this closed *chain* of diagrams form the NLO contribution to $\Gamma_2(G)$.
Summing the infinite number of NLO diagrams is easy to perform [79][17], finding

$$\Gamma_2^{NLO}(G) = \frac{i}{2}\int_{\mathcal{C}} d^4x\;\; \ln[B(G)](x,x) \tag{377}$$

where

$$B(x,y;G) = \delta^4(x-y) + i\frac{\lambda}{6N}\, G_{ab}(x,y)\, G_{ab}(x,y) \tag{378}$$

It is interesting to understand the meaning of the ln in (377) by expanding

$$\int_{\mathcal{C}} d^4x\ \ln[B(G)](x,x) = \int_{\mathcal{C}} d^4x\ \Big(i\frac{\lambda}{6N}\, G_{ab}(x,x)\, G_{ab}(x,x)\Big) -$$
$$-\frac{1}{2}\int_{\mathcal{C}} d^4x\, d^4y\, \Big(i\frac{\lambda}{6N}\, G_{ab}(x,y)\, G_{ab}(x,y)\Big)\Big(i\frac{\lambda}{6N}\, G_{a'b'}(y,x)\, G_{a'b'}(y,x)\Big) +$$
$$+... \tag{379}$$

8.4.3 Important Quantities

As we are performing an approximation to the 2PI effective action, we ought to compute the quantities appearing in the evolution equations obtained in (366) in such approximation. Actually we need the components of the self-energy in terms of F and ρ.

The self-energy is obtained by differentiating Γ_2 with respect to $G_{ab}(x,y)$, in agreement with (349). From (376) we obtain the LO and from (377) the NLO is computed. Both contributions are

$$\Sigma_{ab}(x,y;G) = -i\frac{\lambda}{6N}\Big(\sum_c G_{cc}(x,x)\Big)\,\delta_{ab}\,\delta^4(x-y) - i\frac{\lambda}{3N} G_{ab}(x,y) B^{-1}(x,y;G) \tag{380}$$

and from that expression we can compute the components of the self-energy and introduce them into equations (366) in order to obtain the approximate evolution equations.

As we have previously done, we focus upon the symmetric case ($\bar{\phi} = 0$) and consider a $O(N)$ symmetric action, so G will be diagonal in the field components. We will make use of this property below.
It is handy to define a new quantity that will help us write the expressions in a simpler way

$$I(x,y) \equiv iB^{-1}(x,y) - i\delta^4(x-y) \tag{381}$$

and we also define the components of this quantity by:

$$I(x,y) = I_F(x,y) - \frac{i}{2} I_\rho(x,y) sign(x^0 - y^0) \tag{382}$$

in a way that $I_F(x,y) = I_F(y,x)$ e $I_\rho(x,y) = -I_\rho(y,x)$.
So expressing all quantities in terms of G, and it in terms of F and ρ, it results for the components of Σ:

$$\begin{aligned}
\Sigma_F(x,y) &= -\frac{\lambda}{3N}\Big(F(x,y)I_F(x,y) - \frac{1}{4}\rho(x,y)I_\rho(x,y)\Big) \\
\Sigma_\rho(x,y) &= -\frac{\lambda}{3N}\Big(F(x,y)I_\rho(x,y) + \rho(x,y)I_F(x,y)\Big) \\
M^2(x) &\equiv m^2 + \Sigma^{(0)}(x) = m^2 + \lambda\frac{N+2}{6N}\,F(x,x)
\end{aligned} \tag{383}$$

and for the I ones:

$$\begin{aligned}
I_F(x,y) &= \tfrac{\lambda}{6}\Big(F^2(x,y) - \tfrac{1}{4}\rho^2(x,y)\Big) - \\
&-\tfrac{\lambda}{6}\int d^3\mathbf{z}\Bigg[\int_0^{x^0} dz^0 I_\rho(x,z)\Big(F^2(z,y) - \tfrac{1}{4}\rho^2(z,y)\Big) - \\
&\qquad -2\int_0^{y^0} dz^0 I_F(x,z)F(z,y)\rho(z,y)\Bigg] \\
I_\rho(x,y) &= \tfrac{\lambda}{3}F(x,y)\rho(x,y) - \tfrac{\lambda}{3}\int d^3\mathbf{z}\int_{y^0}^{x^0} dz^0 I_\rho(x,z)F(z,y)\rho(z,y)
\end{aligned} \tag{384}$$

Thus, (383) and (384) together with evolution equations (366) are the 2PI-1/N approximation.

8.5 Evolution in Classical Field Theory

In the rest of this section, we will define the classical counterparts of F and ρ. Once a suitable definition of the self-energy is given, the resulting classical evolution equations will become identical to those obtained for the quantum case. The difference will reside in the expression of the self-energy for both cases. We will use these formulas to compare the classical and quantum evolution within the same set of approximations (loop or 1/N). This will give us a classicality condition valid at least up to the order taken in the corresponding approximation.

8.5.1 Definitions and evolution equations

Consider a real scalar field with N components and an action given by (367). The classical equation of motion will be:

$$\Big[\Box_x + m^2 + \frac{\lambda}{6N}\phi_b(x)\phi_b(x)\Big]\phi_a(x) = 0 \tag{385}$$

whose solution requires the specification of $\phi_a(0,\mathbf{x}) = \phi_a(\mathbf{x})$ and $\pi_a(0,\mathbf{x}) = \pi_a(\mathbf{x})$ with $\pi_a(x) = \partial_{x^0}\phi_a(x)$. We define the classical mean field as

$$\bar{\phi}_{a,cl}(x) = \langle\phi_a(x)\rangle_{cl} \equiv \int D\pi\, D\phi\; W_0[\pi,\phi]\phi_a(x) \tag{386}$$

where $W_0[\pi,\phi]$ stands for the initial-time normalized probability functional. The measurement indicates a functional integration in phase-space

$$\int D\pi\, D\phi = \int \prod_{a=1}^{N}\prod_{x} d\pi_a(x) d\phi_a(x) \tag{387}$$

The *classical statistical two-point function* has the form

$$F_{ab,cl}(x,y) + \bar{\phi}_{a,cl}(x)\bar{\phi}_{b,cl}(y) = \langle\phi_a(x)\phi_b(y)\rangle_{cl} = \int D\pi\, D\phi\, W_0[\pi,\phi]\phi_a(x)\phi_b(y) \tag{388}$$

and clearly, the *classical spectral function* will be the classical counterpart of the quantum spectral function, which is obtained by replacing $-i[\,,\,]$ by $\{\,,\,\}$ (Poisson bracket)

$$\rho_{ab,cl}(x,y) = -\langle\{\phi_a(x),\phi_b(y)\}_{PoissonBracket}\rangle_{cl} \tag{389}$$

From there the equal-time relations for the classical spectral function can be deduced

$$\rho_{ab,cl}(x,y)|_{x^0=y^0} = 0\;;\;\partial_{x^0}\rho_{ab,cl}(x,y)|_{x^0=y^0} = \delta_{ab}\delta(\mathbf{x}-\mathbf{y}) \tag{390}$$

although the origin is different, they end up being the same as in the quantum case. As a reminder, we explicitly write the meaning of the Poisson bracket

$$\{A(x),B(y)\}_{PB} = \sum_{a=1}^{N}\int d\mathbf{z}\,\Big[\frac{\delta A(x)}{\delta\phi_a(\mathbf{z})}\frac{\delta B(y)}{\delta\pi_a(\mathbf{z})} - \frac{\delta A(x)}{\delta\pi_a(\mathbf{z})}\frac{\delta B(y)}{\delta\phi_a(\mathbf{z})}\Big] \tag{391}$$

Now we find the evolution equations for the classical correlators starting from the differential equation for the free correlators. We choose $W[\pi, \phi]$ invariant under $O(N)$ symmetry with $\bar{\phi}_a = 0$. So

$$F_{ab,cl}(x, y) = F_{cl}(x, y)\delta_{ab} \tag{392}$$

and the same for $\rho_{ab,cl}(x, y)$. The free spectral function ρ_0 (either quantum or classical) is a solution of the homogeneous equation

$$\Big[\Box_x + m^2\Big]\rho_0(x, y) = 0 \tag{393}$$

with initial conditions given by the equal-time relations (390). In the same way, the statistical propagator F_0 will be the solution of the equation

$$\Big[\Box_x + m^2\Big]F_0(x, y) = 0 \tag{394}$$

with initial conditions given by the initial probability functional.

To reach at the evolution equations formulated in the same way that in the quantum case, we ought to define additional quantities. We start by introducing two 2-point functions, the retarded and advanced classical Green functions

$$G^R_{cl}(x, y) = \Theta(x^0 - y^0)\rho_{cl}(x, y) = G^A_{cl}(y, x) \tag{395}$$

We define the retarded classical self-energy as the difference between the inverse of the free and full retarded Green functions

$$\Sigma_{R,cl}(x, y) = (G^R_{cl})^{-1}(x, y) - (G^R_0)^{-1}(x, y) \tag{396}$$

where the free retarded Green function has the form

$$G^R_0(x, y) = \Theta(x^0 - y^0)\rho_0(x, y) \tag{397}$$

and solves the homogeneous equation

$$\Big[\Box_x + m^2\Big]G^R_0(x, y) = \delta(x - y) \tag{398}$$

with retarded boundary conditions. In the same way the advanced self-energy $\Sigma_{A,cl}$ is defined. Clearly, the retarded Green functions and self-energies vanish

when $x^0 < y^0$, and the advanced when $x^0 > y^0$. With these definitions we write (396) and its homologous equation for the advanced Green function as

$$\begin{aligned} G^R_{cl} &= G^R_0 - G^R_0 \cdot \Sigma_{R,cl} \cdot G^R_{cl} \\ G^A_{cl} &= G^A_0 - G^A_0 \cdot \Sigma_{A,cl} \cdot G^A_{cl} \end{aligned} \tag{399}$$

where we are making use of the compact notation

$$A \cdot B = A \cdot B(x,y) = \int dz A(x,z) B(z,y) \tag{400}$$

It is clear from the definition of G^R_{cl} y G^A_{cl} previously given that $\rho_{cl} = G^R_{cl} - G^A_{cl}$. Making use of it and combining equations (399) we get the *Schwinger-Dyson equation* for the classical spectral function

$$\rho_{cl} = \rho_0 - G^R_0 \cdot \Sigma_{R,cl} \cdot G^R_{cl} + G^A_0 \cdot \Sigma_{A,cl} \cdot G^A_{cl} \tag{401}$$

There is a similar expression for the classical statistical two-point function F_{cl}. Making again use of equations (399) we reach the following identity

$$F_{cl} = F_0 - G^R_0 \cdot \left[\Sigma_{R,cl} - (G^R_{cl})^{-1}\right] \cdot F_{cl} - F_0 \cdot \left[\Sigma_{A,cl} + (G^A_0)^{-1}\right] \cdot G^A_{cl} \tag{402}$$

Now we can define the *statistical component of the classical self-energy* as

$$\Sigma_{F,cl} = -(G^R_{cl})^{-1} F_{cl} (G^A_{cl})^{-1} + (G^R_0)^{-1} F_0 (G^A_0)^{-1} \tag{403}$$

and find the *Schwinger-Dyson equation* for the statistical propagator

$$F_{cl} = F_0 - G^R_0 \cdot \Sigma_{R,cl} \cdot F_{cl} - F_0 \cdot \Sigma_{A,cl} \cdot G^A_{cl} - G^R_0 \cdot \Sigma_{F,cl} \cdot G^A_{cl} \tag{404}$$

At last we are going to define the *classical spectral self-energy* by making manifest the retarded nature of $\Sigma_{R,cl}$ and the advanced of $\Sigma_{A,cl}$, by writing

$$\begin{aligned} \Sigma_{R,cl}(x,y) &= \Sigma^{(0)}_{cl}(x)\delta(x-y) + \Theta(x^0 - y^0)\Sigma_{\rho,cl}(x,y) \\ \Sigma_{A,cl}(x,y) &= \Sigma^{(0)}_{cl}(x)\delta(x-y) + \Theta(y^0 - x^0)\Sigma_{\rho,cl}(y,x) \end{aligned} \tag{405}$$

and is clearly obtained

$$\Sigma_{\rho,cl}(x,y) = \Sigma_{R,cl}(x,y) - \Sigma_{A,cl}(x,y) = -\Sigma_{\rho,cl}(y,x) \tag{406}$$

With all this, acting $\left[\Box_x + m^2\right]$ on (401) and (404), operating with all Θ functions, and having into account expressions (393), (394) and (398), we finally arrive to the exact evolution equations for ρ_{cl} and F_{cl}

$$\begin{aligned}\left[\Box_x + M_{cl}^2(x)\right] \rho_{cl}(x,y) &= -\int_{y^0}^{x^0} dz\, \Sigma_{\rho,cl}(x,z)\rho_{cl}(z,y) \\ \left[\Box_x + M_{cl}^2(x)\right] F_{cl}(x,y) &= -\int_{0}^{x^0} dz\, \Sigma_{\rho,cl}(x,z)F_{cl}(z,y) + \int_{0}^{y^0} dz\, \Sigma_{F,cl}(x,z)\rho_{cl}(z,y)\end{aligned} \tag{407}$$

where we have defined

$$M_{cl}^2(x) \equiv m^2 + \Sigma_{cl}^{(0)}(x) \tag{408}$$

and where abbreviated notation is used in the integration limits

$$\int_{t_1}^{t_2} dz \equiv \int_{t_1}^{t_2} dz^0 \int_{-\infty}^{\infty} d\mathbf{z} \tag{409}$$

The form of the classical evolution equations is the same as the quantum ones. If the initial conditions are equally chosen, the differences between the classical and quantum evolution come from the self-energies taking part in both equations. That means that when having a Gaussian-kind evolution (Hartree, LO in Large N, ...) the classical and quantum evolution will coincide, since Σ_F and Σ_ρ vanish in the same way as $\Sigma_{F,cl}$ and $\Sigma_{\rho,cl}$, and the $\Sigma^{(0)}$ and $\Sigma_{cl}^{(0)}$ contributions are the same.

8.5.2 2PI-Loop Approximation

We have found in the section of quantum fields, as is shown in (370), the expressions for the components of the self-energy $\Sigma_0, \Sigma_F, \Sigma_\rho$ in terms of the correlation functions F, ρ for the case of 2PI approximation on Loop-Expansion up to order $\hbar^3$. We see that such expressions indicate these quantities up to order λ^2.

On the other hand we have seen that F_{cl}, ρ_{cl} are the classical analogous of F, ρ, and they are in fact the same for the free case. So, as the evolution equations (366) and (407) have the same form, is clear that $\Sigma_{F,cl}, \Sigma_{\rho,cl}$ have to see the classical analogous of Σ_F, Σ_ρ. This means that we can calculate

the components of classical self-energy if we take the components of quantum self-energy given by (370), recover the $\hbar$ factors, and do the limit $\hbar \to 0$. Once the computation is performed one obtains [17]

$$\begin{aligned}
\Sigma_{cl}^{(0)}(x) &= \frac{N+2}{6N}\lambda F_{cl}(x,x) \\
\Sigma_{\rho,cl}(x,y) &= -\frac{N+2}{6N^2}\lambda^2 \rho_{cl}(x,y) F_{cl}^2(x,y) \\
\Sigma_{F,cl}(x,y) &= -\frac{N+2}{18N^2}\lambda^2 F_{cl}^3(x,y)
\end{aligned} \tag{410}$$

8.5.3 2PI-1/N Approximation

We can also make an analogy with the 2PI-1/N approximation previously studied in QFT. As explained above, we make the computation for QFT with the corresponding $\hbar$ factors and then take the classical limit $\hbar \to 0$. The expression for the self-energy components are [42][17]

$$\begin{aligned}
\Sigma_{cl}^{(0)}(x) &= \frac{N+2}{6N}\lambda F_{cl}(x,x) \\
\Sigma_{\rho,cl}(x,y) &= -\frac{\lambda}{3N}\Big(F_{cl}^2(x,y) I_{\rho,cl}(x,y) - \rho_{cl}(x,y) I_{F,cl}(x,y)\Big) \\
\Sigma_{F,cl}(x,y) &= -\frac{\lambda}{3N} F_{cl}(x,y) I_{F,cl}(x,y)
\end{aligned} \tag{411}$$

and for I_{cl}

$$\begin{aligned}
I_{F,cl}(x,y) &= \frac{\lambda}{6} F_{cl}^2(x,y) \\
&-\frac{\lambda}{6}\left[\int_0^{x^0} dz I_{\rho,cl}(x,z) F_{cl}^2(z,y) - 2\int_0^{y^0} dz I_{F,cl}(x,z) F_{cl}(z,y)\rho_{cl}(z,y)\right] \\
I_{\rho,cl}(t,t') &= \frac{\lambda}{3} F_{cl}(x,y)\rho_{cl}(x,y) - \frac{\lambda}{3}\int_{y_0}^{x^0} dz I_{\rho,cl}(x,z) F_{cl}(z,y)\rho_{cl}(z,y)
\end{aligned} \tag{412}$$

8.5.4 Classicality Condition

In the case of Loop Expansion (to 3 loops), if we compare (370) with (410) and the initial condition is the same then the quantum and classical evolution coincide approximately if

$$F^2(x,y) \gg \frac{3}{4}\rho^2(x,y) \quad \forall x,y \tag{413}$$

We can also consider the case of Large N at NLO and compare (383) and (384) with (457) and (458), obtaining the same classicality condition replacing the factor 3/4 by 1/4.
Of course, both conditions are valid as long as the approximations work well. When it is necessary to consider higher order diagrams the conditions can be modified.

8.6 2PI approximation for Quantum Mechanics

8.6.1 2PI Effective Action

For our purpose of testing the 2PI approximation in systems with a few degrees of freedom where the exact quantum evolution is available, we need to restrict the above methods to the particular case of quantum mechanics.
We will note the N degrees of freedom of a quantum mechanical system through a vector x with N components $x_a(t)$ only time dependent. Analogous quantities to the ones defined in the case of the 2PI effective action in QFT can be defined. And the same reasoning can be followed to obtain the corresponding evolution equations.
The *path-integral* with a local source $J(t)$ and a bilocal source $K(t,t')$ would be in this case

$$Z(J,K) = e^{iW(J,K)} = \int Dx\ exp\Big(i\Big[S(x) + \int dt\ J_a(t)x_a(t) + \\ + \frac{1}{2}\int dtdt'\, x_a(t)K_{ab}(t,t')x_b(t')\Big]\Big) \tag{414}$$

Now we define the expectation value of x_a as $\bar{x}_a$ and the connected 2-point function G_{ab} by means of variations of W with respect to the sources and being these sources present

$$\frac{\delta W(J,K)}{\delta J_a(t)} = \bar{x}_a(t)$$
$$\frac{\delta W(J,K)}{\delta K_{ab}(t,t')} = \frac{1}{2}[\bar{x}_a(t)\bar{x}_b(t') + G_{ab}(t,t')] \tag{415}$$

Here we also have a free propagator for the displaced action around $\bar{x}$

$$i\hbar G^{-1}_{0,ab}(t,t') = \frac{\delta^2 S(\bar{x})}{\delta\bar{x}_a(t)\delta\bar{x}_b(t')} \tag{416}$$

The effective action is defined by the corresponding double Legendre transform

$$\Gamma(\bar{x},G) = W(J,K) - \int dt \bar{x}_a(t) J_a(t) - \frac{1}{2}\int dt\, dt' K_{ab}(t,t')\bar{\phi}_a(t)\bar{\phi}_b(t') - \frac{1}{2}Tr(KG) \tag{417}$$

and taking derivatives the resultant equations are

$$\begin{aligned} \frac{\delta\Gamma(\bar{x},G)}{\delta\bar{x}_a(t)} &= -J_a(t) - \int d^4t'\, K_{ab}(t,t')\bar{x}_b(t') \\ \frac{\delta\Gamma(\bar{x},G)}{\delta G_{ab}(t,t')} &= -\frac{1}{2}K_{ab}(t,t') \end{aligned} \tag{418}$$

giving place to the stationary equations for $\bar{x}$ and G once the sources are removed.

We define $\Gamma_2(\bar{x},G)$ in compact matrix notation as

$$\Gamma(\bar{x},G) = S(\bar{x}) + \frac{i}{2}Tr(lnG^{-1}) + \frac{i}{2}Tr(G_0^{-1}(\bar{x})G) + \Gamma_2(\bar{\phi},G) \tag{419}$$

taking variations of this expression with respect to $G(t,t')$ the *Schwinger-Dyson Equation* follows

$$G^{-1}_{ab}(t,t') = G^{-1}_{0,ab}(t,t') - iK_{ab}(t,t') - \Sigma_{ab}(t,t') \tag{420}$$

where we have:

$$\Sigma_{ab}(t,t') \equiv 2i\frac{\delta\Gamma_2(\bar{\phi},G)}{\delta G_{ab}(t,t')} \tag{421}$$

This Σ_{ab} is actually the self-energy, that is, the contribution of all diagrams 1PI built with the propagator $(G^{-1}_{0,ab} - iK_{ab})^{-1}$. It will be the traditional self-energy once the sources are removed.

In the same manner as in QFT, here Γ_2 is made by the contribution of all 2PI diagrams with lines representing G_{ab} and vertices corresponding to the interaction of the displaced action around $\bar{x}$, $S_{int}(\bar{x},x')$.

Evolution equations

We take also here the symmetric case ($\bar{x}=0$) and an action with a $O(N)$ symmetry. Hence the propagator is then diagonal in the field components:

$$G_{ab}(t,t') = G(t,t')\delta_{ab} \tag{422}$$

We define, in an analogous way to QFT, the statistical and spectral functions and the self-energy components

$$\begin{aligned}
&\rho(t,t') \equiv i\big\langle [x(t), x(t')]\big\rangle \\
&F(t,t') \equiv \frac{1}{2}\big\langle \{x(t), x(t')\}\big\rangle \\
&\Sigma(t,t') = -i\Sigma^{(0)}(t)\delta(t-t') + \Sigma_F(t,t') - \frac{i}{2}\Sigma_\rho(t,t')sign(t-t') \\
&M^2(t) \equiv m^2 + \Sigma^{(0)}(t)
\end{aligned} \tag{423}$$

The relationship between propagator G and F, ρ still holds

$$G(t,t') = F(t,t') - \frac{i}{2}\rho(t,t')sign(t-t') \tag{424}$$

And also symmetry properties with respect to argument interchange remain the same: F, Σ_F are symmetric whereas ρ, Σ_ρ are antisymmetric.

Following a similar reasoning that in QFT, we arrive to the analogous set of evolution equations

$$\begin{aligned}
\left[\partial_t^2 + M^2(t)\right]\rho(t,t') &= -\int_{t'}^{t} dt''\,\Sigma_\rho(t,t'')\rho(t'',t') \\
\left[\partial_t^2 + M^2(t)\right]F(t,t') &= -\int_0^t dt''\,\Sigma_\rho(t,t'')F(t'',t') + \int_0^{t'} dt''\,\Sigma_F(t,t'')\rho(t'',t')
\end{aligned} \tag{425}$$

8.6.2 2PI-Loop Approximation

We consider the action

$$S(x) = \int dt \left[\frac{1}{2}\dot{x}_a(t)\dot{x}_a(t) - \frac{1}{2}w^2(t)x_a(t)x_a(t) - \frac{\lambda}{4!\,N}(x_a(t)x_a(t))^2\right] \tag{426}$$

As it is $O(N)$ symmetric the propagator is diagonal. Furthermore we consider the symmetric case $\bar{x} = 0$. In the same way as in QFT we consider the 2PI diagrams contributing to Γ_2 up to 3 loops, which are the ones that were shown in Fig. 64 having

$$\Gamma_2^{(3loop)} = -\frac{\lambda(N+2)}{24}\int dt\, G^2(t,t) + \frac{i\lambda^2(N+2)}{144N}\int dt\, dt'\, G^4(t,t')$$

here the self-energy components in this approximation are obtained

$$\Sigma^{(0)}(t)\delta(t-t') = \lambda\frac{N+2}{6N}F(t,t')\delta(t-t')$$
$$\Sigma_\rho(t,t') = -\lambda^2\frac{N+2}{6N^2}\rho(t,t')\left[F^2(t,t') - \frac{1}{12}\rho^2(t,t')\right]$$
$$\Sigma_F(t,t') = -\lambda^2\frac{N+2}{18N^2}F(t,t')\left[F^2(t,t') - \frac{3}{4}\rho^2(t,t')\right] \qquad (427)$$

Numerical implementation

From (425) and (427), in order to implement the numerical evolution on a computer we need initial values for ρ and F. In fact, from the equal-time commutation relations of the quantum variables, we obtain relations for ρ similar to the obtained in (359)

$$\rho(t,t')|_{t=t'} = 0 \quad ; \quad \partial_t\rho(t,t')|_{t=t'} = \delta(t-t') \qquad (428)$$

Which means that using a time step a_t in the discretization, initial values of ρ are given, being in a_t units

$$\rho(0,0) = \rho(1,1) = 0 \quad ; \quad \rho(1,0) = -\rho(0,1) = a_t \qquad (429)$$

And are also given the diagonal and immediate under and above diagonal values for any other time

$$\rho(n,n) = 0 \quad ; \quad \rho(n+1,n) = -\rho(n,n+1) = a_t \qquad (430)$$

So on, in order to follow the evolution we really need the following initial values of F

$$F(0,0) \;\; ; \;\; F(1,0) = F(0,1) \;\; ; \;\; F(1,1) \qquad (431)$$

The first is obtained directly from the initial wave-function. The last is computed by making a single step in the exact numerical evolution of the wave-function and getting the $< x^2(1) >= F(1,1)$. Or by making a single step in the Gaussian evolution which will be exact up to order a_t. Also we can make one step with the classical evolution.
The remaining term can be deduced from $< p^2(0) >$ and $< x^2(1) >$

$$F(1,0) = \frac{1}{2}\left[< x^2(1) > + < x^2(0) > -a_t^2 < p^2(0) >\right] \qquad (432)$$

Now we have all the necessary to implement the numerical evolution. It will allow us to find the usual expectation values for every time in the following way

$$\begin{aligned}
&\big\langle x^2(t)\big\rangle = F(t,t)\\
&\frac{1}{2}\big\langle\{x(t),p(t)\}\big\rangle = \partial_t F(t,t)\\
&\big\langle p^2(t)\big\rangle = \partial_t\partial_{t'}F(t,t)
\end{aligned} \tag{433}$$

8.6.3 2PI-1/N Approximation

In the same way as in the QFT case, we consider the 2PI effective action Γ_2 for a quantum mechanical system and we keep the diagram shown in Fig. 65 and the infinite sum of diagrams from Fig. 66. This gives an expression for the self-energy in the form:

$$\Sigma_{ab}(t,t') = -i\frac{\lambda}{6N}\Big(\sum_c G_{cc}(t,t)\Big)\,\delta_{ab}\,\delta^4(t-t') - i\frac{\lambda}{3N}G_{ab}(t,t')B^{-1}(t,t') \tag{434}$$

We also define the quantity I in a similar way

$$I(t,t') \equiv iB^{-1}(t,t') - i\delta^4(t-t') \tag{435}$$

and its components

$$I(t,t') \equiv I_F(t,t') - \frac{i}{2}I_\rho(t,t')sign(t-t') \tag{436}$$

We also restrict ourselves to the symmetric case ($\bar{x}=0$) and consider a $O(N)$ symmetric action. Performing the computations in a similar way as in QFT, we can find the different quantities incoming in the evolution equations in terms of F and ρ. We obtain for the self-energy components

$$\begin{aligned}
\Sigma_F(t,t') &= -\frac{\lambda}{3N}\Big(F(t,t')I_F(t,t') - \frac{1}{4}\rho(t,t')I_\rho(t,t')\Big)\\
\Sigma_\rho(t,t') &= -\frac{\lambda}{3N}\Big(F(t,t')I_\rho(t,t') + \rho(t,t')I_F(t,t')\Big)\\
M^2(t) &\equiv m^2 + \Sigma^{(0)}(t) = m^2 + \lambda\frac{N+2}{6N}\,F(t,t)
\end{aligned} \tag{437}$$

and for the I components

$$I_F(t,t') = \frac{\lambda}{6}\Big(F^2(t,t') - \frac{1}{4}\rho^2(t,t')\Big) -$$
$$-\frac{\lambda}{6}\Bigg[\int_0^t dt'' I_\rho(t,t'')\Big(F^2(t'',t') - \frac{1}{4}\rho^2(t'',t')\Big) -$$
$$-2\int_0^{t'} dt'' I_F(t,t'')F(t'',t')\rho(t'',t')\Bigg]$$
$$I_\rho(t,t') = \frac{\lambda}{3}F(t,t')\rho(t,t') - \frac{\lambda}{3}\int_t^{t'} dt'' I_\rho(t,t'')F(t'',t')\rho(t'',t') \quad (438)$$

We find these equations a little more simpler than in QFT as expected, since they have integrations where only the temporal variable is involved in.

These expressions together with the evolution equations (425) conform the 2PI approximation on Large N.

Numerical Implementation

As mentioned previously we perform the numeric implementation in the same way as in the 2PI approximation on Loop Expansion case. Some differences arise though. The needed initial quantities are the same than before with the addition of the initial components of I. They are easy to obtain from the known initial values of F and ρ. Focusing in (438), initially the integrated terms vanish, and we have in a_t units

$$I_F(0,0) = \frac{\lambda}{6}F^2(0,0) \;\; ; I_\rho(0,0) = 0 \quad (439)$$

since I_ρ is antisymmetric we also have

$$I_\rho(1,1) = 0 \quad (440)$$

Analyzing the integrated term in the I_ρ expression it is easily seen

$$I_\rho(1,0) = -I_\rho(0,1) = \frac{\lambda}{3}F(1,0)\rho(1,0) \quad (441)$$

and also analyzing the integrated terms for I_F it results

$$I_F(1,0) = I_F(0,1) = \frac{\lambda}{6}\Big(F^2(t,t') - \frac{1}{4}\rho^2(t,t')\Big) - \frac{\lambda}{6}a_t I_\rho(1,0)F^2(0,0) \quad (442)$$

Hence all the needed for the implementation of the numeric evolution is now achieved.

8.7 2PI Approximation for Classical Mechanics

As mentioned, we need to restrict the expressions obtained for fields to the case of zero space-dimensions. This is also valid for the 2PI method in the classical case.
In an analogous way to CFT, we can define classical quantities for a classical mechanics system in a way that a set of evolution equations formally equal to the quantum mechanics case are obtained, and where F_{cl} and ρ_{cl} are the classical analogous of F and ρ. For this we consider a classical distribution function $W(x,p)$ in phase-space (in the studied cases this function will be the Wigner function).

We take a real classical variable with N components and an action given by (426). The classical equations of motion for each component will be

$$\left[\partial_t^2 + m^2 + \frac{\lambda}{6N} x_b(t) x_b(t)\right] x_a(t) = 0 \tag{443}$$

which solution requires to specify $x(0)$ and $p(0)$ with $p_a(t) = \dot{x}_a(t)$. We define the mean value of the classical variable as:

$$\bar{x}_{a,cl}(t) = \langle x_a(t) \rangle_{cl} \equiv \int Dx\, Dp\; W(x,p) x_a(t) \tag{444}$$

where W is normalized at initial time.
The *connected statistical classical propagator* has the form

$$F_{ab,cl}(t,t') + \bar{x}_{a,cl}(t)\bar{x}_{b,cl}(t') = \langle x_a(t) x_b(t') \rangle_{cl} = \int Dx\, Dp\, W(x,p) x_a(t) x_b(t') \tag{445}$$

and the *classical spectral function* will be

$$\rho_{ab,cl}(t,t') = -\langle \{x_a(t), x_b(t')\}_{PoissonBracket} \rangle_{cl} \tag{446}$$

From where the equal-time relations for the classical spectral function are deduced

$$\rho_{ab,cl}(t,t')|_{t=t'} = 0 \; ; \; \partial_t \rho_{ab,cl}(t,t')|_{t=t'} = \delta_{ab} \tag{447}$$

and though the origin is different, they result to be the same as the quantum case. We explicitly write the meaning of the Poisson bracket

$$\{A(t), B(t')\}_{PB} = \sum_{a=1}^{N} \Big[\frac{\delta A(t)}{\delta x_a(0)} \frac{\delta B(t')}{\delta p_a(0)} - \frac{\delta A(t)}{\delta p_a(0)} \frac{\delta B(t')}{\delta x_a(0)} \Big] \tag{448}$$

From now on we consider $W(x,p)$ having $O(N)$ symmetry and that we are in the symmetric regime ($\bar{x} = 0$). So F and ρ will be diagonal in the components of the quantum variable.

Now we introduce the retarded and advanced classical Green functions

$$G^R_{cl}(t,t') = \Theta(t-t')\rho_{cl}(t,t') = G^A_{cl}(t',t) \tag{449}$$

And we define the retarded and advanced classical self-energy

$$\Sigma_{R,cl}(t,t') = (G^R_{cl})^{-1}(t,t') - (G^R_0)^{-1}(t,t') = \Sigma_{A,cl}(t',t) \tag{450}$$

where the free retarded Green function is

$$G^R_0(t,t') = \Theta(t-t')\rho_0(t,t') = G^A_0(t',t) \tag{451}$$

With respect to the self-energy components, we define on one hand

$$\Sigma_{F,cl} = -(G^R_{cl})^{-1} F_{cl} (G^A_{cl})^{-1} + (G^R_0)^{-1} F_0 (G^A_0)^{-1} \tag{452}$$

and the other components are

$$\begin{aligned} \Sigma_{R,cl}(t,t') &= \Sigma^{(0)}_{cl}(t)\delta(t-t') + \Theta(t-t')\Sigma_{\rho,cl}(t,t') \\ \Sigma_{A,cl}(t,t') &= \Sigma^{(0)}_{cl}(t)\delta(t-t') + \Theta(t'-t)\Sigma_{\rho,cl}(t',t) \\ M^2_{cl}(t) &\equiv m^2 + \Sigma^{(0)}_{cl}(t) \end{aligned} \tag{453}$$

The $\Sigma_{F,cl}$ is symmetric whereas the $\Sigma_{\rho,cl}$ is antisymmetric with respect to argument interchange.

Applying the classical equations of motion and reasoning in the same way as in the CFT case we arrive to the same equations as the obtained for a quantum mechanics system, but replacing the quantum quantities by the classical

ones

$$\left[\partial_t^2 + M_{cl}^2(t)\right] \rho_{cl}(t,t') = -\int_{t'}^{t} dt'' \, \Sigma_{\rho,cl}(t,t'')\rho_{cl}(t'',t')$$
$$\left[\partial_t^2 + M_{cl}^2(t)\right] F_{cl}(t,t') = -\int_{0}^{t} dt'' \, \Sigma_{\rho,cl}(t,t'')F_{cl}(t'',t') + \int_{0}^{t'} dt'' \, \Sigma_{F,cl}(t,t'')\rho_{cl}(t'',t') \tag{454}$$

8.7.1 2PI-Loop Approximation

In an analogous way to the CFT case, we can obtain the components of the self-energy if we recover the $\hbar$ factors in the quantum mechanical case and take the classical limit. We obtain the analogous expressions to the CFT case

$$\Sigma_{cl}^{(0)}(t) = \frac{N+2}{6N}\Big[\lambda F_{cl}(t,t) - \lambda^2 \int_0^t dt'' \; \rho_{cl}(t,t'')F_{cl}(t,t'')F_{cl}(t'',t'')\Big]$$
$$\Sigma_{\rho,cl}(t,t') = -\frac{N+2}{6N^2}\lambda^2 \rho_{cl}(t,t')F_{cl}^2(t,t')$$
$$\Sigma_{F,cl}(t,t') = -\frac{N+2}{18N^2}\lambda^2 F_{cl}^3(t,t') \tag{455}$$

Classicality Condition

In the case of the 2PI approximation on Loop Expansion it is possible to compare (427) with (455) and the following classicality condition is immediately obtained:

$$F^2(t,t') >> \frac{3}{4}\rho^2(t,t') \tag{456}$$

Clearly, since only up to λ^2 order diagrams have been considered, this classicality condition would be only valid (in principle) whereas the approximation applies. That means that in case of a highly non-lineal behavior where other orders must be considered, this condition will be modified and its validity will be not ensured as is exposed. For that reason, we will probe it numerically in some particular cases.

8.7.2 2PI-1/N Approximation

Here also, analogous expressions to CFT are obtained. For the self-energy components

$$\Sigma_{cl}^{(0)}(t) = \frac{N+2}{6N}\lambda F_{cl}(t,t)$$
$$\Sigma_{\rho,cl}(t,t') = -\frac{\lambda}{3N}\Big(F_{cl}^2(t,t')I_{\rho,cl}(t,t') - \rho_{cl}(t,t')I_{F,cl}(t,t')\Big)$$
$$\Sigma_{F,cl}(t,t') = -\frac{\lambda}{3N}F_{cl}(t,t')I_{F,cl}(t,t') \tag{457}$$

and for the I_{cl} components:

$$I_{F,cl}(t,t') = \frac{\lambda}{6}F_{cl}^2(t,t')$$
$$-\frac{\lambda}{6}\left[\int_0^t dt'' I_{\rho,cl}(t,t'')F_{cl}^2(t'',t') - 2\int_0^{t'} dt'' I_{F,cl}(t,t'')F_{cl}(t'',t')\rho_{cl}(t'',t')\right]$$
$$I_{\rho,cl}(t,t') = \frac{\lambda}{3}F_{cl}(t,t')\rho_{cl}(t,t') - \frac{\lambda}{3}\int_{t'}^t dt'' I_{\rho,cl}(t,t'')F_{cl}(t'',t')\rho_{cl}(t'',t') \tag{458}$$

Classicality Condition

Comparing (457) and (458) with (437) and (438) we obtain the classicality condition arising in this approximation:

$$F^2(t,t') >> \frac{1}{4}\rho^2(t,t') \tag{459}$$

We see that it is less restrictive than the condition obtained in the Loop Expansion case, since the fraction in the right side was 3/4.

9 New Results for 2PI Approximations

In this chapter, we will present some new results about the 2PI approximation. First of all we will show that the 2PI classicality condition presented in the previous chapter is indeed a sufficient condition independent of the level of approximation used. Next we will present a new method which we will call *Hybrid Method*, which combines the 2PI approximation (classical and quantum) with the full classical approximation.
The remaining part of this chapter will be devoted to testing the 2PI approximation for several simple quantum mechanical systems. The first systems to be analyzed are the time-dependent Hamiltonians used to mimick the hybrid inflation model presented in chapter 1. Later in this chapter we will present the results of our systematic study, in which we will monitor the accuracy of the 2PI approximations as a function of the dimensionless control parameters r_1 and r_2 introduced earlier. This will be done for two types of quartic potentials: a single well potential with its minimum at $x = 0$, and a double well potential with two minima. These potentials are widely used in QFT, and serve as prototypes of symmetric and symmetry-breaking conditions.
The previous numerical results were obtained for the 2PI-Loop, the 2PI-1/N approximations to NLO and for the hybrid method. The 2PI-Loop case, however, blows up for large times, so we excluded it from the systematic study. This divergent behavior has been reported in the literature [87][91]. The classicality condition will also be tested.
From now on, we take natural units ($\hbar = c = 1$).

9.1 Sufficient condition for classicality from 2PI

For QFT, the classicality condition (413) (with the corresponding factor) tell us that the square of the statistical two-point function must be much greater than the square of the spectral function for any x, y. As we said, this condition is valid as long as the 2PI-Loop approximation or the 2PI-NLO approximation are valid. If the influence of the non-linear term becomes large then it would be necessary to consider other orders and the corresponding expressions could lead to a different classicality condition.
On the other hand, the Schwinger-Dyson equation relates the full propagator $G(x, y) = \langle T(\phi(x)\phi(y))\rangle$ with the free propagator $G_0(x, y) = \langle T(\phi_0(x)\phi_0(y))\rangle$ and the self-energy $\Sigma(x, y)$. As mentioned, Σ comes from the contribution of

all 1PI diagrams with lines associated to G_0, but it can also be built with the contribution of all 1PI diagrams with lines associated to G and a sign change.

Now we will employ the Fourier modes $F(t,t';k)$, $\rho(t,t';k)$, $\Sigma_F(t,t';k)$ and $\Sigma_\rho(t,t';k)$, where we take into account that the two point functions only depend of one mode k. The expressions for these components of the self-energy can be seen in [17] for the two approximations that we are using, in the quantum and classical case. The classicality condition take the form

$$|F(t,t';k)F(t,t';k')| >> |\rho(t,t';k)\rho(t,t';k')| \tag{460}$$

This condition has to be fulfilled for all times and all momenta to ensure that quantum and classical evolution agree (as long as the used approximations work well).

We can also apply the Fourier transform to the free and full propagator, and separate their real and imaginary parts

$$\begin{aligned} G(t,t';k) &= F(t,t';k) - \tfrac{i}{2}\text{sign}(t-t')\rho(t,t';k) \\ G_0(t,t';k) &= G_{k,S}(t,t') + i\text{sign}(t-t')G_{k,A}(t,t') \end{aligned} \tag{461}$$

where we have used (245). The symmetry properties of $F(t,t';k), \rho(t,t';k)$ are the same as $G_{k,S}(t,t'), G_{k,A}(t,t')$ respectively.

Remember now the perturbative expansion shown in chapter 6 for the equal-time propagator $G(t,t;k)$. The series (351) involves $\Sigma(t',t'';k)$ for different times although we only have considered equal times in G, then this case actually includes all diagrams that contribute to the self-energy. So the contribution of all 1PI diagrams with solid lines associated to $G_{k,S}$ and dotted lines associated to $G_{k,A}$ corresponds to self-energy $\Sigma(t,t';k)$. And the contribution of the same diagrams replacing $G_{k,S}(t,t';k) \to F(t,t';k)$ and $G_{k,A}(t,t';k) \to (-1/2)\rho(t,t';k)$ corresponds to $-\Sigma(t,t';k)$. But the difference between the quantum and classical evolution was the contribution of non-minimal diagrams, which came from transform pairs of solid lines with a common vertex inside minimal diagrams into dotted lines (and a possible additional factor $\leqslant 3$). Therefore, if we demand the condition that each minimal diagram has a contribution much greater than any associated non-minimal one, then we can deduce a condition that ensures the classical behavior involving all perturbative orders. Thus, we have a condition as in (460) but now with the status of *Sufficient Condition*

$$|F(t,t';k)F(t,t';k')| >> \frac{1}{4}|\rho(t,t';k)\rho(t,t';k')| \tag{462}$$

If we suppose that evolve a system to time t, we can write this condition in an equivalent form

$$max\Big[\frac{\rho^2(t',t'';k)}{4F^2(t',t'';k)}\Big] \ll 1 \tag{463}$$

for any $t', t'' \leqslant t$. Of course, there may be many cases with a classical behavior where the condition (463) is not fulfilled, as we will show later.
In the particular case of Quantum Mechanics we can follow the same reasoning than above and the condition (462) results

$$F^2(t,t') \gg \frac{1}{4}\rho^2(t,t') \tag{464}$$

Thus, when one evolve the system to time t, the condition analogous to (463) is

$$\max\Big[\frac{\rho^2(t',t'')}{4F^2(t',t'')}\Big] \ll 1 \tag{465}$$

for any $t', t'' \leqslant t$. This condition can be written in a more suitable form. We define

$$\begin{aligned} B(t') &\equiv \max_{t''<t'}\Big[\frac{\rho^2(t',t'')}{4F^2(t',t'')}\Big] \\ C(t) &\equiv \max_{t'<t}[B(t')] \end{aligned} \tag{466}$$

Now we can rewrite the condition (465) as

$$C(t) \ll 1 \tag{467}$$

The value of $B(t')$ can increase or decrease along time. But the value of $C(t)$ is always increasing.

9.2 Hybrid Method

We present here the hybrid method as an alternative method to perform non-linear quantum evolution.
When we consider the 2PI-Loop (to 3 loops) approximation or the 2PI-1/N to NLO approximation we choose a subset of all diagrams that contribute to the self-energy. We can involve more diagrams if we perform the 2PI-Loop approximation to $n > 3$ loops. Also if we perform the 2PI-1/N to NNLO approximation or higher orders. Anyway, each diagram with a definite topology

is associated to a set of diagrams (with the same topology) with solid and dashed lines that represent F and $(-1/2)\rho$ respectively (see last chapter). In the quantum case this set includes minimal and non-minimal diagrams. In the classical case only minimal diagrams are included. Thus, in any of these approximations, all classical diagrams are included in the set of quantum diagrams and the difference is a subset of non-minimal diagrams.
On the other hand, as we have said in last chapter, all diagrams that contribute to $\Sigma(t', t''; k)$ are included in the Rules that we saw in chapter 4 and extended to QFT in chapter 5. Therefore, if we focus on the series similar to (351) for the unequal time two-point function $G(t, t'; k)$ then we deduce that the same Rules are valid for this case, and the diagrams are the same with different times in the external vertices.
Moreover, remember that the classical approximation involve the full set of classical (minimal) diagrams. Thus, suppose that we choose a 2PI approximation (Loop or 1/N to a concrete order) for the quantum case and use it to evolve our system and calculate any two-point function $A_{2PI}(t, t'; k)$, then we can use the same approximation for the classical case and calculate $A_{2PI-Cl}(t, t'; k)$. Also we can perform the full classical evolution and calculate $A_{Cl}(t, t'; k)$. All diagrams involved in the calculation of $A_{2PI-Cl}(t, t'; k)$ are included in the calculation of $A_{2PI}(t, t'; k)$ and $A_{Cl}(t, t'; k)$. However, $A_{2PI}(t, t')$ involve no-minimal diagrams that are not included in the other two-point functions. Therefore, if we define a new two-point function as

$$A_{Hybrid}(t, t'; k) \equiv A_{Cl}(t, t'; k) + A_{2PI}(t, t'; k) - A_{2PI-Cl}(t, t'; k) \qquad (468)$$

then $A_{Hybrid}(t, t'; k)$ involve all classical (minimal) diagrams and the non-minimal ones included in $A_{2PI}(t, t'; k)$. We note this method as *Hybrid Method* and we expect it to work better than the classical and the 2PI approximation. We will show this later for systems in QM.
The case of QM is a particular case where one can follow the same reasoning that above. Thus, if we calculate a two-point function A with the 2PI approximation (in any of their different methods) ($A_{2PI}(t, t')$), with the 2PI Classical approximation ($A_{2PI-Cl}(t, t')$) and with the full classical approximation ($A_{Cl}(t, t')$), we can define a new two-point function $A_{Hybrid}(t, t')$ similarly to (469)

$$A_{Hybrid}(t, t') \equiv A_{Cl}(t, t') + A_{2PI}(t, t') - A_{2PI-Cl}(t, t') \qquad (469)$$

It is interesting to test if the Hybrid Method give us a new classicality condition, i.e., if the relative difference between $A_{2PI}(t, t')$ and $A_{2PI-Cl}(t, t')$

represents the genuine difference between the true quantum value $A_Q(t,t')$ and classical one $A_{Cl}(t,t')$. We plain check this inside of the systematic study about the methods.

9.3 Analysis of simple QM systems: $w^2(t) = c_0 - u_0 t$

As in the case studied in chapter 6, we take a Hamiltonian where the coefficient of the quadratic term of the potential depends linearly on time

$$H(x,p,t) = \frac{1}{2}p^2 + \frac{1}{2}(c_0 - u_0 t)x^2 + \frac{\lambda}{24}x^4 \tag{470}$$

All the parameters are dimensionless as shown in (176). The values of these parameters are the same as in chapter 6 and can be seen in (177). The initial condition is again the ground state of the system with $\lambda = 0$ at $t = 0$, as one can see in (178).
We have used the 2PI approximation to calculate the evolution of two-point functions, and we are going to compare the results with the exact and the classical evolution. We show in Fig. 68 the evolution of $\langle x^2(t)\rangle$ for the numerical exact and the classical case as well as for the 2PI-Loop approximation to 3 loops (noted as 2PI-3Loop) and the 2PI-1/N to NLO approximation. The classical evolution work very well. The NLO 2PI-1/N evolution presents a little delay and has a damping in its oscillations. The 2PI-3Loop evolution work well at first but blows up at later times.

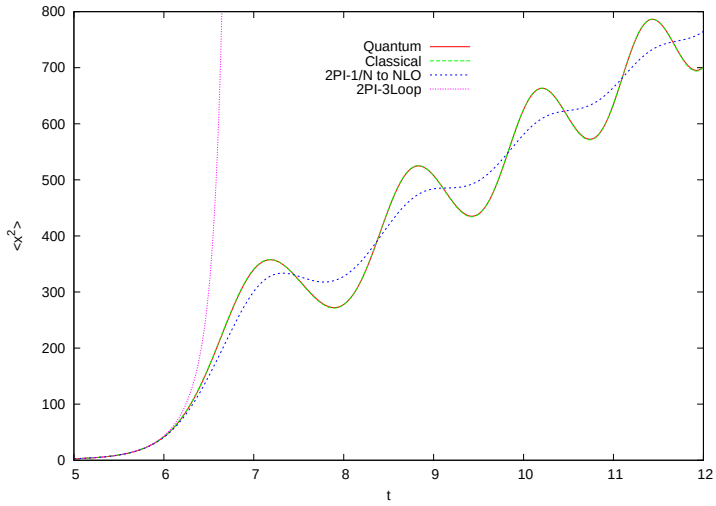

Figure 68: $\langle x^2(t)\rangle$ for the numerical exact quantum evolution and for the different approximations.

We also display the result for $\langle p^2(t)\rangle$ in Fig. 69. The classical approximation works well. The 2PI-1/N to NLO approximation presents here more delay and damping in its oscillations and its mean value tends to become smaller at later times. Again the 2PI-3Loop approximation behaves properly at early times, but diverges at larger ones. This feature is presented in all the cases studied. To see this, we display in Fig. 70 the relative difference between the quantum evolution and the 2PI approximations. At early times the 2PI-3Loop evolution is better than the NLO one, but afterwards becomes divergent. This behavior makes this approximation not useful in most of cases, except for checking the validity of other approximations in the first instants of evolution. Therefore, as mentioned, we will discard the 2PI-3Loop approximation later (except in the case of hyperbolic tangent that we will see in the following section). In a previous section we presented a sufficient condition for classicality (467) extracted from the perturbative expansion. We want to test if this condition is fulfilled in our case. We show in Fig. 71 the value of $B(t)$. The curve of $C(t)$ is the same up to the maximum value of $B(t)$ (at t=6.34), an after their has a constant value. Clearly, the condition is valid for our system. On the other hand, we have seen that the classical evolution works very well, so we expect that the 2PI-1/N to NLO evolution and the 2PI-1/N to NLO Classical evolution agree. Indeed one can see this

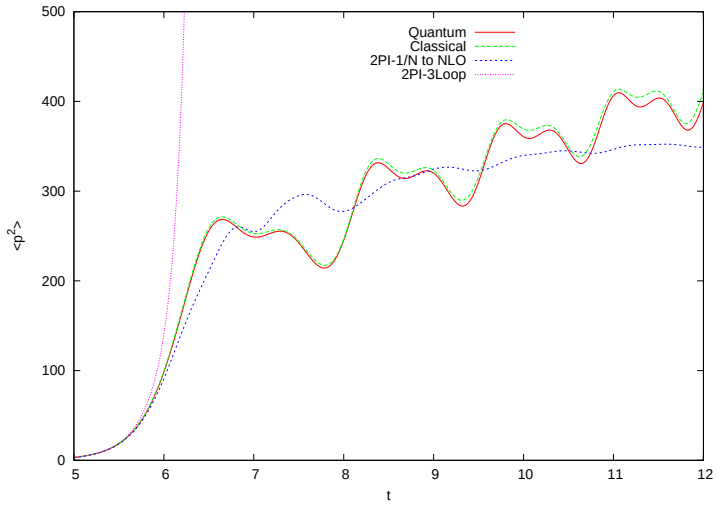

Figure 69: The same as in Fig. 68 for the $\langle p^2(t)\rangle$.

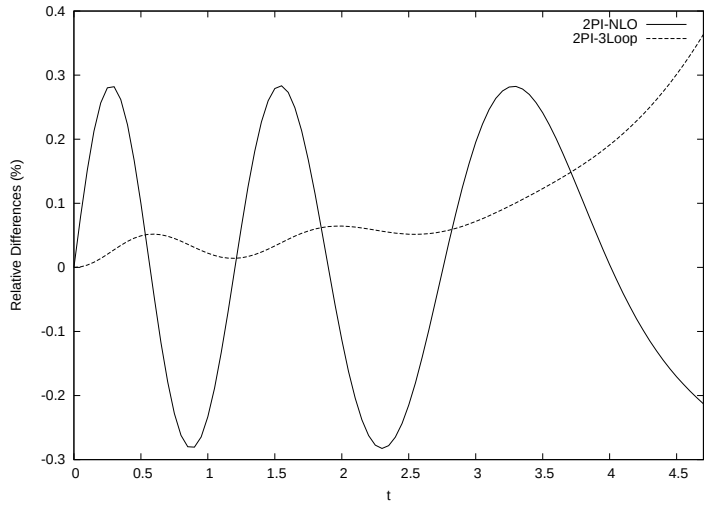

Figure 70: Relative differences between the quantum evolution and the 2PI approximations that we are using.

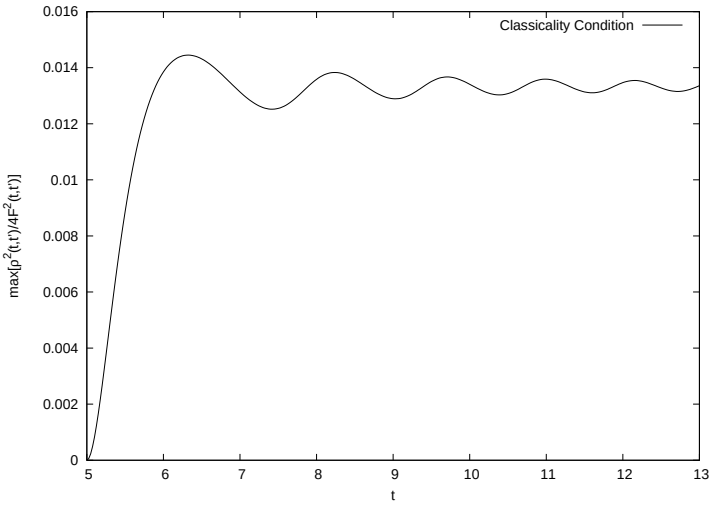

Figure 71: In this case the sufficient classicality condition is fulfilled.

in Fig. 72, where both evolutions completely match. This means that in our system, the hybrid method and the classical approximation also match.

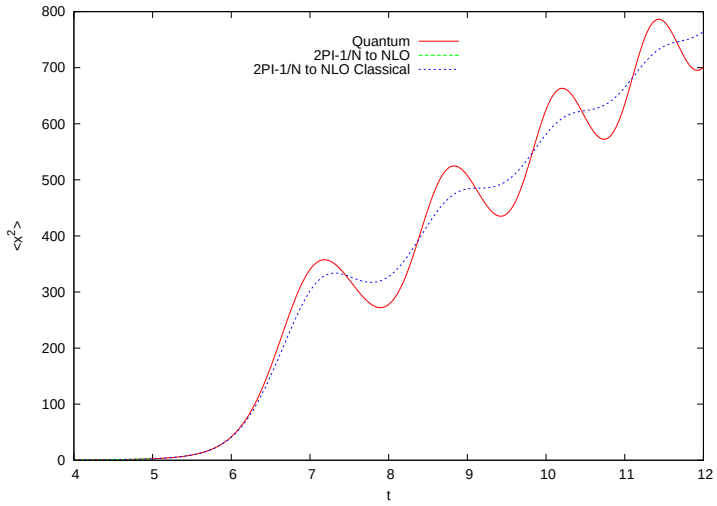

Figure 72: The 2PI-1/N to NLO evolution and the 2PI-1/N to NLO Classical evolution completely match, and this is an indication that the classical evolution works well.

9.4 Analysis of simple QM systems: $w^2(t) = 4\tanh(c_0 - u_0 t)$

Now we will present the results for a Hamiltonian similar to (470), but such that the coefficient of quadratic term of potential has the form $w^2(t) = 4tanh(c_0 - u_0 t)$. Again all quantities and parameters are dimensionless. The value of parameters and the initial condition can be viewed in (190). The initial state is the same as in the previous case.
We display in Fig. 73 the value of $\langle x^2(t)\rangle$ for the quantum evolution and for the different approximations. The classical evolution works very well. The 2PI-1/N to NLO evolution has a little delay in the first oscillation and an increasing advance in the subsequent oscillations, besides the characteristic damping around the mean quantum value. The 2PI-3Loop approximation work well at first but blows up later. In Fig. 74 we show the result for $\langle p^2(t)\rangle$. The classical approximation works well. The 2PI-1/N to NLO approximation has a fast damping although it oscillates around the quantum mean value (unlike the linear case). The 2PI-3Loop approximation acquires again a divergent behavior.

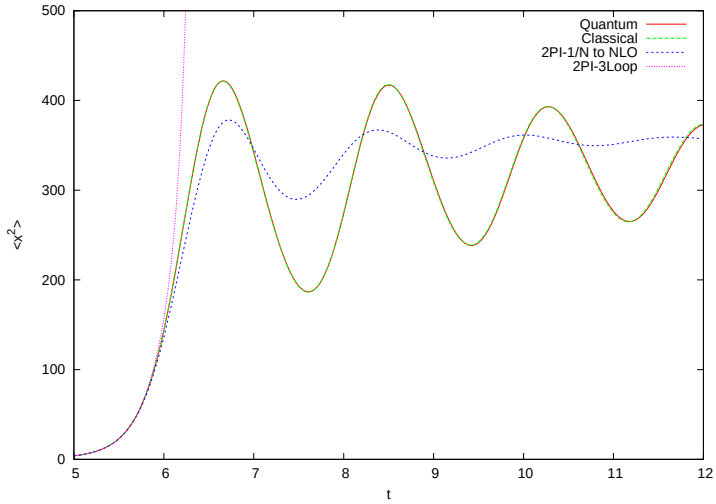

Figure 73: $\langle x^2(t)\rangle$ for the numerical exact quantum evolution and for the different approximations in the case of hyperbolic tangent.

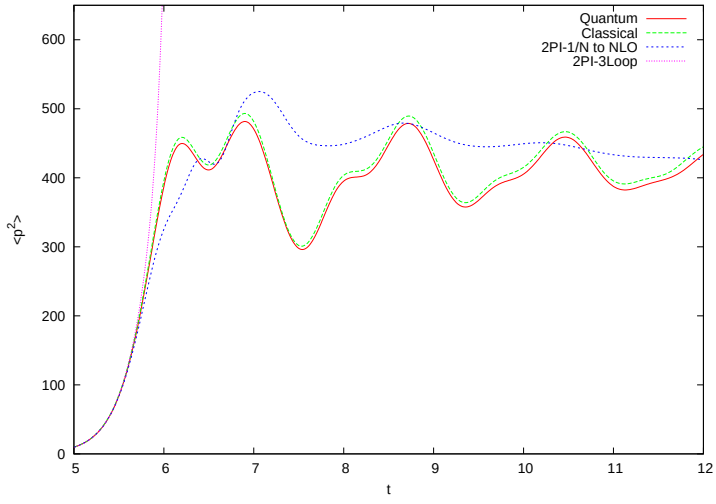

Figure 74: The same as in Fig. 73 for the $\langle p^2(t)\rangle$.

As in the linear case, the 2PI-3Loop evolution works better than the 2PI-1/N to NLO one at the initial times and after becomes divergent. This can be seen in Fig. 75.

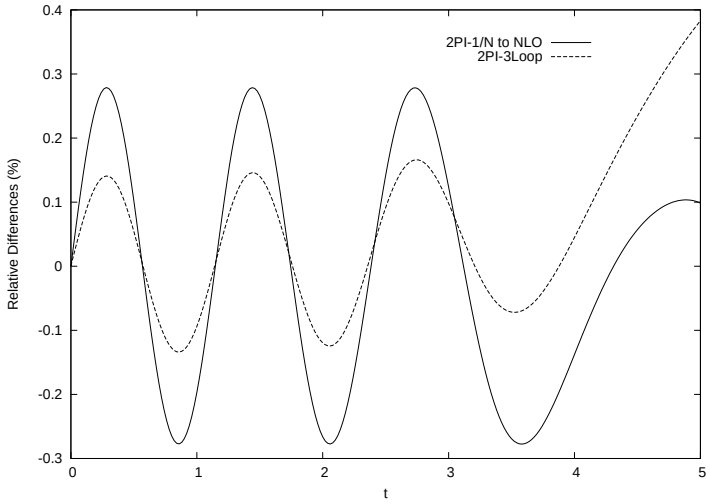

Figure 75: Relative differences between the quantum evolution and the 2PI approximations.

In order to test the condition (465) we display $B(t)$ for each fixed value of t in Fig. 76. The condition holds even better than in the linear case.

Finally, we test if the difference between the 2PI-1/N to NLO quantum and classical evolution is indicative of the classical behavior of the system. One can observe in Fig. 77 how the 2PI-1/N to NLO quantum and classical evolutions match, indicating that the classical approximation has to work well, as indeed occurs.

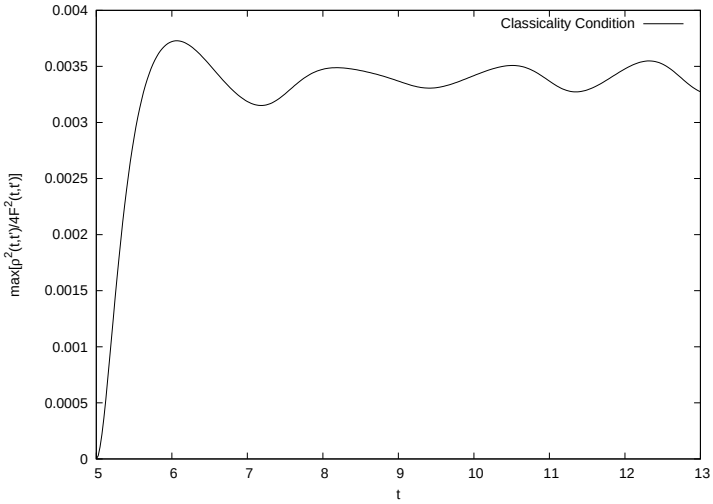

Figure 76: In this case the sufficient classicality condition is fulfilled.

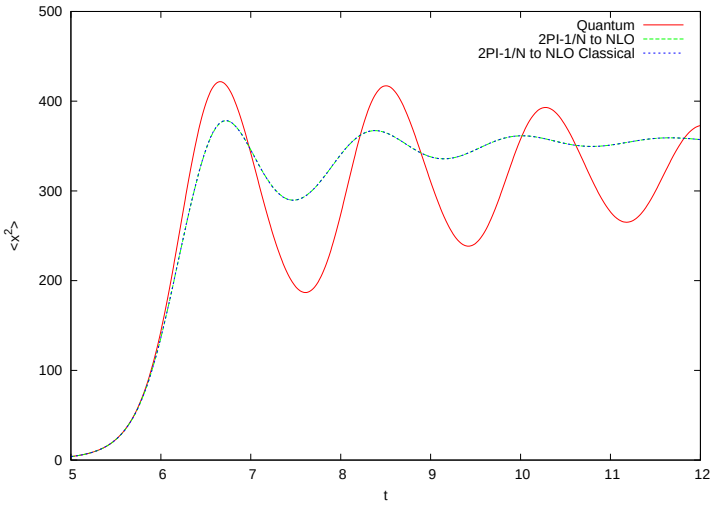

Figure 77: The 2PI-1/N to NLO evolution and the 2PI-1/N to NLO Classical evolution completely match.

9.5 Systematic study of time-independent quartic quantum mechanical systems

As mentioned earlier, we will perform a systematic study for different values of the parameters r_1, r_2, r_s shown in (196), for a single well and a double well quartic potential. With this study we plain to test the 2PI-1/N to NLO approximation and compare it with the classical approximation (we discard here the 2PI-3Loop approximation that becomes divergent). Also we will test the classicality condition obtained from the 2PI approximation, and the Hybrid Method explained above.
We study the same systems as in section 5.4 and will present a selection of them in the following tables. The errors are the same that in the mentioned section, because the errors for the 2PI approximations are significantly lower than those of the classical approximation.

9.5.1 Single well quartic potential

We take a Hamiltonian

$$H(x,p) = \frac{1}{2m}p^2 + \frac{1}{2}mw^2x^2 + \frac{\lambda}{24}x^4 \tag{471}$$

where w is time independent. The initial state is a gaussian state whose Wigner function is

$$W(x,p;t=0) = \frac{1}{\pi}e^{\frac{-x^2}{2\sigma_x^2}}e^{\frac{-p^2}{2\sigma_p^2}} \tag{472}$$

We calculate the evolution with the different approximations for several values of the parameters of the Hamiltonian and of the initial state, that can be encoded in the dimensionless control parameters r_1, r_2, r_s. We recall here these parameters

$$r_1 \equiv \frac{m^2w^3}{\lambda\sigma_x\sigma_p} \quad ; \quad r_2 \equiv \frac{w\sigma_p}{\lambda\sigma_x^3} \quad ; \quad r_S \equiv \frac{m^2\sigma_x}{\sigma_p} \tag{473}$$

The three parameters are not independent, but only two among themselves. In this system the expectation values show an oscillatory pattern that allow us to identify successive maxima and minima. In what follows, T will stand for the period of the $\lambda = 0$ system. We focus in the first few maxima and test the different results in each one.

We show in Table 10 the relative differences (in %) for different maxima between the Quantum value of $\langle x^2(t)\rangle$ and the value from the Classical, 2PI-1/N to NLO and Hybrid approximation. This is useful to compare all methods. Also one can see the relative difference between the 2PI-1/N to NLO and 2PI-1/N to NLO Classical evolution, which is an indication of how the classical approximation works. In all cases we define T_i as the difference between the position of the two successive minima, around the maximum M_i. And when we compare the value of a curve with the exact quantum evolution at a maximum M_i, we do not consider the result if the time delay for both maxima is greater than $T_i/4$. t_1 indicates the time for which the corresponding relative difference between a curve and the exact quantum evolution reaches 0.5%.
From the values shown in Table 10 (and other test not included in the table) we can draw the following conclusions:
– The most important influence about the validity of the different methods comes from the value of r_1.
– The value of r_s has a greater influence than the value of r_2 for the same range of variation.
– The classical approximation has the smallest delay, although the value can be worse than in other approximations.
– For small values of r_1 ($r_1 \leqslant 5$) the 2PI-NLO and Hybrid approximation work better than the Classical approximation, but have an increasing delay in time with respect to the quantum evolution. Hence, they present less damping than the classical evolution but more delay.
– For intermediate values of r_1 ($r_1 \approx 10$) the 2PI-NLO and Hybrid evolution have less delay than for smaller values. The classical evolution is better than the 2PI-NLO one, but clearly the hybrid evolution is the best.
– For large values of r_1 ($r_1 \geqslant 20$) the classical approximation work well and the best behavior is for the Hybrid evolution.
– In almost all cases the relative difference between the 2PI-NLO and the 2PI-NLO Classical evolution is inside the interval $[40\%, 70\%]$ with respect to the relative difference between the quantum and classical evolution. Therefore, these differences are of the same order, and we have a good test of classicality.

Thus, we can say that the Hybrid evolution work better than the classical and 2PI-NLO evolution from intermediate values of r_1.

We also have verified if the sufficient classicality condition (465) is fulfilled.

The quantity $B(t)$ reaches the value of 1 for times inside the interval $[0.1, 1.2]$, and later has a fast growth to very high values. So the 2PI classicality condition is violated in this case, despite in the lower half of the table the classical approximation works well.

As an example to illustrate the Hybrid method we display the quantum, classical, 2PI-NLO and hybrid evolution of $\langle x^2(t)\rangle$ calculated for two systems where the classical evolution has clearly a different behavior.
For the system shown in Fig. 78 the classical approximation presents a fast damping and has important differences respect to the quantum evolution. The hybrid evolution has the best behavior and represent a remarkable improvement.
In Fig. 79 we consider a system where the classical approximation work better. Again the hybrid method is the best and implies a substantial improvement.

	r_1	r_2	r_S	M_1	M_2	M_3	M_4	M_5	$\frac{2t_1}{T}$
Q vs Cl	0.4	0.4	1.00	4.14	11.9	18.3	21.1	20.3	0.29
Q vs 2PI				3.48	5.61	2.52			0.20
Q vs Hybrid				1.20	2.45	4.52			0.33
2PI vs 2PI-Cl				2.84	8.45	13.5			
	2.0	2.0	1.00	0.51	1.91	3.65	5.23	6.44	0.55
				0.29	0.45	0.72	0.82	0.71	0.41
				0.14	1.07	1.90	2.39	2.51	0.67
				0.22	0.83	1.74	2.82	3.90	
	2.0	50.0	(5.00)	0.41	2.90	7.79	13.48	20.6	0.59
				1.27	1.99	2.76			0.43
				0.35	1.34	4.54			0.71
				0.06	1.52	3.16			
	5.0	2.0	1.58	0.64	2.42	4.96	7.82		1.39
				0.35	1.20	2.16	2.86		1.78
				0.32	1.35	2.61	3.79		1.84
				0.27	1.05	2.30	3.91		
	5.0	50.0	(3.16)	0.35	0.98	3.30	6.18	9.19	0.81
				0.31	1.20	3.22	4.35		0.67
				0.30	0.38	1.52	2.81		1.00
				0.03	0.59	1.73	3.22		
	10.0	0.4	5.00	0.26	0.94	1.79	2.64	3.60	2.27
				2.07	6.64	10.61	11.73		0.53
				0.15	0.52	0.85	1.09		3.41
				0.11	0.40	0.85	1.39		
	10.0	50.0	(2.24)	0.32	0.14	1.02	2.24	3.72	2.01
				0.10	0.27	0.87	1.63	2.40	1.92
				0.27	0.037	0.47	1.13	1.87	2.91
				0.11	0.18	0.55	1.10	1.80	
	20.0	2.0	3.16	0.08	0.32	0.71	1.22	1.81	3.92
				0.24	0.93	1.99	3.26		2.30
				0	0.20	0.43	0.73		> 4.45
				0	0.12	0.27	0.48		
	20.0	50.0	(1.58)	0.12	0.10	0	0.35	0.76	> 4.45
				0	0	0	0.15	0.29	> 4.45
				0	0	0	0.10	0.24	$\gg 4.45$
				0	0	0	0.24	0.40	

Table 10: Relative difference ratio (%) in maxima and $(2t_i/T)$ for $\langle x^2(t)\rangle$. Quadratic term > 0

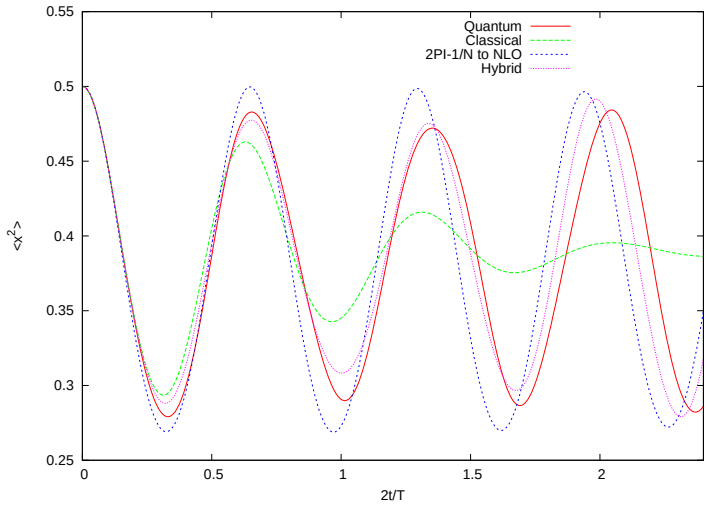

Figure 78: We show the $\langle x^2(t)\rangle$ for quantum, classical, 2PI-NLO and hybrid evolution. Here $r_1 = r_2 = 0.4$.

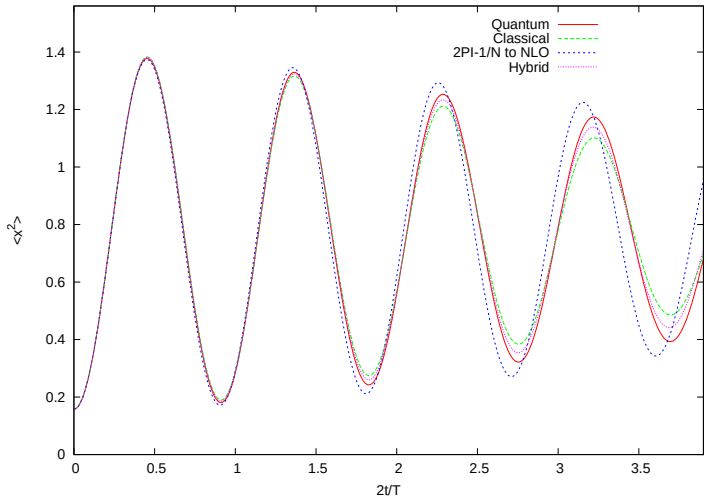

Figure 79: The same as in Fig. 78 for $r_1 = 5$ and $r_2 = 50$.

9.5.2 Double-well quartic potential

Now the Hamiltonian is the same as in (471) with coefficient of the quadratic term in the potential less than zero. As mentioned in section 5.4, in this case the obtained curves for the expectation values do not present a simple oscillatory configuration as in the former section, but appear secondary oscillations that do not allow us a clear identification between the maxima for different methods. Thus, we recover the definitions of section 5.4 and show in Table 11 the value of $2t_1/T$ for different parameters, where T is the period of Hamiltonian with $\lambda = 0$ and coefficient of the quadratic term greater than zero, and t_1 is the time for which the corresponding relative difference (for $\langle x^2(t)\rangle$) between a selected approximate evolution and the exact evolution reaches the 1%.

We can extract the following conclusions of all studied cases:
–The influence of parameters r_1, r_2, r_s is as in the previous section. So the greatest influence corresponds to the value of r_1.
–In general, as we said in section 5.4, all methods work worse in this case and we need higher values of the parameters to achieve a good behavior.
–In all cases the 2PI-1/N to NLO approximation is the worst and the hybrid one is the best.
–When the classical approximation works well, the differences with the hybrid method are insignificant.

Thus, also in this case the best behavior corresponds to hybrid evolution.

We also have verified that, unlike the previous section, here the difference between the 2PI-1/N to NLO and the 2PI-1/N to NLO Classical evolution is not indicative of the difference between the quantum and classical evolution. The first one is enough to improve the result with the hybrid method, but has small values in many cases where the classical approximation do not work. Nevertheless, the sufficient classicality condition (465) seems to work well. So we write in Table 12 the value of $2t_{con}/T$ and $2t_{Cl}/T$ for several parameters. We define t_{con} as the time in which $C(t)$ reaches the value of 1. And t_{Cl} is the time at which the curve of classical evolution (for the $\langle x^2(t)\rangle$) changes its tendency respect to the quantum one and both begin to behave differently. We estimated the errors $\nabla 2t_{con}/T = \nabla 2t_{Cl}/T = \pm 0.1$.
We deduce that, for $r_1 \geqslant 10$, the 2PI classicality condition represents a lower

bound that cover at least the 80% of the zone in which the quantum and classical approximation match. After this zone both evolutions behave differently but the differences can be small and the classical approximation can work well depending of the value of r_1 (as mentioned). When r_1 grows then t_{con} is increasing, and this explains why in the studied cases with temporal dependence the sufficient classicality condition work well.

	r_1	r_2	r_S	$\frac{2t_1}{T}$
Q vs Cl	0.4	2.0	(2.24)	0.37
Q vs 2PI				0.30
Q vs Hybrid				0.49
	0.4	50.0	(11.18)	0.83
				0.24
				0.96
	2.0	2.0	1.0	0.63
				0.44
				1.22
	2.0	50.0	(5.0)	1.37
				0.42
				1.41
	5.0	50.0	(3.16)	2.03
				0.55
				2.05
	10.0	10.0	1.0	2.62
				0.68
				2.64
	20.0	2.0	3.16	3.17
				0.64
				3.18

Table 11: Value of $2t_1/T$ for different parameters. Quadratic term < 0

To illustrate all this we display in Fig. 80 the $\langle x^2(t)\rangle$ for quantum, classical and hybrid evolution for a small value of r_1. The hybrid method present the best behavior, although there comes a time when all approximations fail.
The same is shown in Fig. 81 for quantum, classical, 2PI-NLO and 2PI-NLO Classical evolution. Now we have a greater value of r_1 and the 2PI-NLO and

r_1	r_2	r_S	$\frac{2t_{con}}{T}$	$\frac{2t_{cl}}{T}$
0.4	2.0	(2.24)	0.2	0.4
0.4	50.0	(11.18)	0.1	0.7
2.0	2.0	1.0	1.3	1.5
2.0	50.0	(5.0)	0.2	1.5
5.0	50.0	(3.16)	0.2	1.7
10.0	10.0	1.0	2.2	2.3
20.0	2.0	3.16	2.4	2.8
50.0	10.0	2.24	2.6	2.9
100	100	1.0	2.9	3.4
200	50.0	2.0	2.8	3.3
200	200	1.0	2.9	3.4
300	100	1.73	3.0	3.5
500	25	4.47	3.6	4.2

Table 12: $2t_{con}/T$ and $2t_{cl}/T$ for several parameters. Quadratic term < 0

2PI-NLO Classical approximation agree. This means that the hybrid evolution is equal to the classical one.
Also we display in Fig. 82 an example to see the behavior of sufficient classicality condition. The quantum and classical evolution begin to behave differently shortly after the value of $\rho^2(t,t')/4F^2(t,t')$ started to grow quickly over 1. We have multiplied this by 500 in order to better observe the result.

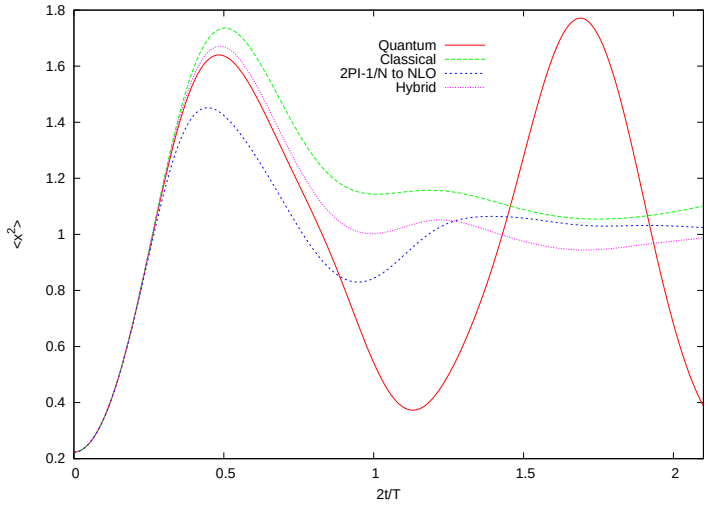

Figure 80: $\langle x^2(t) \rangle$ for quantum, classical and hybrid evolution. Here $r_1 = 0.4$ and $r_2 = 2$.

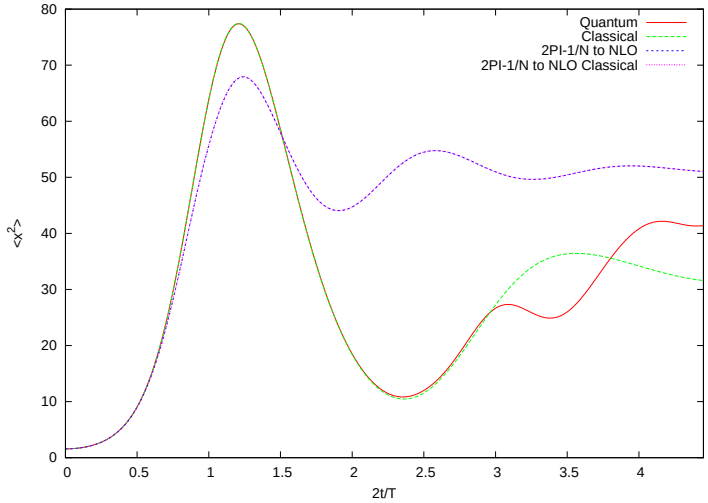

Figure 81: $\langle x^2(t) \rangle$ for quantum, classical, 2PI-NLO and 2PI-NLO Classical evolution. Here $r_1 = 20$ and $r_2 = 2$. Clearly in this case the hybrid evolution matches with the classical one.

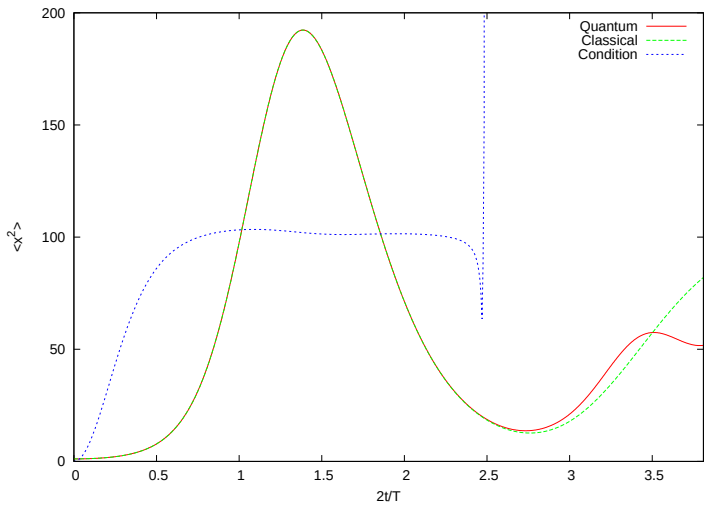

Figure 82: $\langle x^2(t)\rangle$ for quantum, and classical evolution. Also shown $500 \times \rho^2(t,t')/4F^2(t,t')$ for each fixed value of t. Here $r_1 = 50$ and $r_2 = 10$.

10 Complex Langevin Method

10.1 Introduction

Lately, one of the most interesting methods of non linear evolution, boosted by the increased possibilities of computational calculus, is called *Complex Langevin method*. It is based on the ideas introduced by Parisi and Wu in [92] about *stochastic quantization*, applied in the euclidean space-time. They start from the Langevin equation appearing on the non equilibrium statistical mechanics and introduce in that equation an additional fictional time parameter (Langevin time). They apply their method to scalar and gauge fields quantization, aiming to build a new perturbation theory within the gauge theories removing the need of fixing the gauge. Later in [93] it is demonstrated for scalar fields that Parisi and Wu's perturbative theory gives the usual Feynman diagrams when the Green's functions are calculated. There also were stochastic based descriptions for fermions, tensorial fields and supersymmetric theories. A deep review can be found in [94].
The extension of these ideas to the real time case for quantum-mechanical systems was introduced in [58][59] involving Langevin equations with complex drift terms. The description for QFT in Minkowski was presented in [95]. Here the authors propose a modification of Parisi and Wu's stochastic quantization method called *complex Langevin method*. They introduce a generalized Langevin equation with a complex drift term that transforms the field into a complex one even if it was real at first. Just like in the euclidean case, this equation evolves with a fictional time parameter called Langevin time. The real time Green's functions are obtained as limits of the equilibrium of the correlation functions for the complex process, in the context of the distributions. They do a stochastic diagrammatic expansion and prove that it is equivalent to the usual perturbative expansion. In the same way, in [96] a stochastic perturbative expansion for gauge fields based on this method is done, but they find that the connection with the usual perturbative expansion is not that simple and present a recursive method that allows to obtain Feynman diagrams from stochastic ones. There are non perturbative proofs about the complex Langevin equation's evolution leading to a stationary distribution which correlation functions coincide with the ones obtained from the usual scalar fields quantization. So in [97] the Fokker-Planck equation related to the complex Langevin function for a real distribution is deduced. They obtain from it a complex pseudo-distribution that it is dependent on

the real part for the field and prove that the limit of equilibrium leads to the same distribution involved in the usual formalism of the path integral ($\sim e^{iS}$). The same is proved in [98] using a functional integral formulation. Note that, in all these cases, the noise in the Complex Langevin equation can be either real or complex provided it fulfills the properties of a white gaussian noise.

Although the analytical study of the method shows a correct convergence, when it has to be implemented numerically suffers from severe instability problems. This is, unlike the euclidean action, due to the drift term in the Complex Langevin equation having a complex action that is not delimited in all the range of values of the field (complex now), so some initial values lead to a infinite field modulus in a finite Langevin time (an analysis for some cases with usual variables can be read in [99]). It can be proved (as we will see later) that if we eliminate the noise, the differential equation we get has instability points, and discretizing the process and adding the noise raises the odds of stepping near such points. We could avoid this problem finding the real distribution that give us the actual correlations with our complex field, but though the Fokker-Planck equation that satisfies this distribution is known [97], it has been only obtained for the free case ($\lambda = 0$) [100] [99]. Another way of solving the problem is reducing the probability of the instability making the steps for the Langevin time very small, but this leads to very high computing times. So other possibilities have been studied to cope with the unstable configurations found in the numerical evolution. Sometimes the unstable configurations are just discarded and the correlation functions are calculated with the configurations left [101] [102]. Other times, when the configuration diverges they go back till a value outside the instability zone and evolve again changing the seed [61]. Recently, [62] some techniques have been used that change the discretization step for the Langevin time, making it smaller if the drift term increases.
Anyway, even avoiding the instabilities in the numerical simulation, it could happen that some configurations, due to being near an instability zone, deviate from the correct evolution and lead to an unexpected distribution. This is usually the main concern when using this method, so the results must be assessed carefully and check if they fulfill certain premises dependent on the studied system. So in [102] they show the Fokker-Planck equation associated with the complex Langevin equation as an evolution equation with a complex Hamiltonian not self adjoint, study its eigenvalues and try to know

under what conditions has a good convergence. They do a numeric simulation for the case of one anharmonic quantum oscillator with one variable which mass is complex. They obtain that when the real part of the mass is higher than zero, the evolution seems to behave correctly, but when it is lower or equal to zero needs a small imaginary part because in any other case the configurations they use become unstable and even discarding them they note evidences of an erroneous convergence. We must stress that in many cases (in fact in all our cases) the complex Langevin equation has a pure imaginary mass, beside the interaction term also being imaginary, so it is perfectly possible that it could be an erroneous convergence. Along the same lines, it is argued in [103] that the existing proofs of complex Langevin method converging to the physical solution are strictly formal, and not completely rigorous. Then they provide some conditions that have to be fulfilled for the system in order to have, at least analytically, a correct convergence when applying such method. But the conditions are so restrictive that many cases of interest do not fulfill them, and even doing it is not assured that we have the expected convergence in the numerical implementation.

With that in mind, the method has been applied to many cases. Ref. [104] shows how to obtain transition amplitudes from the perturbative expansion applied to quantum systems. In [61] the method is applied to scalar fields out of equilibrium and two point-functions for the free case and $\lambda\phi^4$ are calculated. An analysis about the possible applications of the method in quantum field theory can be found in [105], where the advantages of this method against others like 2PI or classical approximation are discussed. It also comments that the convergence proofs are formal and the general convergence properties in a numerical implementation are not clear yet. A good review about stochastic quantization and the complex Langevin method for scalar and gauge fields can be found in [106]. The stability and convergence problems in the numerical implementation are also discussed. As an example, computational simulations for gauge theory SU(2) in 3+1 dimensions are run. A quantum anharmonic oscillator is also studied. In both cases is noticed that even avoiding instabilities (reducing the discretization step for example), the convergence to the physical solution seems only reasonable for a small range of real time (in the anharmonic oscillator case they do not run even half an oscillation of the two point functions), and increasing the range can lead to stationary non physical solutions. Additional test would be required to check when that happens.

Another example of application is found in [107], where a relativistic Bose gas

with a non zero chemical potential is studied. They show how the complex Langevin method leads to a stationary solution independent of the initial conditions and avoid the sign problem present in this system. An extension of this article to study the model XY with a finite chemical potential is found in [108]. In [63] two different quantum mechanical systems with complex actions are studied, and its convergences when applying the complex Langevin method are analyzed for a real noise and an imaginary one as well. It is found that the inclusion of an imaginary part in the noise causes that the stationary distribution function having an imaginary part with limited decay, so the evolution leads to a non physical solution. Therefore they conclude the noise have to be real. When that happens the convergence seems to behave correctly although the correct solution is not assured so they advise to compare the results with other methods. An extension of the last article can be found in [64]. Here they do a more detailed analysis of the analytic convergence towards the physical solution and show that even at this level the result can be wrong if the observables do not satisfy some criteria checked for the same examples of the last article. In those cases they test the criteria for a pair of observables and is seems to work, although this do not prove the correct convergence as to do it they should prove it for infinite observables. They advise again to use a real noise in the simulations. They argue that the causes for the wrong results can be more general. Such causes are the fast growth of the imaginary part of the observables and the slow decay of the imaginary part of the equilibrium distribution.

Thus, the analytical study of the complex Langevin method shows a correct convergence to desired final stationary state, but when it has to be implemented numerically suffers from severe instability problems. These instabilities can be avoid with different methods, but there are also problems of convergence.
Along this Chapter we are going to analyze the instabilities produced in the method and how to avoid them. We will also check its convergence properties. In order to do it we will study quantum mechanical systems which the exact numerical solutions are known, so we can compare results and discuss how the method works.

10.2 Langevin equation

An stochastic process is characterized by a group of stochastic variables $\{x_1(\theta), ..., x_n(\theta)\}$ dependent on a continuous variable θ and related between them by an equation called *Langevin equation*. We are going to consider Markovian processes with the following general form for this equation

$$\frac{dx_i}{d\theta} = c_i(\mathbf{x}, \theta) + b_i(\mathbf{x}, \theta)\eta_i(\mathbf{x}, \theta) \tag{474}$$

where η is a gaussian white noise, i.e., characterized by a gaussian distribution which only has local correlations.

$$\begin{aligned} &\langle \eta_i(\mathbf{x}, \theta) \rangle = 0 \\ &\langle \eta_i(\mathbf{x}, \theta)\eta_j(\mathbf{x}, \theta') \rangle = \sigma^2 \delta_{ij} \delta(\mathbf{x} - \mathbf{x}')\delta(\theta - \theta') \end{aligned} \tag{475}$$

It is usual to call c_i drift term and b_i^2 diffusion term, respect to x_i. To achieve our goals, it is enough to restrict us to the case which every diffusion terms are constants equal to one and the drift term does not depend explicitly on θ

$$b_i = 1 \quad , \quad c_i = c_i(\mathbf{x}) \quad \forall i \tag{476}$$

θ is usually considered as a time variable, and therefore (474) as an evolution equation for stochastic variables. Thus, an equation associated to the evolution of the probability density exists; it is called Fokker-Planck equation. For the case of (474) and taking into account (476) the associated equation has the form

$$\frac{\partial}{\partial \theta}\rho(\mathbf{x}, \theta) = -div\big(\mathbf{c}(\mathbf{x})\rho(\mathbf{x}, \theta)\big) + \frac{\sigma^2}{2}\Delta\rho(\mathbf{x}, \theta) \tag{477}$$

The stationary distribution ρ_s is the one which satisfies $\partial_\theta \rho_s = 0$. If the drift term is the negative gradient of a function $S(\mathbf{x})$, $\mathbf{c}(\mathbf{x}) = -\nabla S(\mathbf{x})$, is easily noticed that $\rho_s(\mathbf{x})\ \alpha\ exp\{-2S(\mathbf{x})/\sigma^2\}$, therefore

$$\sigma^2 = 2 \quad \Rightarrow \quad \rho_s(\mathbf{x})\ \alpha\ exp\{-S(\mathbf{x})\} \tag{478}$$

10.3 Stochastic quantization

The starting point of this approach is the analogy between the euclidean quantum field theory and the classical statistical mechanics. The measurement of the euclidean path integral is closely related to the Boltzmann distribution of a statistical system on equilibrium, so the euclidean Green's

functions can be understood as correlation functions of such system. So the euclidean Green's functions for a scalar field are obtained ($\hbar = 1$)

$$\langle \phi(x_1)....\phi(x_m)\rangle = \frac{\int D\phi\, exp[-S_E]\, \phi(x_1)....\phi(x_m)}{\int D\phi\, exp[-S_E]} \tag{479}$$

where S_E is the euclidean action.
The basic idea of the *stochastic quantization* [92] is to consider the measurement of the euclidean path integral $exp[-S_E]/\int D\phi exp[-S_E]$ as a stationary distribution of a stochastic process. For that, the following three steps are taken:
1) A new coordinate is added to the field, the fictional time parameter θ

$$\phi(x) \to \phi(x,\theta) \tag{480}$$

Here $x = (x_0, x_1....x_{n-1})$ denote a vector in the n-dimensional euclidean space, and the fictional time parameter θ should not be mistaken with the usual euclidean time x_0. Now the euclidean action will be

$$S_E = \int d\theta\, d^n x\, \mathcal{L}_E\big(\phi(x,\theta), \partial_x\phi(x,\theta)\big) \tag{481}$$

So, if we use as an example the $\lambda\phi^4$ theory, we would have

$$S_E = \int d\theta d^n x \Big[\frac{1}{2}\pi^2(x,\theta) + \frac{1}{2}\big[(\partial_x\phi^2(x,\theta))^2 + m^2\phi^2(x,\theta)\big] + \frac{\lambda}{24}\phi^4(x,\theta)\Big] \tag{482}$$

2) It is considered that the evolution of ϕ respect to the fictional time parameter θ is governed by a stochastic process which Langevin equation has the following form

$$\frac{\partial\phi(x,\theta)}{\partial\theta} = -\frac{\delta S_E}{\delta\phi(x,\theta)} + \eta(x,\theta) \tag{483}$$

where η is a gaussian white noise with correlations given by

$$\begin{aligned} &\langle \eta(x,\theta)\rangle = 0 \\ &\langle \eta(x_1,\theta_1)\eta(x_2,\theta_2)\rangle = 2\delta^n(x_1 - x_2)\delta(\theta_2 - \theta_2) \end{aligned} \tag{484}$$

the subscripts indicate different coordinate vectors.
Therefore, given an initial condition $\phi(x, \theta = 0)$, solving Langevin equation

will lead us to $\phi(x,\theta)$. That is, let's call $P(x,\theta)$ to the functional distribution that allows us to calculate the correlation functions at the same fictitious times through the corresponding functional integral, the expression will be

$$\langle\phi(x_1,\theta)....\phi(x_k,\theta)\rangle_\eta = \int D\phi\, P(\phi,\theta)\, \phi(x_1)....\phi(x_k) \tag{485}$$

(the subscript η indicates that the correlation is calculated respect to the process we are considering, and it is written to differentiate it from (479)). Then, chosen an initial distribution $P(x,0)$, its evolution will be governed by the Fokker-Planck equation associated to (483)

$$\frac{\partial P}{\partial\theta} = \int d^n x\, \frac{\delta}{\delta\phi(x,\theta)}\Big(\frac{\delta S_E}{\delta\phi(x,\theta)} + \frac{\delta}{\delta\phi(x,\theta)}\Big)P \tag{486}$$

which is obtained with the correct generalization of what it was shown in the previous section.
3) The main characteristic of the stochastic quantization is that can be proved [92] [94] that in the limit $\theta\to\infty$ it reaches an equilibrium state. Thus, in this limit we will reach a stationary distribution respect to the stochastic process given by (483), and with arguments similar to the ones used in the previous section, we will have

$$\lim_{\theta\to\infty} P(\phi,\theta) \equiv P_{eq}(\phi) = \frac{exp[-S_E]}{\int D\phi\, exp[-S_E]} \tag{487}$$

Therefore, taking into account (479), we have

$$\lim_{\theta\to\infty}\langle\phi(x_1,\theta)....\phi(x_k,\theta)\rangle_\eta = \langle\phi(x_1)....\phi(x_k)\rangle \tag{488}$$

Actually, the equilibrium state it is reached no matter what the initial condition $P(x,0)$ would be, although this one can influence the speed to reach such state.
A perturbative description of the stochastic quantization can be found in [93] [94]. The correlation functions are expanded in diagrammatic form and it is proved that, for every order (488) is satisfied. This formulation is useful when the method is extended to real time (explained in the next section), as it is the base of another analogous proof that demonstrate the desired convergence.

10.4 Stochastic quantization in real time

We are going to extend the method described in the previous section in order to apply it to the evolution of systems in real time, i.e., in the Minkowski space-time. For this we replace the Langevin equation for a scalar euclidean time given by (483) with the following generalized Langevin equation for scalar fields in the Minkowski space

$$\frac{\partial\phi(x,\theta)}{\partial\theta} = i\frac{\delta S}{\delta\phi(x,\theta)} + \eta(x,\theta) \tag{489}$$

where now S is the action in the Minkowski space and η, as before, is a gaussian white noise with correlations

$$\begin{aligned}\langle\eta(x,\theta)\rangle &= 0\\ \langle\eta(x,\theta)\eta(x',\theta')\rangle &= 2\delta^n(x-x')\delta(\theta-\theta')\end{aligned} \tag{490}$$

In this context, the fictional time parameter θ is usually called Langevin time. Taking into account that the equation (489) is complex, in this case the field will be also complex $\phi = \phi_R + i\phi_I$. The noise can be real or complex, as the limit towards the stochastic process converges does not depend on that.
We are going to consider, as an example, the theory $\lambda\phi^4$; then the action will be

$$S = \int d^4x \left[\frac{1}{2}(\partial_\mu\phi)(\partial^\mu\phi) - \frac{1}{2}m^2\phi^2 - \frac{\lambda}{24}\phi^4\right] \tag{491}$$

furthermore, by simplicity, we will restrict to the usual 4 dimensions space-time ($n = 4$).
Let's analyze what this method implies in the case of a free field ($\lambda = 0$). If we transform the field to Fourier modes, the Langevin equation (489) becomes

$$\dot{\phi} = i(k^2 - m^2)\phi + \eta \tag{492}$$

The solution with $\phi(k,0) = 0$ is given by

$$\phi(k,\theta) = \int_0^\theta d\tau\, exp\{i(k^2-m^2)(\theta-\tau)\}\eta(k,\tau) \tag{493}$$

and thus, taking into account (490) (actually its Fourier transform), the two point function is

$$\begin{aligned}\langle\phi(k,\theta)\phi(k',\theta)\rangle &= 2(2\pi)^4\int_0^\theta d\tau\, exp\{i(k^2-m^2)(\theta-\tau)\}\delta^4(k+k') =\\ &= (2\pi)^4\delta^4(k+k')\frac{i}{k^2-m^2}\left[1 - exp\{2i(k^2-m^2)\theta\}\right]\end{aligned} \tag{494}$$

It seems we have reached a problematic situation, because the limit when $\theta \to 0$ of (494) does not exist. But we have to remember that in the Minkowski space Green's functions have to be interpreted as distributions. Thus, the equation (494) must be integrated on the momenta k and k' after being multiplied by a test function in the momenta space. Then (494) can be considered as a distribution and it can be operated using the distribution properties, as can be seen in [95] [94]. We arrive to the following expression

$$\lim_{\theta\to\infty} \langle \phi(k,\theta)\eta(k',\theta)\rangle = (2\pi)^4\delta^4(k+k')\frac{i}{k^2-m^2+i0} \tag{495}$$

that is, of course, a distribution. Therefore, the generalized equilibrium limit for the stochastic process (492) leads us to the usual Feynman propagator. An alternative to arrive to (495) is adding an imaginary negative mass term $-(1/2)\epsilon\phi^2$ to the action, and making ϵ approach to zero after the calculations have been done.

It is possible to generalize what was already done in the euclidean case and expand perturbatively as described in [95]. Starting from the fact that the limit is correct to zero order, a diagrammatic description of this method is given and it is proved that for each order, the diagrams approach to the corresponding ones of the usual theory in the limit $\theta \to \infty$ (in fact, they prove it to first order and then proceed by induction). This proves that at least analytically this generalization leads to the desired equilibrium limit, although when implementing this method numerically some problems arise to approach that limit.

Note that the correct limit is reached independently of the initial conditions, although it can influence the speed which the process approaches to the equilibrium state.

The method just described is what is usually called *Complex Langevin method*.

10.5 Complex Langevin in quantum mechanics

Remember that our aim is implementing the complex Langevin method in quantum mechanical systems, the ones which have an exact numerical solution known by us. This will allow us to evaluate the behavior of such method. Subsequently, we have to implement what we learned for quantum field theory to the quantum mechanics case, like we did in other chapters. By simplicity, we restrict to the case of one quantum variable $x(t)$, as the extension to more variables is immediate. Analogously to the previous section,

we add a fictional time coordinate to our variable, the Langevin time θ

$$x(t) \to x(t,\theta) \tag{496}$$

Consider the action

$$S = \int dt\, d\theta \left[\frac{m}{2}(\partial_t x(t,\theta))^2 - \frac{1}{2}mw^2x^2(t,\theta) - \frac{\lambda}{24}x^4(t,\theta)\right] \tag{497}$$

and we build the corresponding stochastic process governed by a complex Langevin analogous to (489)

$$\frac{\partial x(t,\theta)}{\partial\theta} = i\frac{\delta S}{\delta x(t,\theta)} + \eta(t,\theta) \tag{498}$$

where η is gaussian and satisfies

$$\begin{aligned} &\langle\eta(t,\theta)\rangle = 0 \\ &\langle\eta(t,\theta)\eta(t',\theta')\rangle = 2\delta(t-t')\delta(\theta-\theta') \end{aligned} \tag{499}$$

Our quantum variable is now complex $x = x_R + ix_I$. The noise can be chosen real or complex.
Thus, we can expect that if we start from an initial distribution and reiterate the process till we have θ values large enough, we will reach a stationary distribution respect to θ that will give us the correct quantum expectation values.
As we are going to consider actions of the kind (497), then the variation of the action in (498) has this form

$$\frac{\delta S}{\delta x(t,\theta)} = -m(\partial_t^2 x) - mw^2x - \frac{\lambda}{6}x^3 \tag{500}$$

From this expression is easy to realize that the Langevin time units are not like the normal time ones, but those of a squared time (remember that $\hbar = 1$): $[\theta] = [t^2]$.

10.6 Numerical implementation

We have already said that the implementation of the method usually leads to instabilities that can make the process diverge or converge to an incorrect state. We are going to consider some of our example systems and we will analyze how these instabilities arise, and some approaches to avoid them.

10.6.1 Discretization and initial conditions

To make the evolution governed by (498) we need an initial distribution $\rho(x,t;\theta=0)$. In order to reach the desired stationary state, in principle, any ρ is valid, but a specific election of the Wigner's function in the initial time $W(x,p;t=0)$ for the system studied impose certain restrictions on ρ. First, $\rho(x,0;0)$ will have to coincide with $W(x,p;0)$ integrated in p, i.e.

$$\rho(x,0;0)=\int dp\, W(x,p;0)=|\psi(x)|^2 \tag{501}$$

where $\psi(x)$ is the initial wave function, which sets the distribution to the random variable $x(t=0,\theta=0)$. On the other hand, given that in (498) appears a second derivative of x with respect to t, is necessary to set also the random variable $x(t=t_a,\theta=0)$ at another time t_a in the distribution. But discretizing the time t with a step of δt, sets the distribution for $x(t=\delta t,\theta=0)$, and we obtain the expression

$$\rho(x,\delta t;0)=\int dp\, W(x-\delta t p/m,p;0) \tag{502}$$

We discretize the Langevin time with a step of $\delta\theta$ too. For an action as in (497) the discretized equation (498) results in

$$\begin{aligned} x(t_l,\theta+\delta\theta)=x(t_l,\theta)-i\delta\theta\Big[m\frac{x(t_l+\delta t,\theta)+x(t_l-\delta t,\theta)-2x(t_l)}{(\delta t)^2}+\\ +mw^2x(t_l)+\frac{\lambda}{6}x^3(t_l)\Big]+\delta\eta(t_l,\theta) \end{aligned} \tag{503}$$

where $\delta\eta(t_l,\theta)$ is a gaussian noise that satisfies

$$\begin{aligned} &\langle\delta\eta(t_l,\theta)\rangle=0\\ &\langle\delta\eta(t_l,\theta)\delta\eta(t_j,\theta')\rangle=2\delta\theta\delta_{lj}\delta_{\theta\theta'} \end{aligned} \tag{504}$$

and some Kronecker deltas appear for being t and θ discretized.
Therefore, the steps we have to take to implement the Complex Langevin method are the following:

1) Discretize the time with a step of δt and in a range $t\in[0,t_{max}]$. This range must be chosen in each particular case as it fits. The value $x(t_{max},\theta)$

will need certain boundary condition valid for every Langevin time. It can be a periodic condition, to set certain derivative... So, t_{max} must be large enough for the boundary effect being negligible in the range of times chosen.

2) Generate a sample of the initial Wigner's function, so we will have a group of values $M_0 \equiv (x_i, p_i)$ with $i = 1, ..., N$. From here we are going to take a valid initial sample composed of N paths $x_i(t, \theta = 0)$ that will have to evolve in θ. The initial point in each path, $x_i(0, 0)$, coincides with the value x_i of M_0 labeled with the same subscript. And the next point will be $x_i(\delta t, 0) = x_i(0, 0) + \delta t p_i/m$. The rest of the points of each path can be set as we wish, as long as we take into account the boundary condition chosen in t_{max}. An usual election is setting them to zero (except in t_{max} and maybe in $t_{max} - \delta t$ because the boundary condition). Another one consists in setting each path as the result of the classical evolution.

3) Apply reiteratively the complex Langevin equation (503). Although initially the path points have been chosen real, they will acquire an imaginary part later. We will continue until the paths form a stationary distribution, i.e., until the expectation values calculated by them do not change significantly increasing θ. These expectation values are calculated as mean values over all the paths and they will be usually complex, although once reaching the stationary state they should be real and coincide with the true quantum expectation values (theoretically at least).

10.6.2 Instabilities

As we commented before, implementing numerically the complex Langevin method leads to severe instability problems. There are paths where some point diverges, affecting the rest and making divergent the entire path. The number of divergent paths usually decreases reducing the steps $\delta\theta$ (see [61]), which proves that such divergences are artifacts of the discretization.
We will try to analyze which is the origin of such instability. We begin discarding the part of the noise in (503) to see how, despite discarding it, a path can be divergent. We define *condition 1* as the one that appears when the modulus of a point $x_i(t_l, \theta)$ of a path i reach a value large enough so the evolution is only governed by the cubic term, and the influence of neighboring points can be disregarded. Then denoting $x \equiv x_i(t_l, \theta)$ by simplicity, (503) it

can be expressed as

$$\frac{\partial x}{\partial \theta} = -i\frac{\lambda}{6}x^3 \tag{505}$$

If we call $a \equiv -ix^2$ the equation becomes $\partial_\theta a = (\lambda/3)a^2$ with the following result

$$a(\theta) = \frac{a_0}{1 - \frac{\lambda}{3}a_0\theta} \quad ; \quad a_0 = a(\theta = 0) \tag{506}$$

As $a_0 = -ix_0^2$, if $x_0^2 = ir$ with $r > 0$ real then the denominator of (506) could be zero. That happens when we have $Re(x_0) \approx Im(x_0)$. In that case, the value θ_B for which a (and therefore x) diverges, is

$$\theta_B = \frac{3}{2\lambda Re(x_0)Im(x_0)} \tag{507}$$

and due to the large denominator, θ_B will be small. In fact, as we will see later, if this happens to a point of the path, the divergence grows very fast and the noise variations do not avoid it. We name these divergences *type 1*. We have checked that some divergent paths come from the previous case. Nevertheless, there are other paths that still diverge even when the previous case do not happen. Consequently, there must be other instability causes. Thus, we are going to discard the noise and define *condition 2*, that it is fulfilled when the modulus of our point x has increased enough to ignore the influence of its neighbors, but not so much as to ignore linear term. Then (504) results in

$$\frac{\partial x}{\partial \theta} = -i\Big[-\frac{2mx}{(\delta t)^2} + mw^2x + \frac{\lambda}{6}x^3\Big] \tag{508}$$

Being as before $a \equiv -ix^2$ and renaming $\alpha \equiv m^2 - (2m/(\delta t)^2)$, then the equation can be expressed as

$$\frac{\partial a}{\partial \theta} = -2i\alpha a + \frac{\lambda}{3}a^2 \tag{509}$$

which solution is

$$a = \frac{1}{Be^{2i\alpha\theta} - i\frac{\lambda}{6\alpha}} \quad ; \quad B \equiv \frac{1}{a_0} + i\frac{\lambda}{6\alpha} \tag{510}$$

Therefore, if we observe the inverse of a

$$\frac{1}{a} = \big(\frac{1}{a_0} + i\frac{\lambda}{6\alpha}\big)e^{2i\alpha\theta} - i\frac{\lambda}{6\alpha} \tag{511}$$

which represents an oscillating complex number, that describes a circumference of radius R as θ grows with

$$R^2 = Re^2\big(\frac{1}{a_0}\big) + \Big(Im\big(\frac{1}{a_0}\big) + \frac{\lambda}{6\alpha}\Big)^2 \tag{512}$$

and centered in $-i\lambda/(6\alpha)$ for $\alpha > 0$ and in the opposite point for $\alpha < 0$, inside the complex plane belonging to $1/a$. This is shown in Fig. 83. Therefore a critical radius $R_c = |\lambda/(6\alpha)|$ exists for which $1/a$ becomes zero for certain value of θ, which means that a (and therefore x) will become divergent.

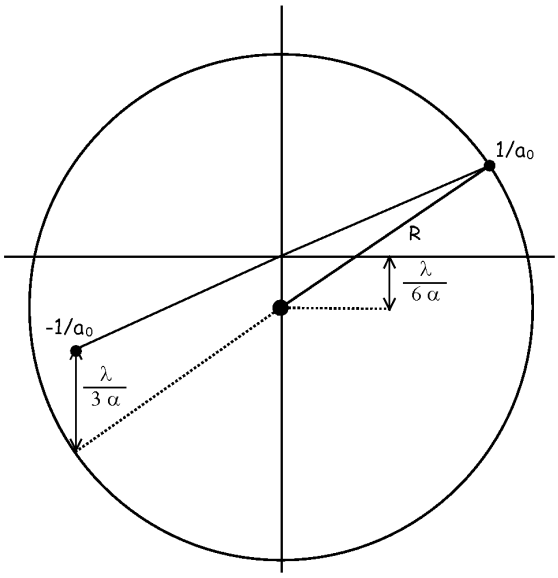

Figure 83: The evolution of $1/a$ under *condition 2* is an oscillating complex number with radius R.

Thus, if our $x(t_i)$ is large enough to ignore its neighbors and to make $1/a$ to approach to the critical radius, can be a good candidate for divergence. In principle, if the radius of the circumference in which $1/a(\theta)$ oscillates is close to R_c, it should not be any problem because such radius will remain constant. But when $1/a$ approaches to zero, then $|x|$ becomes too large and any of the errors inherent to the discretized equation (503) are amplified and can divert the path into the critical radius. On the other hand, when we include the

noise in the equation, it is more probable that random leaps could divert the path so that $1/a$ approaches to R_c, and if that happens in the zone near zero then the point would have a divergence so fast that it could not recover from it with later leaps. And even if in a first step near zero the points recovers its stability but remains near the critical radius and fulfilling the *condition 2*, may not have so much luck on the next cycle.
Logically, if the characteristic amplitude of the leaps that the noise causes on the circular path of $1/a$ is around the same order than the distance between $1/a$ to the critical radius, then there is a possibility that some leap could take $1/a$ to the critical radius around zero. This amplitude is related with the gaussian noise width $\delta\eta$, that is proportional to $\sqrt{\delta\theta}$, therefore is expected that reducing $\delta\theta$ the possibilities of diverge will decrease.
Furthermore, we have to take into account that if R_c is large, then $1/a$ can approach to the critical radius without the corresponding $|x|$ having to be very big (although *condition 2* must be fulfilled). Thus the probability of having a divergence will be larger as R_c increases, which will lead to a bigger number of divergent paths. In fact, if $R_c = |\lambda/(6\alpha)| \approx 0$, then will not be a priori any divergent path due to the causes we are considering (it could be some due to the *condition 1*). Therefore the larger λ is more divergent paths will appear. Respect to the value of α, remember that it has the following expression

$$\alpha = m^2 - \frac{2m}{(\delta t)^2} \tag{513}$$

therefore, for fixed m, w, the value of δt is going to influence noticeable in the value of α. If we observe the equation (509), we notice that the larger $|\alpha|$ is the bigger change x will have in each Langevin time step, and the discretization errors will be more important. Furthermore the oscillation frequency of $1/a$ depends directly on $|\alpha|$ as can be seen in (511), and increasing such value will increase the number of times that $1/a$ passes near zero for paths near the critical radius, so the possibilities of divergence will also increase. Therefore, if we want to reduce δt to obtain more precise results, we have to reduce $\delta\theta$ if we do not want to increase the number of divergent paths. This has to be taken into account to choose the value of the time step.
These divergences we have just discussed will be named *type 2* divergences. Of course, a *type 2* divergence where the real and imaginary parts of x have the same sign, can degenerate into a *type 1* divergence, but not necessarily all the time. If we study (512) we see that the approach to R_c can happen also when $Re(x)$ and $Im(x)$ have different sign, besides the fact that the linear

term with x can be significant.

10.6.3 Erroneous convergence

Another problem of the complex Langevin method is that even when the group of paths end converging towards a stationary state, it is possible that such state may not be the correct one. We have seen that if one point of the path fulfills any of the conditions analyzed before then the path can diverge. *Condition 1* causes very fast divergences and usually can not be avoided. But if one point fulfills *condition 2* and it is near the critical radius, then the amplification of the discretization errors when it is near zero, coupled with the random leaps due to the noise, can deviate the point from the right path, and make an erroneous convergence. Moreover, as these paths have points with large moduli, they will have an important weight in our calculation of expectation values, therefore causing large errors.

10.6.4 Adaptive step-size evolution

One of the most successful approaches to improve the method and avoid the divergent paths has been the adaptive step evolution [62]. In this approach, after each step in θ, it is evaluated if any path is near a critical zone and in that case the value of $\delta\theta$ is decreased to avoid such zone. When the divergence danger passes the step is increased again. Generally, the step is adapted depending on the value of the drift term in the evolution. So [62], if θ_n represents the $n-th$ step in Langevin time, for a path i this can be defined

$$\begin{aligned} K_R(t_l,\theta_n) &= Re\big(\frac{\delta S}{\delta x_i(t_l,\theta_n)}\big) \\ K_I(t_l,\theta_n) &= Im\big(\frac{\delta S}{\delta x_i(t_l,\theta_n)}\big) \\ K_n^{max} &= max_{t_l}\sqrt{K_R^2(t_l,\theta_n)+K_I^2(t_l,\theta_n)} = max_{t_l}|K(t_l,\theta_n)| \end{aligned} \quad (514)$$

(where the expressions have been adapted to the quantum mechanical case). With this, for a given path, if the value of K_n^{max} increases then $\delta\theta$ decreases and viceversa, so the product of both stays inside a certain range. Logically, depending on the system, this improvement can slow the evolution so much. In our case we are going to do an alteration that takes into account the maximum value of $|x_i(t_l,\theta_n)|$ in each path i. The idea is that in each step,

the variation of each point $x_i(t_l, \theta_n)$ given by (503) respect to $|x_i(t_l, \theta_n)|$ do not exceed a certain percentage chosen by us. So, it has to be satisfied

$$\frac{K_n^{max}\delta\theta}{max_{t_l}|x_i(t_l,\theta_n)|} < b \tag{515}$$

where b is a parameter of our choosing and which represents the maximum percentage of variation. If the condition is not satisfied the value of $\delta\theta$ is reduced until it is satisfied.

10.6.5 Improvement by discretization tuning

We are going to introduce another improvement in the method tuning the discretization of the complex Langevin equation with respect to θ. Ignoring the noise at the moment, the equation (503) shows

$$x(t_l,\theta+\delta\theta) = x(t_l,\theta) - i\delta\theta\Big[m\frac{x(t_{l+1},\theta)+x(t_{l-1},\theta)-2x(t_l,\theta)}{(\delta t)^2} + \\ +mw^2x(t_l,\theta)\frac{\lambda}{6}x^3(t_l,\theta)\Big] = x(t_l,\theta) + i\delta\theta K(t_l,\theta) \tag{516}$$

using the $K(t_l, \theta)$ defined in (514). This means that we have

$$\partial_\theta x(t_l,\theta) = iK(t_l,\theta) \tag{517}$$

Expanding $x(t_l, \theta+\delta\theta)$ to order $(\delta\theta)^2$ and taking into account (516) and (517) we can write

$$x(t_l,\theta+\delta\theta) = x(t_l,\theta) + \delta\theta\partial_\theta x(t_l,\theta) + \frac{1}{2}(\delta\theta)^2\partial_\theta^2 x(t_l,\theta) = \\ = x(t_l,\theta) + i\delta\theta K(t_l,\theta) - \frac{i}{2}(\delta\theta)^2\Big[m\frac{\partial_\theta(x(t_{l+1},\theta)+x(t_{l-1},\theta)-2x(t_l,\theta))}{(\delta t)^2} + \\ +\big(mw^2+\frac{\lambda}{2}x^2(t_l,\theta)\big)\partial_\theta x(t_l,\theta)\Big] = \\ = x(t_l,\theta) + i\delta\theta K(t_l,\theta) + \frac{1}{2}(\delta\theta)^2\Big[m\frac{K(t_{l+1},\theta)+K(t_{l-1},\theta)-2K(t_l,\theta)}{(\delta t)^2} + \\ +\big(mw^2+\frac{\lambda}{2}x^2(t_l,\theta)\big)K(t_l,\theta)\Big] \tag{518}$$

and adding the noise, we have the expression of our improvement.
Of course, we can combine this with the adaptive step, expecting to increase the efficacy of the method.

10.7 Results

We have obtained numerically diverse results in order to check all we have mentioned before, that related to the stability and divergence analysis and the improvements to the complex Langevin method as well. The noise in our tests is always real.

10.7.1 Divergent paths

We have used a typical system, with an action of the form (497). As in above sections, we will work with dimensionless parameters and quantities

$$x \equiv mx\,(\sigma \equiv m\sigma) \quad , \quad t \equiv mt \quad , \quad w \equiv w/m \quad , \quad \lambda \equiv \lambda/m^2 \quad , \quad \theta \equiv \theta/T^2 \tag{519}$$

where T is the usual period of the system with $\lambda = 0$. With this, the initial state and the potential parameters are shown next

$$\begin{aligned} &\psi(x, t=0) = \frac{1}{(2\pi m^2\sigma^2)^{1/4}} e^{-\frac{x^2}{4\sigma^2}} \\ &w^2 = 0.5 \quad , \quad \lambda = 0.45 \quad , \quad \sigma = 0.45 \end{aligned} \tag{520}$$

Thus, we have calculated the initial Wigner function and have obtained a sample of it, which give us the distributions for $x(0,0)$ and $x(\delta t, 0)$. For $x(t_{max}, 0)$ we have set the same fixed value for every path (and therefore its distribution is uniform), chosen like $\sqrt{\langle x^2 \rangle}$ at such moment from the classical evolution for each path. Furthermore, the boundary condition chosen is $\partial_t^2 x(t_{max}, \theta) = 0$. Several values of $\delta\theta$ and δt have been chosen for the discretization, and they have evolved with the equation (503). Moreover, in every graph it has been taken as the **base step** in θ the value $\delta\theta = 10^{-5}/T^2$ and always the number of steps is referred to it, although we also evolve with larger steps.

Condition 1

For a fixed δt, we have taken values of $\delta\theta$ that help the creation of several divergent paths. Next we reduced such step and noticed how the unstable paths decreased drastically. Nevertheless, it has been checked that for a number of paths large enough there always remains a small number of divergent paths. Specifically, we have used the described parameters with a $\delta t = 0.5$, a $t_{max} = N_t \delta t = 26.0$ and even a $\delta\theta = 10^{-5}/T^2$, and for 200 path only one was

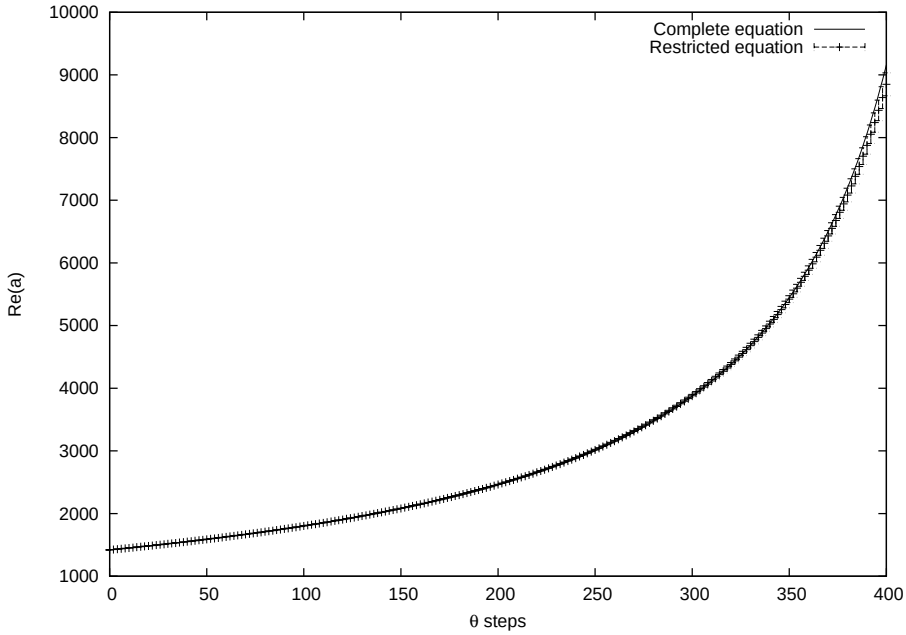

Figure 84: $Re(a)$ for complete evolution and restricted evolution (from *condition 1*) vs θ steps number ($\delta\theta = 10^{-5}/T^2$).

divergent. Using the arguments of the previous section, we have checked if such path had a *type 1* divergence, for which we have focused in the first time it diverges (and that later pulls the rest) and we have analyzed if it fulfills (506). We can see in Fig. 84 the real part of a resulting from the whole evolution and the restricted equation which solution is (506), and they coincide quite well. Fig. 85 shows, for the whole evolution, how the real and imaginary parts of x tend to equal. These *type 1* divergences are not probable, as we expected, but they are difficult to avoid. Sometimes they remain despite reducing $\delta\theta$ till our computation characteristics allow. An approach to avoid them [61] consists of going back in the evolution to a value of θ which still do not have divergent conditions, and evolve again with another seed for the noise. This slows the process, of course. Another possibility is discarding the divergent paths and to calculate the expectation values with the rest.

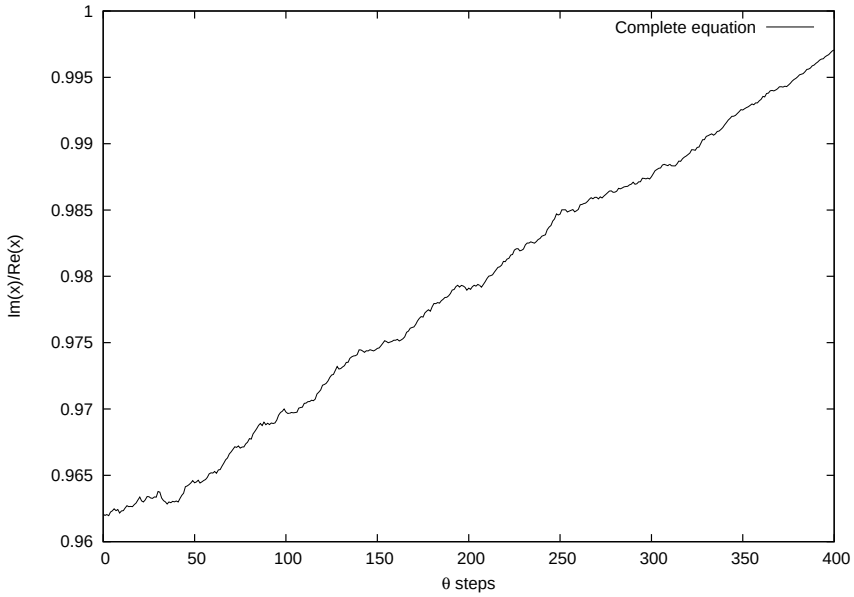

Figure 85: $Im(x)/Re(x)$ for complete evolution. The value of a is more and more real.

Condition 2

Now we take a small number of paths to limit the possibilities of *type 1* divergences. Specifically, we choose the system described by (520) and evolve 20 paths. The usual time has the same δt and t_{max} as in the previous section. The final Langevin time is $\theta_{max} = 25/T^2$ which is much later than the time in which the system stabilizes, as we will show in the next section. For a step $\delta\theta = 10^{-3}/T^2$ the 20 paths are divergent in θ_{max}. Reducing the step decreases the divergent paths so for $\delta\theta = 10^{-5}/T^2$ there is no divergent path left, as it is shown in Fig. 86. This indicates that they are *type 2* divergences. So, we have taken $\delta\theta = 10^{-4}/T^2$ and have checked that the 6 divergent paths diverge when they approach to the critical radius $R_c = 0.01$, thus they can be considered *type 2*. Some degenerate into *type 1* divergences but others do not. We can see in Fig. 87 the approach to R_c of one of them when it diverges. In Fig. 88 we see for the same path how $Re(x)$ and $Im(x)$ become equal in the divergence, indicating that it has degenerated into a *type 1* divergence. Observe how the curve pass through the value 1, after that $|x|$ diverges very fast, with $Im(x)$ greater than $Re(x)$, as can be seen in Fig. 89

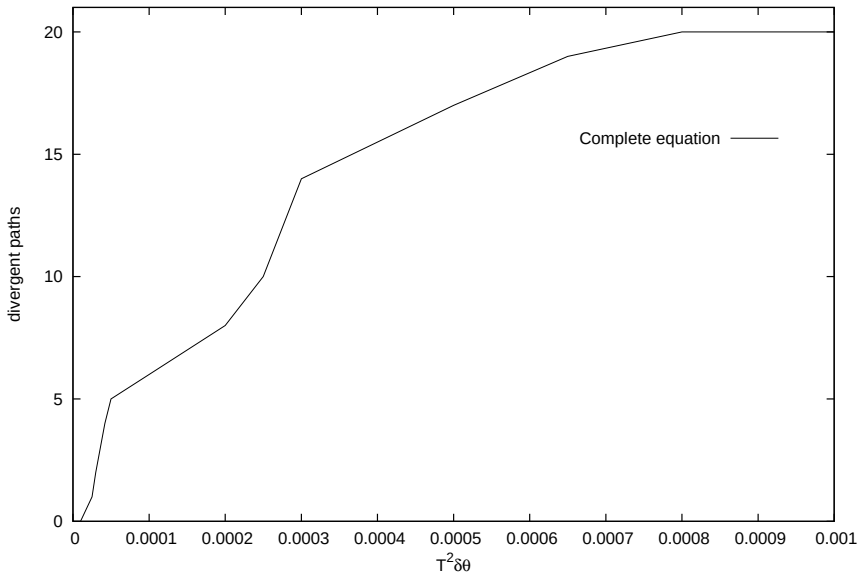

Figure 86: Number of divergent paths (complete evolution). For $\delta\theta = 10^{-3}/T^2$ all paths are divergent. For $\delta\theta = 10^{-5}/T^2$ there are not divergent paths.

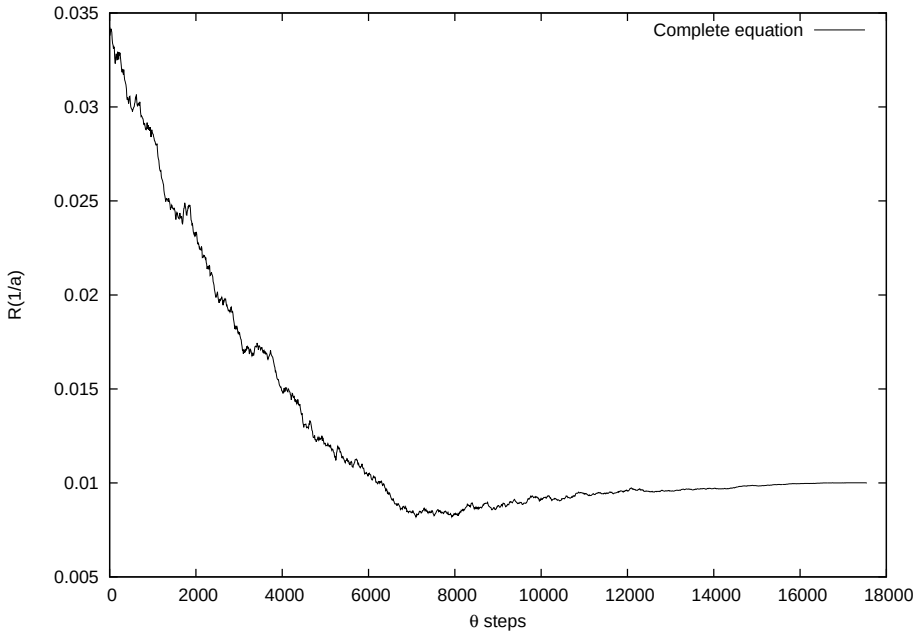

Figure 87: In this path, $R(1/a)$ tends to $R_c = 0.01$.

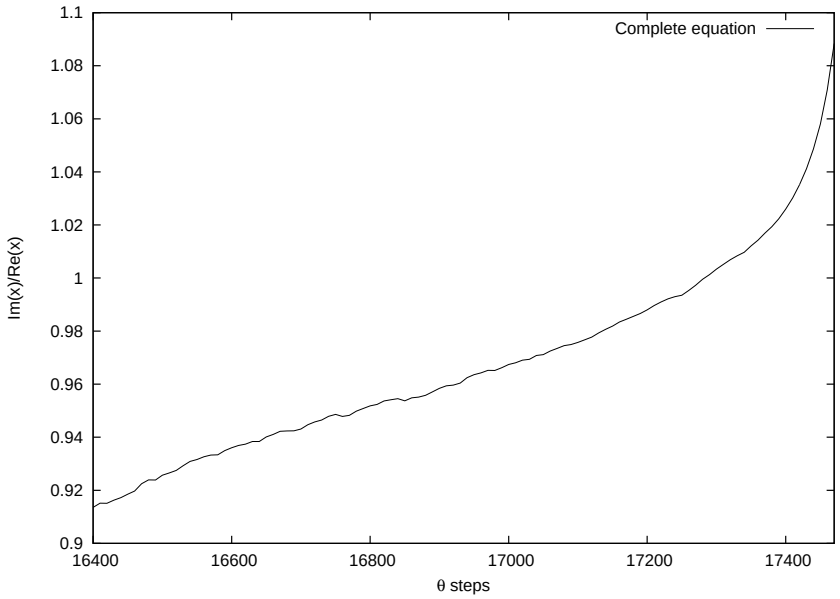

Figure 88: $Im(x)/Re(x)$ tends to one. It seems that the path end like *type 1*.

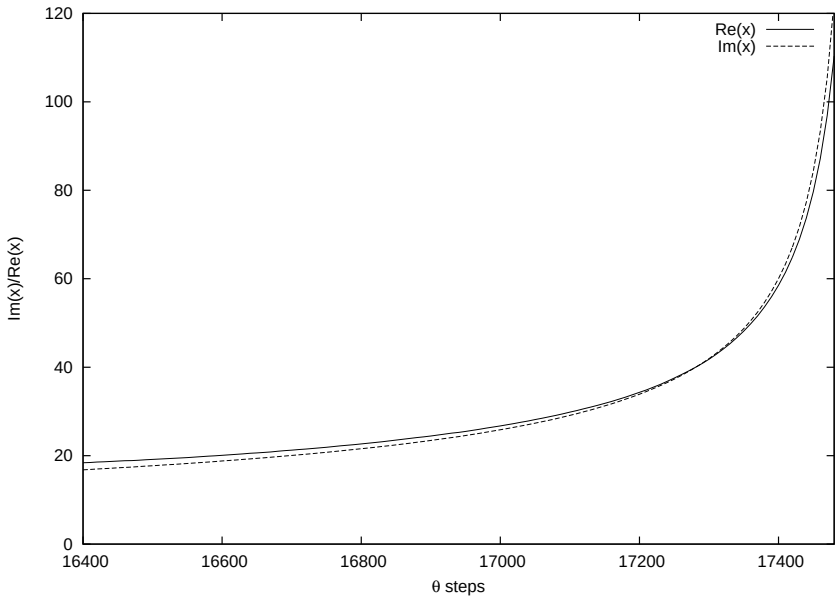

Figure 89: $Re(x)$ and $Im(x)$ are more and more equal until a *type 1* divergence appears.

In Fig. 90 we show the same that in Fig. 87 for another path. But now, although there is a range in which the real and imaginary part of x seem to become equal as $|x|$ increases, this change before the divergence, and they are not as close as the previous case. Moreover, the tendency changes when $|x|$ is not as big as to be out of control due to the instability, since we have checked that this happens when the modulus is one order of magnitude bigger than the present one. So it seems that this divergence is thoroughly a *type 2*. This is shown in Fig. 91.

Of the 6 paths, 4 degenerate into *type 1* divergences and the other 2 remain as *type 2*. In the first case the 4 paths show behaviors like the one described by Fig. 88, with the real part of x approaching to the imaginary part and with the curve crossing the value 1. As an example, we have represented in Figs. 92 and 93 the same as in Figs. 87 and 88 respectively, but for a new path respect to the 4 mentioned. We see that the approach to the critical radius is now from a lower radius. Likewise, for the other *type 2* paths, the behavior is similar to Figs. 90 and 91, and we show it in Figs. 94 and 95. In this case the approach to R_c is also from a lower radius.

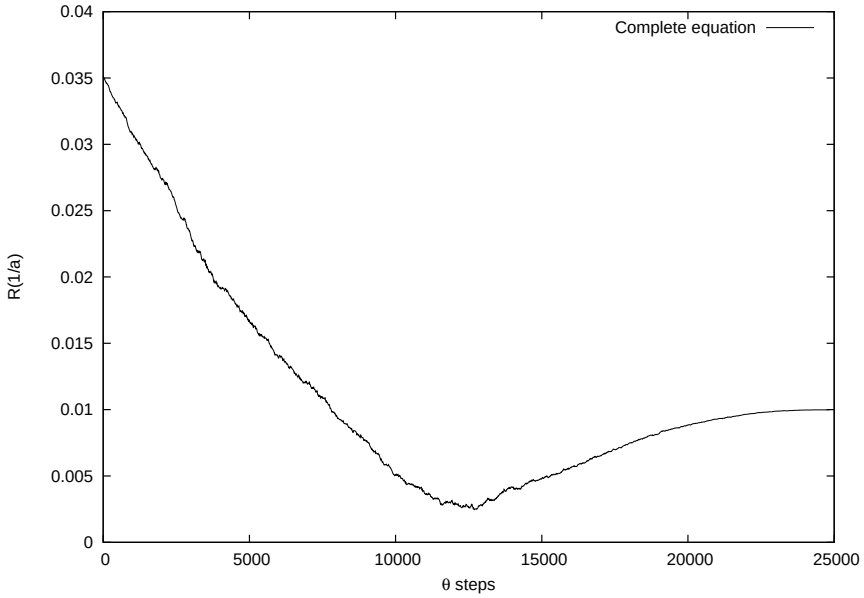

Figure 90: Like Fig. 87 for another path.

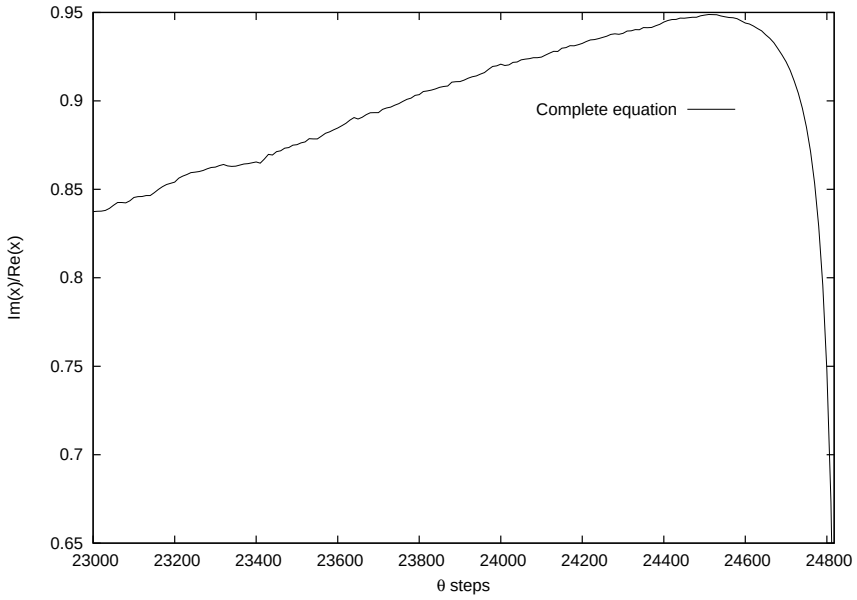

Figure 91: The difference between $Re(x)$ and $Im(x)$ is greater than 5%. The path remains like *type 2*.

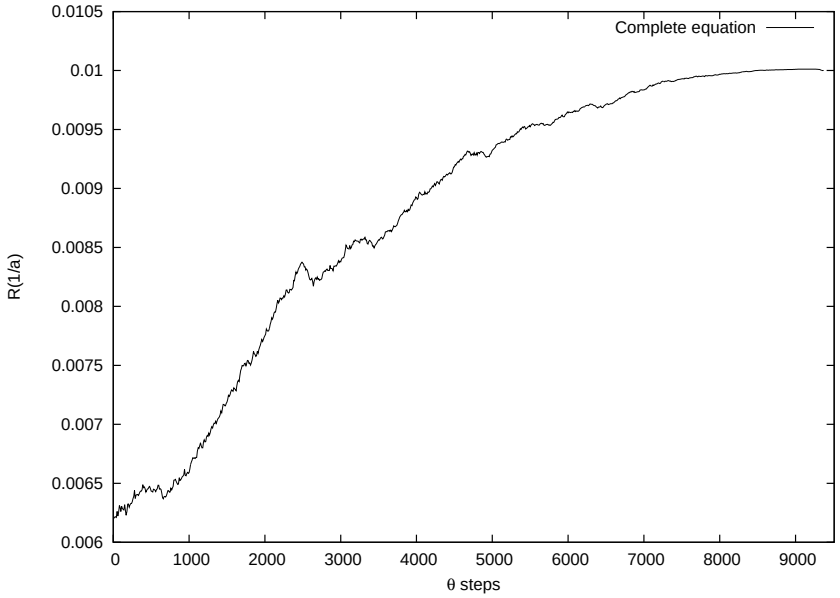

Figure 92: Like Fig. 87 for a new path. The curve tends to R_c from smaller radius.

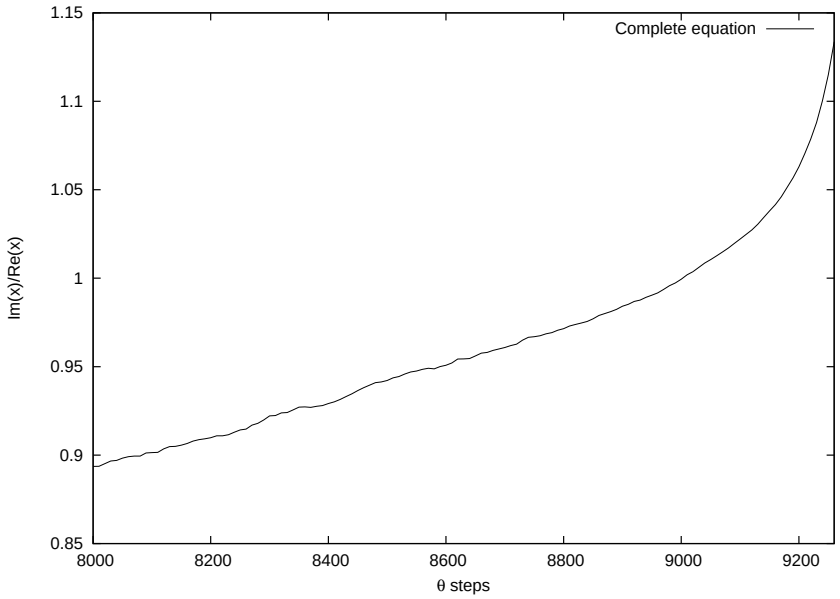

Figure 93: Like Fig. 88, the curve crosses also value 1.

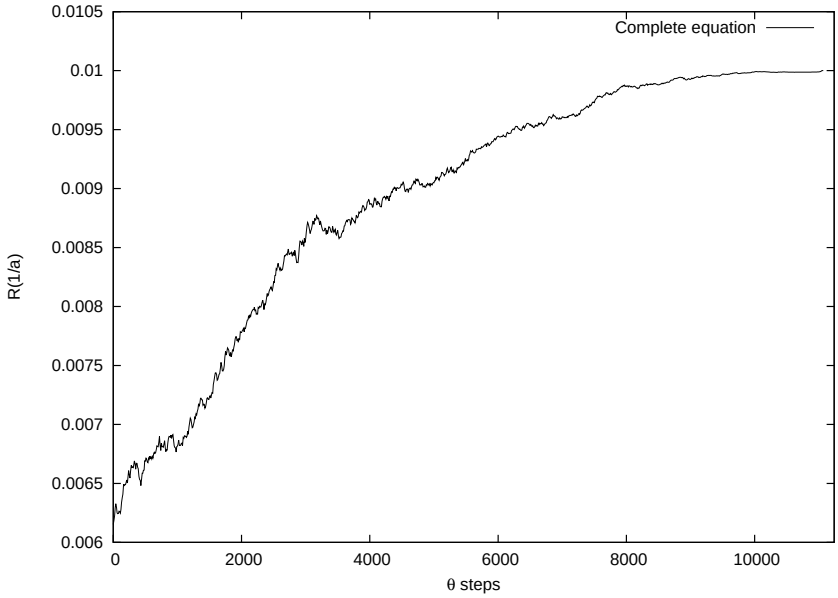

Figure 94: Like Fig. 90 for the other path that remains in *type 2*. $R(1/a)$ tends to R_c from a radius less than critical radius

.

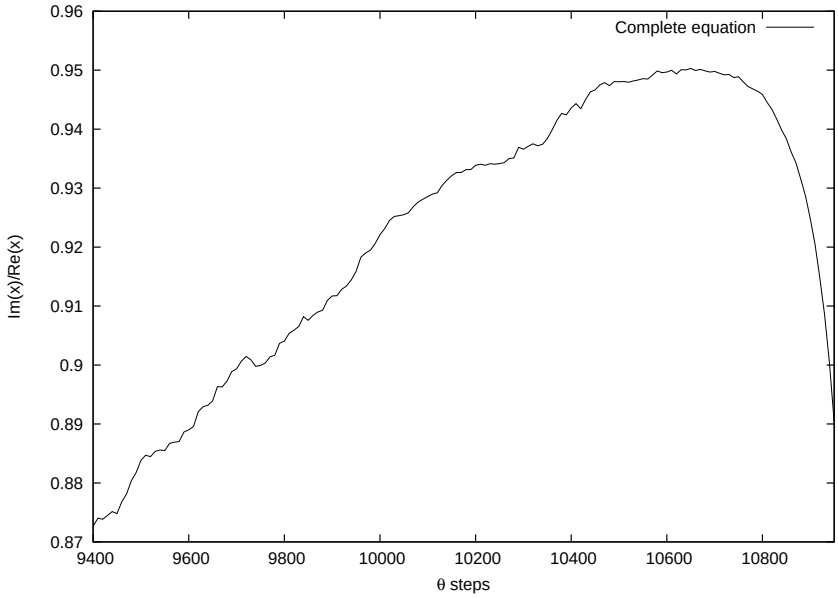

Figure 95: Like Fig. 91, $Im(x)/Re(x) \leq 0.95$.

So the results seem to confirm our previous analysis about the unstable paths. The gradual reduction of the step in the Langevin time ends removing the *type 2* paths, as expected.
It is important to stress that we also evolved the same 20 paths (from the same initial conditions) with the whole equation but without the noise term. We got as result that no path were divergent even for $\delta\theta = 10^{-3}/T^2$. This means that, as we already mentioned, is precisely the noise the main cause of the paths approaching to the critical radius. Of course, the discretization errors also influence it.

Discretization tuning

The improvement described by the equation (518) (plus the noise term) represents a more accurate evolution and should help us to reduce the divergences. To test it we have run the evolution with such improvement for different values of $\delta\theta$. Of course, reducing $\delta\theta$ makes the number of divergent paths also decrease, but we expect a more pronounced effect than without the improvement. That is actually what it happens, as we can see in Fig. 96. For $\delta\theta = 10^{-3}/T^2$ the divergent paths have been reduced from 20 to 18. Furthermore, without the improvement we have to reach $\delta\theta = 10^{-5}/T^2$ to remove the divergences, while with the improvement they disappear for $\delta\theta = 2.8 \times 10^{-5}/T^2$, a value that almost triples the former.

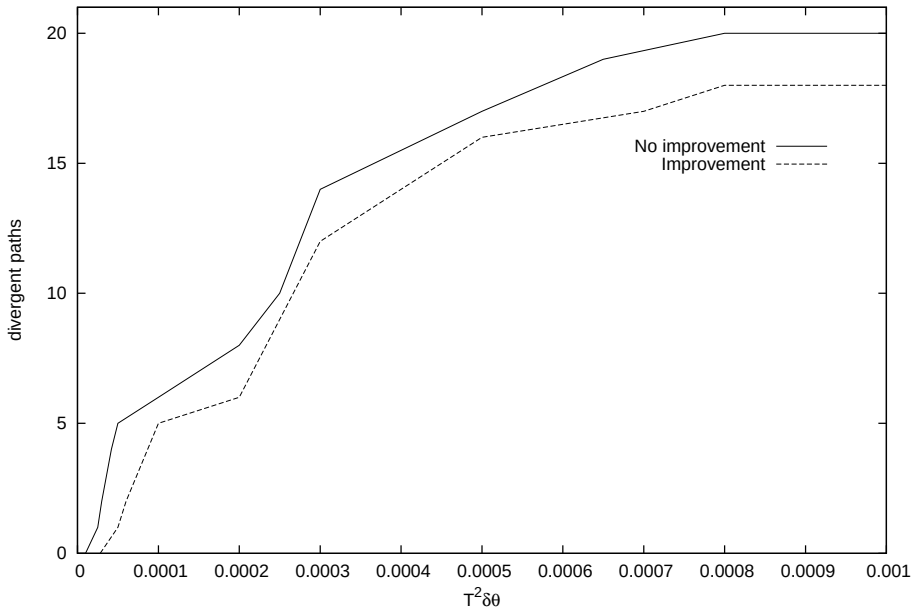

Figure 96: Number of divergent paths for evolution without improvement and with improvement.

It is remarkable that the computation time without the improvement is only a 23% lower than with the improvement.

Adaptive step-size

It is to be expected that introducing an adaptive step-size in the method improve the results and reduce significantly the divergent paths. Of course this modification comes at a greater computational cost. This can be checked in the following table, which compares the number of divergences among the basic method (without discretization improvement or adaptive step), with improvement, with adaptive step, and also both. We also show the computation times in each case, and the value $\delta\theta_0$ for which the divergences are removed as well. For these data these parameters were set $\delta\theta = 10^{-4}/T^2$, $b = 0.1$ (remember that b is chosen to make more or less restrictive the condition given by (515)).

	Basic	Improved	Adaptive	Impr. + Adap.
Num. div. paths	6	5	1	0
computation time	1.4 min	1.6 min	7.7 min	670 min
$\delta\theta_0$	$10^{-5}/T^2$	$2.8 \times 10^{-5}/T^2$	$8 \times 10^{-5}/T^2$	$1.1 \times 10^{-4}/T^2$

It is also interesting to show the number of divergences and the computation time for $\delta\theta = 10^{-3}/T^2$. We can see it in the following table

	Basic	Improved	Adaptive	Impr. + Adap.
Num. div. paths	20	18	6	4
computation time	1.4 min	1.6 min	7.7 min	670 min

Therefore the adaptive step-size is a significant improvement, more so if it is combined with the discretization improvement, although this is unpractical due to the larger computation times. So, each case should be evaluated on the basis of the computation time cost.

Parameter variations

We have also run the evolution changing some parameters of the potential and the discretization as well. So we can check if the behavior is as expected. First, we have observed that if we reduce δt the number of divergent paths increases, but this can be balanced reducing $\delta\theta$ too. We see an example of this in the following table, for basic evolution and with the discretization improvement. The time step has been halved respect to the previous one, and the number of divergent paths is shown for both:

	$\delta\theta = 6 \times 10^{-5}/T^2$		$\delta\theta = 2 \times 10^{-5}/T^2$	
	Basic	Improved	Basic	Improved
$\delta t = 0.5$	5	2	1	0
$\delta t = 0.25$	19	13	12	9

We have also test it with an adaptive step-size evolution for $\delta\theta = 10^{-4}/T^2$. In this case, when $\delta t = 0.5$ we had only 1 divergent path; but using $\delta t = 0.25$ gives 8 divergent paths. As we can see, in every case reducing δt increases the computation costs steeply, as we must reduce $\delta\theta$ considerably.
On the other hand we have changed λ. Reducing it makes the critical radius smaller and thus a lower number of divergences it is to be expected, so

we want to check it. With this objective we show in the following table the number of divergent paths for different values of λ, calculated for the basic evolution with $\delta t = 0.5$ and $\delta\theta = 10^{-4}/T^2$:

λ	1.0	0.45	0.1	0.045	0.0
div. paths	8	6	2	1	0

and indeed we confirm what we expected.
The boundary condition in t_{max} has also been changed. As an example, changing that condition for another one like $\partial_t^3 x(t_{max}, \theta) = 0$ then the number of divergent paths remains unchanged. We also checked the periodic boundary condition, but this is somewhat forced because the point $x(0, \theta)$ is fixed in each path, and in fact the number of divergences increases around a 25% in this case.
Furthermore, we have taken for $x(0, \theta)$ y $x(\delta t, \theta)$ uniform distributions with a value of $\sqrt{\langle x^2 \rangle}$ in each case. Likewise we have altered the initial value of the points in each path that were always set to zero (except the two first and the last one). Last we have tested different values of $x(t_{max}, 0)$. In all these cases, the number of divergent paths for different values of $\delta\theta$ oscillates around the values obtained in the previous sections, and on average they range between one divergent path more or less respect to the previous ones, which is within the error due to counting integers.
In short, as we expected the different elections of the boundary and initial conditions have a limited influence on the instability of our results. What it really influences it are the different values of the parameters, both the potential and the discretization ones.

10.7.2 Convergence

We have seen how to reduce or even remove the divergences that appear when implementing the complex Langevin method, but we want to check if that is enough to have a correct convergence. First we must confirm that our system has reached a stationary state in the range of θ we are considering. In order to do it we have chosen $\delta t = 0.5$, $t_{max} = N_t \delta t = 26$, $\delta\theta = 10^{-5}/T^2$, and 20000 paths which have been evolved in θ. The value $x(t_{max})$ is the one obtained from the classical evolution and its boundary condition is $\partial_t^2 x(t_{max}, \theta) = 0$. As result, it has been represented in Fig. 97 $Re[\langle x^2(t, \theta) \rangle]$ for a certain value of t, and we can see how it stabilizes around $\theta = 12/T^2 \approx 0.16$.

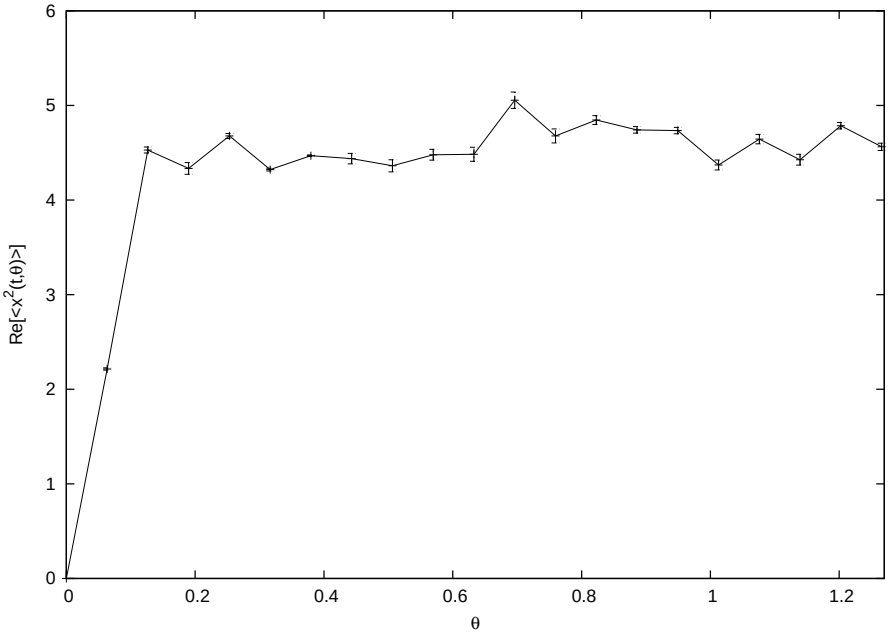

Figure 97: $Re[\langle x^2(t,\theta)\rangle]$ for $t = 2.0$.

Respect to the imaginary part, it stabilizes a time later and oscillates with a greater amplitude than the real part, as it can be observed in Fig. 98. Notice that such imaginary part is never zero, as we should expect if the stationary state is the right one.

To achieve less dispersion we can calculate $\langle x^2(\theta)\rangle$, i.e., doing the average not only with all the paths but with all the values of t in each of them. We represent the real and imaginary parts in Figs. 99 and 100, and in this case both can be considered stabilized around $\theta = 18/T^2 \approx 0.22$. Here the imaginary part also does not approach to zero. Consequently, although this system seems to have reached a stationary state, the results obtained are unexpected. We can see in Fig. 101 how $\langle x^2(t,\theta)\rangle$ oscillates around a stationary value; but in Fig. 102 we see that this value is different to the one obtained with the numerical quantum evolution of the system.

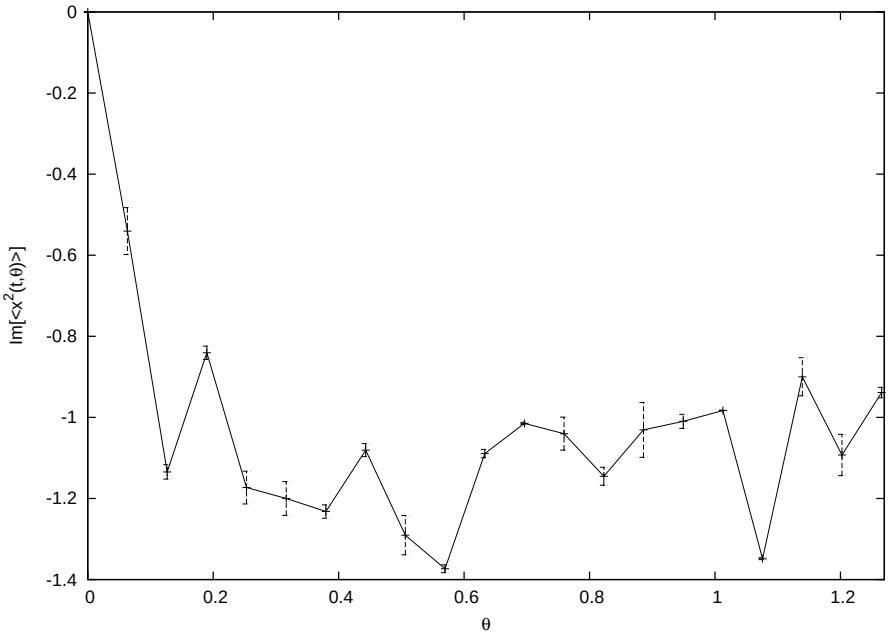

Figure 98: $Im[\langle x^2(t,\theta)\rangle]$ for $t = 2.0$. The value does not tend to 0.

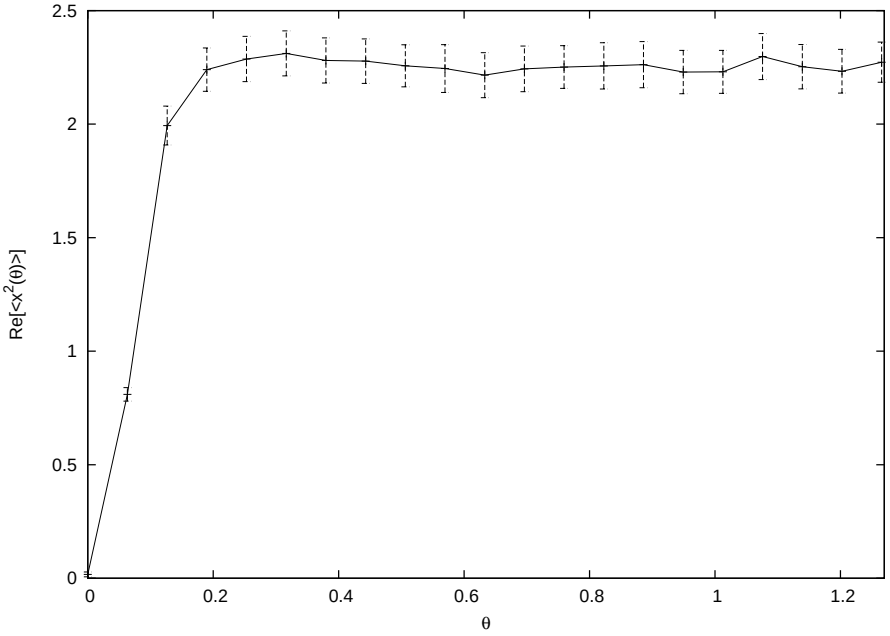

Figure 99: $Re[\langle x^2(\theta)\rangle] = (1/N_t)\sum_t Re[\langle x^2(t,\theta)\rangle]$.

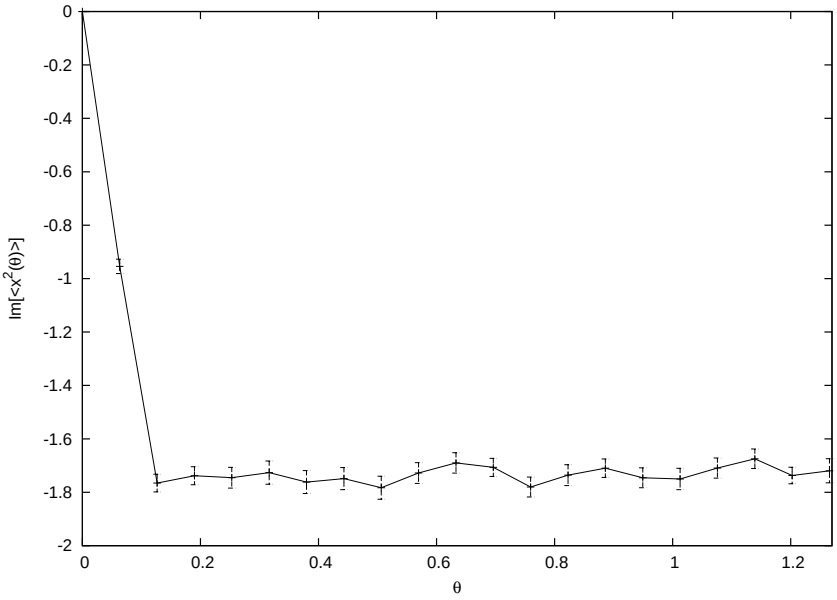

Figure 100: $Im[\langle x^2(\theta)\rangle]$. It does not tend to zero.

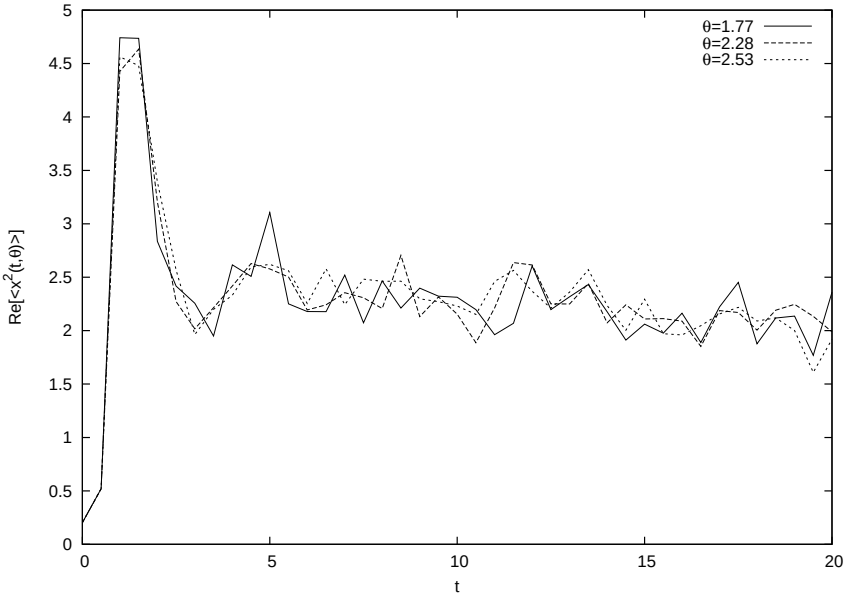

Figure 101: $\langle x^2(t,\theta)\rangle$ for several values of θ and once the system has become stabilized.

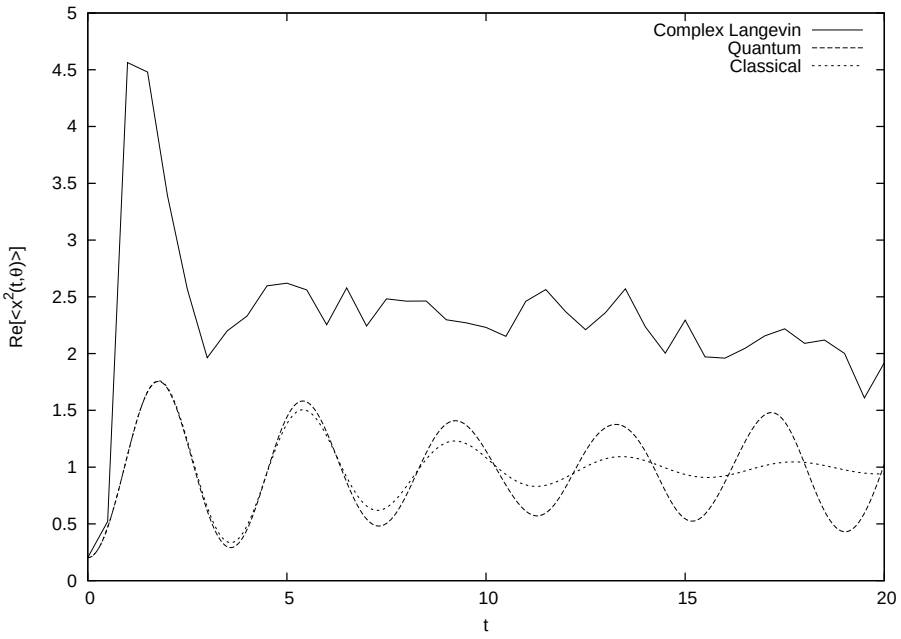

Figure 102: $Re[\langle x^2(t,\theta)\rangle]$ for the Complex Langevin method (at $\theta = 1.26$), the Quantum evolution and the Classical one.

Parameter variation

We have seen that the system does not reach the correct limit. We will study how changing parameters of potential or discretization affects the convergence.

For the same system, we have changed the boundary condition at t_{max} from $\partial_t^2 x = 0$ to $\partial_t^3 x = 0$. Near t_{max} one can observe differences between both conditions, but in the remaining times (where the boundary has no influence) the expectations values reach similar values. We show in Fig. 103 the $Re[\langle x^2(\theta)\rangle]$ once removed the border influence, and the results are compatible.

Also we have changed the value of t_{max} and it seems that the final stationary state is the same than for the previous range of times. We can see in Fig. 104 the same that in Fig. 103 for two different values of t_{max} and the curves are compatible.

In other hand we have checked if the final state depends on the used method (Basic, O(2) or Adaptive). We found that the time to achieve the stationary state can change a little but the three methods lead to similar state. We display in Fig. 105 the $Re[\langle x^2(t,\theta)\rangle]$ for the three methods and the behavior is similar. We have tested this for several values of θ and the three curves fluctuate around the values showed in Fig. 105.

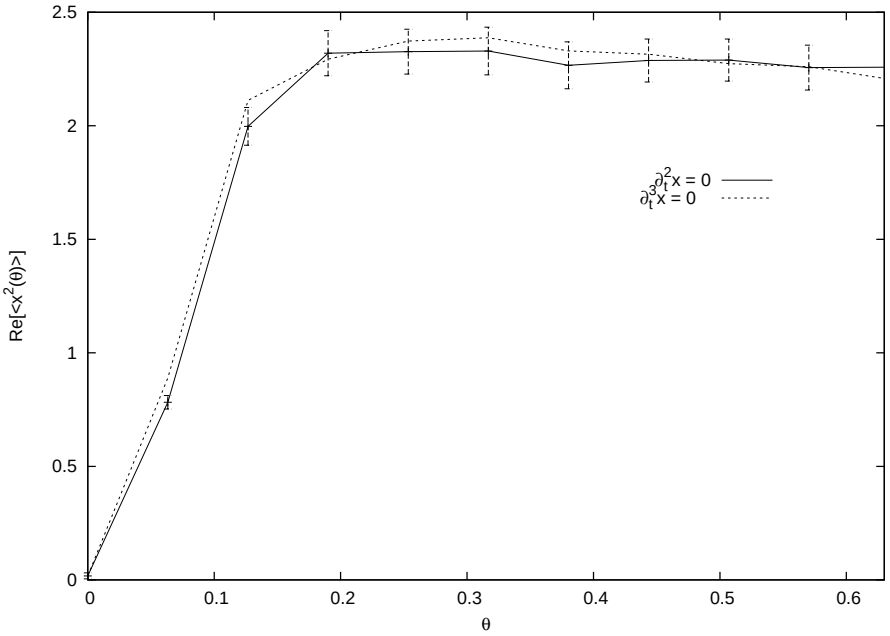

Figure 103: $Re[\langle x^2(\theta)\rangle]$ for different boundary conditions.

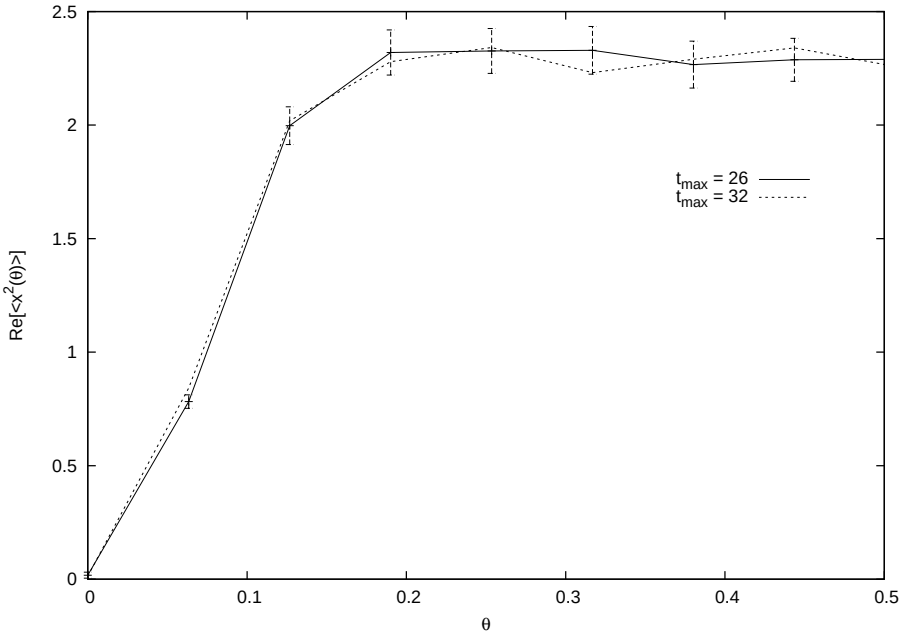

Figure 104: $Re[\langle x^2(\theta)\rangle]$ for different values of t_{max}.

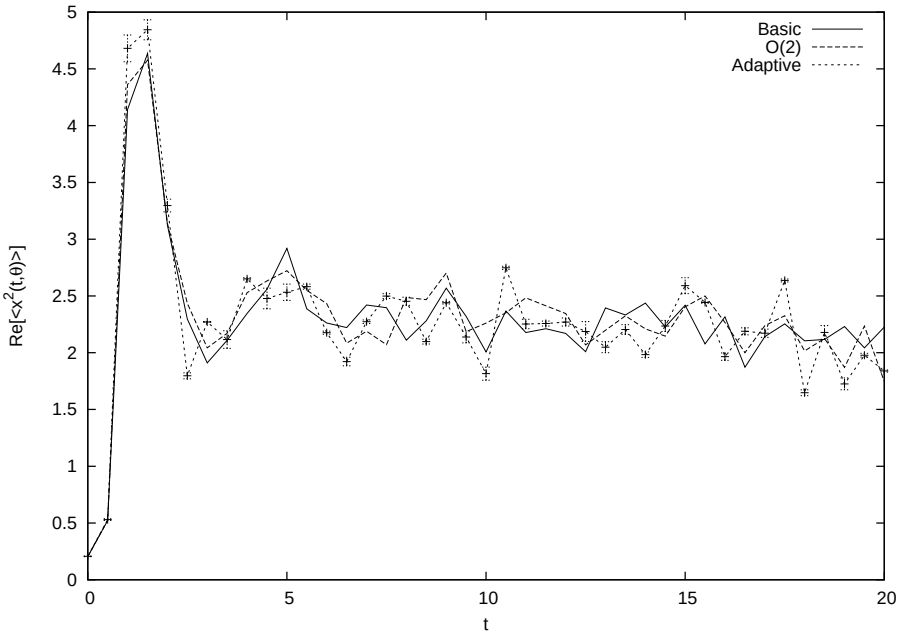

Figure 105: $Re[\langle x^2(t,\theta)\rangle]$ at $\theta = 0.51$.

Of course, we have tested the behavior when we increase the statistic. The curves become a bit softer but they show the same values.
Moreover, we have taken two different initial conditions (at $\theta = 0$) in order to test if the final stationary state is the same irrespective of the initial conditions (as one hopes). The usual initial condition is already explained in previous sections and correspond to fix the intermediate values of trajectories to zero. The classical initial condition (also mentioned above) corresponds to take initially the set of classical trajectories (and therefore the value at $x_i(t_{max})$ changes in each trajectory). Indeed the system reaches the same stationary state and we display an example in Fig. 106 for $\theta = 0.51$. Again, for increasing values of θ, the curves oscillate around the same values. Also we display the $Re[\langle x^2(\theta)\rangle]$ in Fig. 107 and clearly the different initial conditions lead to the same final stationary state.
Thus, the result appears to be robust and we are in the case of a wrong limit that lead to an incorrect final stationary state.

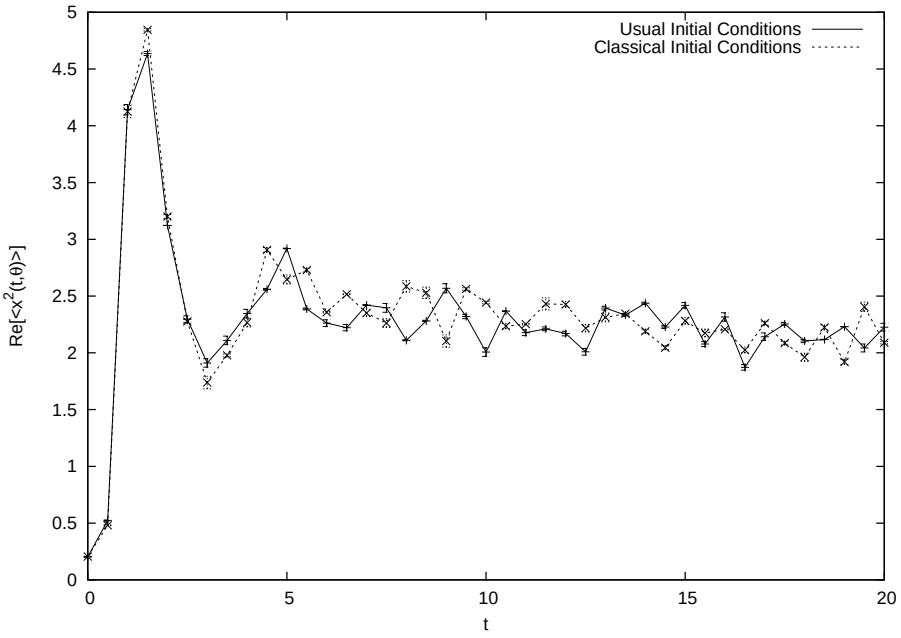

Figure 106: $Re[\langle x^2(t,\theta)\rangle]$ at $\theta = 0.51$ for two different initial conditions.

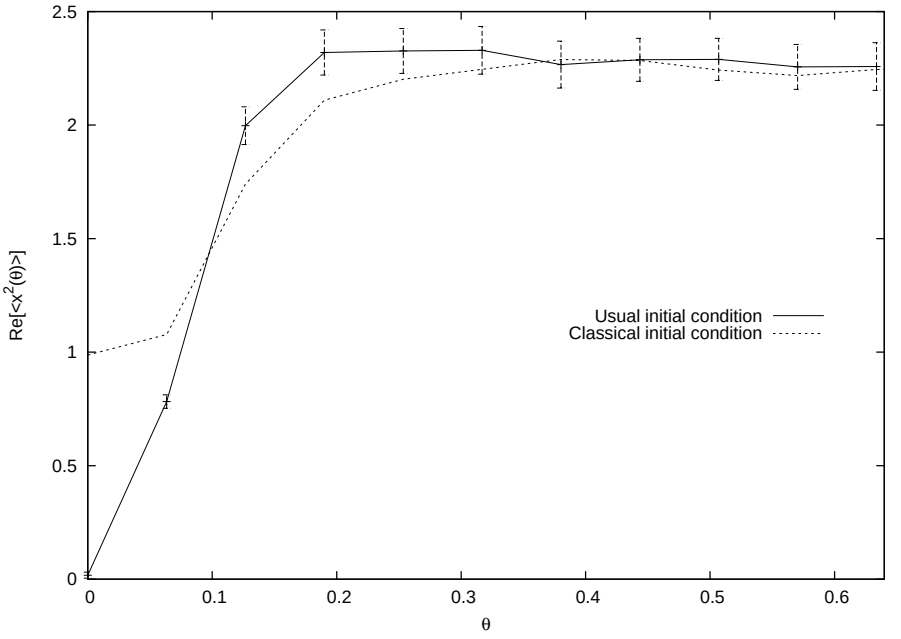

Figure 107: $Re[\langle x^2(\theta)\rangle]$ for two different initial conditions.

Finally we evolve the system with $\lambda = 0$. All divergences are absent in this case and we want to check if the final stationary state is correct. We found that when we start from the classical initial condition the curves of the expectation values oscillate around the correct shape when θ is increasing. And if we start from the usual initial condition there is a transition to the mentioned correct shape. We can see in Fig. 108 the $Re[\langle x^2(t,\theta)\rangle]$ coming from the two different initial conditions. The curves are approximately the correct shape and period. If θ grows, then both curves oscillate around the displayed values maintaining the correct period. Moreover, in this case the number of divergent trajectories is zero, as we hope.

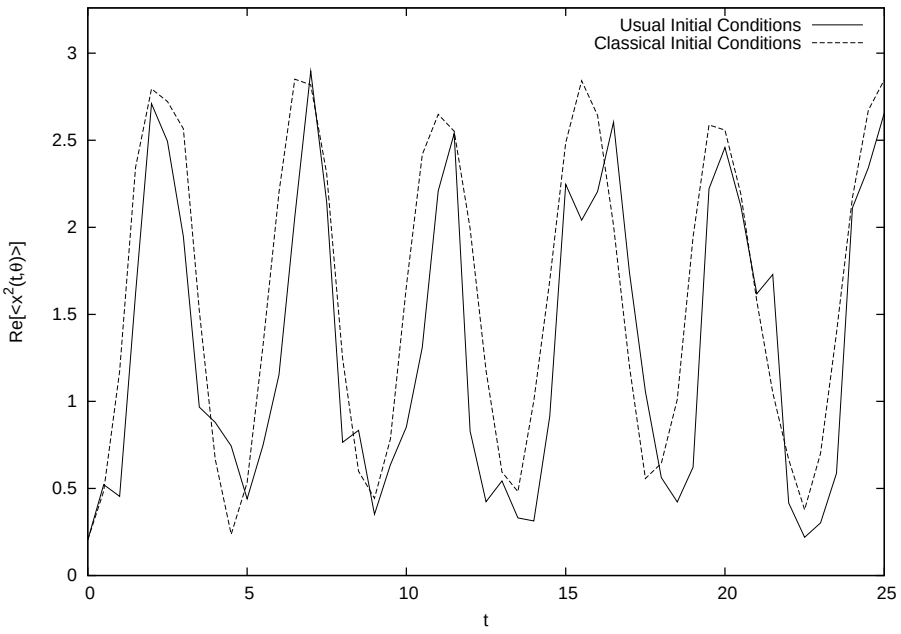

Figure 108: $Re[\langle x^2(t,\theta)\rangle]$ for the system with $\lambda = 0$.

11 nQC Method

In this chapter we will try to generate the Wigner function quantum evolution equation by means of a Langevin process. A typical Langevin dynamical process cannot do the job, since it preserves the positive character of the probability density. Hence, we need a non-trivial modification of the standard technique to apply to this case. In what follows we will see how this comes out exactly.

11.1 Langevin approach to quantum evolution

We start considering the case of one variable. The generalization to the case of several variables will be shown later. We take an usual quartic potential with the form

$$H = \frac{1}{2m}p^2 + \frac{1}{2}\mu^2 x^2 + \frac{\lambda}{24}x^4 \tag{521}$$

Let us begin by writing the classical evolution equations with the addition of a random force:

$$\dot{x}(t) = \tfrac{p(t)}{m} \tag{522}$$

$$\dot{p}(t) = -V'(x(t)) + F(t) \tag{523}$$

Our goal will be to study the properties of the force $F(t)$ to recover the equation for the Wigner function. In order to do so in a simplified manner, let us discretize the time variable and write the equation relating $x' \equiv x(t+\delta t)$ and $p' \equiv p(t\ +\delta t)$ to $x \equiv x(t)$ and $p \equiv p(t)$:

$$\begin{aligned} x' &= x + \delta x = x + \delta t\, \tfrac{p}{m} \\ p' &= p + \delta p = p - V'(x')\, \delta t + \delta F(t) \end{aligned} \tag{524}$$

As we will see, to spell out the x dependence of the random force, we should write $\delta F(t) = x^{1/3}(t)\eta(t)$, where the distribution of the variable $\eta(t)$ is controlled by a function $\rho(\eta)$. Now, let us write the distribution function for x' and p', which by definition is $W(x', p'; t + \delta t)$. We get

$$W(x', p'; t+\delta t) = \int d\eta \int dx\, dp\ \rho(\eta)\, W(x, p, t)\, \delta(x' - x - \delta x)\, \delta(p' - p - \delta p) \tag{525}$$

Now we should eliminate the integrals over x and p with the use of the delta functions. For that purpose we should make use of the time-reversed evolution equations

$$x = x' - \delta t \, \frac{p}{m} \equiv f(x', p', \eta) \tag{526}$$

$$p = p' + V'(x') \, \delta t - x^{1/3} \eta \equiv g(x', p', \eta) \tag{527}$$

We get

$$W(x', p', t + \delta t) = \int d\eta \, \rho(\eta) \; W(f(x', p', \eta), g(x', p', \eta), t) \; J(x', p') \tag{528}$$

where J is the Jacobian of the change of variables. Finally, we expand the equation in powers of δt and η. Keeping terms linear in δt only, we obtain a discretized version of the quantum Liouville equation provided we demand

$$\begin{aligned} &\textstyle\int d\eta \, \rho(\eta) = 1 \\ &\langle \eta^n \rangle \equiv \textstyle\int d\eta \, \rho(\eta) \; \eta^n = 0 \quad \text{for } 0 < n \neq 3 \end{aligned} \tag{529}$$

and

$$\langle \eta^3 \rangle \equiv \int d\eta \, \rho(\eta) \; \eta^3 = \frac{\lambda \hbar^2 \, \delta t}{4} \tag{530}$$

It is quite obvious that if the variable η is real, the previous equations are incompatible with a positive definite distribution function $\rho(\eta)$, since in that case $\langle \eta^{2n} \rangle \geq 0$ or all moments should be 0. Despite this fact in the next section we will see how we can relate the equation to that of a truly positive-definite distribution function, for which sampling statistical methods are applicable. The generalization of the previous formulas to the case of several variables is fairly straightforward. In principle, the force is now replaced by a vector of forces δF_i. These forces are functions of several random variables with non-positive definite distribution functions. A simple way to parametrize these forces is

$$\delta F_i = \eta \chi_i \tag{531}$$

where the distribution function of $\rho(\eta)$ coincides with the one of a single variable. The remaining variables χ_i can be distributed according to standard positive-definite distributions.

As an example consider the case of the O(N) symmetric potential. In this case one can write $\chi_i = x_i \tau + \xi_i$ and choose a simple positive definite distribution function $\tilde{\rho}(\tau, ||\vec{\xi}||)$ to recover the time-discretized version of the Wigner-function equation. We leave the details to the reader.

For the case of a d-dimensional lattice field potential given in Chapter 2, a choice like $\chi_i = x_i^{1/3}\xi_i$ will do, provided the ξ_i are independent random variables with vanishing average and $\langle \xi_i^3 \rangle = 1$.

11.2 A new computational method

In the previous section we have seen how to reproduce the evolution equation for the Wigner function by means of a Langevin approach with a random force with non-positive definite distribution function. This is the starting point for a new procedure to approximate the quantum evolution which we will explain in this section. The method depends on three steps or approximations which are intimately connected among themselves. The first part is a coarse-grain approximation in the momenta p_i, with a characteristic coarse-graining parameter ϵ. Next we will show how one can reproduce the effect of the non-positive definite distribution function $\rho(\eta)$ by means of a purely Markovian process involving ordinary probability measures. This will allow the use of standard sampling techniques to generate the distribution. The last step will be the introduction of a parameter κ multiplying the quantum term in the evolution equation for the Wigner function. The parameter interpolates between a purely classical evolution ($\kappa = 0$) and the full quantum evolution (for $\kappa = 1$). The whole procedure can be used to compute the evolution of quantum expectation values in powers of κ. This is similar to an expansion in powers of $\hbar^2$, although part of the $\hbar$ dependence sits in the initial condition and is left unchanged. This expansion in powers of κ allow us to denote the method as nQC, where n means that we consider the expansion to order κ^n. Thus, for *1QC* or *Linear QC* we expand to order κ, for *2QC* or *Quadratic QC* we expand to order κ^2, and so on.

As mentioned in the previous paragraph, our first step is a coarse-grain approximation, which will amount to an approximation to the non-positive definite $\rho(\eta)$. For that purpose, we might relax the condition that $\langle \eta^n \rangle = 0$ for $n > 3$. One possible realization of the conditions is achieved by the following family of distribution functions:

$$\rho_N(\eta) = \delta(\eta) + \sum_{i=1}^{M_N} \frac{\gamma_i}{\epsilon^3}(\delta(\eta - \epsilon\alpha_i) - \delta(\eta + \epsilon\alpha_i)) \tag{532}$$

where γ_i are positive numbers, α_i are real values, and ϵ is a free parameter. Although not explicitly indicated, the coefficients γ_i and α_i do depend on

N. They are determined by imposing that all even moments vanish and odd moments, given by

$$\mu_{2p+1} \equiv \langle \eta^{2p+1} \rangle_N = 2 \sum_{i=1}^{M_N} \gamma_i \, \alpha_i^{2p+1} \epsilon^{2(p-1)} \tag{533}$$

vanish for $p \leq N$, with the exception of $p = 1$ given by Eq. 530. If we take, without loss of generality, that the parameters α_i are of order 1, this condition implies that

$$\gamma_i \propto \frac{\lambda \, \hbar^2 \, \delta t}{8} \tag{534}$$

In general, the solution to the set of constraints will not determine the parameters γ_i and α_i uniquely. This freedom in the choice of the parameters is a bonus, since one can test the effects of the coarse-graining on the results, by exploring different choices. Furthermore, a better approximation is obtained by taking larger values of N, which will be referred as the level of the approximation. The number of terms M_N has to grow as N grows. An alternative method to improve the accuracy would be to reduce the value of ϵ, thus reducing the effect of higher order derivatives of the Wigner function. As we will see later, there is a limitation to the minimal value of ϵ, which is dictated by the range of time for which the method would be applicable.
The next ingredient will be that of relating the Wigner function to a positive-definite distribution function, which can be approximated by samples. The same can be done for the distribution function $\rho(\eta)$ as follows. Let us introduce a positive-definite function $\hat{\rho}(\eta, \sigma)$ involving a discrete Ising-like variable $\sigma = \pm 1$. This function is related to $\rho(\eta)$ by

$$\rho(\eta) = \mathcal{N} \sum_{\sigma = \pm 1} \hat{\rho}(\eta, \sigma) \, \sigma \tag{535}$$

The function $\hat{\rho}(\eta, \sigma)$ is normalized as a probability distribution

$$\sum_{\sigma} \int d\eta \, \hat{\rho}(\eta, \sigma) = 1 \tag{536}$$

and hence the prefactor is given by:

$$\frac{1}{\mathcal{N}} = < \sigma >_{\hat{\rho}} \equiv \sum_{\sigma} \int d\eta \, \hat{\rho}(\eta, \sigma) \, \sigma \tag{537}$$

The construction can be extended to the coarse-grained version given before. Hence, we define

$$\hat{\rho}_N(\eta,\sigma) = \frac{1}{\mathcal{N}}\left[\frac{1+\sigma}{2}\,\delta(\eta) + \sum_{i=1}^{M_N}\frac{\gamma_i}{\epsilon^3}\,\delta(\eta-\epsilon\alpha_i\sigma)\right] \tag{538}$$

The normalization condition implies

$$\mathcal{N} = 1 + 2\sum_{i=1}^{M_N}\frac{\gamma_i}{\epsilon^3} \tag{539}$$

A similar procedure can be applied to the Wigner function

$$W(x,p;t) = K(t)\sum_{\sigma=\pm1}\hat{W}(x,p,\sigma;t)\,\sigma \tag{540}$$

where $\hat{W}(x,p,\sigma;t)$ is a well-defined probability distribution. This is equivalent to writing the Wigner function as the difference of two positive definite functions. If we label by $\langle\ \rangle_{\hat{W}}$ the expectation values with respect to $\hat{W}(x,p,\sigma;t)$, then the expectation values with respect to the Wigner function are given by

$$\int dx\,dp\ O(x,p)\,W(x,p;t) = \frac{\langle\sigma\,O(x,p)\rangle_{\hat{W}}}{\langle\sigma\rangle_{\hat{W}}} \tag{541}$$

Now, one can obtain a time-discretized evolution equation for $\hat{W}(x,p,\sigma;t)$ involving $\hat{\rho}(\eta,\sigma)$ as follows:

$$\hat{W}(x,p,\sigma;t+\delta t) = \sum_{\mu=\pm1}\int d\eta\,\hat{\rho}(\eta,\mu)\hat{W}(x-\delta x,p-\delta p,\mu\cdot\sigma;t) \tag{542}$$

where the displacements δx-δp are those coming from the classical equations of motion with a force proportional η (as before). Summing the previous equation over σ and using the previous definitions, we re-obtain the discretized evolution equation for the Wigner function provided

$$K(t+\delta t) = \mathcal{N}K(t) \tag{543}$$

We see that this implies that the normalization factor grows exponentially, and this is precisely the main numerical limitation of the method.

Having set up an evolution equation for the probability distribution $\hat{W}(x,p,\sigma;t)$ we can employ standard sampling techniques to approximate it. This leads us to the concept of *signed* samples: a collection of $\mathcal{M}$ points $\{x^{(a)},p^{(a)},\sigma^{(a)}\}$ such that

$$\int dx\,dp\sum_{\sigma=\pm1}\hat{W}(x,p,\sigma;t)\,O(x,p;\sigma)\approx\frac{1}{\mathcal{M}}\sum_{a=1}^{\mathcal{M}}O(x^{(a)},p^{(a)};\sigma^{(a)}) \tag{544}$$

From Eq. 542 one can determine the time evolution of samples given a realization of the noise η. This is a Markovian process where $\hat{\rho}(\eta,\mu)$ determines the conditional probability for a transition from one point in phase-space to a new one and a possible change of sign of the discrete Ising variable.
If we use the coarse-grained distribution $\hat{\rho}_N(\eta,\mu)$, then with a certain probability we would simply evolve the system with the classical equations of motion, and with probability proportional to δt we would produce a jump in the value of momentum and a possible flip of the sign of σ. The reason for referring to the first approximation as coarse-graining in momentum space, has to do with the discrete magnitude of the jump (of order ϵ) at each step of the time-evolution. If the Wigner function would be a polynomial in p, the approximation would be exact.
If we start the evolution with a positive definite Wigner function, then $\frac{1+\sigma}{2}W(x,p,t=0)=\hat{W}(x,p,\sigma,t=0)$. Hence, all points in the sample have $\sigma^{(a)}=1$. As time evolves some of the points acquire a negative value of $\sigma^{(a)}$. At time $t=n\delta t$ the probability that a point in the sample has negative σ is given by

$$P_-=\frac{1-\langle\sigma\rangle_{\hat{W}}}{2}=\frac{1}{2}\left(1-(<\sigma>_{\hat{\rho}})^n\right)\approx\frac{1}{2}\left(1-e^{-At\lambda\hbar^2/\epsilon^3}\right) \tag{545}$$

with A a number of order 1, which depends on the detailed form of $\hat{\rho}_N$. The probability approaches $1/2$ exponentially in time. Once this happens we encounter a severe sign problem in computing averages according to the formula Eq. 541, since the averages result from strong cancellations from $\sigma=1$ and $\sigma=-1$. At this point the method breaks down. The typical time when this happens is given by

$$T\approx\frac{\epsilon^3}{\lambda\hbar^2} \tag{546}$$

Clearly things get worse as we decrease ϵ and improve as we decrease λ and $\hbar$. However, the magnitude of ϵ must be related to the typical range of

variation in p of the Wigner function. Otherwise, corrections involving higher order derivatives of the Wigner function become large. The systematic errors associated to the coarse-graining can be checked by varying ϵ or by using different choices of N. For small enough ϵ, the approximation should behave better for larger N.

Once the maximum acceptable value of ϵ is selected, the method stated before only allows the computation of quantum expectation values for a range of times. This limitation, although important, does not destroy the usefulness of the method. Time-range limitations are already present in studying the classical evolution equation of a quantum field theory discretized on a lattice. The moment that the fluctuations become sizable at the cut-off scale, the discretized evolution equation fail to reproduce the continuum evolution. Fortunately, in many applications a good part of the interesting physical processes take place in a relatively short period of time. This is the case, for example, in the context of preheating in the early universe, which is one of the main motivations that we had for embarking in the present work.

In situations in which a reliable full quantum evolution can only be carried for a too short lapse of time, the method can be used to compute first-order quantum corrections as follows. This is the third ingredient that we anticipated in the first paragraph of this section. The strategy is to consider a modified evolution equation with a new parameter κ multiplying the last term of Eq. 61. This can be interpreted as multiplying $\hbar$ by $\sqrt{\kappa}$. In this fashion one extends the time range of applicability of our method by the multiplicative factor $1/\kappa$. Now, evolving the system for several other smaller values of κ, one can determine the evolution of the expectation values as a power series in κ.

A practical problem concerns accuracy. Since, our goal is to estimate the quantum fluctuations, we realize that when reducing κ, they have decreased by the same factor. To maintain the signal to noise ratio one should increase the size of the sample by κ^2, which would increase the computation time by the same factor. Since the reduction in κ was dictated by the necessity to extend the range in time of the simulation, we conclude that this can be done at a cost in computer time which only grows polynomially with this range.

Of course, the drawback is that one does not compute the full quantum effects but only to leading order in κ (i.e. $\hbar^2$). This by itself is an important result because it would serve as a measure of the size of quantum effects and as a next-to-leading correction to the classical approximation. Higher order powers of κ are also computable at a higher cost in computer time.

To test these ideas we decided to study several simple quantum mechanical systems for which the exact quantum evolution can be determined by numerical integration of the Schroedinger equation. The results will be presented in the next section and compared to other extensions of the classical approximation given in the literature.
Before closing this section, we should comment on the modifications necessary to extend the procedure defined previously to the case of many degrees of freedom. Our method might not be optimal for the case of very few degrees of freedom, however, it was designed to be extensible in an affordable way to the case of many degrees of freedom. In this respect it differs from other proposals in the literature based on histogramming which seem impossible to extend to a large number of variables.
The formal extension of all the approximations involved in the method to the case of several degrees of freedom is indeed trivial. In the way that the Langevin process was extended above, it turns out that there is a unique *random variable* η having a non positive definite distribution function with similar or exact properties as the one appearing for the one-variable case. Thus, the coarse graining $\rho \longrightarrow \rho_N$ and extension to positivity $\rho(\eta) \longrightarrow \hat{\rho}(\eta, \sigma)$ remains exactly the same irrespective of the number of variables. The rest of random variables entering the force are of the conventional type and their number increases linearly with the number of degrees of freedom, and so does the computation time for a given time-step. The sample now, however, involves trajectories in the multidimensional state of the system. This is exactly the same as for the classical evolution (with random initial conditions), except that now there is a single additional Ising-like variable σ. Thus, for a fixed number of trajectories the computational cost will grow in a similar fashion to that of the classical evolution. A new question to worry about is whether the number of trajectories needed to obtain results with a reasonable accuracy depend upon the number of degrees of freedom. This will be studied in later for one particular example.

11.3 Testing the classical approximation and its extensions

Here we will present the results of our tests of the classical approximation and of our proposed method to obtain quantum corrections, together with other proposals. The first cases are particularly simple situations with one or two

degrees of freedom for which the exact quantum evolution can be obtained through the numerical integration of the Schroedinger equation. Later we will explore the first steps towards a possible application to quantum field theory.

11.3.1 Anharmonic oscillator

Our first example will be a simple anharmonic oscillator at intermediate values of the self-coupling. The potential is that given in Eq. (521) with the following choice of parameters:

$$m = 1 \quad ; \qquad \mu^2 = 0.5 \quad ; \qquad \lambda = 0.45 \tag{547}$$

The value of the dimensionless control parameters mentioned in Chapter 2 are given by $r_1 = r_2 = 1.57$. We choose as initial condition a gaussian pure state with width given by $\sigma\mu^{2/3} = 0.45/2^{1/3}$. Our main observable was taken to be the expectation value of the square of the position operator Q^2 as a function of time, which is noted $\langle Q^2 \rangle(t)$. The Hamiltonian, the initial state and the observable were used in a paper with a similar spirit to us [89]. However, for illustrative purposes we are presenting the results for a higher value of the self-coupling λ, for which quantum effects are stronger.
The main results are collected in Fig. 109(a)-109(b). In the first figure the time evolution of the observable is displayed in units of the half-period of the $\lambda = 0$ system. This expectation value performs oscillations with a frequency close to that of the $\lambda = 0$ system. The classical approximation, also displayed in the figure, oscillates as well, but the amplitude gets damped very fast with time. This damping is a typical feature of the classical approximation which has been pointed out repeatedly (including Ref. [89]). The figure also shows two other curves. The first being the 2PI approximation obtained by keeping only the leading and next-to-leading (NLO) diagrams in a 1/N expansion [51]. Notice that in this case the amplitude of the oscillation is not decreasing, but there is a shift in the period oscillation. This might not be a serious drawback in extracting average properties over time. Finally, we also present the result of the new method explained before, which includes the classical approximation and the leading $\hbar^2$ correction. The exact details are explained below.
In Fig. 109(b) we present relative error of each approximation, namely the difference between the quantum evolution and the corresponding approximation, divided by the quantum result. The first line corresponds to the

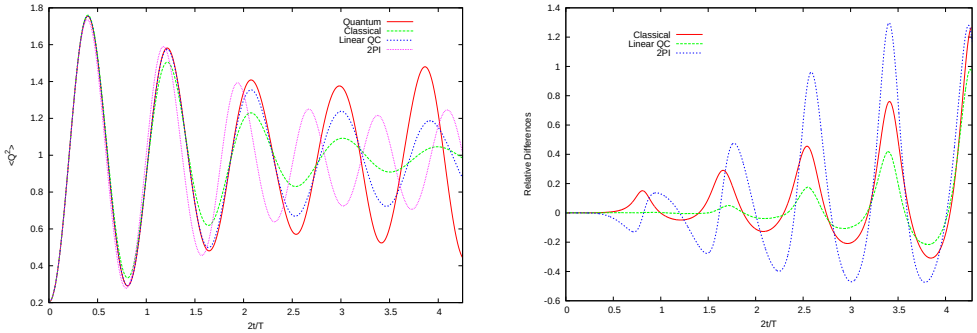

Figure 109: (a): Time evolution of $\langle Q^2 \rangle$ compared to the classical approximation, the 2PI truncation to NLO order in 1/N expansion, and the method proposed in this chapter. (b): Relative error committed in each of the approximations as a function of time.

classical approximation, which oscillates with increasing amplitude. Quantum corrections start being negligible and grow to a 20% level at $2t/T \approx 0.8$, and 40% level at $2t/T \approx 2.5$. The 2PI curve appears to be the worst, but this is due to the shift in period with respect to the quantum curve. A more fair presentation should involve a comparison of the height of the maxima, for which 2PI is certainly better than the classical approximation. The last curve is our calculation including quantum effects up to linear order in $\hbar^2$, using the method described in the previous section. Notice, that it provides a very accurate description of the quantum effects up to $2t/T \approx 1.4$. Beyond this point it has more sizable errors, but certainly smaller than the classical approximation. Furthermore, it provides at least an estimate of the errors committed by employing the classical approximation.

The actual procedure that we followed to determine the leading quantum correction (LQC) is the following. We re-scaled the size of the quantum term of quantum Liouville equation by using κ. Then, we used the coarse-grained approximation to $\rho(\eta)$ up to the second level ($N = 2$, $\langle \eta^5 \rangle = 0$ but $\langle \eta^7 \rangle \neq 0$), and the sampling method described in the previous section, to study the quantum evolution equation for a given value of κ. The formula to obtain the approximation (LQC) including the contribution linear in $\hbar^2$ to any observable O is

$$O_{\rm LQC} = O_{\rm clas} + \frac{1}{\kappa}(O_\kappa - O_{\rm clas}) \tag{548}$$

The curves depicted in Fig. 109 were obtained using $\kappa = 1/6$.
To check whether $\kappa = 1/6$ is in the linear regime, and to give an estimate of the size of the higher order terms in $\hbar^2$, we repeated the procedure and obtained O_κ for several values of κ ($\kappa = 0, 1/10, 1/8, 1/6, 1/5, 1/4, 1/2$). In this way we get an idea about how the value of the observable interpolates between the classical ($\kappa = 0$) and the quantum value ($\kappa = 1$). In Fig 110 we display the result obtained for the expectation value of Q^2 at the position of the third maximum ($2t/T = 2.1$). The y-axis gives the values obtained for the different values of κ mentioned previously. We also display the value for the classical approximation ($\kappa = 0$) and the full quantum result ($\kappa = 1$). It is quite clear that the results follow an approximate linear dependence for $\kappa < 1/3$. The straight line is the result of a linear fit (1 free parameter) in this range. The extrapolation to $\kappa = 1$ of the straight line is very approximately our estimate of the quantum evolution up to next-to-leading order in $\hbar^2$ (the leading order being the classical approximation). In this particular case we see that the linear quantum correction term (LQC) accounts for 80% of the quantum effects. Thus, with the addition of the classical approximation, we reproduce the exact quantum result with a 3% error. In principle, one could go beyond the linear approximation and determine higher order corrections in $\hbar^2$. If we add the result of $\kappa = 0.5$ to the data and fit the results to a second degree polynomial in $\hbar^2$ we get an even better approximation to the quantum result (second line in Fig. 110).
Although the previous results by themselves show that our procedure cannot be completely misguided, we have analyzed the different sources of error in the determination of the $\hbar^2$ correction presented above. Using jack-knife methods we can quantify the purely statistical errors. They increase with time but remain always at the level of a few percent. A much more difficult estimate is the effect of the coarse-graining in momenta. This can be estimated by changing the value of ϵ and/or adding more terms in the discretization to impose $\langle \eta^{2p+1} \rangle = 0$. In particular, we have used results at $\epsilon = 0.3$ and three levels of discretization. The parameter p indicates the level of discretization and we have taken $p = 1, 2, 3$. So, in Level 3 we have $\langle \eta^7 \rangle = 0$. We can see in Fig. 111(a) that the effect is more pronounced at the maxima and minima of the oscillations and the better the approximation, the closer the results to the actual quantum evolution. From the results displayed in Fig. 111(a) we estimate that, at most, errors (to the quantum correction) could be of the order of 10-15% at the third maximum ($2t/T = 2.1$) rising up to 20-25% at the fourth maximum ($2t/T = 3.0$).

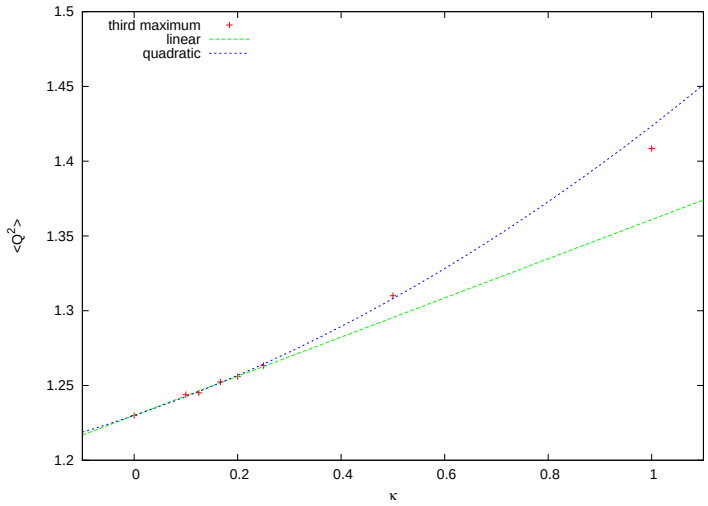

Figure 110: The value of $\langle Q^2 \rangle$ at the third maximum in time computed using several values of κ (see text). The lines are linear and quadratic fits.

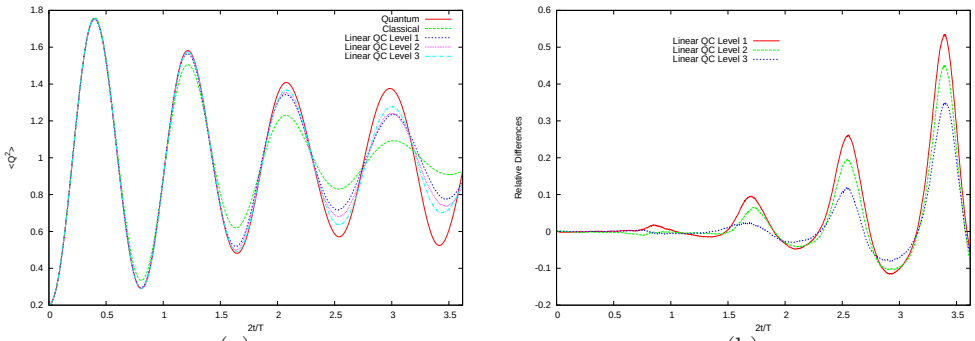

(a) (b)

Figure 111: (a): Time evolution of $\langle Q^2 \rangle$ compared to the classical approximation and the Linear QC for different levels of discretization. (b): Relative error committed in each of the levels as a function of time.

The same conclusion follows both by comparison of the different levels as well as by extrapolation in ϵ^α (with $\alpha \approx 3$) to $\epsilon = 0$. The conclusion is that, even if the errors are sizable, the method provides a good estimate of the quantum effects.

11.3.2 Time dependent potential

Before embarking into the generalization to several variables, we tested the situation for another case having several distinct features which are present in some of the phenomenological applications to cosmology. We considered a potential of the form

$$V(x,t) = -\frac{1}{2}\mu^2 \tanh(\alpha t)x^2 + \frac{\lambda}{4!}x^4 \tag{549}$$

with the parameters chosen to be

$$\mu^2 = 2 \quad ; \qquad \alpha = 0.2 \quad ; \qquad \lambda = 0.4 \tag{550}$$

This time-dependent potential provides a smooth interpolation between a single-well and a double-well potential mimicking the situation occurring in hybrid inflationary models. Notice that tunneling effects are possible now. The initial condition is a pure state given by a gaussian with $\sigma\mu^{2/3} = 1/4^{1/3}$. The same observable as before, $\langle Q^2 \rangle$, is displayed in Fig. 112(a) for a range of times for which the potential has basically evolved to the future asymptotic potential. Hence, as expected, the expectation value migrates from its initial value to performing oscillations around x^2_{min}, where x_{min} is the minimum of future asymptotic potential. Also shown, is the corresponding curve for the same 2PI approximation mentioned earlier. Although following the pattern of the quantum result, the differences are substantial. On the other hand, the classical evolution works quite well for this case. However, the addition of the Linear Quantum correction (LQC) using our method (with $\kappa = 1/2$) makes the result much better, as can be seen when looking at Fig. 112(b), where we display the relative differences with respect to the quantum evolution as before.

11.3.3 Extension to QFT

Since our ultimate goal is that of studying the quantum evolution of fields, it is crucial to determine how does the new method that we have presented depend upon the number of degrees of freedom. The standard non-perturbative treatment of quantum fields proceeds through a lattice discretization and a subsequent continuum limit. Renormalization is a crucial ingredient in the process to obtain meaningful physical results. The latter aspect lies somewhat far from the scope of this chapter. The focus here is rather upon the

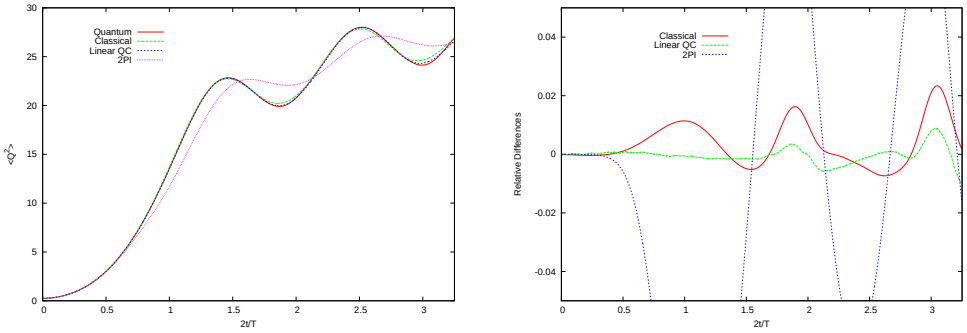

(a) (b)

Figure 112: (a): The same as Fig. 109(a) but for the potential in Eq. 549. (b): Relative differences as in Fig. 109(b).

numerical feasibility of the procedure. For attaining acceptable results one has to reach a number of variables within the range of those customary for these kind of simulations. A priori, the method presented here is capable of doing so, since its computational effort is comparable to that involved in the classical approximation for a given number of sampling trajectories, which has been used successfully in this context.
However, there is a point of concern which we want to address. It might well happen that the number of trajectories needed to attain a given precision in the estimation of the quantum corrections grows with the number of degrees of freedom: A polynomial growth is acceptable, an exponential growth is not. As a testing example we have considered a lattice version of a two-dimensional scalar field theory which has been studied by other authors in this same context [46]. We take a real scalar quantum field in $1+1$ dimensions with Hamiltonian

$$H(t) = \int dx \Big[\frac{1}{2}\pi^2(x,t) + \frac{1}{2}(\nabla\phi(x,t))^2 + \frac{1}{2}\mu^2\phi^2(x,t) + \frac{\lambda}{24}\phi^4(x,t) \Big] \quad (551)$$

where μ^2 may depend on t. We have already explained the influence of $\hbar$ factors, so from now on we assume natural units, $\hbar = c = 1$. The dimensionless field ϕ and its conjugate momentum $\pi = \dot{\phi}$ satisfy equal-time canonical commutation relations

$$[\pi(x), \phi(y)] = -i\,\delta(x-y) \quad (552)$$

which gives $\pi(x)$ dimensions of inverse length.
The next step is to consider the lattice version of the previous Hamiltonian. Continuous space is approximated by a discrete number of points $x_n = na$ separated by a distance a, the lattice spacing. To deal with a finite number of variables we must, in addition, put the system in a box of size L with periodic boundary conditions. Altogether, we end up having $N = L/a$ variables $\phi_n(t) \equiv \phi(na, t)$. The corresponding conjugate momenta $\pi_n(t)$ satisfy the commutation relations

$$[\pi_n, \phi_m] = -\frac{i}{a}\,\delta_{nm} \tag{553}$$

where the factor of a is necessary to preserve the dimensions of the conjugate momentum. Naive discretization then leads to the Hamiltonian

$$H = \sum_{n=0}^{N-1} a\Big[\frac{1}{2}\pi_n^2 + \frac{1}{2}(\nabla\phi_n)^2 + \frac{1}{2}\mu^2\phi_n^2 + \frac{\lambda}{24}\phi_n^4\Big] \tag{554}$$

with $\nabla\phi_n = (\phi_{n+1} - \phi_n)/a$. After a suitable rescaling of the variables and of the parameters the Hamiltonian can be cast in the form Eq. 70.
After presenting our system and its discretized version, let us consider the dynamical process that we will study following Ref. [46]. The idea is to study the evolution of the system after a *quench*. In practice, this means that the μ^2 parameter flips its sign abruptly at time $t = 0$ from a positive value to a negative one. This can be seen as a limiting version of our previously smooth (tanh) transition from single to double-well.
In practice, what we will consider is the evolution of the system for positive times starting (at $t = 0$) from an initial state given by the ground state of the Hamiltonian with $\lambda = 0$ and positive μ^2. This initial state is therefore gaussian as in previous examples, and is easily generated. For our numerical simulation we have taken the parameters of the model to be

$$\lambda = 3m^2 \qquad a = 0.8/m \tag{555}$$

where the unit of mass m is given by $m = \sqrt{-2\mu^2}$. Then we have studied this model for N = 2,4,8,16 and 32.
For a real quantum field theory application one has to study the limit of a going to 0, with a suitable tuning of the parameters dictated by the renormalization conditions. For very small lattice spacings one might even encounter problems of critical slowing down, but these will affect other methods too.

Here, we will be content with scaling the number of degrees of freedom and focusing on statistical significance and computational load alone.
Finally, let us select our observables and present our results. Rather than working with the field variables we can work with their Fourier modes $\hat{\phi}_k(t)$, since they decouple in the $\lambda = 0$ limit. We use the following normalization for the discrete Fourier transform

$$\hat{\phi}_k(t) = \frac{\sqrt{L}}{N} \sum_{n=0}^{N-1} e^{-i\frac{2\pi}{N}nj}\, \phi_n \tag{556}$$

where $k = (2\pi/L)j$ for $j = -N/2+1, -N/2+2, \ldots, N/2$. A similar expression applies for the modes $\hat{\pi}_k(t)$. Reality of our original field implies $\hat{\phi}^*_k(t) = \hat{\phi}_{-k}(t)$ (and the same for π).
As mentioned previously for $\lambda = 0$ and positive μ^2 all the modes oscillate with a characteristic frequency $\omega(k) = \sqrt{4\sin^2(j\pi/N)/a^2 + \mu^2}$. At the classical level, the flip in sign of μ^2 produces that the low lying modes acquire an imaginary $\omega(k)$, and start growing exponentially. In the presence of a non-zero λ the growth ceases once the non-linear effects become important.
In Fig. 113 we present our results for the sum of expectation values of the square of each mode $\langle \sum_k |\hat{\phi}_k|^2(mt)\rangle$ for two degrees of freedom $N = 2$. As a matter of fact this observable is just a discretized version of $\int dx\, \phi^2(x)$. The time evolution as a function of mt is given, as obtained from the numerical integration of the $N = 2$ Schroedinger equation. The result of the classical approximation and of our LQC method obtained from $\kappa = 1/3$ are also shown. The exact numerical integration has negligible errors at the scale of this and the following figures. The errors of the remaining approximations were obtained by applying a jack-knife method to the sample of trajectories. The total number of trajectories used for this data was $\mathcal{M} = 8 \times 10^6$.
The results show the same pattern as before. The classical approximation captures the main features, but our LQC approximation calculation is capable of reducing the discrepancy substantially. Only at the latest times this difference exceeds the level of the statistical errors. In Fig. 114(a) and Fig. 114(b) we display the corresponding results for $N = 8$ and $N = 32$ with a sample of size $\mathcal{M} = 4 \times 10^7$. Here we do not have an exact result to compare with, so the main issue is the dependence of the errors on N for a fixed sample size. Errors of our method are larger than those of the classical approximation as expected, but do not seem to depend crucially on the number of variables. The intermediate values of N, not shown, display exactly the same pattern.

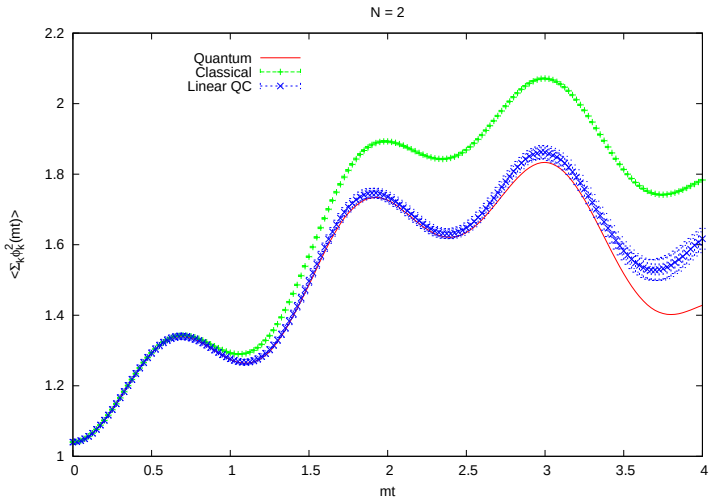

Figure 113: Time evolution of $\langle \sum_k |\phi_k|^2(mt) \rangle$ for $N = 2$, for the fully quantum, classical approximation and LQC method for $\kappa = 1/3$.

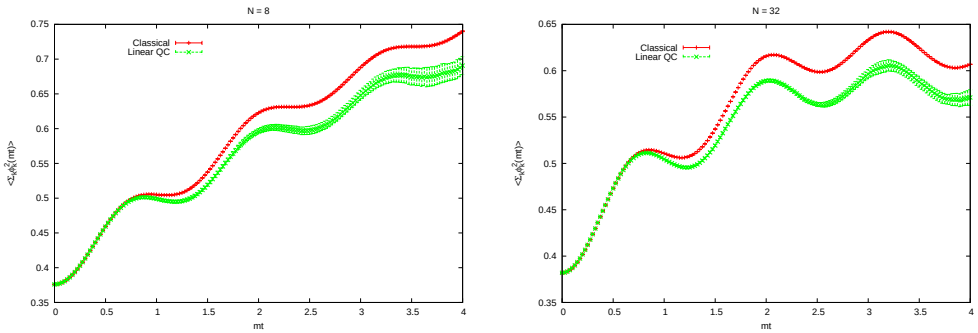

(a) (b)

Figure 114: The same as Fig. 113 but for $N = 8$ (a) and $N = 32$ (b).

For all values of N the relative difference between classical and linear QC approximation approaches a constant with errors diminishing as the sample size $\mathcal{M}$ grows. For the maximum values studied of order $\mathcal{M} = 5 \times 10^7$, we can estimate the quantum correction at our latest times $mt \approx 3$ with an accuracy of 10% without a significant dependence on the number of degrees of freedom.

In conclusion, the proposed method seems to scale reasonably well with the number of degrees of freedom. The computational cost is only a certain factor higher than that involved in the classical approximation. Thus, phenomenologically interesting applications are addressable within present high performance computing capabilities.

12 Conclusions

Along this work we have analyzed several approximate methods that are frequently used to perform non-linear quantum evolution for time dependent or time independent Hamiltonians. We have also proposed new alternative methods. Now, we will review the main results and conclusions that we have obtained.

A very important approximation, given the number of results obtained with it in the cosmology literature, is the *classical approximation*. Thus, a good part of our study has centered in giving criteria to test in what circumstances is the approximation expected to work and what are the errors induced by its use.

Within this context, for a potential with a quartic interaction term and gaussian initial conditions, we have presented a particular form of the perturbative expansion in λ that uses the same rules for the fully quantum result and its classical approximation. It involves two types of propagators. The formalism is developped for the general case including a time dependent mass term. With this formalism we extract an important conclusion: the classical diagrams are a subset of the quantum ones. The classical approximation is exact at zero order (gaussian approximation). In fact, we show that for $\langle x^2(t)\rangle$ the quantum and classical perturbative evolution agree at first order as well. Thus, for small values of λ, the classical approximation has to work well in the first stage of the evolution for the mentioned expectation value. Nevertheless, other observables like $\langle x^4(t)\rangle$, are more sensitive to quantum corrections, deviating already at first order. These results are verified by our numerical results explained below. From our expansion, we also derive a perturbative classicality condition (PCC). All these results generalize to the case of fields.

For larger values of the coupling we have studied the system numerically. We considered the case of a few degrees of freedom where the exact evolution can be obtained by the numerical integration of the Schroedinger equation. Our goal has been to test the classical approximation and to extract appropriate criteria to quantify the errors committed by using it.

Our first tests concern a toy version (with one degree of freedom) of the

hybrid inflationary model presented in chapter 1. In this way we can compare the two-stage proposal of Ref. [33] with the exact quantum evolution. The general arguments in favor of the validity of their approach (gaussian approximation in the first stage and the classical approximation in the second stage) also apply for this simple model. Our results give evidence that the approximation is a fairly good description of the quantum evolution. Moreover, we verify that the perturbative evolution improves the results in both stages. We also check that there exist a time window where one can do the connection of the two stages, and that the later classical evolution is the same. Outside this window the later evolution is very different.

The argument given to support approximate classical behaviour at the connection times is that the Wigner function corresponds to a squeezed state. The exact quantum evolution brings the system to a very different state. Nevertheless, in our systems, the long-time classical behavior for lower order expectation values is still fairly classical.

There are two additional assumptions of the approximations made in the study of the hybrid inflationary model of chapter 1, which have also been tested. The first assumption was that of setting to zero the initial conditions for the non-tachyonic modes. The claim was that the coupling of these modes with the tachyonic long wavelength modes will induce classical behavior for the former as well. This setting was replicated by a simple model with two degrees of freedom (x, y), where x is tachyonic and y is not. We find that, for x, the classical approximation works well and the perturbative connection represents a significant improvement with respect to the gaussian one. We have determined the time range within which to choose the connection time (as in the case of 1 dof). Nevertheless, the classical behavior of x is not enough to induce a classical behavior over y. Moreover, a variation of the quadratic coefficient of y only produces a small delay in the evolution of x. Thus, in our inflationary model, it seems that indeed one can neglect the influence of the modes that are not classical.

The second assumption was that the effect of the inflaton can be well accounted by time-dependent mass term of the Higgs. In our second 2 DOF toy model we withdraw this assumption and study a Higgs-inflaton system with initial conditions and couplings tuned to reproduce the conditions of the field theoretical case. Thus, the potential for the two degrees of freedom

x, y is taken to be time-independent, but the initial expectation value of p_y is non-zero inducing a time-dependent expectation value for $\langle y \rangle$ (the inflaton). The coupling to the x (Higgs) acts as a time-dependent mass. This is a more realistic situation where we do not assume any time dependence. At the connection time, we employ a factorised Wigner functions for each dof and the classical approximation does not work for x, despite their Wigner function is squeezed and positive. Next, we use the full Wigner function $W(x, p_x, y, p_y)$ neglecting the negative part. The curves are closer but there remains a notable difference. Finally, we calculate the negative part of the whole Wigner function and this part is not negligible. The positive and negative volumes are stabilized before the connection time and then they increase slowly. stabilized before the connection time and then increase slowly. We have evolved the system with the classical approximation considering the positive and negative parts, and now the quantum and classical evolution indeed coincide. In conclusion, the qualitative behavior is different between the cases of one and two degrees of freedom. The negative part of the Wigner function is non negligible. We also have found that the back-reaction has a large influence in the evolution, and this again confirms that this case is essentially different to the one degree of freedom case.

What is more influential in determining the validity of the classical approximation? Is it the values of the parameters in the potential? Or is it the shape and squeeziness of the initial state? These questions are explored for quartic time-independent potentials. There are two basically different cases: the single and double well shapes differing in the sign of the quadratic term. The different parameters can be arranged into several dimensionless combinations labeled r_1, r_2, r_S and defined in Eq. 196. We conclude that the most important influence on the classicality of the system corresponds to parameter r_1, and the classical approximation works well for large values of r_1. Once r_1 is set, he approximation improves if r_S (or r_2) is increasing. As expected, for the case of single-well potentials the value of r_1 necessary to obtain a classical behavior is lower than in the case of double-well potentials (for which it is around five times higher).

The values of dimensionless control parameters r_i were also evaluated at the initial time for the time-dependent potential cases studied earlier. Higher values are needed to ensure the classical behavior. Furthermore, we verified that the value of r_1 is increasing along the evolution. This explains the classical

behavior of those systems. We also have verified the perturbative classicality condition (PCC) for the case of single well potentials. We conclude that, for this case, PCC is a good classicality condition.

Having studied the classical approximation and its limitations, we turned now to methods holding the promise of incorporating quantum effects. We focus only on those methods that are capable of dealing with the situation of quantum fields. Apart from perturbation theory, there are two methods which have been used lately in this context: the 2PI approximation and complex Langevin. Both methods can be downgraded to the case of a finite number of degrees of freedom (0 spatial dimension) and tested against the exact quantum evolution obtained by numerical methods.

We focus first upon the 2PI approximation. As a matter of fact the idea starts by deriving exact Schwinger-Dyson type equations for the two-point functions. To become practical one needs a truncation of the building block terms appearing in the self energy. There are two options, one based on the number of loops and the other on the corresponding power of $1/N$ (N being the number ficticious identical flavours of the field). They are called 2PI-Loop and 2PI-1/N approximations. We have studied both types up to next to leading order and tested them for the same systems that were used previously for the study of the classical approximation. In all studied cases, the 2PI-Loop approximation to 3 loops works very well at early times, but becomes unstable and blows up at later times. The 2PI-1/N to NLO approximation, in general works better than the classical approximation at early times, but tends to deviate more for larger t.
The 2PI methods leads to the 2PI classicality condition, that is valid as long as the approximation is. However, from our particular perturbative expansion, we have proved that this is a sufficient classicality condition.

The 2PI approximation amounts to a resummation of certain classes of diagrams. There exist a similar type of approximation for classical evolution called 2PI-classical. Of course, the 2PI-loop and 2PI-1/N represent a truncation in the number of classes of diagrams involved. These truncations seem unnecessary in this case since the numerical integration of the classical equations of motion includes all types. That is not possible for the full quantum evolution. However, as mentioned previously the diagrams involved in the classical case are a subset of the quantum ones, and they can be resummed!

This idea led us to proposing a new method called *Hybrid*, because it tries to capture "the best of both worlds": the classical approximation and 2PI. Indeed, in our systematic tests on quartic potentials we found that the hybrid method gives the best results for intermediate values of r_1. Our study also tests the validity of certain *classicality conditions* derived from 2PI. This works well for the case of double-well potentials.

We also analysed the Complex Langevin Method. The method involves the evolution of complexified fields in an additional fictitious time θ called *Langevin time*. The method was downgraded to the quantum mechanics situation (finite number of dof) and tested for our prototype systems. Naive discretization of the langevin evolution equations gives rise to instabilities and run-offs. These have been reported earlier. We distinguish among two types of divergences noted as *type 1* and *type 2*. We have analysed the problem and traced the origin of these divergences to numerical instabilities of the discretized equations in the absence of noise. Thus, the number of unstable trajectories diminishes as the discretization step θ-step is reduced. Making this step small enough to eliminate these divergences is prohibitively expensive. Indeed, a way-out has been proposed: adaptive step-size. This makes the discretization finer only whenever it is needed to avoid instabilities. The problems are also considerably reduced when using a higher order discretization, i.e. correct up to higher powers of the step size.

Using the previous methods we were able to circumvent the problem of instabilities but the resulting calculation of the time histories of the two-point function differs considerably from the exact result. For the single-well case, it does not even show the oscillatory pattern characteristic of the gaussian system. The imaginary part is also non-zero. Is this indicative of a transient behaviour and will the correct behaviour be recovered at larger Langevin times? We tested this hypothesis and it seems not be the case and/or the approach takes place at prohibitively long Langevin times. Furthermore, we tested that this negative result is robust against changes in the boundary conditions, the range of ordinary times studied and the methodology used to avoid instabilities. The problem disappears for the gaussian ($\lambda = 0$) case, however. Indeed, the problem of convergence to a wrong solution has been reported earlier and there is no clear-cut way out that we know of. Thus, unfortunately, the complex Langevin method is not competitive with the other methods presented here to study our generic quartic systems.

A very interesting point of view about the nature of quantum fluctuations arises by looking at the Wigner distribution function. Its non-positive definite character is a distinctive quantum feature. Furthermore, the classical approximation has a nice understanding if one looks at the Moyal evolution equation for the Wigner function. For our quartic systems, only one term in this equation is responsible for the quantum effects. Dropping this term not only recovers the positivity, but also the deterministic character of classical evolution. Thus, we analysed how can a random force alter the equation and give rise to a Fokker-Planck equation identical to Moyal equation. A priori this seems an impossible goal. Indeed one can set up a markovian process of the Langevin type with a random force which does the role, but the expectation values of the moments of the force needed to achieve this goal demand a non positive distribution function for the force.

This idea led us to devise a new numerical method, noted as *nQC Method*. The non-positive definite distribution function for the force is constructed in terms of a bona fide distribution function with an additional Ising-like random variable. This property is inherited by the Wigner function. Altogether, it allows the use of sample theory to approximate expectation values of the new distribution function. The original quantum expectation values are now obtained in terms of these averages but with contributions having opposite signs. As time evolves the mutual cancellations tend to grow until the signal is buried by the statistical errors. This is a typical sign problem. The time at which this happens can be estimated. Still the method is capable of producing an accurate description of the quantum evolution for a range of time, and this suffices in certain physical problems where fast processes are involved, like the preheating era in the early universe. Extending the range of time is feasible if we drop the goal of estimating the full quantum evolution, and attempt only to obtain the corrections to the classical approximation in powers of $\hbar^2$. This is a way to go beyond the classical approximation and estimate its errors. These ideas have been tested against the exact quantum evolution and the results of other methods, for the simple 1 dof models, with single and double-well potentials, studied earlier. The results are quite satisfactory and agree with expectations.

In devising the afore-mentioned method we had in mind the necessity to make it applicable for the case of quantum fields. The computational time

in applying the method is, for a given sample size, comparable to that of the classical approximation. However, there is the risk that the sample size necessary to preserve a given statistical significance in the calculation of quantum corrections grows with the number of degrees of freedom in such a way as to make the method impractical for the case of fields. This and other questions were explored for a 1+1 dimensional field theory discretized on a one dimensional periodic spatial lattice. The model has been the subject of study in the context of cosmological investigations by other authors. Our results are positive and the we found that the statistical errors on the quantum effects of our observables, for a fixed sample size, remain stable with the number of degrees of freedom. A full study of this model including the effects of renormalization is underway. Extension to more realistic situations in 3+1 dimensions, though computationally demanding seem feasible with present day technology.

13 Conclusiones

A lo largo de este trabajo hemos analizado varios métodos aproximados que son frecuentemente utilzados para realizar evolución cuántica no lineal con Hamiltonianos que pueden depender o no del tiempo. También se han propuesto nuevos métodos alternativos. Vamos a resumir a continuación los principales resultados y conclusiones que hemos obtenido.

Una importante aproximación, con la que se han obtenido un gran número de resultados en la literatura sobre Cosmología, es la *aproximación clásica*. Por ello, una buena parte de nuestro estudio se ha centrado en establecer criterios para testar en qué circunstancias se puede esperar que la aproximación clásica funcione bien, y cuales son los errores inducidos por su utilización.

Dentro de este contexto, para un potencial con un término de interacción cuártico y unas condiciones iniciales gaussianas, hemos presentado una forma particular de realizar el desarrollo perturbativo en λ que utiliza reglas similares para la evolución cuántica y la clásica. Están involucrados dos tipos de propagadores. El formalismo se desarrolla para el caso general incluyendo el caso en el que el término de masa depende del tiempo. Con este formalismo extraemos una importante conclusión: los diagramas clásicos son un subconjunto de los cuánticos. La aproximación clásica es exacta a orden cero

(aproximación gaussiana). De hecho, vemos que para $\langle x^2(t)\rangle$ la evolución cuántica y clásica coinciden hasta primer orden. así, para pequeños valores de λ, la aproximación clásica debe de funcionar bien en la primera etapa de la evolución para el mencionado valor esperado. Sin embargo,otros observables como $\langle x^4(t)\rangle$, son más sensibles a las correcciones cuánticas, desviándose ya a primer orden. Estas afirmaciones son ratificadas por nuestros resultados numéricos expuestos más adelante. Por otro lado, de nuestro desarrollo perturbativo deducimos una condición de clasicidad perturbativa (PCC). Todos estos resultados se generalizan al caso de campos.

Hemos estudiado numéricamente varios sistemas con distintos valores del acoplo. Hemos considerado el caso de pocos grados de libertad, donde la evolución exacta puede obtenerse integrando numéricamente la ecuación de Schroedinger. Nuestro objetivo ha sido testar la aproximación clásica y extraer criterios para cuantificar los errores cometidos en su uso.

Nuestros primeros tests representan una versión sencilla (1 dof) del modelo de inflación híbrida presentado en el capítulo 1. De esta forma podemos comparar las dos etapas de evolución propuestas en la Ref. [33] con la evolución cuántica exacta. Los argumentos generales en favor de la validez de su propuesta (aproximación gaussiana en la primera etapa y aproximación clásica en la segunda) son también aplicables a nuestro modelo simplificado. Nuestros resultados evidencian que la aproximación es una descripción bastante buena de la evolución cuántica. Además, hemos verificado que la evolución perturbativa mejora los resultados en ambas etapas.
Hemos comprobado también que existe una ventana de tiempos de conexión que producen una posterior evolución clásica muy similar. Fuera de esta ventana la aproxación da resultados muy diferentes. Esto sirve como un criterio de aplicabilidad de la aproximación clásica en sistemas donde la evolución exacta no es accesible.

El argumento habitualmente esgrimido para justificar el comportamiento clásico en el punto de conexión es que la función de Wigner se corresponde con un estado squeezed. La evolución cuántica exacta lleva al sistema a un estado bien diferente. Sin embargo, en nuestros sistemas, se da el comportamiento clásico a largo tiempo para los valores esperados de orden bajo.

Existen 2 asunciones adicionales sobre las aproximaciones hechas en el estu-

dio del modelo de inflación híbrida del Capítulo 1, las cuales han sido también testadas. La primera consiste en poner a cero los modos no taquiónicos. Queremos comprobar si el acoplo de estos modos con los modos taquiónicos de longitud de onda larga podrían inducir un comportamiento clásico en los anteriores. Este panorama ha sido replicado en un modelo simple con 2 grados de libertad (x, y), donde x es taquiónico e y no lo es. Encontramos que, para x, la aproximación clásica funciona bien y la conexión perturbativa representa una significativa mejora con respecto a la gaussiana. También hemos identificado un rango de tiempos donde se puede elegir el tiempo de conexión (como en el caso de un grado de libertad). Sin embargo, el comportamiento clásico de x no es suficiente para inducir un comportamiento clásico en y. Además, una variación del coeficiente cuadrático de y sólo produce un pequeño retraso en la evolución de x. Así, en nuestro modelo inflacionario, parece que efectivamente se puede despreciar la influencia de los modos que no son clásicos.

La segunda asunción es que el efecto del inflatón puede ser tenido en cuenta introduciendo un término de masa dependiente del tiempo para el Higgs. En nuestro segundo modelo sencillo con 2 dof testamos esta asunción y estudiamos un sistema Higgs-inflaton con condiciones iniciales y acoplos ajustados para reproducir las condiciones del caso teórico de campos. Así pues, el potencial para los dos grados de libertad x, y es ahora independiente del tiempo, pero el valor esperado inicial de p_y no es cero, induciendo un valor esperado dependiente del tiempo para $\langle y \rangle$ (el inflaton). El acoplo con x (Higgs) actúa como una masa dependiente del tiempo. Esta es una situación más realista donde no asumimos ninguna dependencia temporal. En el tiempo de conexión, empleamos funciones de Wigner factorizadas para cada dof y la aproximación clásica no funciona para x, a pesar de que su función de wigner es squeezed y positiva. A continuación, utilizamos la función de Wigner completa $W(x, p_x, y, p_y)$ despreciando la parte negativa. Las curvas se acercan más pero sigue existiendo una notable diferencia. Finalmente, calculamos la parte negativa de la función de Wigner completa y vemos que es no despreciable. Sus volúmenes positivo y negativo se estabilizan antes del tiempo de conexión y después crecen lentamente. Hemos evolucionado el sistema con la aproximación clásica considerando la parte positiva y la negativa, y ahora la evolución cuántica y clásica efectivament coinciden. En conclusión, el comportamiento cualitativo es diferente entre los casos de 1 y 2 grados de libertad. La parte negativa de la función de Wigner no es despreciable.
Hemos comprobado también que el back-reaction tiene una gran influencia

en la evolución, y esto confirma de nuevo que este caso es esencialmente diferente al de un grado de libertad.

Qué tiene más influencia en la validez de la aproximación clásica?. Es el valor de los parámetros del potencial?. O es la forma y grado de squeezing del estado inicial?. Estas cuestiones son exploradas para potenciales cuárticos independientes del tiempo. Hay 2 casos básicamente diferentes: el single-well y el double-well, que se diferencian en el signo del término cuadrático. Los diferentes parámetros pueden ser agrupados en diferentes combinaciones adimensionales etiquetadas como r_1, r_2, r_S y definidas en la Eq. 196. Concluimos que la influencia más importante en la clasicidad del sistema se corresponde con el parámetro r_1, y la aproximación clásica funciona bien para valores grandes de r_1. Una vez fijado r_1, la aproximación mejora si r_S (o r_2) se incrementan. Como esperábamos, para el caso de potenciales single-well, el valor de r_1 necesario para obtener un comprtameinto clásico es más bajo que en el caso de potenciales double-well (para los cuales es alrededor de 5 veces superior).

Los valores de los parámetros de control adimensionales r_i fueron también evaluados inicialmente para los casos de potenciales con dependencia temporal estudiados anteriormente. Los valores son suficientes para asegurar el comportamiento clásico. Además, hemos comprobado que el valor de r_1 se incrementa a lo largo de la evolución. Esto explica el comportamiento clásico de esos sistemas.
Hemos verificado también la condición de clasicidad perturbativa (PCC) para el caso de potenciales single-well. Concluimos que es una buena condición de clasicidad.

Una vez estudiada la aproximación clásica y sus limitaciones, abordamos ahora otros métodos recordando la promesa de incorporar efectos cuánticos. Nos centramos sólo en aquellos métodos que son utilizados en teoría cuántica de campos. Aparte de la teoría de perturbaciones, hay dos métodos que han sido largamente utilizados en este contexto: la aproximación 2PI y el método de complex Langevin. Ambos métodos pueden ser implementados para un número finito de grados de libertad (0 dimensiones espaciales), y comparados con la evolución exacta obtenida por cálculos numéricos.

Abordamos primero la aproximación 2PI. La idea proviene de derivar ecua-

ciones exactas de tipo Schwinger-Dyson para las funciones a dos puntos. Para implementarlas en la práctica se necesita una truncación de los infinitos términos que aparecen en la autoenergía. Hay dos opciones, una basada en el número de loops y la otra en la correspondiente potencia de $1/N$ (siendo N el número de componentes del campo). Se denominan respectivamente aproximaciones 2PI-Loop y 2PI-1/N. Hemos estudiado ambas hasta orden next-to-leading y las hemos testado para los mismos sistemas utilizados previamente para el estudio de la aproximación clásica. En todos los casos estudiados, la aproximación 2PI-Loop hasta 3 loops funciona muy bien al principio, pero se transforma en inestable y explota para tiempos posteriores. La aproximación 2PI-1/N hasta NLO, funciona en general mejor que la aproximación clásica en los primeros instantes, pero tiende a desviarse más en tiempos posteriores. Los métodos 2PI conducen a la condición de clasicidad 2PI, que es válida tan lejos como lo es la aproximación. De todas formas, a partir de nuestro particular desarrollo perturbativo, hemos probado que ésta es una condición suficiente de clasicidad.

La aproximación 2PI incluye una resumación de ciertas clases de diagramas. Existe un tipo similar de aproximación para la evolución clásica llamada 2PI-clásica. Por supuesto, la 2PI-loop y la 2PI-1/N representan una truncación en el número de clases de diagramas involucrados. Esta truncación parece innecesaria en este caso, ya que la integración numérica de las ecuaciones clásicas de movimiento incluye todos los tipos de diaramas. Esto no es posible para la evolución cuántica completa. De todas formas, como se mencionó previamente, los diagramas involucrados en el caso clásico son un subconjunto de los cuánticos, y pueden ser resumados. Esta idea nos lleva a proponer un nuevo método denominado *método híbrido*, porque trata de capturar lo mejor de ambos mundos: la aproximación clásica y la 2PI. Efectivamente, en nuestros test sistemáticos sobre potenciales cuárticos hemos encontrado que este método da los mejores resultados a partir de valores intermedios de r_1.
Nuestro estudio también testa la validez de la condición suficiente de clasicidad 2PI. Esta funciona bien para el caso de potenciales double-well.

Hemos analizado también el método de complex Langevin. Este método involucra la evolución de campos complexificados en un tiempo ficticio adicional θ denominado *tiempo de Langevin*. El método fue implementado para sistemas mecano-cuánticos (número finito de grados de libertad) y testado

para un sistema prototipo. La discretización básica de las ecuaciones de evolución de Langevin dan lugar a inestabilidades. Esto ha sido reportado en la literatura. Identificamos dos tipos de divergencias denominadas *tipo 1* y *tipo 2*. Hemos analizado el problema y trazado el origen de estas divergencias hacia inestabilidades numéricas de la ecuación discretizada en ausencia de ruido. Así, el número de trayectoria inestables disminuye cuando se reduce el paso de discretización θ-step. Hacer este paso suficientemente pequeño para eliminar las divergencias es muy costoso. Por ello ha sido propuesto otro camino: el paso adaptativo. Esto afina el paso solamente cuando es necesario para evitar inestabilidades. Los problemas se reducen también considerablemente cuanso se utiliza una discretización de orden mś alto, es decir, con correcciones de orden más alto en el paso.

Usando los métodos anteriores podemos circunvenir el problema de las inestabilidades, pero hemos visto que el resultado del cálculo de las historias temporales de las funciones a dos puntos difiere considerablemente del resulatdo exacto. Para el caso del potencial single-well, incluso no aparece el patrón oscilatorio característico del sistema gaussiano. Además la parte imaginaria es distinta de cero. Es esto indicativo de un comportamiento transitorio y será recuperado el comportamiento correcto para tiempos Langevin más largos?. Hemos testado esta hipótesis y, o bien este no es el caso, o bien los tiempos Langevin donde se recupera el buen comportamiento son prohibitivamente largos. Hemos comprobado que este resultado negativo es robusto bajo cambios en las condciones de contorno, en el rango de tiempos estudiado, y en la metodología utilizada para evitar inestabilidades. De todas formas, el problema desaparece para el caso gaussiano ($\lambda = 0$). Efectivamente, el problema de la convergencia hacia una solución incorrecta ha sido reportado en la literatura, y no hay una clara solución hasta donde conocemos. Así pues, desafortunadamente, este método no es competitivo frente a los otros utilizados aquí para estudiar nuestros sistemas cuárticos.

Un punto de vista muy interesante acerca de la naturaleza de las fluctuaciones cuánticas surge de la función de Wigner. Su carácter no positivo es una característica cuántica distintiva. Además, la aproximación clásica se entiende bien si nos fijamos en la ecuación de evolución de Moyal para esta función. Para nuestros sistemas cuánticos, sólo un término de dicha ecuación es responsable de los efectos cuánticos. Eliminando este término, no sólo se recupera la positividad sino también el carácter determinista de la evolución clásica. Así,

hemos analizado cómo puede una fuerza aleatoria alterar la ecuación y dar lugar a una ecución de Fokker-Planck idéntica a la de Moyal. A priori esto parece imposible. Pero efectivamente se puede ajustar un proceso markoviano de tipo Langevin con una fuerza aleatoria que consiga lo que queremos. Pero los valores esperados de los momentos de la fuerza necesaria para lograr nuestro objetivo requieren una distribución no positiva para dicha fuerza.

Esta idea nos lleva a presentar un nuevo método numérico, denominado *Método nQC*. La distribución no positiva para la fuerza es construida en términos de una apropiada función de distribución con una variable aleatoria adicional tipo Ising. Esta propiedad es heredada por la función de Wigner. Esto permite el uso de la teoría de muestras para aproximar los valores esperados de la nueva distribución. Los valores esperados cuánticos originales son ahora obtenidos en términos de estos valores medios pero con contribuciones de distinto signo. Al evolucionar el tiempo las mutuas cancelaciones tienden a crecer hasta que la señal es barrida por el error estadístico. Este es un típico sign-problem (problema de signo). El tiempo para el cual esto sucede puede ser estimado. Y el método es capaz de producir una descripción precisa de la evolución cuántica para un rango de tiempos, lo cual es suficiente en ciertos problemas físicos donde se involucran procesos rápidos, como en la época de preheating en el universo primordial. Extender este rango de tiempo es factible si se descarta como objetivo el calcular la evolución cuántica completa, y se intentan obtener correcciones cuánticas a la aproximación clásica en potencias de $\hbar^2$. Esta es también una forma de ir más allá de la aproximación clásica y estimar sus errores. Estas ideas han sido testadas comparando los resultados con la evolución exacta, así como con otros métodos. Esto se ha hecho para los sistemas sencillos de 1 dof estudiados antes, con potenciales single-well and double-well. Los resultados han sido muy satisfactorios y están de acuerdo con nuestras espectativas.

Al diseñar el mencionado método tuvimos en mente la necesidad de poder aplicarlo al caso de campos cuánticos. El tiempo de computación al aplicar el método es, para una muestra fija, comparable al de la aproximación clásica. Aunque existe el riesgo de que el tamaño de la muestra necesario para mantener una precisión estadística dada en el cálculo de correcciones cuánticas, crezca con el número de grados de libertad de tal forma que sea impracticable para el caso de campos. Esta y otras cuestiones han sido exploradas para la teoría de campos en 1+1 dimensiones discretizada en un retículo espacial

monodimensional periódico. El modelo ha sido estudiado por otros autores en el contexto de Cosmología. Nuestros resultados son positivos, y encontramos que los errores estadísticos en los efectos cuánticos de nuestros observables, para un tamaño de muestra fijo, permanecen estables con el número de grados de libertad.
Un estudio completo de este modelo, incluyendo efectos de renormalización, está previsto. La extensión a situaciones más realistas en 3+1 dimensiones, aunque computacionalmente más costoso, es factible con la tecnología actual.

14 Agradecimientos

Mi más sincero agradecimiento a todos aquellos que menciono a continuación:

–A Patricia, cuanto le debo a Patricia!. Su cariño y su comprensión han sido como un bálsamo para mí en este largo y tortuoso camino.
–A D. Antonio González-Arroyo, que me ofreció la extraordinaria oportunidad de realizar esta tésis en uno de los mejores departamentos de Física Teórica del planeta.
–A mis compañeros Andrés Díaz-Gil, Alfonso Sastre, Alberto Ramos, Emilio Ambite y Nuria López. Su amistad y su colaboración han sido absolutamente indispensables para mí.
–A toda mi familia. En especial a mis padres, mis hermanos y mis sobrinos. Su incondicional apoyo y confianza han sido para mí inestimables. Hago votos para que haya más doctores en la familia.
–A Peluchín, que me ha dado cariño y suerte en la última etapa de mi viaje.

References

[1] Claude Cohen, Bernard Diu, and Franck Laloe. *Quantum Mechanics*. John Wiley and Sons, 1977.

[2] Albert Messiah. *Quantum Mechanics*. Dover Publications, 1999.

[3] R. W. Hamming. *Numerical Methods for Scientists and Engineers*. Dover Publications, 1987.

[4] John H. Mathews. *Numerical Methods For Mathematics, Science, and Engineering*. Prentice Hall College Div, 1992.

[5] William H. Press, Saul A. Teukolsky, William T. Vetterling, and Brian P. Flannery. *Numerical Recipes: The Art of Scientific Computing*. Cambridge University Press, 1992.

[6] Michael E. Peskin and Daniel V. Schroeder. *An Introduction to Quantum Field Theory*. Addison-Wesley, 1995.

[7] Michele Maggiore. *A Modern Introduction to Quantum Field Theory*. Oxford Master Series in Physics, 2004.

[8] Istvan Montvay and Gernot Munster. *Quantum Fields on a Lattice*. Cambridge University Press, 1997.

[9] Jan Smit. *Introduction to Quantum Fields on a Lattice*. Cambridge University Press, 2002.

[10] Heinz Rothe. *Lattice Gauge Theories: An Introduction*. World Scientific Publishing, 2012.

[11] Kenneth G. Wilson. Confinement of Quarks. *Phys.Rev.*, D10:2445–2459, 1974.

[12] Malvin H. Kalos and Paula A. Whitlock. *Monte Carlo Methods*. John Wiley and Sons, 2008.

[13] E.Y. Loh, J.E. Gubernatis, R.T. Scalettar, S.R. White, D.J. Scalapino, et al. Sign problem in the numerical simulation of many-electron systems. *Phys.Rev.*, B41:9301–9307, 1990.

[14] Philippe de Forcrand. Simulating QCD at finite density. *PoS*, LAT2009:010, 2009.

[15] Julian S. Schwinger. Brownian motion of a quantum oscillator. *J. Math. Phys.*, 2:407–432, 1961.

[16] L. V. Keldysh. Diagram technique for nonequilibrium processes. *Zh. Eksp. Teor. Fiz.*, 47:1515–1527, 1964.

[17] Juergen Berges. Introduction to nonequilibrium quantum field theory. *AIP Conf.Proc.*, 739:3–62, 2005.

[18] A. Capella. Microscopic models of heavy ion interactions. *Lect.Notes Phys.*, 652:1–34, 2004.

[19] Debasish Banerjee, Jajati K. Nayak, and Raju Venugopalan. Two introductory lectures on high energy QCD and heavy ion collisions. *Lect.Notes Phys.*, 785:105–137, 2010.

[20] Alan H. Guth and So-Young Pi. The Quantum Mechanics of the Scalar Field in the New Inflationary Universe. *Phys. Rev.*, D32:1899–1920, 1985.

[21] Viatcheslav F. Mukhanov, H.A. Feldman, and Robert H. Brandenberger. Theory of cosmological perturbations. Part 1. Classical perturbations. Part 2. Quantum theory of perturbations. Part 3. Extensions. *Phys.Rept.*, 215:203–333, 1992.

[22] David Polarski and Alexei A. Starobinsky. Semiclassicality and decoherence of cosmological perturbations. *Class. Quant. Grav.*, 13:377–392, 1996.

[23] Claus Kiefer, David Polarski, and Alexei A. Starobinsky. Quantum to classical transition for fluctuations in the early universe. *Int.J.Mod.Phys.*, D7:455–462, 1998.

[24] J. Lesgourgues, David Polarski, and Alexei A. Starobinsky. Quantum-to-classical transition of cosmological perturbations for non-vacuum initial states. *Nucl. Phys.*, B497:479–510, 1997.

[25] Claus Kiefer and David Polarski. Why do cosmological perturbations look classical to us? *Adv.Sci.Lett.*, 2:164–173, 2009.

[26] Jurjen F. Koksma, Tomislav Prokopec, and Michael G. Schmidt. Decoherence in an Interacting Quantum Field Theory: Thermal Case. *Phys.Rev.*, D83:085011, 2011.

[27] Lev Kofman, Andrei D. Linde, and Alexei A. Starobinsky. Reheating after inflation. *Phys.Rev.Lett.*, 73:3195–3198, 1994.

[28] Lev Kofman, Andrei D. Linde, and Alexei A. Starobinsky. Towards the theory of reheating after inflation. *Phys.Rev.*, D56:3258–3295, 1997.

[29] Patrick B. Greene, Lev Kofman, Andrei D. Linde, and Alexei A. Starobinsky. Structure of resonance in preheating after inflation. *Phys.Rev.*, D56:6175–6192, 1997.

[30] S. Yu. Khlebnikov and I. I. Tkachev. Classical decay of inflaton. *Phys. Rev. Lett.*, 77:219–222, 1996.

[31] Tomislav Prokopec and Thomas G. Roos. Lattice study of classical inflaton decay. *Phys. Rev.*, D55:3768–3775, 1997.

[32] Gary N. Felder and Lev Kofman. The development of equilibrium after preheating. *Phys. Rev.*, D63:103503, 2001.

[33] Juan Garcia-Bellido, Margarita Garcia Perez, and Antonio Gonzalez-Arroyo. Symmetry breaking and false vacuum decay after hybrid inflation. *Phys. Rev.*, D67:103501, 2003.

[34] Jan Smit and Anders Tranberg. Chern-Simons number asymmetry from CP violation at electroweak tachyonic preheating. *JHEP*, 0212:020, 2002.

[35] Juan Garcia-Bellido, Margarita Garcia-Perez, and Antonio Gonzalez-Arroyo. Chern-Simons production during preheating in hybrid inflation models. *Phys. Rev.*, D69:023504, 2004.

[36] Anders Tranberg and Jan Smit. Baryon asymmetry from electroweak tachyonic preheating. *JHEP*, 0311:016, 2003.

[37] Meindert van der Meulen, Denes Sexty, Jan Smit, and Anders Tranberg. Chern-Simons and winding number in a tachyonic electroweak transition. *JHEP*, 0602:029, 2006.

[38] Anders Tranberg, Jan Smit, and Mark Hindmarsh. Simulations of cold electroweak baryogenesis: Finite time quenches. *JHEP*, 0701:034, 2007.

[39] Juan Garcia-Bellido, Daniel G. Figueroa, and Alfonso Sastre. A Gravitational Wave Background from Reheating after Hybrid Inflation. *Phys. Rev.*, D77:043517, 2008.

[40] Andres Diaz-Gil, Juan Garcia-Bellido, Margarita Garcia Perez, and Antonio Gonzalez-Arroyo. Magnetic field production during preheating at the electroweak scale. *Phys. Rev. Lett.*, 100:241301, 2008.

[41] Andres Diaz-Gil, Juan Garcia-Bellido, Margarita Garcia Perez, and Antonio Gonzalez-Arroyo. Primordial magnetic fields from preheating at the electroweak scale. *JHEP*, 07:043, 2008.

[42] Gert Aarts and Juergen Berges. Classical aspects of quantum fields far from equilibrium. *Phys.Rev.Lett.*, 88:041603, 2002.

[43] Gert Aarts. Spectral function at high temperature in the classical approximation. *Phys. Lett.*, B518:315–322, 2001.

[44] Andrei D. Linde. Hybrid inflation. *Phys.Rev.*, D49:748–754, 1994.

[45] T.S. Bunch and P.C.W. Davies Quantum Field Theory in de Sitter Space: Renormalization by Point Splitting *Proc.Roy.Soc.Lond.*, A360:117–134, 1978.

[46] M. Salle, J. Smit, and J.C. Vink. New initial conditions for quantum field simulations after a quench. *Nucl.Phys.Proc.Suppl.*, 106:540–542, 2002.

[47] Andreas Albrecht, Robert H. Brandenberger, and Richard Matzner. INFLATION WITH GENERALIZED INITIAL CONDITIONS. *Phys.Rev.*, D35:429, 1987.

[48] Gordon Baym. Selfconsistent approximation in many body systems. *Phys.Rev.*, 127:1391–1401, 1962.

[49] John M. Cornwall, R. Jackiw, and E. Tomboulis. Effective Action for Composite Operators. *Phys.Rev.*, D10:2428–2445, 1974.

[50] E. Calzetta and B.L. Hu. Nonequilibrium Quantum Fields: Closed Time Path Effective Action, Wigner Function and Boltzmann Equation. *Phys.Rev.*, D37:2878, 1988.

[51] Juergen Berges. Controlled nonperturbative dynamics of quantum fields out of equilibrium. *Nucl. Phys.*, A699:847–886, 2002.

[52] Fred Cooper and Emil Mottola. Initial Value Problems in Quantum Field Theory in the Large N Approximation. *Phys.Rev.*, D36:3114, 1987.

[53] D. Boyanovsky and H.J. de Vega. Quantum rolling down out-of-equilibrium. *Phys.Rev.*, D47:2343–2355, 1993.

[54] F.J. Cao and H.J. de Vega. Out-of-equilibrium nonperturbative quantum field dynamics in homogeneous external fields. *Phys.Rev.*, D65:045012, 2002.

[55] Steven Weinberg. Quantum contributions to cosmological correlations. *Phys.Rev.*, D72:043514, 2005.

[56] David Seery. One-loop corrections to a scalar field during inflation. *JCAP*, 0711:025, 2007.

[57] David H. Lyth and David Seery. Classicality of the primordial perturbations. *Phys.Lett.*, B662:309–313, 2008.

[58] John R. Klauder. A LANGEVIN APPROACH TO FERMION AND QUANTUM SPIN CORRELATION FUNCTIONS. *J.Phys.A*, A16:L317, 1983.

[59] John R. Klauder. COHERENT STATE LANGEVIN EQUATIONS FOR CANONICAL QUANTUM SYSTEMS WITH APPLICATIONS TO THE QUANTIZED HALL EFFECT. *Phys.Rev.*, A29:2036–2047, 1984.

[60] G. Parisi. ON COMPLEX PROBABILITIES. *Phys.Lett.*, B131:393–395, 1983.

[61] J. Berges and I.-O. Stamatescu. Simulating nonequilibrium quantum fields with stochastic quantization techniques. *Phys.Rev.Lett.*, 95:202003, 2005.

[62] Gert Aarts, Frank A. James, Erhard Seiler, and Ion-Olimpiu Stamatescu. Adaptive stepsize and instabilities in complex Langevin dynamics. *Phys.Lett.*, B687:154–159, 2010.

[63] Gert Aarts, Erhard Seiler, and Ion-Olimpiu Stamatescu. The Complex Langevin method: When can it be trusted? *Phys. Rev.*, D81:054508, 2010.

[64] Gert Aarts, Frank A. James, Erhard Seiler, and Ion-Olimpiu Stamatescu. Complex Langevin: Etiology and Diagnostics of its Main Problem. *Eur.Phys.J.*, C71:1756, 2011.

[65] Eugene P. Wigner. On the quantum correction for thermodynamic equilibrium. *Phys. Rev.*, 40:749–760, 1932.

[66] M. Hillery, R. F. O'Connell, M. O. Scully, and Eugene P. Wigner. Distribution functions in physics: Fundamentals. *Phys. Rept.*, 106:121–167, 1984.

[67] J. E. Moyal. Quantum mechanics as a statistical theory. *Proc. Cambridge Phil. Soc.*, 45:99–124, 1949.

[68] E. A. Remler. Use of the Wigner Representation in Scattering Problems. *Annals Phys.*, 95:455–495, 1975.

[69] S. John and E. A. Remler. Solution of the quantum liouville equation as a stochastic process. *Annals Phys.*, 180:152–165, 1987.

[70] Stanislaw Mrowczynski and Berndt Muller. Wigner functional approach to quantum field dynamics. *Phys. Rev.*, D50:7542–7552, 1994.

[71] Sangyong Jeon. The Boltzmann equation in classical and quantum field theory. *Phys. Rev.*, C72:014907, 2005.

[72] Teiji Kunihiro, Berndt Muller, Akira Ohnishi, and Andreas Schafer. Towards a Theory of Entropy Production in the Little and Big Bang. *Prog. Theor. Phys.*, 121:555–575, 2009.

[73] A. Bonasera, V. N. Kondratyev, A. Smerzi, and E. A. Remler. Nuclear dynamics in the Wigner representation. *Phys. Rev. Lett.*, 71:505–508, 1993.

[74] Sarah John. Nucleon-nucleon cross sections via stochastic processes in phase space: One-dimensional scattering. *Phys. Rev.*, C76:014002, 2007.

[75] G. Schubert, V. S. Filinov, K. Matyash, R. Schneider, and H. Fehske. Comparative Study of Semiclassical Approaches to Quantum Dynamics. *International Journal of Modern Physics C*, 20:1155–1186, 2009.

[76] Kuang-chao Chou, Zhao-bin Su, Bai-lin Hao, and Lu Yu. Equilibrium and Nonequilibrium Formalisms Made Unified. *Phys.Rept.*, 118:1, 1985.

[77] Juergen Berges and Jurgen Cox. Thermalization of quantum fields from time reversal invariant evolution equations. *Phys.Lett.*, B517:369–374, 2001.

[78] Gert Aarts and Juergen Berges. Nonequilibrium time evolution of the spectral function in quantum field theory. *Phys.Rev.*, D64:105010, 2001.

[79] Gert Aarts, Daria Ahrensmeier, Rudolf Baier, Juergen Berges, and Julien Serreau. Far from equilibrium dynamics with broken symmetries from the 2PI - 1/N expansion. *Phys.Rev.*, D66:045008, 2002.

[80] S. Juchem, W. Cassing, and C. Greiner. Quantum dynamics and thermalization for out-of-equilibrium phi**4 theory. *Phys.Rev.*, D69:025006, 2004.

[81] Juergen Berges, Szabolcs Borsanyi, and Julien Serreau. Thermalization of fermionic quantum fields. *Nucl.Phys.*, B660:51–80, 2003.

[82] J. Berges, S. Borsanyi, and C. Wetterich. Prethermalization. *Phys.Rev.Lett.*, 93:142002, 2004.

[83] Gert Aarts and Jose M. Martinez Resco. Transport coefficients from the 2PI effective action. *Phys.Rev.*, D68:085009, 2003.

[84] J. Berges, Sz. Borsanyi, U. Reinosa, and J. Serreau. Renormalized thermodynamics from the 2PI effective action. *Phys.Rev.*, D71:105004, 2005.

[85] A. Arrizabalaga and U. Reinosa. Finite-temperature Phi**4 theory from the 2PI effective action: Two-loop truncation. *Eur.Phys.J.*, A31:754–757, 2007.

[86] Juergen Berges and Julien Serreau. Parametric resonance in quantum field theory. *Phys.Rev.Lett.*, 91:111601, 2003.

[87] Alejandro Arrizabalaga, Jan Smit, and Anders Tranberg. Tachyonic preheating using 2PI-1/N dynamics and the classical approximation. *JHEP*, 0410:017, 2004.

[88] J. Berges, D. Gelfand, and J. Pruschke. Quantum theory of fermion production after inflation. *Phys.Rev.Lett.*, 107:061301, 2011.

[89] Gert Aarts and Anders Tranberg. Nonequilibrium dynamics in the O(N) model to next-to-next-to-leading order in the 1/N expansion. *Phys.Rev.*, D74:025004, 2006.

[90] Gert Aarts, Nathan Laurie, and Anders Tranberg. Effective convergence of the 2PI-1/N expansion for nonequilibrium quantum fields. *Phys.Rev.*, D78:125028, 2008.

[91] Bogdan Mihaila, Fred Cooper, and John F. Dawson. Resumming the large N approximation for time evolving quantum systems. *Phys.Rev.*, D63:096003, 2001.

[92] G. Parisi and Yong-shi Wu. Perturbation Theory Without Gauge Fixing. *Sci.Sin.*, 24:483, 1981.

[93] W. Grimus and H. Huffel. PERTURBATION THEORY FROM STOCHASTIC QUANTIZATION OF SCALAR FIELDS. *Z.Phys.*, C18:129, 1983.

[94] Poul H. Damgaard and Helmuth Huffel. Stochastic Quantization. *Phys.Rept.*, 152:227, 1987.

[95] H. Huffel and H. Rumpf. STOCHASTIC QUANTIZATION IN MINKOWSKI SPACE. *Phys.Lett.*, B148:104–110, 1984.

[96] H. Huffel and P.V. Landshoff. STOCHASTIC DIAGRAMS AND FEYNMAN DIAGRAMS. *Nucl.Phys.*, B260:545, 1985.

[97] Hiromichi Nakazato. THERMAL EQUILIBRIUM IN MINKOWSKI STOCHASTIC QUANTIZATION. *Prog.Theor.Phys.*, 77:20, 1987.

[98] E. Gozzi. LANGEVIN SIMULATION IN MINKOWSKI SPACE. *Phys.Lett.*, B150:119, 1985.

[99] Jan Ambjorn and S.K. Yang. NUMERICAL PROBLEMS IN APPLYING THE LANGEVIN EQUATION TO COMPLEX EFFECTIVE ACTIONS. *Phys.Lett.*, B165:140, 1985.

[100] Hiromichi Nakazato and Yoshiya Yamanaka. MINKOWSKI STOCHASTIC QUANTIZATION. *Phys.Rev.*, D34:492, 1986.

[101] Ernst-Michael Ilgenfritz and Jochen Kripfganz. COMPLEX LANGEVIN SIMULATION OF REAL TIME QUANTUM EVOLUTION. 1986.

[102] John R. Klauder and Wesley P. Petersen. Spectrum of certain non-self-adjoint operators and solutions of Langevin equations with complex drift. *Journal of Statistical Physics*, 39:20, 1985.

[103] H. Gausterer. On The correct convergence of complex Langevin simulations for polynomial actions. *J.Phys.A*, A27:1325–1330, 1994.

[104] Kazuya Yuasa and Hiromichi Nakazato. Transition amplitude within the stochastic quantization scheme: Perturbative treatment. 1996.

[105] Juergen Berges and Szabolcs Borsanyi. Nonequilibrium quantum fields from first principles. *Eur.Phys.J.*, A29:95, 2006.

[106] J. Berges, Sz. Borsanyi, D. Sexty, and I.-O. Stamatescu. Lattice simulations of real-time quantum fields. *Phys.Rev.*, D75:045007, 2007.

[107] Gert Aarts. Can complex Langevin dynamics evade the sign problem? *PoS*, LAT2009:024, 2009.

[108] Gert Aarts and Frank A. James. The XY model at finite chemical potential using complex Langevin dynamics. *PoS*, LATTICE2010:321, 2010.